UNIVERSITY OF SOUTHAMPTON

FACULTY OF ENGINEERING, SCIENCE & MATHEMATICS

School of Engineering Sciences

Ageing and Strengthening of Cold-rolled Al-Mg(-Cu)-Si-Mn Alloys: Experimental Analysis and Modelling

by

Zhihua ZHU

Thesis submitted for the degree of Doctor of Philosophy

October 2006

UNIVERSITY OF SOUTHAMPTON

ABSTRACT

FACULTY OF ENGINEERING, SCIENCE & MATHEMATICS
SCHOOL OF ENGINEERING SCIENCES

DOCTOR OF PHILOSOPHY

AGEING AND STRENGTHENING OF COLD-ROLLED Al-Mg(-Cu)-Si-Mn ALLOYS: EXPERIMENTAL ANALYSIS AND MODELLING

BY ZHIHUA ZHU

Application prospects in the automotive industry have led to increasing interests in the studies on Al-Mg-Cu-Si alloys. In this PhD thesis, nine Al-(1-3)Mg-(0-0.4)Cu-0.15Si-0.25Mn (in wt%) alloys with potential applications in both packaging and automotive industries have been investigated. The principal aim of the thesis is to elucidate the relation between processing and the final strength of the alloys.

By means of mechanical testing, differential scanning calorimetry (DSC) and transmission electron microscopy (TEM), this study identified several mechanisms that influence the final strength of cold rolled alloys during ageing: solid solution, work hardening, recovery and precipitation. Microstructure analyses using field emission gun scanning electron microscopy (FEG-SEM) and energy dispersive spectroscopy (EDS) revealed the formation of undissolved coarse particles consuming the small Si addition, which influences age hardening behaviour of the alloys. Tensile testing was performed to evaluate the strength and work hardening of the alloys. The integrated results from mechanical testing and microstructural examinations using SEM/EDS, TEM and DSC showed that for cold worked samples, β″ (Mg_2Si) phase contributes to age hardening of Cu-free alloys, whilst both β″ and S (Al_2CuMg) contribute to that of Cu-containing alloys.

Based on experimental findings, a multi-mechanistic yield strength model for hardening and softening has been developed to elucidate the relation between processing and the final strength. The model consists of three main components: i) dissolution of intermetallic phase, most notably the Mg_2Si phase; ii) precipitation of two strengthening phases: β″ and S; iii) strengthening contributions from several mechanisms: solution strengthening, dislocation strengthening (i.e. work hardening and recovery) and precipitation hardening due to the two strengthening phases. The model was calibrated using tensile data and tested using separate unseen tensile data and was applied to predict the yield strength evolution of cold worked samples during ageing. An accuracy of about 8.6 MPa (about 4% of the total range of strengths) has been achieved.

The relation of work hardening with level of cold work, alloy composition and ageing time has been analysed using tensile test data. Three primary findings were obtained: i) cold worked samples usually have the lowest work hardening rate (WHR); ii) WHR increases after 30-minute ageing due to recovery and iii) WHR increases with decreasing level of cold work and increasing Mg and Cu contents. Work hardening models based on the Kocks-Mecking (KM) model and the Kocks-Mecking-Estrin (KME) model have been utilized to explain the main trends. The modelling results showed that the KM model is able to simulate the work hardening behaviour of cold worked samples reasonably well. However, the KME model is insufficient to fully describe the work hardening behaviour of cold-worked-and-aged samples.

List of Contents

List of Tables

Declaration of Authorship

I, …**Zhihua ZHU**…., declare that the thesis entitled
Ageing and Strengthening of Cold-rolled Al-Mg(-Cu)-Si-Mn Alloys: Experimental Analysis and Modelling
and the work presented herein are my own. I confirm that:

- this work was done wholly under the supervision of Professor Marco J. Starink, at the Materials Research Group, School of Engineering Sciences, University of Southampton, while in candidature for a PhD degree at this University during the period of October 2002 to March 2006;
- this thesis does not exceed 75,000 words and no part of the thesis has previously been submitted for a degree or any other qualification at this University or any other institution;
- where the published work of others was consulted, this is always clearly attributed;
- where the work of others have been quoted, the source is always given. With the exception of such quotations, this thesis is original and entirely represents my own work to the best of my knowledge;
- all main sources of help have been acknowledged;
- parts of this work have been published or presented as:

1. Zhu, Z. and Starink, M.J., **A Yield Strength Model for the Ageing Behaviour of Cold-rolled Al-Mg(-Cu)-Si Alloys**, oral presentation in Euromat 2005, 2005: Prague, Czech Republic.
2. Zhu, Z. and Starink, M.J, **Influence of cold work and solutionising temperature on age hardening capability of Al-Mg-Mn alloys with small Cu and Si additions**, in International conference on solid-solid phase transformations in inorganic materials, Howe, J. (Eds), 2005, Phoenix, Arizona, USA: TMS (The Minerals, Metals & Materials Society).
3. Wang, S.C., Zhu, Z. and Starink, M.J., **Estimation of dislocation densities in cold rolled Al-Mg-Cu-Mn alloys by combination of yield strength data, EBSD and strength models**, J MICROSC-OXFORD, 2005, Vol. 217: p. 174.*
   * I contributed to some results of tensile testing experiments.
4. Zhu, Z. and Starink, M.J., **Analysis of intermetallics in cold rolled Al-Mg-Mn alloys microalloyed with Si and Cu**, in Proceedings of the tenth postgraduate conference in engineering materials, 2004, Southampton, UK: p. 40.
5. Zhu, Z. and Starink, M.J. **Recovery and precipitation in cold-rolled Al-(1-3)Mg-(0-0.4)Cu-Mn alloys**, in Proceedings of the ninth postgraduate conference in engineering materials, 2003, Southampton, UK: p. 27.


（Zhihua Zhu）

October 2006

Acknowledgements

I would like to express my cordial gratitude to Professor Marco Starink for his excellent supervision and encouragement. Whatever I gain is indebted to him, his contribution and inspiration that put me in the right direction towards accomplishing my research. I also would like to acknowledge the financial support from the School of Engineering Sciences and Novelis Technology (former Alcan International). I would like to thank the valuable discussion from Drs S. Court, G. Mahon and M. Hao. Dr G. Mahon was specially thanked for his efforts in the production of the materials used in this research.

Thanks are due to the funds for international conferences from Royal Academy of Engineering (RAE), The Armourers & Brasiers' Company and The Institute of Materials, Minerals & Mining (IOM3). Professors W. G. Price and Mark Spearing are acknowledged for their support in my application for these funds.

The valuable and efficient support from the technical staff is gratefully acknowledged, especially that from Mr Eric Bonner, Mr Dave Beckett and Mr Erik Roszkowiak. I would also like to thank Dr Philippa Reed and Mrs Gwyneth Skiller for their kind help in the past years.

Many thanks to all the colleagues in the materials research group for their help and friendship. Special thanks are due to Dr Brian Mellor for his valuable comments and suggestions on this work. Particularly great thanks to Dr Mark Joyce for his help out in tensile tests, Dr Nong Gao for assisting DSC experiments, Dr Shuncai Wang for helping using FEG-SEM, EBSD and TEM, Dr Jialin Yan for valuable discussion in the aspect of yield strength modelling. Thanks to the friendship with Ling, Louise, Pat, Imran, Ali, Jun, Jian, Kern Hauw …, which makes my life easier and happier during the past years in Southampton.

Finally, I would like to express my deep gratitude to my family for their persistent support and encouragement. Special thanks go to my mother, my husband and my baby daughter, to whom I am indebted forever.

Dedicated in the memory of my father

Nomenclature

A	a constant
$\vec{b}$, b	Burgers vector, length of Burgers vector
B_t	a constant
c	instantaneous solute concentration in the matrix
c_0	initial concentration of an alloying element (e.g., Mg or Cu) in the matrix
c_g	gross concentration
c_e	the solubility limits of an alloying element in the matrix
c_{eff}	the effective concentration of an alloying element
d	diameter of a precipitate
D	grain size
e	engineering strain
E	the Young's modulus
E_a	the activation energy
E_{co}	the activation energy for coarsening
E_g	the effective activation energy for dislocation glide
E_{rec}	the activation of energy for recovery
E_{rec0}	a constant (i.e. the activation of energy for recovery at $\sigma = 0$)
E_{ppt}	the activation energy of a precipitation reaction
F	Load during tensile tests
f , $\bar{f}$	volume fraction of precipitates
f_s	volume fraction of S phase formed during ageing
f_β	volume fraction of β phase formed during ageing
f_a	a factor introduced to describe the influence of dislocation-particle

	interactions on the recovery rate
f_i	the volume fraction of cell interior
f_w	the volume fraction of cell walls
f_{cl}	the volume fraction of the clusters
$f_{\sigma\text{-}Hv}$	a conversion factor to convert Vickers hardness to stress
G	the shear modulus of aluminium
h_0	the entry thickness before rolling
h	the exit thickness after rolling
H_v	Vickers hardness
k	a rate constant for precipitation
k_0	a pre-exponential constant for precipitation
k_1	a constant in the KM model controlling dislocation storage/generation
$k_1^{Mg}, k_1^{Cu}, k_1^0$	constants
k_2	a function of temperature and strain rate in the KM model controlling dynamic recovery
k_B	Boltzmann's constant
k_c	a rate constant for coarsening of precipitates
k_{c0}	a pre-exponential factor for coarsening of precipitates
k_{Cu}	solid solution strengthening coefficient due to Cu
k_d	a constant determined by the mean free path or spacing
k_{Mg}	solid solution strengthening coefficient due to Mg
k_{ND}	a constant
k_{rec}	a pre-exponential constant for recovery
K_{wh}	strength coefficient
K_{wh}^{Cu}, K_{wh}^{Mg}	constants

K_{wh}^{0}	a constant
k_{ε}	a constant
$k_{\dot{\gamma}}$	a factor introduced to consider the shear strain rate influence on shear stress
$k_{\dot{\varepsilon}}$	a factor introduced to consider the strain rate influence on polycrystalline stress
K_{rc} , K_{ε}	strength coefficients
$\vec{l}$	the dislocation line
l_d	the precipitate/particle spacing
$\bar{l}$	the average precipitate size
$\bar{l}_0$	the average size of the precipitates at the start of coarsening
$\bar{l}_g$	the average precipitate size at nucleation/growth stage
$\bar{l}_c$	the average precipitate size at coarsening stage
M	the Taylor factor
n	a reaction exponent
n_{ss}	an exponent in solid solution strengthening model
n_{wh}	strain hardening exponent
p_k	a constant
p_1, p_2, p_3	constants
$p_1^{'}$, $p_2^{'}$	constants
$p_1^{''}$, $p_2^{''}$	constants
q_b , q_c , q_w	scaling constants for w, δ and ρ_w , respectively in the Nes Model
r , $\bar{r}$	the mean radius of precipitates
r_c	cold rolling reduction
R	the gas constant
R_{rec}	the extent of the recovery or the fraction residual strain hardening

S	the area of cross section of a tensile specimen
S_0	the original cross section area of a tensile specimen
t	a time
$\hat{t}$	a reference time
$\hat{t}_0$	a constant
t_{eq}	equivalent time
t_p	equivalent time at a peak temperature of a reaction in a DSC curve
T	temperature
T_p	peak temperature of a reaction in a DSC curve
T_s	solutionising temperature
$\hat{T}$	a reference temperature
T_{iso}	an isothermal temperature
v	the average dislocation glide velocity
V	activation volume
V_{rec}	the activation volume of the elementary recovery events
v_0	the attack frequency
v_D	the Debye frequency
υ	the Poisson's ratio
w	cell wall thickness
x_{Mg_2Si}	the amount of undisolved Mg_2Si particles formed during solution treatment
x_s	the amount of S precipitates formed during ageing
x_{su}	the amount of undisolved S particles formed during solution treatment
x_β	the amount of β″ precipitates formed during ageing
X_R	a parameter representing one property of the materials (e.g, yield strength)
X_0	the value of X_R at $t=0$

α	the fraction transformed of a precipitate phase
α_ρ	a constant
α_0, α_1, α_2	constants
α_x	the transformed fraction of phase *x* (*x*=S, cluster etc.)
β_{hr}	heating rate of a DSC scan
δ	cell size
δ_0	cell size at time *t=0*
λ	the angle between the slip direction and the applied stress direction
ϕ	the angle between the applied stress direction and the normal to slip plane
θ	instantaneous work hardening rate
θ_{II}	the slope of the stress-strain curve in stage II
Θ	the average work hardening rate
ρ	dislocation density
ρ_0	the initial dislocation density at $\gamma = 0$ or at the start of ageing
ρ_i	immobile dislocation density in the cell interior
ρ_m	the mobile dislocation density
ρ_{m0}	the initial dislocation density of mobile dislocations
ρ_f	the density of relatively immobile, or forest dislocations
ρ_{f0}	the initial density of forest dislocations
ρ_w	the dislocation density in the cell wall
ρ_c	the dislocation density in the cell interior
γ	shear strain
$\dot{\gamma}$	shear strain rate
$\hat{\dot{\gamma}}$	a reference strain rate
ε	polycrystalline strain

ε_c	a characteristic strain for a material
ε_1	the initial strain at the start of a test
$\bar{\varepsilon}$	von-Mises equivalent strain
ε_e	elastic strain
ε_p	plastic strain
$\dot{\varepsilon}$	polycrystalline strain rate
$\dot{\varepsilon}_p$	the plastic relaxation strain rate
η_i	the impingement exponent
τ	shear stress
$\hat{\tau}$	a reference shear stress
τ_c	the shear stress contribution due to cell
τ_{crss}	critical resolved shear stress
τ_{effx}	effective shear stress
τ_i	friction shear stress
τ_{Orowan}	Orowan stress
τ_p	the shear stress contribution due to non-deformable particles (dispersoids)
τ_s	the saturation shear stress
τ_t	the thermal component to the shear stress
τ_w	the shear stress contribution due to cell wall
τ_ρ	the flow stress due to obstacle/immobile dislocations
$\Delta\tau_{cl}$	the strengthening due to cluster
$\Delta\tau_d$	the critical resolved shear stress contribution due to dislocation strengthening
$\Delta\tau_{d0}$	the value of $\Delta\tau_d$ at a ageing time $t=0$

$\Delta\tau_{d\&ppt}$	the critical resolved shear stress contribution due to dislocation strengthening and precipitation hardening
$\Delta\tau_{ppt}$	the critical resolved shear stress contribution due to precipitation hardening
$\Delta\tau_{S}$	the strengthening due to S precipitates
$\Delta\tau_{ss}$	the contribution of solid solution strengthening to critical resolved shear stress
$\Delta\tau_{tot}$	the total resolved shear stress
σ	polycrystalline stress
σ_0	the flow stress at *t=0*
$\sigma_{0.2}$	the 0.2% proof strength
σ_1	the initial stress at the start of a test
σ_b	the base strength
σ_{ext}	external stress
σ_i	the frictional stress
σ_p	plastic stress
σ_{rex}	the yield strength in the undeformed or fully recrystallized state
σ_{wh}	the yield strength in the deformed state
σ_y	yield strength
$\Delta\sigma_d$	the stress contribution due to dislocation strengthening
$\Delta\sigma_d^0$	the value of $\Delta\sigma_d$ at the ageing time *t=0*
$\Delta\sigma_{wh}$	the yield strength increment due to work hardening
ΔH^x	the formation enthalpy of a phase *x* (*x*=S, cluster etc.)
ΔG	the difference between the shear moduli of the matrix and the clusters
ΔS	the formation entropy of a phase (e.g. S and cluster etc.)
$\Delta\tau_{ppt}$	the extra shear stress required to cut through a precipitate

Abbreviations

3IVM	Three-internal-state-variable model
AA	Aluminium Association
APB	Antiphase boundary
APFIM	Atom probe field ion microscopy
BCC	Body centred cubic
BEI	Backscattered electron image (in SEM)
BF	Bright field
CBS	Can body stock
CES	Can end stock
CRSS	Critical resolved shear stress
CW	Cold work
DC	Direct chill
DF	Dark field
DSC	Differential scanning calorimetry
DWI	Draw and wall iron
D&I	Draw and iron
EBSD	Electron backscattered diffraction
EDS	Energy dispersive spectroscopy
FCC	Face centred cubic
FEG-SEM	Field emission gun scanning electron microscope
GP zone	Guinier-Preston zone
GPB zone	Guinier-Preston-Bagaratsky zone
HCP	Hexagonal close packed

HRTEM	High resolution transmission electron microscopy
HV	Vickers hardness
IADS	International Alloy Designation System
KM	Kocks-Mecking
KME	Kocks-Mecking-Estrin
LSM	Least square method
LSW	Lifshitz-Slyozov-Wagner
NPL	National Physical Laboratory
ODF	Orientation distribution function
OP-S	Oxide polishing suspension
PET	Polyethylene tetraphthalate
PS	Proof strength
RMSE	Root mean squared error
RT	Room temperature
SAD	Selected area diffraction
SFE	Stacking fault energy
SSSS	Supersaturated solid solution
ST	Solution treated
STH	Solution treatment at high temperature, e.g. 550°C
STL	Solution treatment at low temperature, e.g. 500°C
SZ	Starink-Zahra
TEM	Transmission electron microscopy
UTS	Ultimate tensile strength
WHM	Work hardening model
WHR	Work hardening rate

1 Introduction

1.1 Background

Aluminium alloys are used in a wide range of applications in transport, packaging, building and general engineering sectors. The combination of alloys (based on Al-Mg-Mn-(Cu)) and thermo-mechanical processes studied in this work are especially relevant for beverage can and car body panel applications.

Al-Mn (3XXX) and Al-Mg (5XXX) alloys are non-heat-treatable aluminium alloys that have been widely used in beverage cans for decades [1-5]. Specifically, AA3104/3004 and AA5182 alloys have long been used as can body stock and can end stock, respectively [1, 3, 6]. Although the market now is mature, there is a fierce competition coming from alternative materials such as steel, polyethylene tetraphthalate (PET) etc. [1, 2]. The solution to improving the competitiveness of Al alloys is to reduce the costs by improving process efficiency and innovations in weight reduction or downgauging of the canstock [1, 2, 5]. Enhanced surface performance and improved metallurgy (microstructure and properties) are required in order to achieve downgauging of the canstock. Therefore, it is essential to understand (both qualitatively and quantitatively) the relation between processing, microstructure and properties.

In recent decades, there is a new trend in the automobile industry to use aluminium alloys as car body panels to reduce weight and thus improve fuel economy and emissions [7, 8]. Both non-heat-treatable 5XXX Al-Mg alloys and heat-treatable Al-Cu, Al-Mg-Si-Cu and Al-Mg-Si alloys of 2XXX and 6XXX series are used. Although the Al-Mg-Mn 5XXX alloys have good formability, they have a relatively low strength with a tendency of Lüders band formation, which restricts their use to interior structural applications [7]. Hence, for automotive applications, there is a growing trend to exploit new alloys. 5XXX alloys (especially AA5182 and AA5052) with Cu additions are very promising candidates for these applications because of their excellent formability, good strength and the benefits of precipitation hardening during paint-baking due to Cu additions [9-18]. However, precipitation hardening induced by Cu additions may make the interactions between work hardening, recovery and precipitation more complicated during processing.

The alloys used for the above-mentioned canstock and automotive applications are generally based on Al-Mg-Mn alloys with small additions of Cu. The alloys are warm or cold rolled to achieve thin gauge. During the processing of these alloys with low Cu:Mg ratios, precipitation of strengthening phases occurs during hot and cold rolling as well as during heat treatment after cold rolling. In both cases, precipitation will change the yield stress and the work hardening, which will affect subsequent further working of the alloys. After cold rolling, the alloys for beverage can application are used in a work hardened condition, but for car body application, they will be supplied to car manufacturers with O temper (annealed) due to the higher requirement of excellent formability during car body forming. For both applications, coating/painting and baking are needed as a final procedure. Both recovery and precipitation will occur during the baking process of the cold worked alloys.

1.2 Project aims

The present project, in collaboration with Alcan International, one of the world's major producers of aluminium products, aims at providing a detailed quantitative understanding of the relation between processing and the final strength. Consequently, the understanding may provide a sound basis to enable the production of improved quality of cans with reduced wall thickness and car body panels.

As work hardening, recovery and precipitation may occur during processing, it is important to elucidate how these micro-mechanisms influence the final strength and properties through laboratory experiments. The aim of this PhD project is to investigate models that quantitatively describe these mechanisms.

To this aim, nine Al-(1-3)Mg-(0-0.4)Cu-0.15Si alloys will be studied. Similar to Al-Mg-Si alloys, Mg_2Si precipitation may occur in the Cu-free alloys. For the Cu-containing alloys, precipitation is more complicated and involves several precipitates. A complete analysis of precipitate crystallography and multiple precipitation mechanisms in each of the nine alloys is beyond the scope of this PhD thesis. (For selected alloys this is pursued by other industry funded university based groups.) Instead, the work is focussed on devising a model for the relation between processing and strengthening of the cold-rolled and cold-rolled-and-aged alloys, which incorporates existing and some newly obtained understanding of mechanisms. The model will be tested through a detailed quantitative comparison with extensive yield strength data on nine alloys, and a qualitative comparison

with microstructural data obtained from Scanning Electron Microscopy (SEM)/Energy Dispersive Spectroscopy (EDS), Differential Scanning Calorimetry (DSC) and Transmission Electron Microscopy (TEM).

1.3 Methodology

In this study, nine Al-Mg alloys (1-3 wt% Mg) with/without Cu additons (0-0.4 wt%) were designed, cast, homogenized, hot-rolled, solution treated and cold rolled with three different reductions (10%, 40% and 90%).

Work hardening, recovery and precipitation and their interactions in the cold-worked nine alloys during ageing will then be analysed by a combination of detailed experimental studies and modelling techniques. Field Emission Gun Scanning Electron Microscopy (FEG-SEM) combined with EDS technique will be performed for the analysis of coarse intermetallic particles. The experimental results will be compared with thermodynamic calculations (provided by collaborators). Electron Backscatter Diffraction (EBSD) will be conducted for grain structure and texture analysis. DSC will be performed mainly to study precipitation in conjunction with the identification of precipitates by means of TEM. Hardness tests will be performed for a preliminary study of precipitation and recovery in the cold worked alloys during ageing. Hardness tests will also be conducted on solution treated samples to study the precipitation behaviour without the influence of cold work and the influence of solutionising temperature. Based on the initial evaluation of precipitation behaviour in the cold worked alloys studied by hardness tests, the ageing conditions for tensile tests will be determined and tensile tests will be conducted. Strength and work hardening will be obtained from tensile test data. The relation of strength and work hardening with cold rolling reduction, ageing condition and alloy composition will be further analysed. These results will be used for the quantitative modelling of yield strength and work hardening.

To provide a quantitative understanding of the experimental results and predictive tools for predicting yield strength and work hardening, a yield strength model and a work hardening model will be devised. The yield strength model combining the contributions from the base strength, solid solution strengthening due to Mg and Cu, dislocation strengthening (i.e. work hardening and recovery) and precipitation hardening will be developed to quantitatively elucidate the yield strength evolution of the cold worked samples of all the nine alloys during isothermal ageing. One-parameter work hardening

models, e.g. the Kocks-Mecking (KM) [19, 20] and Kocks-Mecking-Estrin (KME) [21, 22] models, will be utilized to model the work hardening behaviour of cold-worked samples and cold-worked-and-aged samples during tensile tests.

1.4 Outline of the thesis

This PhD thesis is divided into 8 chapters. Following on the present introduction, the literature review in Chapter 2 consists of a brief review of processing of wrought aluminium alloys, a review of physical metallurgy of Al-Mg(-Cu)-Si-Mn alloys and their applications for packaging and automotive body. The second part of the literature review in Chapter 3 incorporates an introduction of fundamentals of dislocations, a review of work hardening models, recovery models and precipitation hardening models. A description of materials production and experimental techniques is included in Chapter 4. In Chapter 5, experimental results and a discussion of the results are presented. In Chapter 6, a yield strength model for the ageing behaviour of cold worked samples has been developed and applied to quantitatively describe and predict the yield strength evolution during ageing. The characterisation and preliminary modelling of work hardening is conducted in Chapter 7. Finally, the conclusions from this PhD thesis are drawn and some relevant future work is recommended, which are presented in Chapter 8.

References

1. Courbon, J., Mater. Sci. Forum, **331-337**, 2000, p. 17.
2. Koyama, K., Urayoshi, S. and Tanaka, T., Furukawa Review, **18**, 1999, p. 97.
3. Polmear, I.J., ***Light Alloys: Metallurgy of the Light Metals*** (3rd edition), New York, Halsted Press, John Wiley & Sons, Inc., 1996.
4. Ding, S. and Morris, J.G., Metall. Mater. Trans. A, **28**, 1997, p. 2715.
5. Marshall, G.J., Mater. Sci. Forum, **217-222**, 1996, p. 19.
6. Sanders, R.E., Lege, D.J. and Hartman, I.L., Aluminium, **65**, 1989, p. 941.
7. Burger, G.B., Gupta, A.K., Jeffrey, P.W. and Lloyd, D.J., Mater. Charact., **35**, 1995, p. 23.
8. Cole, G.S. and Sherman, A.M., Mater. Charact., **35**, 1995, p. 3.
9. Delapuente, S.M., Verlinden, B. and Delaey, L., J. Mater. Sci., **29**, 1994, p. 6167.
10. Rabet, L., Ratchev, P., Verlinden, B. and Van Houtte, P., Mater. Sci. Forum, **217**, 1996, p. 465.
11. Ratchev, P., Verlinden, B. and Van Houtte, P., Scripta Metall. Mater., **30**, 1994, p. 599.
12. Ratchev, P., Verlinden, B. and Van Houtte, P., Acta Metall. Mater., **43**, 1995, p. 621.
13. Ratchev, P., Verlinden, B., VanHoutte, P. and De Smet, P., Mater. Sci. Forum, **217**, 1996, p. 1187.
14. Ratchev, P., Verlinden, B., Van Houtte, P. and De Smet, P., Mater. Sci. Eng. A, **A222**, 1997, p. 189.
15. Ratchev, P., Verlinden, B., De Smet, P. and Van Houtte, P., Scripta Mater., **38**, 1998, p. 1195.
16. Ratchev, P., Verlinden, B., De Smet, P. and Van Houtte, P., Acta Metall. Mater., **46**, 1998, p. 3523.
17. Samajdar, I., Ratchev, P., Verlinden, B., Van Houtte, P. and De Smet, P., Mater. Sci. Eng. A, **247**, 1998, p. 58.
18. Ratchev, P., Verlinden, B., and Zahra, A.M., Mater. Sci. Forum, **331-337**, 2000, p. 1095.
19. Kocks, U.F., J. Eng. Mater.-T. ASME, **98**, 1976, p. 77.
20. Mecking, H. and Kocks, U.F., Acta Metall. Mater., **29**, 1981, p. 1865.
21. Estrin, Y., ***Dislocation-Density-Related Constitutive Modeling***, in *Unified Constitutive Laws of Plastic Deformation*, Krausz, A.S. and Krausz, K. (Editors), Toronto, Academic Press, 1996, p. 69.
22. Estrin, Y. and Mecking, H., Acta Metall. Mater., **32**, 1984, p. 57.

2 Al-Mg(-Cu)-Si-Mn Alloys: Physical Metallurgy and Applications in Packaging and Automotive Body

2.1 Processing of wrought aluminium alloys

Aluminium alloys are widely used in the packaging, automobile, aircraft, and building industries. They are usually classified into casting alloys and wrought alloys. The designation 'wrought' indicates that certain aluminium alloys are available primarily in the form of worked products: plate, sheet, foil, extrusions, tube, forgings, bar, and wire etc. Working operations and thermal treatments may transform a cast ingot structure into a wrought one. Microstructure has significant impact on the strength, ductility, corrosion resistance and other material properties [1]. Wrought alloys can be subdivided into two groups: heat-treatable or non-heat treatable according to the method of obtaining mechanical properties.

2.1.1 Wrought alloys and temper designations

An International Alloy Designation System (IADS) for wrought aluminium products to identify alloy composition and temper was introduced in 1970 under the guidance of the Aluminium Association (AA) and is now widely accepted by aluminium producers. According to the IADS, a four-digit number of which the first digit is assigned on the basis of the major alloying element(s) is used to designate wrought aluminium alloys. The second digit identifies alloy modifications (a zero means the original alloy) or impurity limits. The last two digits are not related to composition in a consistent manner except in the 1XXX series where they indicate the minimum purity of aluminium. For example, AA1060 has a minimum purity of 99.60%. In all other series, the 3rd and 4th digits have little meaning and only identify different aluminium alloys in the series.

In order to specify the mechanical properties of an alloy and the method in which these properties were achieved, a system of temper or heat-treatment nomenclature has also been adopted as a part of the IADS, which takes the form of letter and digits that are added as suffixes to the alloy number. The system deals with the non-heat-treatable, strain-hardening alloys and heat-treatable alloys separately [2]. The essential features of the system are highlighted as follows: F stands for fabricated, O for annealed and recrystallised, H for strain hardened, T for aged hardened. More details of temper

designation for aluminium alloys are available in [2-4]. Thus, within this system the AA3104-H38 (or AA5182-H38) alloy signifies an AA3104 (or AA5182) alloy cold worked to a high level of hardness and stabilized. The AA2024 alloy (composition about Al-4Cu-1.5Mg) that is solution treated, cold worked and naturally aged is indicated as AA2024-T3.

2.1.2 Thermal treatment

Three important general methods are widely used to increase the ability to resist plastic deformation of a metal crystal, i.e., work hardening (or cold work), solid solution strengthening and precipitation hardening. The first two have been recognised from ancient times, but the latter technique sprang from Alfred Wilm's observations and experiments during 1906-1909 [5]. This work led to the discovery that some aluminium alloys can achieve high strength by precipitation or age hardening whilst others cannot. Two conditions have to be satisfied for alloys to be precipitation hardened: i) the alloys must contain elements whose solid solubility in the host matrix decreases with decreasing temperature; ii) the phase precipitating from the matrix must create a coherent or semi-coherent precipitate. The heat-treatable alloys can achieve their high strength by precipitation of hardening elements through thermal treatment. The purpose of a thermal treatment is to develop a desired balance of mechanical properties required for consistent service performance. The heat treatment temperatures are schematically shown in Figure 2.1. Solution treatment, quenching and ageing are the three stages in strengthening alloys by precipitation hardening.

2.1.2.1 Solution and homogenising treatments

There are two aims in a solution treatment [6]: one is to dissolve precipitated phases; the other is to homogenize the composition of the matrix phase (in the Al alloys, this is the Al rich phase). In solution treatment, an alloy is heated to a certain temperature (e.g, the indicated temperature range for alloy X in the α area in Figure 2.1) and held for a certain time sufficient to dissolve all, or the majority of dispersed soluble elements into solution. It is a prerequisite to ageing. Ideally it should be carried out at a temperature within the single phase, equilibrium solid solution range for the alloy concerned in order to obtain complete solution of the alloying elements.

2.1.2.2 Quenching

The solution-treated aluminium alloys must be cooled or quenched, usually to room temperature. The aim of a quench is to achieve a supersaturated solid solution (SSSS) of alloying elements in preparation for subsequent ageing. In practice four types of quenching medium are applied: air, oil, water and sprayed droplets of water, which result in different quench rates. Cold water quenching is very effective and is frequently necessary in order to obtain adequate cooling rates in thicker sections. Some alloys may be quenched with hot or boiling water, water sprayed, or even air-cooled after solution treatment, and still show an acceptable response to subsequent age hardening. Quenching rates influence the microstructures of the alloys. During slow cooling there is a tendency of some of the solute elements to precipitate as coarse particles, which reduces the level of supersaturation and hence lowers the subsequent response of the alloys to age hardening. In the grain boundaries, the microstructure may also change at a slow quenching. Particularly segregation to the grain boundaries of solute elements may cause reduced toughness and higher susceptibility to intergranular corrosion in service [2]. Different alloys have different quench sensitivity. Generally, quench sensitivity increases with the concentration of alloying elements and with density of nucleation sites for the precipitates [2].

2.1.2.3 Ageing

Ageing is the final stage in the development of properties in the heat-treatable aluminium alloys. Its aim is to form finely dispersed precipitates through controlled decomposition of the SSSS for convenient ageing times at one and sometimes two or more intermediate temperatures. The complete decomposition of a SSSS is usually a complex process which may involve several stages shown as follows:

SSSS → solute atom clusters/zones (coherent) → intermediate metastable precipitates (semi-coherent) → equilibrium precipitates (incoherent)

Typically, in Al-Cu, Al-Cu-Mg and Al-Zn-Mg heat treatable alloys, Guinier-Preston (GP) or Guinier-Preston-Bagaryatsky (GPB) zones for Al-Cu-Mg alloys and an intermediate precipitate may be formed before the formation of the equilibrium phase. The GP zones are solute-rich clusters of atoms which may be only one or two atom planes in thickness [2]. They retain the structure of the matrix and are coherent with it. The intermediate precipitate is normally much larger in size than a GP/GPB zone and is only partly coherent

(or semi-coherent) with the lattice planes of the matrix. It has a definite composition and crystal structure which generally are slightly different from those of the equilibrium precipitate. Formation of the final equilibrium precipitate involves complete loss of coherency with the parent lattice. The equilibrium precipitate forms at relatively high ageing temperatures with little hardening effects due to coarse dispersion [2].

The size and shape of the precipitate particles, their nature (i.e. whether they are hard or soft), and the nature of the interface between a precipitate and its matrix have a great influence on the mechanical properties of the aged alloy, because these factors often determine whether or not glide dislocations moving in the matrix will by-pass or cut the precipitates [2, 5, 7].

Two types of ageing are used in practice: natural ageing and artificial ageing. The former occurs at room temperature, whilst the latter occurs at elevated temperature. Some alloys undergo natural ageing but most alloys undergo artificial ageing requiring heating for a time interval at one or more elevated temperatures usually in the range 100-190°C. It is necessary to ensure that ageing time is sufficient to allow for the required precipitation to occur.

2.1.3 Work hardening and annealing

Work, or strain hardening, is another way to strengthen materials other than precipitation hardening. It occurs during working and forming of aluminium and its alloys. In heat treatable alloys, work hardening not only supplements the strengths achieved by precipitation, but also may increase the rate of precipitation hardening. On the other hand, products hardened by cold working can be restored to a fully soft, ductile condition by annealing. Annealing eliminates work hardening, as well as the microstructural features developed as a result of cold working.

2.1.3.1 Work hardening

During deformation of metals and alloys, the dislocation density greatly increases (to about 10^{15} m^{-2}) when dislocation generation and multiplication occur faster than annihilation by dynamic recovery. Dislocation tangles, cells and subgrain walls are formed, all of which decrease the mean free slip distance and increase strength [2]. The severer the cold working, the higher the dislocation densities and the smaller the size of dislocation cell structure. Lattice distortions associated with dislocations and interaction stresses

between dislocations are the principal sources of work hardening resulting from cold work [1].

Elements in solid solution can influence work hardening behaviour in several ways. These influences include enhancing the rate at which dislocations multiply, reducing the recovery rate and increasing the effectiveness of dislocations as barriers to metal flow [2].

Commercially pure aluminium (1XXX series) and non-heat-treatable aluminium alloys (e.g. 3XXX and 5XXX series) are usually work hardened. The work hardening superposes on any solution hardening, to give a considerable extra strength. Cold rolling is a common way to achieve work hardening for non-heat-treatable alloys.

2.1.3.2 Annealing

The deformed metal has large strain energy, which makes it unstable. However, annealing gives the atoms enough thermal energy so that they can move under the driving force of this strain energy. Because the strain fields of the closely spaced dislocations interact, the total strain energy can be reduced by rearranging the dislocations into low-angle grain boundaries. These boundaries form the surfaces of irregular cells, which are relatively free of dislocations. During annealing, the deformed grains are replaced by new, undeformed grains [8]. After annealing, a metal will have a comparatively low dislocation density (about 10^{12} m^{-2}) and will be relatively soft and ductile.

Several stages occur during the annealing process. In these stages, structure and properties will change (e.g. see Figure 2.2) [9].

The first stage, occurring at the lowest temperatures and shortest times of annealing, is known as recovery. During recovery, dislocations will annihilate each other and thus dislocation density is reduced. Figure 2.3 shows a clear picture of dislocation evolution during recovery: dislocation tangles formed during deformation are often gradually rearranged into a cellular subgrain structure. With increasing time and temperature of heating, recovery nearly completes and the subgrain size gradually increases. In this stage, many of the subgrains have boundaries that are completely free of dislocation tangles [1].

The major changes come from the second stage—recrystallisation. In this process, new grains nucleate and grow until the whole metal consists of undeformed grains. The dislocation density returns to its original value, as do the values of the hardness and ductility [8]. Recrystallisation occurs with longer times or higher heating temperatures

than does recovery, although some overlap of the two processes usually happens. Recrystallisation changes the properties of the deformed and recovered metal. The properties of recrystallised material are the same as those of the original, unstrained material, except the changed grain size and preferred orientation [1]. Recrystallisation is not only a way to eliminate work hardening, but also an effective method to control the grain size of worked metals. The greater the prior plastic deformation, the finer the recrystallised grain size [8].

Grain growth is a third stage, which occurs after recrystallisation completes. Heating after recrystallisation may cause grain coarsening. The grain size may increase by a gradual and uniform growth, identified as normal grain growth, which is promoted by small recrystallised grains, high temperatures and extensive heating. Aluminium alloys that are subjected to some form of pinning or growth restraint occasionally undergo a different kind of grain growth, which is an exaggerated grain growth preceded by the growth of a very few grains in recrystallised metals. Generally, these grains grow only at very high temperatures and may attain diameters of several millimetres. For most alloys, high temperatures are not the only cause of such giant grains. Small primary grain size and well-developed annealing texture are other factors that promote this exaggerated form of grain growth [1].

The above discussed microstructure development occurring during annealing is schematically illustrated in Figure 2.4.

2.2 Physical metallurgy of Al-Mg(-Cu)-Si-Mn alloys

2.2.1 General introduction

Al-Mn (3XXX) and Al-Mg (5XXX) alloys are mostly non-heat-treatable alloys. For Al-Mg based alloys, however, small Cu additions will change their response to heat treatment, i.e., they can also be precipitation hardened to some degree. Due to its very low-equilibrium solid solubility in commercial aluminium alloys [10], manganese will normally exist as finely dispersed particles in the material giving a slight to moderate increase in strength. It usually forms the quaternary phase α-$Al_{12}(Fe, Mn)_3Si$ together with Fe and Si, which are common impurities or additions. Magnesium is present in solid solution and a high content of magnesium (4~5%) will have a dramatic impact on strength

and the resistance against deformation. The two groups of alloys are usually strengthened predominantly by solution strengthening and work hardening.

2.2.1.1 3XXX series Al-Mn alloys

In general, the 3XXX series alloys are used when moderate strength combined with high ductility and excellent corrosion resistance is required. Commercial Al-Mn based alloys contain up to 1.25% Mn although Mn has 1.82% maximum solid solubility in Al. There are two reasons causing this limitation. First, the presence of iron as an impurity reduces the Mn solubility; and second, large, primary particles of Al_6Mn present will have a disastrous effect on local ductility [2]. The addition of Mg provides solid solution strengthening. AA3003 (Al-1.25Mn) is a widely used binary Al-Mn alloy [2]. In this alloy, the presence of finer Mn-containing intermetallic compounds imparts some limited dispersion-hardening. AA3105 (Al-0.55Mn-0.5Mg) alloy is widely used in a variety of strain-hardened tempers. Higher levels of Mn and Mg are present in AA3004 (Al-1.25Mn-1.05Mg). This alloy and the slightly modified version AA3104 (Al-1.0Mn-1.0Mg) are widely used for beverage cans. Their compositions are listed in Table 2.1. Table 2.2 shows the typical mechanical properties of canstock alloy AA3004 in different tempers.

Table 2.1 The compositions of commonly used canstock 3XXX alloys [10]

Alloy	Mg	Mn	Cu	Fe	Si	Cr	Zn	Ti	Al
3004	0.8-1.3	1.0-1.5	0.25	0.7	0.3	–	0.25	–	Bal.
3104	0.8-1.3	0.8-1.4	0.05-0.25	0.8	0.6	–	0.25	0.10	Bal.

Table 2.2 Typical mechanical properties of AA3004 alloy at room temperature [10]

Temper	Tensile strength MPa	Yield strength MPa	Elongation %	Hardness HB	Shear strength MPa
O	180	69	20-25	45	110
H32	215	170	10-17	52	115
H34	240	200	9-12	63	125
H36	260	230	5-9	70	140
H38	285	250	4-6	77	145

2.2.1.2 5XXX series Al-Mg alloys

Mg and Al can form solid solutions over a large range of compositions. Although the maximum solid solubility of Mg in Al is 17.4%, only alloys with up to 5.5% Mg are commercially used in the 5XXX series Al alloys [10]. This is because at higher Mg content, the precipitation of Al_3Mg_2 or Al_8Mg_5 phase at grain boundaries causes

susceptibility to intergranular cracking and stress corrosion [10]. These alloys are widely used for welded applications. In transportation, plate is used for dump truck bodies, large tanks and pressure vessels etc. Their high corrosion resistance makes them suitable for the hulls of small boats and for the super-structures of ocean-going vessels. The compositions of some 5XXX alloys are listed in Table 2.3. AA5182 is one of the most commonly used alloys for container end and car body. Its typical tensile properties are listed in Table 2.4.

In 5XXX alloys, Mg not only provides solution-strengthening (Figure 2.5 (a)), but it is also important as a strengthening element through its effect on work-hardening (Figure 2.5 (b)). The influence of Mg on enhancing strengthening during cold-deformation is microstructurally related to its effect on development and retention of lattice strain [11].

Table 2.3 The compositions of commonly used 5XXX alloys [10]

Alloy	Mg	Mn	Cu	Fe	Si	Cr	Zn	Ti	Al
5042	3.0-4.0	0.20-0.50	0.15	0.35	0.2	0.1	0.25	0.1	Bal.
5052	2.2-2.8	0.10	0.10	0.4	0.25	0.15-0.35	0.10	–	Bal.
5754	2.6-3.6	0.50	0.10	0.40	0.40	0.30	0.20	0.15	Bal.
5182	4.0-5.0	0.20-0.50	0.15	0.35	0.20	0.10	0.25	0.10	Bal.

Table 2.4 Typical tensile properties of AA5182 alloy [10]

Temper	Tensile strength MPa	Yield strength MPa	Elongation %
O	276	138	25
H19	421	393	4
H32	317	234	12
H34	338	283	10

The microstructure of deformed Al alloys shows evidence of mutual dislocation annihilation and extensive dislocation rearrangement into cells and subgrains [11]. The strain-hardened condition of 5XXX alloys is a metastable state in which there is a driving force for internal strain to relax through the process of static recovery [11]. Figure 2.6 shows the gradual drop in strength and increase in tensile elongation with time at ambient temperature for an Al-6% Mg alloy. This behaviour is referred to as “age softening”, which is a temperature and time-dependent recovery process. Therefore, exposure to higher service temperature allows thermally activated recovery mechanisms to proceed at a faster rate, which increases the rate of strength loss [11]. Greater stability of properties with time can be achieved by stabilizing strain hardened 5XXX alloys after cold-working [11]. Such stabilization involves a low temperature thermal operation, typically 120-180°C, to allow a controlled amount of recovery to occur. Figure 2.7 illustrates the

influence of a stabilization treatment on the static properties during natural ageing of an AA5052-H18 alloy. Stabilized tempers are identified commercially with the H3X designation.

Many of the 5XXX alloys offer a high level of formability. The addition of Mg can markedly increase the alloy strength without unduly decreasing their ductility. In annealed condition, Al-Mg alloys exhibit instability during deformation [2, 11]. Two types of instability are observed in Al-Mg alloys. One is Lüder bands/lines, which occur only in annealed alloys. The severity of this behaviour increases with increasing Mg and decreasing grain size [11]. The Lüder bands can be eliminated by introducing dislocations into the microstructure by stretching the piece past the yield point or by a rolling or roller levelling operation [11]. The other is the Portevin-Le Chatelier effect involving repeated, discontinuous localized yielding events. It occurs in strain-hardened as well as annealed tempers associated with a serrated stress-strain curve and a condition of negative strain-rate sensitivity [11]. Only small amounts of Mg are required to produce serrated flow behaviour in Al alloys. Hence all commercial 5XXX alloys have the potential to show this behaviour. There is currently no clear understanding of how to avoid this serrated yielding behaviour [11].

2.2.2 Precipitation in Al-Mg-Si(-Cu) alloys

2.2.2.1 Precipitation in Al-Mg-Si alloys

Al-Mg-Si alloys are heat treatable and widely used in both cast and wrought form. Owing to the good combination of formability, corrosion resistance and weldability, they are widely used for the fabrication of automotive body. Precipitation hardening is the major mechanism to strengthen these alloys. In most Al-Mg-Si based alloys the precipitation sequence is [12, 13]: $\alpha_{ss} \rightarrow$ clusters/GP zones $\rightarrow \beta'' \rightarrow \beta' \rightarrow \beta$ (Mg_2Si)

However considerable confusion remains concerning the early stages of precipitation, i.e. the clustering process, the structures of GP zones and β″ phase, and the compositions of all the intermediate precipitates. Some reports also suggested that several other precipitates may form in addition to those listed above, depending on the composition of the alloys [14].

For the clustering process, different mechanisms of clustering, e.g., from clustering of only Si atoms [15], to separate clustering of Mg and Si atoms and co-clustering of Mg and

Si atoms [16-20] have been proposed. The atomic ratio of Mg:Si atoms in the Mg-Si co-clusters is reported to be close to 1:1 [16-20]. GP zones are generally considered to be spherical clusters with unknown structure. GP I zone and GP II zone were reported in previous work [15, 21-23]. Sometimes the Mg/Si co-clusters/GP zones are referred to as GP I zones, whilst needle shaped β″ precipitates have been referred to as GP II zones [20].

β″ phase is a fine needle-shaped precipitate along $<100>_{Al}$, with a monoclinic structure (different values of the lattice parameters were reported, see Table 1 in [24]), and β′ is a rod-shaped precipitate along $<100>_{Al}$, having a hexagonal crystal structure with a=0.705 nm and c=0.405 nm [25]. However, other lattice parameters for β′ have also been reported (see Table 1 in [24] for details). The β phase is usually reported to be Mg_2Si platelets on {100} of Al having the FCC structure with a=0.64 nm [25].

Si content in the Al-Mg-Si alloys significantly influences the precipitation and precipitates present. For alloys with excess Si, along with β′, three other phases, referred to as type A, B and C, have been reported [26-28].

Although many structural studies of the precipitate phases have been reported, complete crystal structure information of these phases is not always available or unambiguous. Even the compositions of the precipitates are often controversial. Knowledge of the compositions and structures of the precipitates is important in understanding the age-hardening phenomenon. For example, the β″ precipitate is believed to be the main strengthening phase. However, controversy concerning its composition and crystal structure arises in the literature, e.g. the reported Mg:Si (in wt%) ratio ranges from 0.09 to 1.73 (see Table 1 in [24]). This controversy may cause some difficulty in the prediction of the formation of the precipitates and the strengthening of the alloys.

2.2.2.2 Precipitation in Al-Mg-Cu alloys

As shown in Figure 2.8, different precipitation processes will occur during the ageing of Al-Cu-Mg alloys, depending on alloy composition and Cu:Mg ratio. For the alloys with high Cu:Mg ratio in the α+θ region, precipitation of θ (Al_2Cu) is promoted, and the aging sequence can be described as [3]:

$\alpha_{ss} \rightarrow$ GP zones $\rightarrow \theta'' \rightarrow \theta' \rightarrow \theta$ (Al_2Cu)

where GP zones are monolayers of Cu atoms on a {001} Al matrix plane, θ″ is coherent, probably two or more layers of Cu atoms separated by layers of Al atoms, θ' is tetragonal

Al_2Cu with a=4.04Å and c=5.80 Å, and θ is body-centred tetragonal Al_2Cu with a=6.07 Å and c=4.87 Å [2].

For alloys with medium to low Cu/Mg ratio in the α+S region, the precipitation process has been represented as:

$\alpha_{ss} \rightarrow$ clusters/ GPB zones (or GPBI zones) $\rightarrow$ (GPBII zones/S″) $\rightarrow$ S' $\rightarrow$ S (Al_2CuMg)

where GPB zones are Cu/Mg clusters along {001} Al matrix plane. They were termed Guinier-Preson-Bagaryatsky zones and deduced by X-ray measurement to be cylindrical, 1-2 nm in diameter and 4 nm long by Silcock [29]. However, GPB zones have not been unambiguously evidenced by means of TEM, selected area diffraction (SAD) and high resolution TEM (HRTEM) [30, 31]. The detailed debate about the clusters/GPB zones has been recently reviewed by Yan [32]. The incoherent equilibrium S phase is face centred orthorhombic with a=4.00 Å, b=9.23 Å and c=7.14 Å [2, 30]. The semi-coherent S' phase has the same structure as the S phase but different lattice parameters, i.e. a=4.04 Å, b=9.25 Å and c=7.18 Å [2, 30]. Since the S' phase and S phase have the same structure with slightly different lattice parameters, some authors suggest that they should be considered as the same phase [33, 34]. The existence of S″ has not been clearly confirmed [30]. It is beyond the scope of the present literature review to discuss the controversy about the existence and the structure characteristic of the S″ phase. Interested readers are referred to the literature review in [32].

Despite the extensive studies in Cu-rich Al-Cu-Mg alloys for more than 50 years [32, 35-54], due to these controversies discussed above in the literature concerning the existence and structure of clusters/GPB zones, S″ and S', the following variant precipitation sequences have been proposed for Cu-rich Al-Cu-Mg based alloys:

$\alpha_{ss} \rightarrow$ GPB zones (Cu/Mg clusters) $\rightarrow$ (S″) $\rightarrow$ S' $\rightarrow$ S (Al_2CuMg) [30]

$\alpha_{ss} \rightarrow$ GPB zones $\rightarrow$ GPB (or GPBI) + GPBII zones $\rightarrow$ S' $\rightarrow$ S [29]

$\alpha_{ss} \rightarrow$ pre-precipitate stage $\rightarrow$ GPB zones + S $\rightarrow$ S [41]

More recently, the following precipitation sequence for S precipitates has been proposed by Wang et al. [34, 55]: $\alpha_{ss} \rightarrow$ Cu-Mg clusters $\rightarrow$ GPB II/S″$\rightarrow$ S

Relatively few studies have been conducted for Cu-lean Al-Mg-Cu alloys [7, 56-61] (Here Cu-lean alloys are defined as alloys with less than 1wt% Cu). Only few researchers have

studied precipitation in Al-Mn-Mg-Cu alloys with low Cu:Mg ratios [7, 30, 33, 54, 56, 62-68]. The few publications available on ternary Al-Mg-Cu alloy systems with low Cu:Mg ratios between 0.11 and 0.29 in wt% (Cu-lean alloys) indicate that the precipitation processes might be similar to those of Cu-rich alloys, that is, their precipitation sequence follows [7]:

$\alpha_{ss} \rightarrow$ GPB zones (Cu/Mg clusters) $\rightarrow$ S″ $\rightarrow$ S' $\rightarrow$ S (Al_2CuMg)

Vooijs et al. [67] have studied precipitation processes in an industrial Al-1.04Mn-1.36Mg-0.30Cu-0.31Fe-0.17Si alloy (in wt%) by using thermoelectric power and resistivity measurements. This study concluded: ① S′ precipitates (Al_2CuMg) form at annealing temperatures below 225°C. The dislocation density prior to annealing has no significant effect on the precipitation kinetics for S′ precipitation. (However, in other literature [64], dislocation density or pre-deformation was reported to have significant influence on S/S′ precipitation kinetics, i.e., pre-deformation will promote S/S′ precipitation kinetics.) ② Precipitation of Mn occurs at temperatures above 225°C. ③ Only a very small amount of Mg_2Si precipitates at temperatures of 350°C and higher.

In cold-rolled Cu-containing AA3104 aluminium alloys, under certain conditions, S′ phase may form on dislocation networks and cause precipitation hardening [30]. Dion and Starink [69, 70] have studied S phase precipitation in deformed Al-Mg-Mn-(Cu) canstock alloys (AA3104-0.17Cu and Cu-free AA3104) by DSC. Their DSC results showed that cold-worked samples of the Cu-containing alloy reveal no clear S phase precipitation effect whilst samples of the Cu-containing alloy with a small amount of deformation (2-10%) aged at 170°C did contain S precipitates. The study identified two clear precipitate dissolution effects in the aged conditions. One at about 230°C was detected in the alloy aged for two days at 170°C, which is considered due to the dissolution of the precursor of S, the other at about 300°C was detected in the Cu-containing alloy aged for seven days and three weeks, which is related to S dissolution. This work indicates that two stages of precipitation may occur in the AA3104-0.17Cu alloy during ageing: precursor of S and S.

Gouma et al. [7] have studied the precipitation processes in two Al-3Mg-(0.2-0.4)Cu alloys with Cu:Mg ratio of 0.07 and 0.14 (in wt.%) by TEM. Different types of precipitates were found to be present in each alloy. In the Al-3Mg-0.2Cu alloy aged for 16 hours at 200°C, two types of precipitates were detected: the thin laths which are consistent with S and the fine dots which were thought to be GPB zones. It was therefore suggested

that the alloy had retained GPB zones in its structure after aging at 200°C for 16 hours. These zones are likely to act as nuclei for the formation of the stable S precipitates. High resolution TEM (HRTEM) study on the Al-3Mg-0.4Cu alloy aged for 8 hours at 180°C was performed. It suggested that GPB zone formation involves the ordering of Mg-Cu clusters in the matrix of the alloy, which was thought to contribute to the increased strength of the material. HRTEM was also used to further study the early stages of ageing in the Al-3Mg-0.4Cu-0.12Si (wt%) alloy by Kovarik et al. [68, 71]. The HRTEM observations revealed the presence of ordered zones (GPB) consisting of Mg and Cu atoms in the matrix after ageing at 180°C for one hour [71] and the appearance of S″ [68] or GPBII zones which were thought to grow from GPB zones [71] after four-hour ageing. These observations suggested that the initial stage of hardening is mostly caused by the ordered GPB zones, while the precipitation of S″ or GPBII zones becomes increasingly important contribution to the overall age hardening response detected in the alloy. A recent atom probe tomography study of GPB zones in the same alloys by Kovarik et al. [72] revealed that Si atoms are also present in the Cu and Mg containing GPB zones. Furthermore, the amount of Si atoms is higher than that of Cu atoms. Taken together, the studies of Gouma and Kovarik and co-workers indicate the following precipitation sequence in the Cu-lean (Cu:Mg < 0.2 in wt%) Al-Mg-Cu alloys:

$\alpha_{ss} \rightarrow$ GPB zones $\rightarrow$ GPBII/S″$\rightarrow$ S

Ratchev et al. [65] have studied the effect of solution treatment on the precipitation during ageing of an Al-4.22wt.%Mg-0.58wt.%Cu alloy at 180°C by means of DSC, tensile testing and TEM. Both heterogeneous precipitation on dislocation loops and helices and homogeneous precipitation in the matrix have been observed. The rapid initial hardening of the alloy was attributed mainly to cluster-dislocation interactions and the peak of hardness to the homogeneous precipitation of S′ phase. This is different from the interpretations claiming that the first stage of hardening is associated with the formation of GPB zones (Cu/Mg clusters), and the second stage of hardening related to the presence of S″ phases [33].

Verlinden and Zahra have studied the precipitation hardening mechanisms in Cu-lean Al-Mg-Cu alloys by isothermal calorimetric measurements and DSC analyses [73]. They suggested that pure Mg and Mg-rich clusters have already existed after quench, and that GPB zones form from Cu-rich clusters, very slowly at low temperatures, but rapidly at

180°C. The presence of Mg clusters and solute-dislocation interactions thus are thought to strongly influence the as-quenched strength, whilst the formation of GPB zones is proposed to be the origin of the first rapid hardening during ageing. However, it is here noted that without the confirmation of TEM or atom probe field ion microscopy (APFIM) observations, DSC experiments alone in their study cannot provide proof of these suggested reactions.

From the ternary phase diagram shown in Figure 2.8, an Al-Mg-Cu alloy with a Cu:Mg ratio below about one situated in the ternary α+S+T region of the phase diagram might have a different precipitation sequence with T phase formation occurring. However, several studies on ageing of commercial Al-Mg-Cu alloys (Cu:Mg ratio of 0.11-0.29 in wt%) show that in practice T phase does not precipitate [64]. Ratchev et al. suggest that this could be due to the presence of secondary elements such as Si, Fe and Mn in the alloys, which may shift the phase boundaries of the ternary phase diagram [64]. It is also possible that the precipitation of T phase is suppressed due to the activation energy for S phase nucleation being substantially lower than that of T phase.

2.2.2.3 Precipitation in Al-Mg-Si-Cu alloys

Application prospects in automotive industry have led to extensive studies on 6xxx alloys in recent years [14]. These alloys often contain Cu in varying amounts. This leads to the formation of the quaternary Al-Mg-Si-Cu family of alloys. The additions of Cu in the Al-Mg-Si alloys cause the precipitation events in the alloys considerably more complex [14]. In the presence of Cu, several additional clusters and metastable phases have been reported depending on the alloy compositions, especially the Mg:Si ratio. These include quaternary phase Q/Q′ ($Al_5Cu_2Mg_8Si_6$), type A/B/C, L, QP, QC, B′, λ, γ, β_d'', M, Si etc. [14, 74]. Chakrabarti et al. [14] have reviewed the precipitation sequences and precipitate structures for different 6xxx alloy compositions. Details are referred to Table 3 in [14]. The main conclusions from this review are [14]:

(1) Many Al-Mg-Si-Cu alloys contain the common quaternary phase Q.

(2) Complex combinations of precursors observed in this alloy system revealed by HRTEM are influenced by the Mg:Si ratio, the level of excess Si, the presence of Cu and the Cu level.

(3) In Al-Mg-Si-Cu quaternary alloys, significant strengthening effects may be due to the lath shaped, hexagonal precursor phases to Q′ in addition to the generally recognized β″ phase.

The following precipitation sequences are proposed in the literature for 6XXX alloys:

- For a typical 6022 alloy containing a small amount of Cu (0.07wt%), Miao et al. proposed the following sequence: α_{ss} → GP zones → β″ → β' + Q' → β + Si. The increase of Cu content to 0.91wt% changes the precipitation sequence to: α_{ss} → GP zones → β″ → Q' → Q + Si [75].
- Based on recent studies of the precipitation behaviour of AA6111 alloy, the precipitation sequence for this alloy can be described as [76-81]: α_{ss} → clusters/GP zones → β″ + Q' → Q + β (Mg_2Si).

Apart from the microstructural characterisation by means of TEM, DSC has also been extensively used to analyse exothermic effects associated with precipitation reactions. Some selected precipitated phases and the exothermic peaks related with these precipitation reactions in the Al-Mg-Si(-Cu) alloys during DSC run reported in the literature are summarised in Table 2.5.

Table 2.5 Peak temperature for formation of selected precipitates in Al-Mg-Si(-Cu) alloys [74, 80]

ppt	Clusters	β″	β′/B′	Si	Q	Q′
T_p (°)	~80	~250	~290	~330	290	345

Note: T_p is the peak temperature of precipitation reaction.

Some DSC studies on the canstock alloy AA3004 are very informative for the DSC studies of the alloys investigated in this PhD work. For instance, the DSC work on phase transformations in a commercial AA3004 can body stock alloy which contains 1.12 Mg, 1.05 Mn, 0.18 Si, 0.15 Cu and 0.37 Fe by Owen [82] is interesting. The DSC thermograms of as-cast alloys are shown in Figure 2.9. According to their results, β′ and β phase precipitated during a DSC scan for the as-cast AA3004 alloy, which were identified as peak C (around 280°C) and E (around 450°C), respectively shown in Figure 2.9. The precipitation of Mn-containing dispersoids (either Al_6Mn or α-$Al_{15}(MnFe_3)Si_2$) was related to the exothermic peak G at ~520°C. Another interesting study was performed by Chen et al. on the precipitation behaviour of strip cast AA3004 alloy [83]. In their study,

double ageing peaks were detected by isochronal (holding 30 minutes at tested temperatures) hardness testing in an AA3004 alloy with 0.90 Mg, 0.22 Si and 0.98 Mn (in wt%). One occurs at about 260°C and fine, needle-like precipitates were detected in the sample aged at 250°C. The other appears at ~482°C and dense, plate-like particles were found when aged at 454°C. From electron diffraction and microprobe analyses, these were suggested to be $Al_{12}(Mn,Fe)_3Si_2$ with a cubic structure coherent with the matrix. This paper fails to identify the structure of the fine, needle-like precipitates when aged at 250°C. However it is here noted that the precipitates are likely to be β″ phase, because β″ phase is needle like [19] and occurs at a peak temperature around 250°C during a DSC run.

2.2.2.4 The influence of pre-strain on precipitation in Al-Mg-Si(-Cu) alloys

Deformation introduces a large density of dislocations which can alter the precipitation sequence in a number of ways, either by heterogeneous precipitation on dislocations or by modification of kinetics of formation of precipitates in locations away from the dislocations (i.e. kinetics of bulk precipitation) [84]. First, dislocations are favourable nucleation sites for precipitates and short-circuit diffusion paths for solutes, which results in faster and coarser precipitation on dislocations [84]. Moreover, precipitation on structural defects naturally promotes stable rather than metastable phases [84, 85]. Second, the interaction between dislocations and solutes results in a solute flux to dislocations. Hence a lower solute fraction is available for bulk precipitation; therefore, the kinetics of bulk precipitation will be altered.

Given the above possible interactions, the effect of the presence of dislocations on precipitation hardening strongly depends on alloy family [42]. Three different responses can be identified [42]: (1) Enhanced hardening in Al-Cu, Al-Cu-Mg systems. (2) Little change in hardening, e.g. Al-Zn-Mg system. (3) Reduced hardening occurring in special circumstances, e.g. Al-Cu alloys with trace additions of cadmium, indium or tin. Currently the study and understanding of the precipitation in the pre-deformed samples are very limited compared with that of solution-treated samples. In the following, some studies on the effect of cold work on precipitation in Al-Mg-Si(-Cu) alloys will be reviewed.

The microstructure and mechanical properties developed by thermomechanical treatment in an Al-0.78wt%Mg-0.98wt%Si alloy (0.15wt%Fe and 0.3wt%Mn) have been studied by Ismail [86]. The results showed that no modification in the precipitate structure due to deformation prior to ageing at temperatures up to 150°C occurs. However, when aged at

200°C, needle-shaped β″ precipitates were observed in the deformed samples instead of the very fine GP zones present for the lower ageing temperature range up to 150°C. Moreover, the needle-shaped precipitates were noticed to become larger in size and more heterogeneously distributed with increasing deformation from 15% to 25%.

Yassar et al. [85, 87] have studied the effect of cold deformation on the precipitation of metastable phases in an AA6022 alloy (0.55wt%Mg-1.10wt%Si-0.06wt%Cu) by means of DSC and TEM. It was found that the introduction of deformation changes the precipitate type from β″ phase to β′ and Q′ phases during the dynamic heating in a DSC scan at 20°C/min. That is, instead of the sequence: Clusters/GP zones → β″ → β′ + Q′ for the undeformed condition, the following precipitation sequence for metastable phases in a deformed condition was proposed: Clusters/GP zones → β′ + Q′ → Q′ [85]. The comparison of the measured activation energy for precipitate formation showed that cold deformation facilitates precipitation by decreasing the activation energy [87].

The effect of cold work on the precipitation kinetics of an AA6111 alloy (Al-(0.5-1.0)Mg-(0.6-1.1)Si-(0.5-0.9)Cu) has been evaluated by means of tensile testing, DSC and TEM [88]. In this study, the DSC results showed acceleration in the precipitation kinetics and the reduction of the activation energy for formation of β″ phase with increasing level of cold work. Meanwhile, TEM results revealed the increased amount of strengthening precipitates with increasing level of cold work.

Microhardness, electrical conductivity and DSC measurements were employed to investigate the possible use of pre-strain to improve the bake hardening response of a twin-roll cast Al–Mg–Si alloy (0.47%Mg-1.15%Si-0.03%Cu) by Birol [89]. In this study, several changes were noted in the DSC curves upon pre-straining shortly after solution treatment. After one week natural ageing, in contrast to the sample processed without pre-straining, the pre-strained samples reveal an exothermic peak between 100°C and 160°C, which is linked to the formation of GP-1 zones. This effect was found to shift to lower temperatures with increasing pre-strain from 0 to 5%. On the other hand, the dissolution trough for the reversion of the clusters and smaller zones formed during natural ageing is largely missing in the pre-strained samples. The β″ and β′ precipitation peaks have both shifted to lower temperatures with increasing level of cold work, which means that the kinetics of both β″ and β′ precipitation is accelerated with increasing pre-strain. Thus, in general terms, the DSC features show that natural ageing is suppressed whilst β″

precipitation is promoted when deformation is introduced shortly after solution treatment. The dislocations introduced by prestrain not only suppress clustering during natural ageing but also provide heterogeneous nucleation sites for GP-1 zones which readily grow to stable nuclei for the β″ particles.

Zhen et al. have studied the effect of predeformation on microstructure and tensile properties of Al-Mg-Si alloys with various Si contents [90]. Their results show that the strength of Al–Mg–Si alloys in the underaged condition is greatly increased by pre-stretching immediately after quench. Meanwhile, the β″ precipitates are observed to form directly on dislocations with a larger size than those forming in the dislocation free areas. When pre-stretching is less than 5%, the increase in pre-stretching results in increased density of β″ precipitates, whereas pre-stretching by 10% leads to larger sizes but lower density of β″ precipitates.

The effect of plastic deformation on structure and properties of two types of 6XXX aluminium alloys (Al-(1-1.5)Mg-(0.9-1.1)Si-(1.1-1.3)Cu alloys) has been studied by Dutkiewicz et al. [91] through hardness tests and TEM studies. In this study, three different cold-rolling reductions were employed: 30%, 60% and 90%. The results confirm that the kinetics of the precipitation is accelerated with increasing pre-deformation. It also reveals that the precipitates form mainly on dislocations at peak hardness and their density increases with increasing deformation. TEM observations in this study suggest that recovery process occurs after ageing at 165°C but no recrystallisation can be seen at this temperature.

Ratchev et al. [64] have studied the effect of pre-deformation on the precipitation hardening of an Al-4.2wt%Mg-0.6wt%Cu alloy, which is in the ternary α+S+T region in Figure 2.8. It was found that pre-deformation before artificial ageing has a complex influence on precipitation hardening: deformation hampers the GPB zone precipitation but it introduces more heterogeneous nucleation sites. It was suggested that the main precipitation hardening occurring after pre-deformation is due to heterogeneous nucleation and growth of S″ phase. The S″ nucleation might also prevent dislocations annihilation and preserve to some extend the work hardening introduced during pre-deformation.

Ringer et al. have investigated the effect of cold work on precipitation in an Al-4.0Cu-0.3Mg alloy by means of hardness testing and TEM [42]. This study revealed that the responses of the alloy to hardening during natural ageing are reduced by 6% cold working

after quenching due to the retarded formation of GP zones whilst some amount of cold work prior to elevated temperature ageing promotes increased hardening in the alloy.

2.2.3 Microstructure in Al-Mg(-Cu)-Si-Mn alloys

Microstructure can be characterized by the size, type and distribution of the coarse constituent particles, the eutectic element microsegregation and the cell size etc. These features are controlled by alloy composition and processing condition such as casting, preheating and subsequent working condition.

2.2.3.1 As-cast and preheating microstructure of 3XXX alloys

In as-cast 3XXX ingots, the alloy retains characteristics of the dendritic solidification. Between dendrite arms is the eutectic mixture containing coarse Fe-rich intermetallic constituent particles, which can be present in two forms: the orthorhombic $Al_6(Fe,Mn)$ and the cubic α-$Al_{12}(Fe,Mn)_3Si$ phases [11]. The relative amounts of these phases are determined by the specific alloy composition and the solidification rate. Fe, with a very low solubility in Al, has the largest effect on the volume fraction of these constituent phases. Most commercial ingot cooling rates favour the formation of $Al_6(Fe,Mn)$ phase over α-$Al_{12}(Fe,Mn)_3Si$ for the as-cast constituent [11]. The preheats for 3XXX alloys are designed to produce a coarse widely spaced dispersoid distribution with minimum Mn remaining in solid solution. This is generally achieved by a relatively high soak temperature and slow cooling [11].

The typical ingot microstructure of AA3104 contains two intermetallic constituent phases, $Al_6(Fe,Mn)$ and Mg_2Si, decorating the cell boundaries. At the cell boundaries a Mn denuded zone is often observed particularly near to the Fe/Mn bearing coarse constituent particles [92]. During solidification, substantial amounts of Mn are retained in solution in the Al phase. During preheating, the supersaturation is relieved by the precipitation of a fine dispersion of α-$Al_{12}(Fe,Mn)_3Si$ or $Al_6(Fe,Mn)$ if the Si content is very low (<0.07wt%) [11]. The size and density of dispersoids depend on the preheating temperatures as well as ingot structure [93]. Preheating also serves to homogenize the distribution of the more mobile atomic species such as Mg and Cu. If sufficient Si is present, some of the $Al_6(Fe,Mn)$ constituent transforms to the α-$Al_{12}(Fe,Mn)_3Si$ phase (6-to-α transformation). Some spheroidizing of the constituent phases also occurs during high-temperature preheating [11].

2.2.3.2 As-cast and preheating microstructure of 5XXX alloys

The constituent phases in 5XXX alloys can be of various types determined by the specific alloy composition. Mg_2Si is often present in the microstructure as a major constituent phase due to the low solubility of Si in Al at high Mg contents. Like 3XXX alloys, constituent phases containing Fe, Mn and Si are also present, which could be $Al_6(Fe,Mn)$, α-$Al_{12}(Fe,Mn)_3Si$ or Al_3Fe [11]. As Si has been tied up with Mg as Mg_2Si, the $Al_6(Fe,Mn)$ phase will be favoured when Mn is precipitated as a dispersoid during preheating [11].

Hollinshead [94] found that the as-cast microstructure of an AA5182 alloy consists of a network of constituent particles of Al_3Fe, $Al_6(Fe, Mn)$ and Mg_2Si in the cell boundaries shown in Figure 2.10a. Figure 2.10b shows a coarse, equiaxed grain structure with a grain intercept length of approximately 200 μm [94]. The microstructure of the homogenised AA5182 alloy contains Al_3Fe, $Al_6(MnFe)$ and Mg_2Si, which are several μm in size situated mainly along the grain boundaries [63].

Delapuente et al. [60] studied the as-cast microstructure of an AA5182 alloy and an AA5182 alloy modified with 1 wt% Cu. The as-cast microstructure of both alloys consists of dendrites of Al with coarse interdendritic phases. As shown in Figure 2.11(a), in the AA5182 alloy, two types of constituents were found: Al-Mg-Si rich areas (dark) and Al-Mn-Fe rich areas (bright grey), which was thought to be a combination of $AlFe_3$ and $Al_6(Fe,Mn)$ according to SEM-EDS analysis. The Al-Mg-Si rich areas showed a heterogeneous composition by SEM-EDS analysis. It was assumed to be a mixture of two eutectics: Al+Mg_2Si and Al+Mg_2Si+Si produced by non-equilibrium cooling. The AA5182+Cu alloy contains three types of constituents shown in Figure 2.11 (b): Al-Mg-Si, Al-Mn-Fe(+Cu) and Al-Mg-Cu rich areas with oval shapes and sometimes forming a chain-like structure. The Al matrix of both alloys contained Mg as the major solute element. Small amounts (below 1wt%) of Mn and Fe were also found in solid solution. In the AA5182+1wt% Cu alloy Cu is also present in solid solution. No Si was detected in solid solution, all of it being concentrated in the dark interdendritic particles. The distribution of Mg is highly inhomogeneous, with most of it concentrated near grain boundaries and at matrix-particle interfaces [60]. It was also found that for the AA5182+Cu alloy, a preheat at 450°C partially eliminates the Mg and Cu segregation. Higher temperature preheat at 540°C is needed for complete homogenization of the matrix

with the Al-Mg-Cu constituent dissolved [60]. Heating to 540°C leads to the precipitation of $Al_6(Fe,Mn)$ dispersoids in the matrix of both AA5182 and AA5182+Cu alloys [60].

With the addition of 0.5 wt% Cu to an AA5182 alloy, a Cu-bearing constituent phase appears in the as-cast structure, which dissolves completely after homogenisation. All Cu remains in solid solution after quench [66]. In this study, the effect of Cu on dispersoid size and distribution was investigated by TEM [66]. It was found that Cu decreases dispersoid size and increases their number, i.e., decreases interparticle distances. The study also reveals that the as-cast equiaxed grain size averages about 300 μm for a commercial AA5182 alloy and 150 μm for an AA5182 + 0.5 wt% Cu alloy [66]. The addition of 0.5 wt% Cu to the AA5182 alloy reduces the hot ductility of the alloy due to the finer size of the Mn-bearing dispersoids compared with the AA5182 alloy. Hot ductility of the Cu-bearing AA5182 alloy may be improved by modified heat treatment to increase the mean size of dispersoids [66].

2.2.3.3 Features of as-deformed microstructure

After preheating, hot-rolling progressively makes the microstructure homogeneous by breaking up the cell structure, fracturing the constituent particles, and distributing the constituent phases and dispersoid particles more uniformly throughout the microstructure. Precipitation may occur at sub-boundaries formed in the process, and recrystallisation may occur during hot deformation. Texture also changes during deformation. All of the changes are influenced by process parameters. Recrystallisation after extensive hot-rolling results in flat, elongated grains. Final cold-rolling to thin gauge results in a more homogeneous microstructure with uniformly distributed constituents and dispersoids [11].

2.2.4 Crystallographic texture and earing

Crystallographic texture is the principal cause of the directionality of most of the mechanical properties in wrought aluminium products. Cast aluminium tends to have a random distribution of grain orientation, except where columnar grains are formed. However, the random character of the cast structure is drastically changed during hot or cold working, especially during cold working, and this random structure is replaced by highly textured grains in which considerable numbers of the deformed grains assume certain specific orientations [1]. Such texture occurs because deformation, or slip, in aluminium is confined to certain crystallographic planes and directions. These textures

formed during working are normally called rolling textures [1]. The textures achieved vary with the nature of the working process, with the changes in the shape of the workpiece and, to a lesser extent, with the composition of the alloy [1].

The rolling textures of Al sheets are generally identified to be a mixture of three ideal textures: {112}<111> (Copper), {123}<634> (S) and {011}<211> (brass) [1, 95-97], which is named as β fibre rolling texture, running from Brass orientation through S orientation to the Copper orientation [95-97]. The possible textures present in Al and its alloys are listed in Table 2.6.

Table 2.6 The possible textures in Al and its alloys [95]

Orientation name	Miller indices {hkl}<uvw>	Euler angles			Type of texture component
		φ_1	Φ	φ_2	
Copper	{112}<111>	90°	30°	45°	Rolling
S	{123}<634>	59°	34°	65°	Rolling
Brass	{011}<211>	35°	45°	0°/90°	Rolling
Goss	{011}<100>	0°	45°	0°/90°	Rolling/recrystallisation
Cube	{001}<100>	0°	0°	0°/90°	Recrystallisation
$Cube_{RD}$	{013}<100>	0°	22°	0°/90°	Recrystallisation
$Cube_{ND}$	{001}<310>	22°	0°	0°/90°	Recrystallisation
R	{124}<211>	53°	36°	60°	Recrystallisation
P	{011}<122>	65°	45°	0°/90°	Recrystallisation
Q	{013}<231>	45°	15°	10°	Recrystallisation

During annealing, when new grains are formed by recrystallisation, they frequently develop in orientations differing from the principal components of the deformation texture. Therefore, recrystallisation causes a change in the distribution of the crystallographic orientations, and thereby a change in the texture. Such changes are based on the two fundamental mechanisms of recrystallisation: the formation of nuclei and their subsequent growth into the deformed matrix [95]. Studies showed that there is a strong tendency for the new grains to form with a cube plane {100} parallel to the surface of the sheet and a cube edge parallel to the rolling direction [1]. Usually, this cube texture is found to be the dominant component in aluminium alloys after recrystallisation [98]. There are other recrystallisation texture orientations such as R, P and Q orientations as listed in Table 2.6.

The principal problem associated with directionality of properties in aluminium alloys is the formation of ears during deep drawing an article with varied texture. The height and

location of the ears vary with the texture of the sheet. The more pronounced the similar orientation of large groups of crystals in the sheet, the higher the earing will be [1]. In the sheet with rolling texture, four ears are located 45º to the rolling direction. The height of the ears increases roughly in proportion to the strength and intensity of the rolling texture [1]. The cubic texture occurring during annealing under certain conditions causes ears in the rolling direction (0°) and 90° from that direction [99], and the height of the ears increases with the percentage of cubically aligned grains [1]. Figure 2.12 schematically shows the direction of ears occurring under different texture materials. A mixed texture resulting in eight ears in which all have about the same height (four ears each at 45° and at 0°/90° to the rolling direction) can be achieved under certain conditions [99]. The occurrence of eight ears is the best compromise available in deep drawing thin, soft sheet produced from direct chill (DC) cast material [99]. Practical controls over earing are exercised through manipulation of the primary working and annealing schedules [1].

2.3 Al-Mg(-Cu)-Si-Mn alloys for the applications in packaging and automotive body

2.3.1 Introduction

Aluminium alloys are widely used for packaging applications because of their good formability and recyclability. They have been widely used in the beverage business for decades. Over the last decade there has been considerable growth in the use of aluminium alloys for the rigid packaging of foodstuff, with the most significant increase in the beverage container market. Al-Mn-Mg series alloys have been largely used as main materials in the manufacture of beverage cans. Particularly, AA3104/3004 and AA5182 have long been used as can body stock and can end stock, respectively.

The can itself has changed significantly since the introduction of the Draw and Wall Ironed (DWI) can. Despite the aluminium can's excellent properties, it is in fierce competition with cans made from steels and PET bottles [100]. Therefore, it is necessary for aluminium can stock producer to reduce product cost. Improvements in process efficiency and improvements or innovations in light weighting are the key issues to reduce the costs [101]. However, metal sheet having a high earing tendency gives rise to more frequent failure in the forming process, which makes the further down gauging of aluminium can stock very difficult. Metallurgically the can product requirements can be

summarized as low and consistent earing, high strength for manufacturing and filling, and good formability including a high quality surface finish [92].

Weight reduction is becoming a driving force for the design of automobiles in order to reduce fuel consumption. Cu-modified 5XXX series Al-Mg alloys are one of the promising candidates to replace steel for automotive manufacture. For example, AA5182 alloy has excellent formability, corrosion resistance and reasonable strength. However Lüders marks reduce surface quality of its products. Small additions of Cu can improve its mechanical strength, which make it very promising for car-body application [30, 66].

2.3.2 Aluminium canstock processing

Generally, aluminium beverage cans are fabricated from two parts: the can body, generally made from AA3104 sheet, and the can end, typically made using AA5182 alloy due to its higher strength. Typical composition ranges of canstock alloys are shown in Figure 2.13.

Canstock sheet production involves a number of thermomechanical processing steps, starting with DC ingot casting followed by homogenisation, hot rolling, annealing and cold rolling (see Figure 2.14), all of which affect the overall quality of the final thin gauge sheet, and consequently, can performance [102].

Homogenisation usually occurs at two temperatures, e.g. starting at about 570˚C followed by slow cooling to 510˚C [2]. Its main objectives in the can making process are the elimination of microsegreation, the transformation of the β-Al_6(Fe,Mn) coarse particles to α-$Al_{12}(Fe,Mn)_3Si$ particles and the redistribution of Mn from solid solution to coarse particles and dispersoids. During the relatively slow commercial heat up of an ingot, a uniform distribution of Mg, Cu and Si can be achieved after heating up to 500˚C [103].

Hot rolling at about 450˚C to reduce the thickness from around 600 mm to 25 mm is followed by warm rolling at about 275˚C to further reduce the thickness down to hot-band thickness of 2-3 mm. After that, annealing for two hours after slow heating to 350˚C is performed to promote recrystallisation. This is followed by cooling down to room temperature and multi-pass cold rolling to the final gauge around 0.25 mm. The metallurgical requirements of hot rolling are a fine recrystallised grain structure at re-roll and sufficient cube texture to control earing after cold rolling [92].

After hot rolling down to about 250 μm, the can body stock (AA3104/3004) is provided at H19 (extra hard cold rolled) temper for can body making by a draw & iron (D&I) process.

Good sheet formability is required for the D&I process, which involves blanking, cupping and finally drawing and ironing the side-walls (see Figure 2.15). For can body forming, cans are stamped from coiled sheet, and after being deep drawn into the shape of a cup on the cupping press, they are drawn and ironed (see Figure 2.16) on a body maker to obtain the desired can height. They are then trimmed to a uniform height and washed, and the inner and outer surfaces are coated with lacquer and baked. This is followed by the necking of the can body to the outer diameter of the lid. Finally, the can end is attached to the body with the formation of a flange [100]. Figure 2.17 shows a typical cross-sectional diagram of can body design [104].

The can body needs to be able to withstand a minimum dome reversal pressure, and have vertical load bearing capacity, making strength an important consideration too. Higher strength enables thinner sheet to be used and hence a more efficient use of material in the fabrication of the product. Surface qualities of the sheet are also important, both in terms of surface finish for the product and for good frictional characteristics between the sheet surface and the forming dies.

The can end is typically produced by blanking, drawing, curl forming, riveting and production of the score line for the easy-open end [104] (Figure 2.18). As well as high strength, can end stock needs good formability, low earing levels and good surface finish (no streaking). Like can body sheet, AA5182 can end sheet is strengthened by work-hardening, although some softening occurs during the pre-coating operation performed by the sheet manufacturer.

After manufacture, the can body and can end are transported to a filling plant where the beverage is put into the can and the two components are attached using a folded seam and a small amount of a sealing compound.

As a result of the texture of the material, earing may occur during the D&I process. Anisotropy in the mechanical behaviour of the sheet must be minimised to limit the formation of so-called 'ears' on the deep drawn cup. Heavy earing of the cans after the cupping and D&I processes interferes with smooth transport of cans and results in pinholes or cracking during ironing of the can body. Hence the earing level, which is associated with the severity and characteristics of the crystallographic texture components, should be controlled in a lower level. Metal sheet having a high earing tendency gives rise to more frequent failure in the forming operations [98]. Thereby, a high level of earing

creates the problem of wastage because a larger amount of aluminium must be trimmed to avoid valleys in the edge of the can with higher level of earing [100]. Earing is also produced in the sidewall of the can by a necking process following the D&I process. The earing trend during the necking process is the same as that occurring during the D&I process. Both are caused by the texture of the material. Earing during the necking process is manifested as variation in flange width and results in a poor fit to the lid. With a further progress in lid diameter reduction taking place, the appearance of earing during the necking process has become a major problem [100].

In order to reduce earing during can making process, it is important to optimise processing parameters in order to control texture during hot rolling and cold rolling. The crucial parameter in order to obtain minimal earing in the final cold-rolled sheet, is the optimisation of the cube texture component after hot rolling [100, 105].

2.3.3 Al-Mg-Mn-Cu alloys for car body application

There is a trend in the automobile industry to replace steel for automotive body panels by lighter materials to reduce car weight and its fuel consumption. The alternative materials should be strong enough with good formability, corrosion resistance and surface appearance. Aluminium alloys are the most promising candidates. An optimal combination of strength and formability requires careful control of alloy composition, working and heat treatment. Alloys from the 3XXX (e.g. AA3004), 5XXX (eg. AA5052, AA5182) and 6XXX (e.g. AA6061) series are selected for automotive applications. However, there are some problems when using these alloys for automotive applications: AA3004 alloy has a relatively low strength, some 5XXX alloys have problems with Lüders band formation [2, 60, 63, 64] during body forming and AA6061 has limited formability [2]. These problems led to the development of new alloys. One possible method is to use different aluminium alloys, e.g. AA2008, AA2036, AA6009, AA6010 and AA6013 that respond to heat treatment and can be strengthened by age hardening during paint baking operation [2]. Another possibility is to modify the above-mentioned conventional alloys with Cu additions to change their response to heat treatment and increase the strength. For example, the 5XXX series Al-Mg alloys, such as AA5182 and AA5052 alloys have been used for car body applications due to their good combination of strength, corrosion resistance and formability. However, Lüders bands/marks formed in these alloys restrict their application. According to some reports alluded to in [106], small

additions of Cu may increase their mechanical strength and introduce some precipitation hardening and reduce the tendency for Lüders bands at the same time. However, according to specialists at a leading aluminium manufacturer [107], the addition of Cu would not inhibit the formation of Lüders bands. Due to the benefits coming from Cu addition, there is a recent development in car body manufacture to use AA5182 alloy modified with Cu. There are some research studies on the influence of Cu on the mechanical properties of 5XXX alloys [30, 60, 63-66]. Thus it is important to understand the effects of Cu addition on microstructural evolution during different heat treatments and the influences of the developed microstructure on the mechanical properties in order to adopt the 5XXX series alloys as car body materials.

Figure 2.19 shows a photo of a car body structure and Figure 2.20 shows a schematic of a car body manufacture system. The process of car body stock manufacture is in many ways similar to that of can stock. It also includes DC casting, preheating, hot rolling, annealing and cold rolling down to a target thickness. For car body stock the cold-rolled sheet should be annealed/solutionised to O-temper whilst for can stock it is provided with H19. As illustrated in Figure 2.20, the complex car body making involves a series of steps, which includes pretreatment, pressing, adhesive applications, spot welding, sub-assembly and assembly of the body. This is followed by thermal cure/paint baking as a final process.

Figures

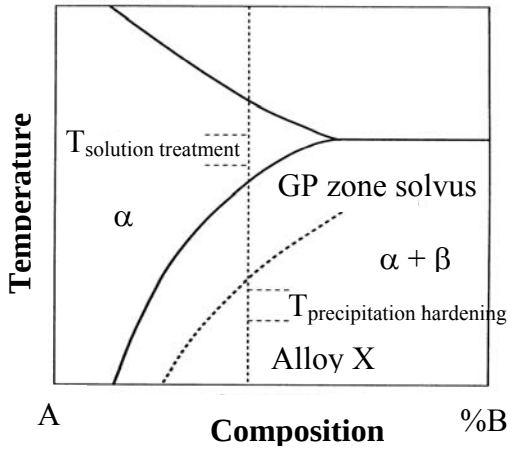

Figure 2.1 Schematic phase diagram including GP zone solvus indicating heat treatment temperature for alloy X (Redrawn from [3])

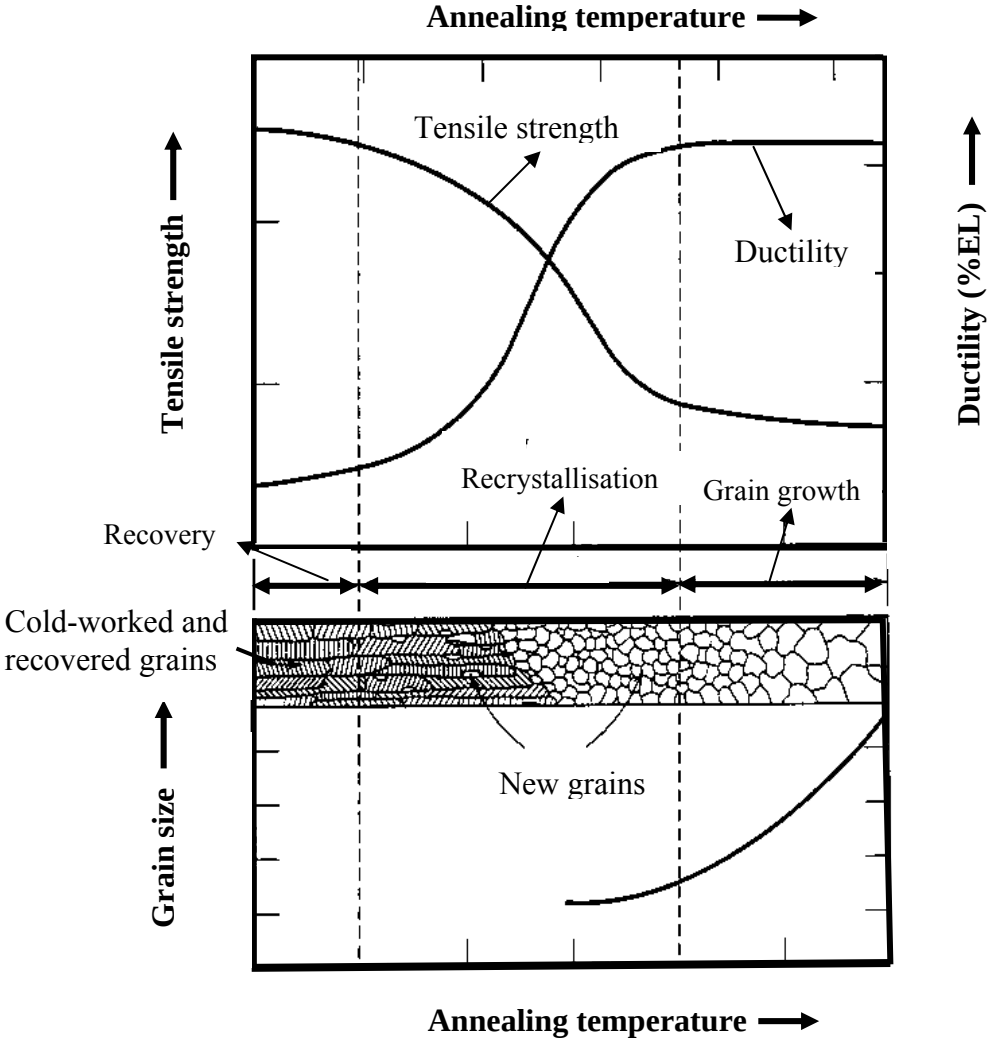

Figure 2.2 The sketch to show the influence of annealing temperature on the tensile strength and ductility (Redrawn from [9])

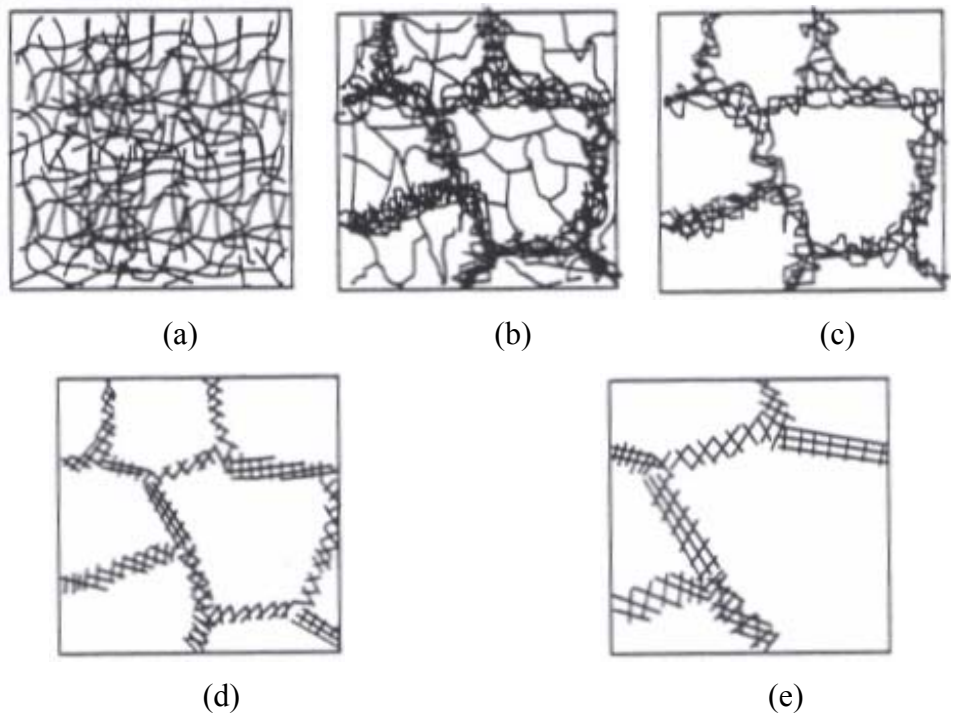

Figure 2.3 Sketch of dislocation evolution during recovery of a deformed material: a) dislocation tangles, b) cell formation, c) annihilation of dislocations within cells, d) subgrain formation, e) subgrain growth [108]

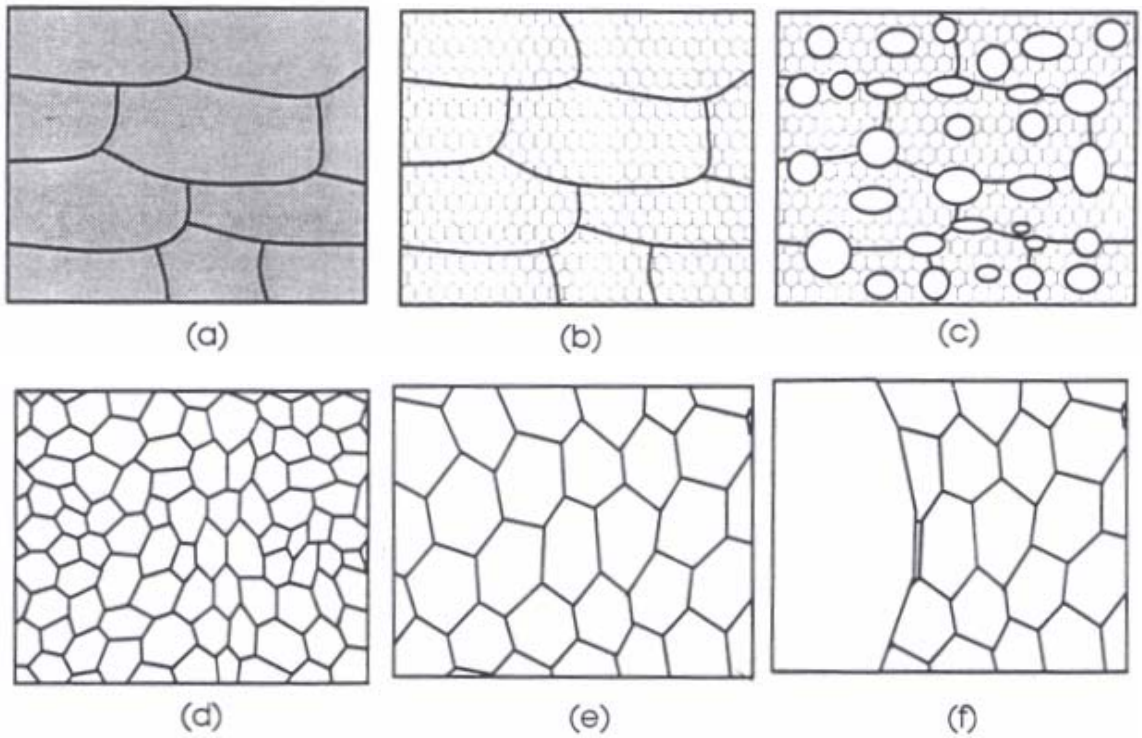

Figure 2.4 Sketches of the annealing processes a) deformed, b) recovered, c) partially recrystallised, d) fully recrystallised, e) grain growth, f) abnormal grain growth [108]

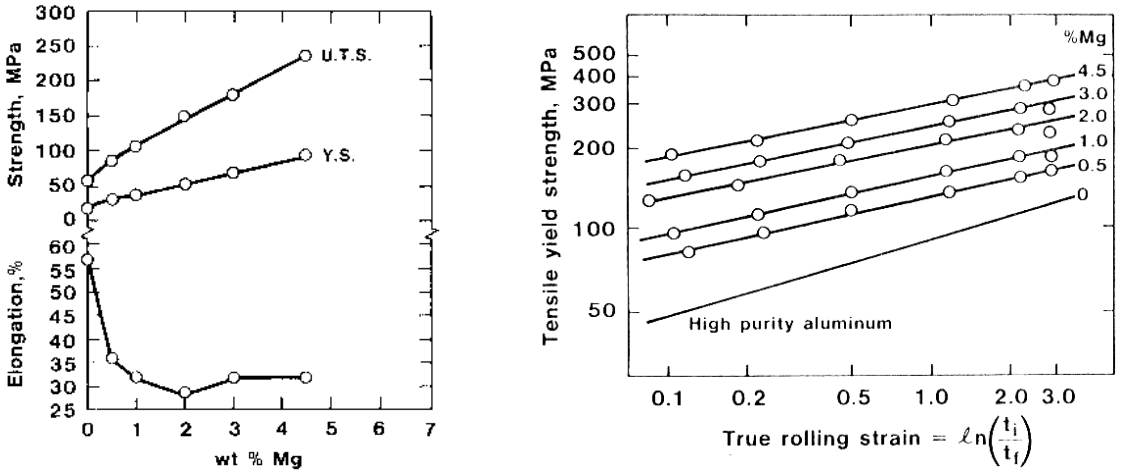

(a) (b)

Figure 2.5 (a) Effect of Mg in solution on the tensile properties of annealed Al-Mg alloys and (b) strain-hardening response of Al-Mg alloys during cold rolling [11]

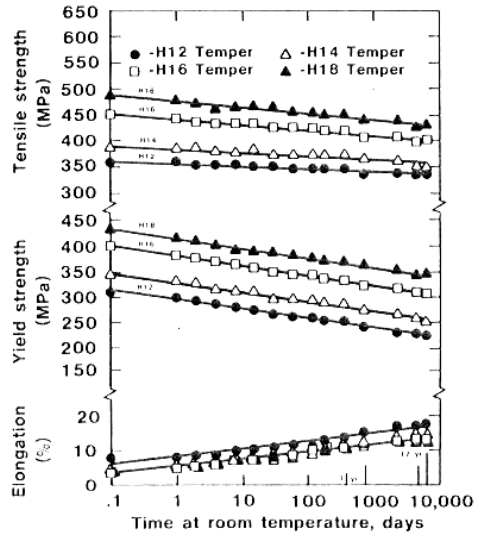

Figure 2.6 Age-softening at room temperature of a cold-rolled Al-6%Mg alloy [11]

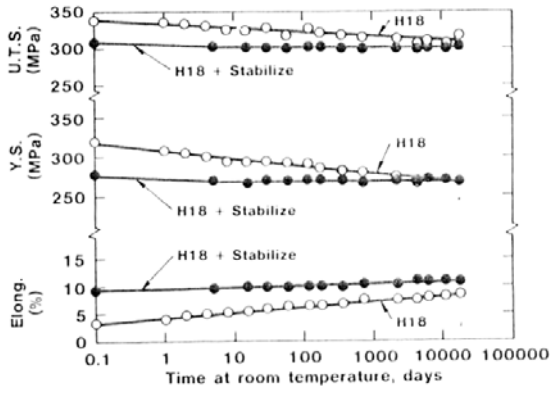

Figure 2.7 Age-softening of an AA5052-H18 alloy with and without stabilization treatment (eight hours at 143°C) [11]

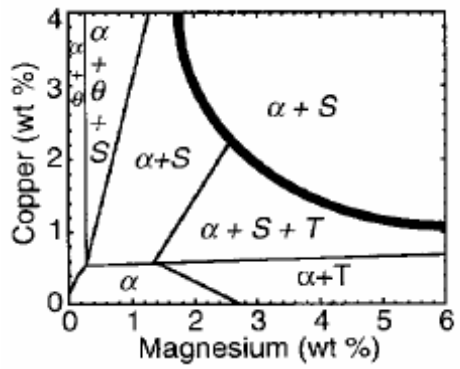

Figure 2.8 Al-Cu-Mg phase diagram showing phase boundaries at 190°C (thin lines). The thick solid line defines the α/α+S phase boundary at 500°C [33]

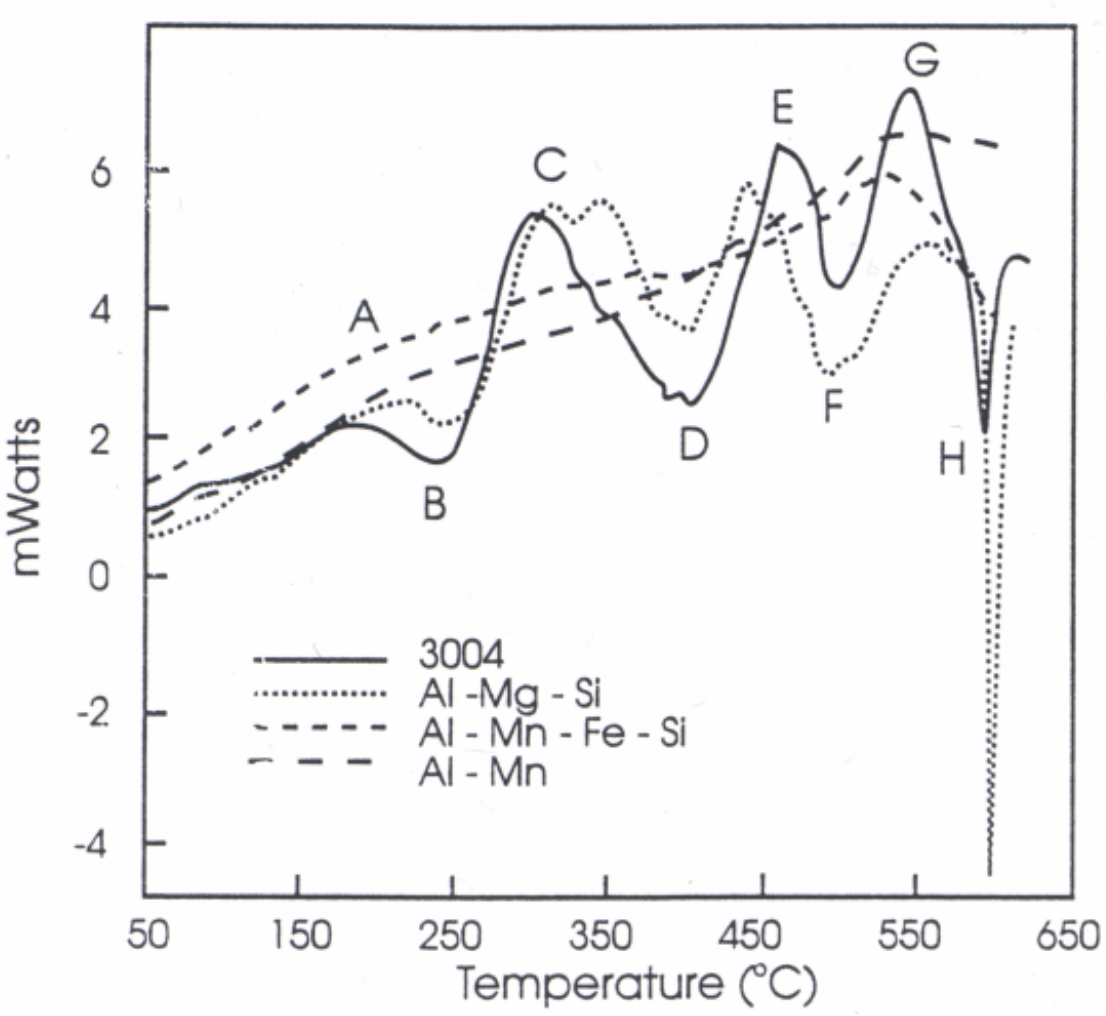

Figure 2.9 DSC traces of some Al alloys including an as-cast AA3004 alloy [82]

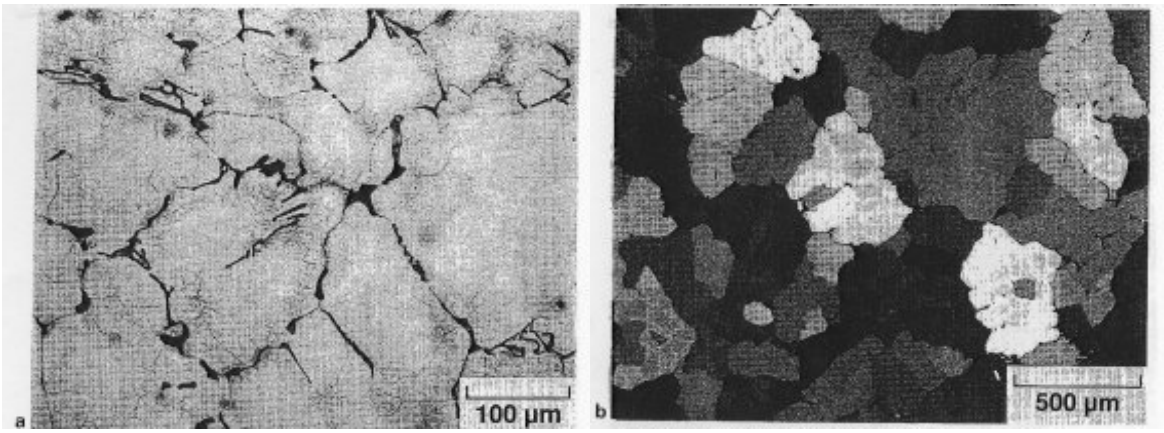

Figure 2.10 As-cast microstructure of an AA5182 alloy [94]: (a) network of constituent particles (b) coarse, equiaxed grains

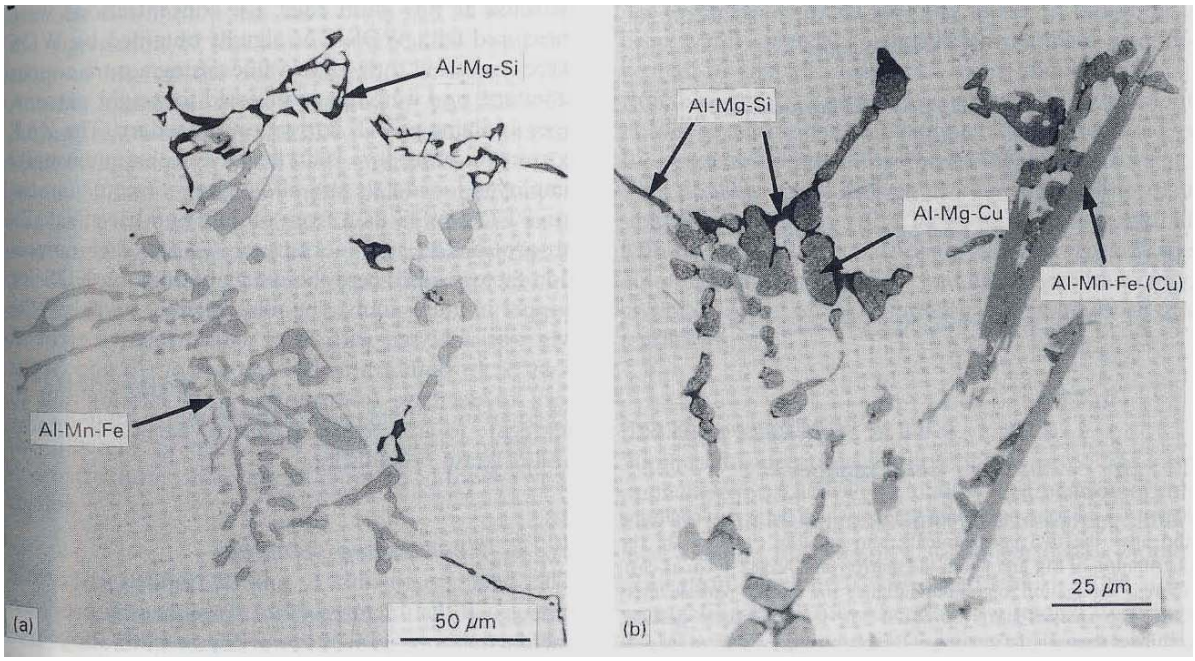

Figure 2.11 Coarse constituents in the as-cast microstructure of alloys (a) AA5182 (b)AA5182+1wt%Cu [60]

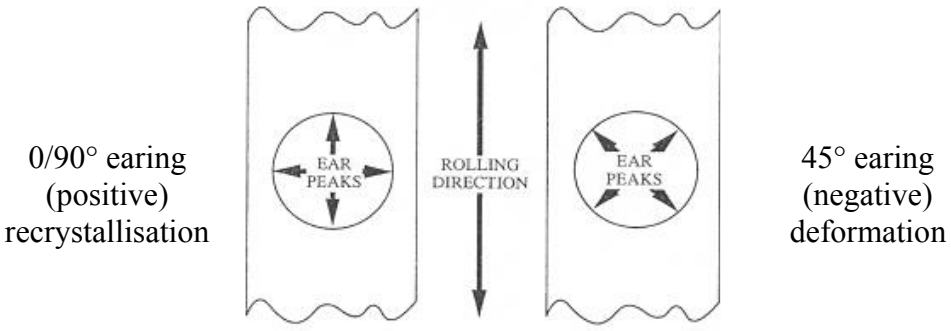

Figure 2.12 Earing directions under rolling/recrystallisation texture [109]

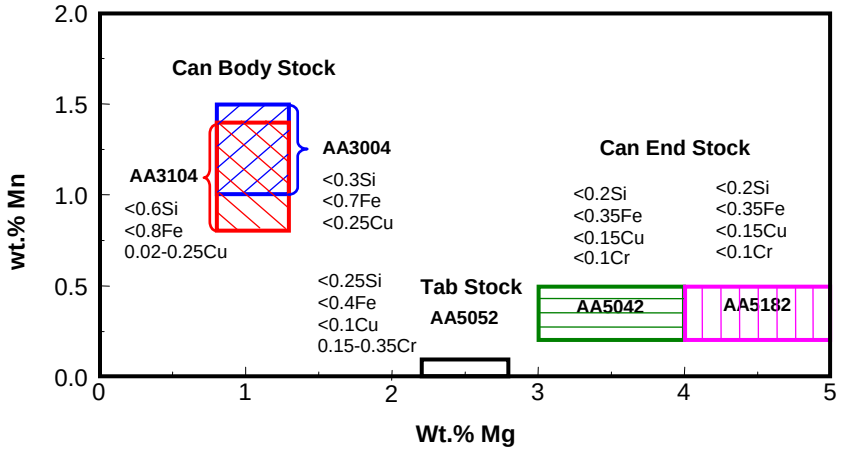

Figure 2.13 Compositions of canning alloys [109]

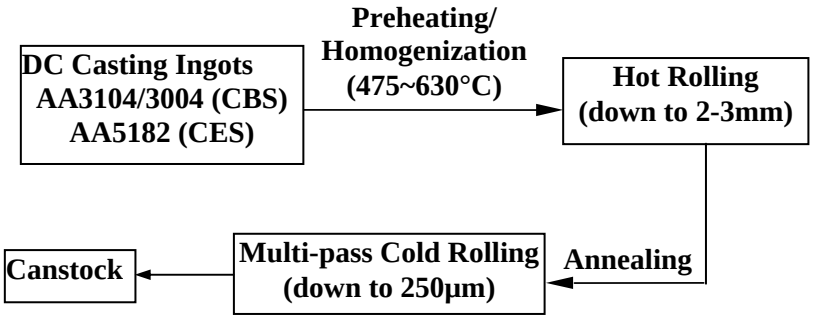

Figure 2.14 Typical processing route for canstock (CBS: Can body stock and CES: can end stock)

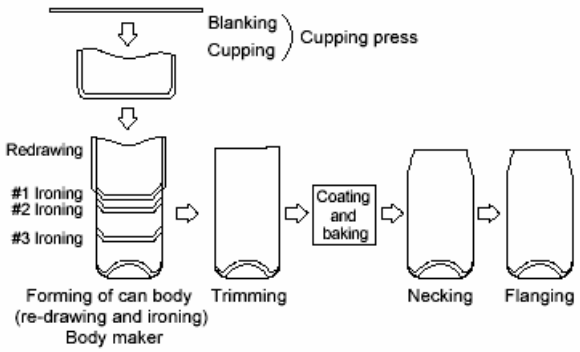

Figure 2.15 Manufacturing process for aluminium D&I can bodies [70]

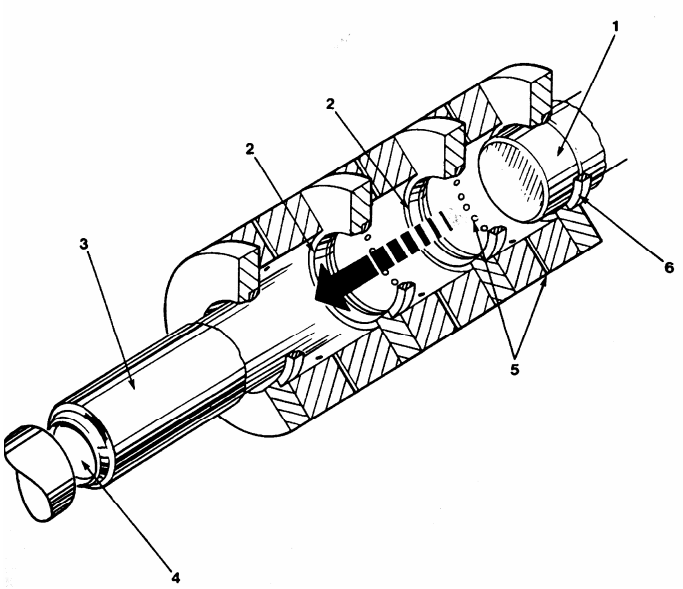

1-Cup on punch 2-Ironing dies 3-Ironed untrimmed can 4-Dome tooling 5-Cooling ports 6-Redraw die

Figure 2.16 D&I process of can body [109]

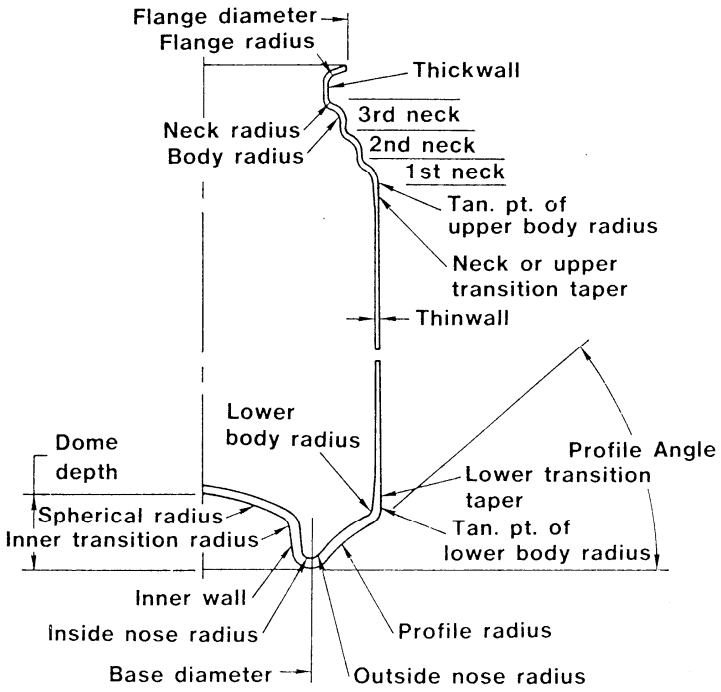

Figure 2.17 Cross-section diagram of typical beverage can design [104]

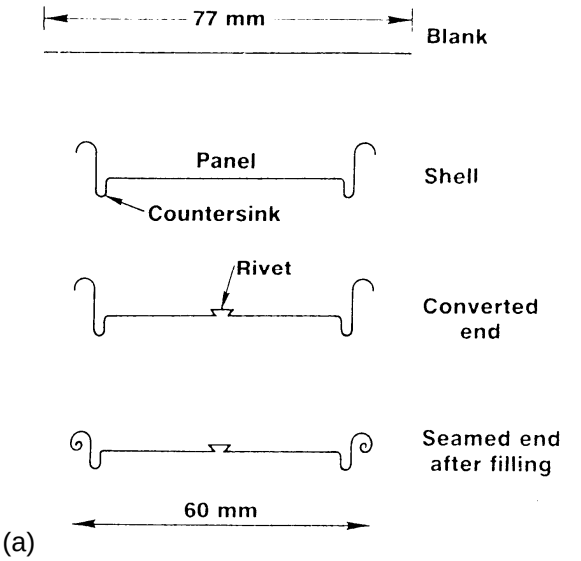

Figure 2.18 (a) Manufacture process of can end [104] (b) photos of can end at different processing stages [109]

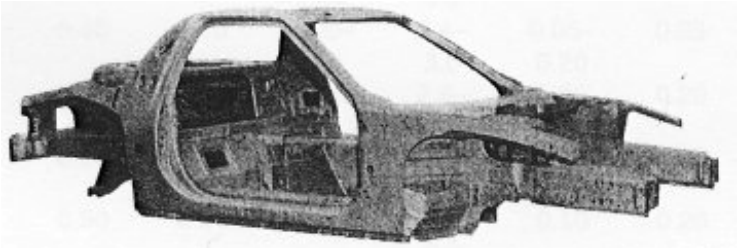

Figure 2.19 A photo of a car body structure [99]

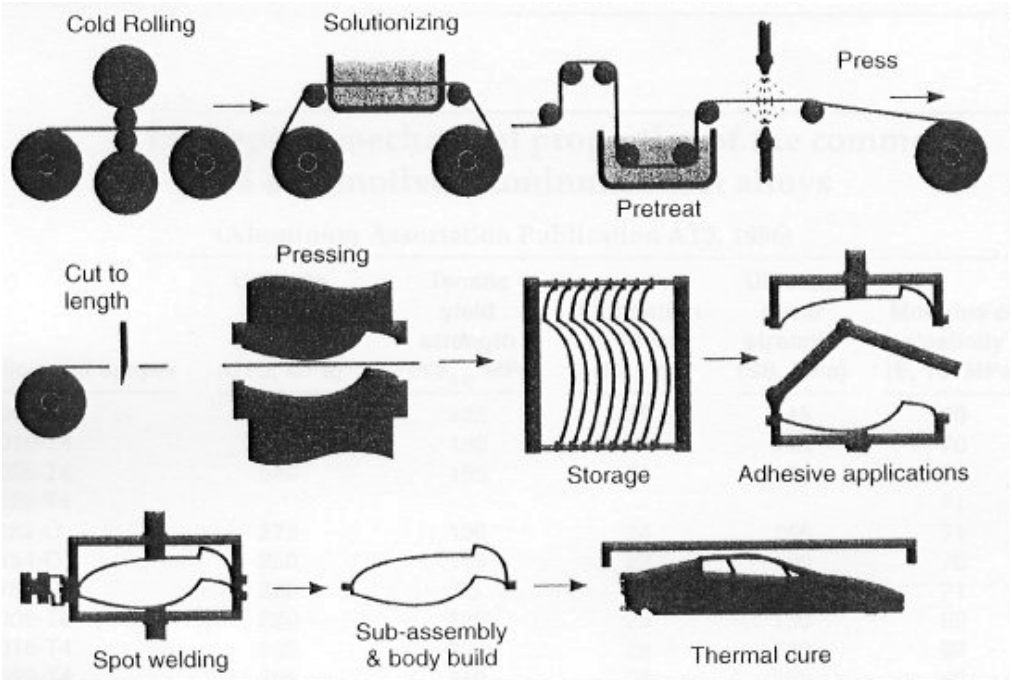

Figure 2.20 A schematic description of a car body manufacture system [99]

References

1. Hatch, J.E., ***Aluminum Properties and Physical Metallurgy*** (1st edition), Ohio, American Society for Metals, 1984.
2. Polmear, I.J., ***Light Alloys: Metallurgy of the Light Metals*** (3rd edition), New York, Halsted Press, John Wiley & Sons, Inc., 1996.
3. Gregson, P.J., ***Aluminium alloys: physical metallurgy, processing and properties***, in *High performance materials in aerospace*, Flower, H.M. (Editor), London, Chapman & Hall, 1995, p. 49.
4. Smith, W.F., ***Structure and Properties of Engineering Alloys*** (2nd edition), McGraw-Hill, 1992.
5. Martin, J.W., ***Precipitation hardening***, Oxford, Pergamon Press, 1968.
6. Vlack, L.H.V., ***Materials Science for Engineers*** (2nd edition), London, Addison-Wesley Publishing Company, 1971.
7. Gouma, P.I., Lloyd, D.J. and Mills, M.J., Mater. Sci. Eng. A, **319**, 2001, p. 439.
8. Ashby, M.F. and Jones, D.R.H., ***Engineering Materials 2: An Introduction to Microstrucures, Processing and Design***, International Series on Materials Science and Technology, Vol. 39, Oxford, Pergamon Press, 1986.
9. Callister, W.D., ***Materials Science and Engineering: An Introduction*** (5th edition), New York, Wiley, 2000.
10. Davis, J.R., ***ASM Specialty Handbook®: Aluminium and Aluminium Alloys***, ASM International®, 1993.
11. Sanders, R.E., Baumann, S.F. and Stumpf, H.C., ***Wrought Non-Heat-Treatable Aluminum Alloys***, in *Aluminium Alloys---Contemporry Research and Applications*, Vasudevan, A.K. and Doherty, R.D. (Editors), London, Academic Press, Inc., 1989.
12. Burger, G.B., Gupta, A.K., Jeffrey, P.W. and Lloyd, D.J., Mater. Charact., **35**, 1995, p. 23.
13. Marioara, C.D., Andersen, S.J., Jansen, J. and Zandbergen, H.W., Acta Mater., **51**, 2003, p. 789.
14. Chakrabarti, D.J. and Laughlin, D.E., Prog. Mater. Sci., **49**, 2004, p. 389.
15. Dutta, I. and Allen, S.M., J. Mater. Sci. Lett., 1991, p. 323.
16. Edwards, G.A., Stiller, K. and Dunlop, G.L., App. Surf. Sci., **76/77**, 1994, p. 219.
17. Edwards, G.A., Stiller, K., Dunlop, G.L. and Couper, M.J., Mater. Sci. Forum, **217-222**, 1996, p. 713.
18. Edwards, G.A., Stiller, K., Dunlop, G.L. and Couper, M.J., Acta Mater., **46**, 1998, p. 3893.
19. Murayama, M. and Hono, K., Acta Mater., **47**, 1999, p. 1537.
20. Murayama, M., Hono, K., Saga, M. and Kikuchi, M., Mater. Sci. Eng. A, **250**, 1998, p. 127.

21. Lutts, A., Acta Met., **9**, 1961, p. 577.
22. Panseri, C. and Federighi, T., J. Inst. Met., **94**, 1966, p. 99.
23. Shchegoleva, T.V., Phys. Met. Metall., **25**, 1968, p. 56.
24. Ravi, C. and Wolverton, C., Acta Mater., **52**, 2004, p. 4213.
25. Jacobs, M.H., Phil. Mag., **26A**, 1972, p. 1.
26. Matsuda, K., Gamada, H., Fujii, K., Uetani, Y., Sato, T. and Kamino, A., J. Mater. Sci., **35**, 2000, p. 179.
27. Matsuda, K., Ikeno, S., sato, T. and Kamino, A., Mater. Sci. Forum, **707**, 1996, p. 217.
28. Matsuda, K., Vetani, Y., Sato, T. and Ikeno, S., Metall. Mater. Trans. A, **32**, 2001, p. 1293.
29. Silcock, J.M., J. Inst. Metals, **89**, 1960-61, p. 203.
30. Ratchev, P., Verlinden, B., De Smet, P. and Van Houtte, P., Acta Metall. Mater., **46**, 1998, p. 3523.
31. Wang, S.C. and Starink, M.J., Mater. Sci. Eng. A, **386**, 2004, p. 156.
32. Yan, J., ***Strength modelling of Al-Cu-Mg type alloys***, PhD thesis, School of Engineering Sciences, University of Southampton, 2006.
33. Ringer, S.P., Sakurai, T. and Polmear, I.J., Acta Mater. Mater., **45**, 1997, p. 3731.
34. Wang, S.C., Starink, M.J. and Gao, N., Scripta Mater., **54**, 2006, p. 287.
35. Badini, C., Marino, F. and Verne, E., Mater. Sci. Eng. A, **191**, 1995, p. 185.
36. Xiao, D.H., Wang, J.N., Ding, D.Y. and Chen, S.P., J. Alloy. Compd., **343**, 2002, p. 77.
37. Sofyan, B.T., Raviprasad, K. and Ringer, S.P., Micron, **32**, 2001, p. 851.
38. Shih, H.C., Ho, N.J. and Huang, J.C., Metall. Mater. Trans. A, **27**, 1996, p. 2479.
39. Riontino, G. and Zanada, A., Mater. Lett., **37**, 1998, p. 241.
40. Ringer, S.P., Hono, K., Polmear, I.J. and Sakurai, T., Acta Mater., **44**, 1996, p. 1883.
41. Ringer, S.P., Hono, K., Polmear, I.J. and Sakurai, T., Appl. Surf. Sci., **94-5**, 1996, p. 253.
42. Ringer, S.P., Muddle, B.C. and Polmear, I.J., Metall. Mater. Trans. A, **26**, 1995, p. 1659.
43. Ringer, S.P., Polmear, I.J. and Sakurai, T., Mater. Sci. Eng. A, **217**, 1996, p. 273.
44. Ringer, S.P., Yeung, W., Muddle, B.C. and Polmear, I.J., Acta Metall. Mater., **42**, 1994, p. 1715.
45. Mukhopadhyay, A.K., Mater. Trans. JIM, **38**, 1997, p. 478.
46. Mukhopadhyay, A.K., Metall. Mater. Trans. A, **33**, 2002, p. 3635.
47. Mukhopadhyay, A.K., Singh, V., Prasad, K.S. and Chakravorty, C.R., Acta Mater., **44**, 1996, p. 3115.
48. Li, B.Q. and Reynolds, A.P., J. Mater. Sci., **33**, 1998, p. 5849.

49. Hong, S.K., Choi, J.C., Lin, D.Z., Tezuka, H., Sato, T. and Kamio, A., J. Jpn. Inst. Met., **60**, 1996, p. 569.
50. Gao, X., Nie, J.F. and Muddle, B.C., Mater. Sci. Forum, **217**, 1996, p. 1251.
51. Gao, N., Davin, L., Wang, S., Cerezo, A. and Starink, M.J., Mater. Sci. Forum, **396-4**, 2002, p. 923.
52. Eskin, D.G., Mater. Sci. Forum, **396-4**, 2002, p. 917.
53. Eskin, D.G., J. Mater. Sci., **38**, 2003, p. 279.
54. Ratchev, P., Verlinden, B., De Smet, P. and Van Houtte, P., Mater. Trans. JIM, **40**, 1999, p. 34.
55. Wang, S.C. and Starink, M.J., Int. Mater. Rev., **50**, 2005, p. 193.
56. Samajdar, I., Ratchev, P., Verlinden, B., Van Houtte, P. and De Smet, P., Mater. Sci. Eng. A, **247**, 1998, p. 58.
57. Zuo, Y. and Chang, Y.A., Mater. Sci. Forum, **215**, 1996, p. 141.
58. Suzuki, Y., Matsuo, M., Saga, M. and Kikuchi, M., Mater. Sci. Forum, **217**, 1996, p. 1789.
59. Ayciriex, M.D., Romero, R. and Somoza, A., Scripta Mater., **35**, 1996, p. 135.
60. Delapuente, S.M., Verlinden, B. and Delaey, L., J. Mater. Sci., **29**, 1994, p. 6167.
61. Ringer, S.P. and Hono, K., Mater. Charact., **44**, 2000, p. 101.
62. Ratchev, P., Verlinden, B. and Van Houtte, P., Scripta Metall. Mater., **30**, 1994, p. 599.
63. Ratchev, P., Verlinden, B. and Van Houtte, P., Acta Metall. Mater., **43**, 1995, p. 621.
64. Ratchev, P., Verlinden, B., De Smet, P. and Van Houtte, P., Scripta Mater., **38**, 1998, p. 1195.
65. Ratchev, P., Verlinden, B., and Zahra, A.M., Mater. Sci. Forum, **331-337**, 2000, p. 1095.
66. Ratchev, P., Verlinden, B., Van Houtte, P. and De Smet, P., Mater. Sci. Eng. A, **A222**, 1997, p. 189.
67. Vooijs, S., Davenport, B. and Zwaag, S.v.d., Mater. Sci. Forum, **331-337**, 2000, p. 933.
68. Kovarik, L., Gouma, P.I., Kisielowski, C., Court, S.A. and Mills, M.J., Mater. Sci. Forum, **396-4**, 2002, p. 845.
69. Dion, A. and Starink, M.J., ***DSC Analysis of Heavily Deformed Al-Mg-Mn-(Cu) Based Alloys for Canstock***, Report, Materials Research Group, School of Engineering Sciences, Universitiy of Southampton, Southampton, 2001.
70. Starink, M.J. and Dion, A., Thermochim. Acta, **417**, 2004, p. 5.
71. Kovarik, L., Gouma, P.I., Kisielowski, C., Court, S.A. and Mills, M.J., Acta Mater., **52**, 2004, p. 2509.

72. Kovarik, L., Miller, M.K., Court, S.A. and Mills, M.J., ***Atom probe tomography study of GPB zones in Al-Mg-Cu(-Si) alloys***, in *International conference on solid-solid phase transformations in inorganic materials 2005*, Howe, J. (Editor), Phoenix, Arizona, USA, TMS (The Minerals, Metals & Materials Society), 2005.
73. Verlinden, B. and Zahra, A.M., Mater. sci. Forum, **426-4**, 2003, p. 423.
74. Yao, J.Y., Graham, D.A., Rinderer, B. and Couper, M.J., Micron, **32**, 2001, p. 865.
75. Miao, W.F. and Laughlin, D.E., Metall. Mater. Trans. A, **31**, 2000, p. 361.
76. Chakrabarti, D.J., Cheong, B.K. and Laughlin, D.E., ***Precipitation in Al-Mg-Si-Cu alloys and the role of the Q phase and its precursors***, in *Automotive Alloys II*, Das, S.K. (Editor), Warrendale, USA, TMS, 1998, p. 27.
77. Chakrabarti, D.J., Peng, Y.G. and Laughlin, D.E., Mater. Sci. Forum, **396-4**, 2002, p. 857.
78. Lloyd, D.J., Evans, D.R. and Gupta, A.K., Can. Metall. Quarterly, **39**, 2000, p. 475.
79. Go, J., Poole, W.J., Militzer, M. and Wells, M.A., Mater. Sci. Forum, **426-432**, 2003, p. 291.
80. Esmaeili, S., Wang, X., Lloyd, D.J. and Poole, W.J., Metall. Mater. Trans. A, **34**, 2003, p. 751.
81. Wang, X., Poole, W.J., Esmaeili, S., Lloyd, D.J. and Embury, J.D., Metall. Mater. Trans. A, **34**, 2003, p. 2913.
82. Owen, N.J., Lykins, M.L., Stanton, G. and Malin, A.S., ***Differential Scanning Calorimetry of Aluminum Alloy-3004***, in *Recrystallization 90 - International Conference on Recrystallization in Metallic Materials*, 1990, p. 649.
83. Chen, L. and Morris, J.G., Scripta Metall Mater, **18**, 1984, p. 1365.
84. Deschamps, A., Livet, F. and Brechet, Y., Acta Mater., **47**, 1999, p. 281.
85. Yassar, R.S., Field, D.P. and Weiland, H., Scripta Mater., **53**, 2005, p. 299.
86. Ismail, Z.H., Scripta Metall. Mater., **32**, 1995, p. 457.
87. Yassar, R.S., Field, D.P. and Weiland, H., Metall. Mater. Trans. A, **36**, 2005, p. 2059.
88. Quainoo, G.K. and Yannacopoulos, S., J. Mater. Sci., **39**, 2004, p. 6495.
89. Birol, Y., Scripta Mater., **52**, 2005, p. 169–173.
90. Zhen, L. and Kang, S.B., Mat. Sci. Technol., **14**, 1998, p. 317.
91. Dutkiewicz, J. and Litynska, L., Mater. Sci. Eng. A, **324**, 2002, p. 239.
92. Marshall, G.J., Mater. Sci. Forum, **217-222**, 1996, p. 19.
93. Sun, T.C., ***The effect of preheating on AA3104 Aluminum alloy ingot structure and particulate composition***, in *Aluminum alloys for packaging*, Morris, J.G., Merchant, H.D., Westerman, E.J. and Morris, P.L. (Editors), Chicago, The Minerals, Metals & Matierals Society (TMS), 1992, p. 31.
94. Hollinshead, P.A., Mat. Sci. Technol., **8**, 1992, p. 57.
95. Engler, O., Mat. Sci. Technol., **12**, 1996, p. 859.

96. Liu, W.C. and Morris, J.G., Scripta Mater., **47**, 2002, p. 743.
97. Huh, M.Y., Cho, S.Y. and Engler, O., Mater. Sci. Eng., **A315**, 2001, p. 35.
98. Ding, S. and Morris, J.G., Metall. Mater. Trans. A, **28**, 1997, p. 2715.
99. Altenpohl, D.G., ***Aluminum: Technology, Applications, and Environment–A Profile of a Modern Metal*** (6th edition), Kaufman, J.G. and Das, S.K. (Editors), Warrendale, Pennsylvania, The Aluminum Association Inc. and The Minerals, Metals & Materials Society (TMS), 1998.
100. Koyama, K., Urayoshi, S. and Tanaka, T., Furukawa Review, **18**, 1999, p. 97.
101. Courbon, J., Mater. Sci. Forum, **331-337**, 2000, p. 17.
102. Kamat, R.G., JOM, 1996, p. 34.
103. Bolingbroke, R.K., Marshall, G.J. and Ricks, R.A., ***Microstructural development during preheating of AA3004***, in *the 3rd International conference on Aluminium alloys*, Arnberg, L., Lohne, O., Nes, E. and Ryum, N. (Editors), Trondheim, Norway, 1992, p. 285.
104. Sanders, R.E., Lege, D.J. and Hartman, I.L., Aluminium, **65**, 1989, p. 941.
105. Daaland, O. and Nes, E., Acta Mater., **44**, 1996, p. 1389.
106. Ratchev, P., Verlinden, B., VanHoutte, P. and De Smet, P., Mater. Sci. Forum, **217**, 1996, p. 1187.
107. Court, S.A., ***Personal communication***, Southampton, 2004.
108. Humphreys, F.J. and Hatherly, M., ***Recrystallization and related annealing phenomena*** (2nd edition), Oxford, Elsevier Science Ltd., 2002.
109. Cama, H., ***Intermetallics and Aluminium for (Beverage) Cans***, 2002, www.msm.cam.ac.uk/phase-trans/2002/havovy/hec.htm.

3 Models for Work Hardening, Recovery and Precipitation Hardening

Dislocations influence materials mechanical properties. Materials can be strengthened by work hardening due to an increase in the number of dislocations, which tangle each other during deformation. On the other hand, strength is reduced by recovery due to dislocations annihilating each other during the annealing. Precipitation hardening occurs due to the interactions between dislocations and precipitates. In this chapter, the models for work hardening, recovery and precipitation hardening will be reviewed.

3.1 General introduction to dislocations

A dislocation is a line defect existing in a crystal. It especially influences and controls the behaviour of plastic deformation of a material. In practice, virtually all crystalline materials contain some dislocations, introduced during solidification, plastic deformation, or as a consequence of thermal stresses that result from rapid cooling.

The dislocation density (ρ) in a material is defined as the total dislocation length per unit volume, or equivalently, the number of dislocations that intersect a unit area of a random section [1]. Dislocation densities as low as 10^9 m^{-2} are typical for carefully solidified metals. For heavily deformed metals, the density may be as high as 10^{15}–10^{16} m^{-2}. Heat treating a deformed materials can diminish the density to the order of 10^{11}–10^{12} m^{-2} [1, 2] after full recrystallisation. For recovered samples, the dislocation density is about 10^{14} m^{-2} [2]. Mean dislocation spacing (l_d) is often used to characterise dislocations, which is inversely proportional to the dislocation density expressed as:

$$l_d = \rho^{-1/2} \qquad \textbf{(3.1)}$$

The density and the mobility of dislocations influence plastic deformation of a material. Under plastic deformation, dislocations will be generated under applied shear stress, which strengthens the material. On the other hand, dislocations may be annihilated when the deformed material is annealed, i.e. recovery occurs, which reduces the strength of a material.

Precipitation hardening is the result of the interactions between dislocations and precipitates. Precipitates act as a field of obstacles for dislocation movements. For slip to

occur, the dislocation must either move around (by-pass) the precipitates particles, or cut through the particles. An active dislocation will select from the various paths available to it, i.e., the path where the least energy is expended will be chosen. A slip plane is formed when a dislocation avoids the particles or obstacles. A dislocation loop may be formed if the dislocation bows out between the particles by the Orowan mechanism. In both cases, energy must be supplied to increase the total length of dislocation lines. If the obstacles are weak and closely spaced, then it will be energetically favourable for the dislocations to shear the particles [3].

3.2 Work hardening models

A primary goal of a theory of work hardening is to predict or explain the stress-strain curve, which is linked to the development of dislocation substructure [4]. The theory of work hardening or work hardening models have been developed by a range of researchers including Taylor, Ashby, Kocks, Mecking, Estrin and Nes etc.

3.2.1 KM model

In the 1960-1980's, Kocks and Mecking [5-11] developed a work hardening model, which is generally referred to as the KM model. It is a phenomenological approach to macroscopic plasticity of metals [12].

A. Dislocation evolution equation

In the model, the average dislocation density ρ is selected as the only governing structure parameter. The change in dislocation density consists of two components [6]:

$$d\rho = d\rho_{stor} - d\rho_{\mathrm{Recov}} \qquad \textbf{(3.2)}$$

The first term describes obstacle density increasing due to dislocation storage. The second term considers dislocation density change due to dislocation annihilation. Thereby, the evolution equation can be written as:

$$\frac{d\rho}{d\gamma} = \frac{d\rho_{stor}}{d\gamma} - \frac{d\rho_{\mathrm{Recov}}}{d\gamma} \qquad \textbf{(3.3)}$$

where γ is shear strain.

In the KM model, the evolution equation takes the following form [6, 12]:

$$\frac{d\rho}{d\gamma} = k_1 \rho^{1/2} - k_2 \rho \qquad \textbf{(3.4)}$$

In equation (3.4), the first term in the right side is related with the athermal storage of moving dislocations which become immobilized after having travelled a distance proportional to the average spacing between the dislocations (i.e. $\rho^{-1/2}$) [12]. Accordingly k_1 is a constant evaluated by the following equation [12]:

$$k_1 = 2\frac{\theta_{II}}{\alpha_0 G b} \qquad \textbf{(3.5)}$$

where α_0 is a constant, G is shear modulus, b is Burgers vector and θ_{II} is the slope of the stress-strain curve in stage II. For f.c.c. metals, θ_{II} is expressed as [12]:

$$\theta_{II} \approx \frac{G}{200} \qquad \textbf{(3.6)}$$

The second term in equation (3.4) is associated with dynamic recovery. Since dynamic recovery is thermally activated, k_2 is a function of temperature (T) and strain rate $\dot{\gamma}$ [12]:

$$k_2 = k_2(\dot{\gamma}, T) \qquad \textbf{(3.7)}$$

By integrating equation (3.4), the following relation of dislocation density with strain (γ) is obtained:

$$\rho = \rho_s \{1 - [1 - (\frac{\rho_0}{\rho_s})^{1/2}] e^{-\frac{k_2}{2}\gamma}\}^2 \qquad \textbf{(3.8)}$$

where ρ_0 is the initial dislocation density at $\gamma = 0$ and $\rho_s = (\frac{k_1}{k_2})^2$.

B. Kinetic equation

The component of the flow stress due to obstacle/immobile dislocations τ may be linked to the dislocation density by the following relation [6]:

$$\tau = \alpha_\rho G b \rho^{1/2} \qquad \textbf{(3.9)}$$

where α_ρ is a constant. τ is also known as the mechanical threshold strength of the obstacles to dislocations glide [7, 13].

C. Work hardening coefficient

The work hardening coefficient is defined by [6]:

$$\theta = \left.\frac{\partial \tau}{\partial \gamma}\right|_{\dot{\gamma},T} \qquad \textbf{(3.10)}$$

Therefore, the hardening coefficient at constant strain rate can be given as follows:

$$\theta = \theta_0 (1 - \frac{\tau}{\tau_s}) \qquad \textbf{(3.11)}$$

where $\theta_0 = \frac{1}{2}\alpha_\rho G b k_1$ and $\tau_s = \alpha_\rho G b (k_1 / k_2)$

3.2.2 KME models

From the 1980's, Estrin and co-workers have further developed the KM model [12-24] to consider the influence of second phase particles on dislocation generation. These models are usually referred to as the Kocks-Mecking-Estrin (or KME) models [25].

3.2.2.1 Modified KM model

In the KM model, the mean free path of dislocations is assumed to be proportional to $\rho^{-1/2}$, which is appropriate for coarse-grained single-phase materials. However, such assumption is no longer reasonable when the spacing between nonshearable obstacles is geometrically determined. In particle strengthened or very fine-grained materials, the mean free path is described by the particle spacing or by the grain size [12]. In such case, Estrin proposed an appropriate assumption that the mean free path is constant. The modified KM model is derived based on the assumption, and it is considered applicable to a material with high density of geometric obstacles, i.e, a particle strengthened material.

A. Dislocation evolution equation

Based on the assumption that the mean free path is constant, the modified dislocation evolution equation reads as the following form [12, 17]:

$$\frac{d\rho}{d\gamma} = k_d - k_2 \rho \qquad \textbf{(3.12)}$$

where k_d is a constant determined by the mean free path or spacing l_d between these geometric obstacles, bearing the following relation [12, 17]:

$$k_d = (bl_d)^{-1} \quad \textbf{(3.13)}$$

By integrating equation (3.12), the following relation can be obtained:

$$\rho = k_r - (k_r - \rho_0)e^{(-k_2\gamma)} \quad \textbf{(3.14)}$$

where $k_r = \frac{k_d}{k_2}$. ρ_0 is the initial dislocation density at $\gamma = 0$.

B. Kinetic equation

The kinetic equation takes the same form as that in the KM model. So it can be expressed as follows:

$$\tau = \alpha_\rho Gb[k_r - (k_r - \rho_0)e^{(-k_2\gamma)}]^{1/2} \quad \textbf{(3.15)}$$

C. Work hardening coefficient

The work hardening coefficient at constant strain rate can then be given as

$$\theta = \frac{\alpha_\rho Gb}{2}(k_d\rho^{-1/2} - k_2\rho^{1/2}) \quad \textbf{(3.16)}$$

Multiplying by τ at both sides of equation (3.16) yields:

$$\theta\tau = \theta_0^*[1-(\frac{\tau}{\tau_s^*})^2] \quad \textbf{(3.17)}$$

where $\theta_0^* = \frac{1}{2}k_d(\alpha_\rho Gb)^2$ and $\tau_s^* = \alpha_\rho Gb(\frac{k_d}{k_2})^{1/2}$.

3.2.2.2 Hybrid model

In a material where geometric obstacles substantially outnumber the dislocation related ones, the modified KM model is reasonable. However, if the number of two types of obstacles is almost at the same level, then the hybrid model, which considers the superposition of both types of obstacles, is more suitable.

A. Dislocation evolution equation

In the hybrid model, the dislocation evolution equation is given by [12, 17]:

$$\frac{d\rho}{d\gamma} = k_d + k_1\rho^{1/2} - f_a k_2 \rho \qquad \textbf{(3.18)}$$

which superposes the increase of dislocation density due to geometric obstacles and dislocation related ones. f_a is a factor introduced to consider the influence of dislocation-particle interactions on the recovery rate. It is a function of stress and temperature [17].

B. Kinetic equation

The kinetic equation also takes the same form as that in the KM model given by (3.9).

C. Work hardening coefficient

The hardening coefficient at constant strain rate in the hybrid model is given by:

$$\theta = \frac{\alpha_\rho Gb}{2}(k_d\rho^{-1/2} + k_1 - f_a k_2 \rho^{1/2}) \qquad \textbf{(3.19)}$$

Multiplying by τ at both sides of equation (3.19) gives:

$$\theta\tau = \frac{1}{2}(\alpha_\rho Gb)^2(k_d + k_1\rho^{1/2} - f_a k_2 \rho) \qquad \textbf{(3.20)}$$

For the hybrid model, there is no simple analytical expression for dislocation evolution, thus a numeric solution is required to use the model.

In the above sections, shear stress τ and shear strain γ were used to describe the work hardening behaviour of materials. However, most materials are polycrystalline containing many grains, therefore it is better to use the polycrystalline stress σ and strain ε to describe the work hardening behaviour of materials. The following relations exist [7, 17]:

$$\sigma = M\tau \qquad \textbf{(3.21)}$$

$$\gamma = M\varepsilon \qquad \textbf{(3.22)}$$

where M is the Taylor factor.

3.2.3 Multi-internal-state-variable models

Both the KM model and KME model are one parameter models. However, a model employing just one internal variable (dislocation density ρ) is not enough for deformation histories involving rapid changes of the deformation path [12]. Hence, multi-internal-variable models have been developed in the last two decades based on better

understanding of the microstructure evolution during deformation with advanced TEM techniques.

3.2.3.1 Two-internal-state-variable models

In the two-internal-variable model, the total dislocation density ρ is differentiated into two types: the mobile dislocation density ρ_m and the relatively immobile, or forest density ρ_f [12, 22]. The evolutions of the two types of dislocation density are coupled with each other. The detailed evolution law proposed by Estrin and Kubin in 1986 are given in [12, 22]. It is beyond the scope of this review to explain the evolution law in detail.

Another type of two-internal-state-variable model was put forward by Estrin and co-workers [23, 26]. In this model the dislocations were distinguished into the dislocation in the cell wall and in the cell interior according to a proposed cell structure (see Figure 3.1). Therefore the two parameters in the model are ρ_w (dislocation density in the cell wall) and ρ_c (dislocation density in the cell interior).

This model can be mainly summarised as follows:

$$\sigma = M(f_i\tau_c + f_w\tau_w) \qquad \textbf{(3.23)}$$

where

$$\begin{cases} \tau_c = \alpha_\rho Gb\sqrt{\rho_c} \\ \tau_w = \alpha_\rho Gb\sqrt{\rho_w} \\ f_w = \dfrac{2wd - w^2}{d^2} \\ f_i = 1 - f_w \end{cases} \qquad \textbf{(3.24)}$$

In the above equations, w and d are the thickness of cell wall and cell size, respectively.

In the model, ρ_w and ρ_c have their own complicated evolution law [23, 26], which is out of the scope of this review.

3.2.3.2 Three-internal-state-variable models (3IVMs)

Roters and Gottstein and co-workers [27-29] put forward a three-internal-state-variable model. The main idea of the model is based on the cell structure shown in Figure 3.2, which derives from contemporary understanding of microstructural evolution and the interaction of dislocations with elements of the microstructure. As shown in Figure 3.2,

there are 3 dislocation classes in the model: dislocations in the cell wall, mobile and immobile dislocations in the cell interior. Therefore the three parameters in the model are: dislocation density in the cell wall (ρ_w) which is a high density, immobile dislocation density in the cell interior (ρ_i) which is relatively low and mobile dislocation density in the cell interior (ρ_m).

Similar to the KM model, KME model and two-internal-state-variable models, the three-internal-state-variable model (3IVM) consists of evolution equations for the mircostructural elements considered and a kinetic equation of state that connects the actual microstructure, temperature and strain rate with the necessary flow stress [28]. The model is summarised as follows.

A. Kinetic equation

The external stress can be written as

$$\sigma_{ext} = M(f_i\tau_i + f_w\tau_w) \qquad \textbf{(3.25)}$$

where f_i and f_w are the volume fractions of cell interior and cell walls, respectively, and

$$\tau_x = \tau_{eff_x} + \alpha_\rho Gb\sqrt{\rho_x} \quad (x = i, w) \qquad \textbf{(3.26)}$$

where the effective shear stress τ_{effx} can be solved from the following equations:

$$\begin{cases} \dot{\gamma} = M\dot{\varepsilon} = \rho_m b v_x \\ v_x = l_{dx} v_0 \exp(-\dfrac{E_g}{k_B T}) \sinh(\dfrac{\tau_{eff_x} V}{k_B T}) \end{cases} \quad (x = i, w) \qquad \textbf{(3.27)}$$

where $\dot{\gamma}$ is strain rate, v is the average dislocation glide velocity, l_d is the mean spacing of obstacles, v_0 is the attack frequency, E_g is the effective activation energy for dislocation glide, V is the activation volume and k_B is Boltzmann's constant.

B. Evolution equation

The complicated evolution equation for the three types of dislocation density can be summarized as the following simple expression:

$$\dot{\rho}_x = \dot{\rho}_x^+ + \dot{\rho}_x^- \quad (x = m, i, w) \qquad \textbf{(3.28)}$$

where $\dot{\rho}_x^+$ represents the dislocation density increase due to work hardening, whilst $\dot{\rho}_x^-$ considers the reduction in dislocation density due to dynamic recovery. The set of evolution equations for the three-category dislocations is very extensive, and it is out of the scope of this review at present. The basic considerations underlying these evolution equations are similar to the simpler KM or KME models described before, and details can be obtained from [27, 28].

3.2.3.3 Nes model

Based on the extensive studies on the evolution of microstructure during deformation, Nes and co-workers [25, 30-45] have developed another multi-internal work hardening model. The Nes model is based on the microstructure shown in Figure 3.3. The mathematically description of this model can be simplified as follows.

A. Kinetic equation

The kinetic equation in the Nes model is given by [36, 40]

$$\tau = \tau_t + \tau_p + \alpha_\rho Gb\sqrt{\rho_i} + \alpha_1 Gb(\frac{1}{\delta} + \frac{1}{D}) \qquad \textbf{(3.29)}$$

where τ_t is the thermal component to the shear stress, τ_p the shear stress contribution due to non-deformable particles (dispersoids), α_ρ and α_1 are constants, δ and D are the cell/sub-grain size and grain size, respectively.

τ_t is based on the Orowan equation given by the following equation [36, 40]:

$$2\sinh(\frac{\tau_t V}{k_B T}) = [b^2 \rho_m B_t v_D]^{-1} \dot{\gamma} \exp(\frac{E_a}{k_B T}) \qquad \textbf{(3.30)}$$

where E_a is an activation energy, v_D is the Debye frequency and B_t is a constant.

τ_p is given by [36, 40]:

$$\tau_p = \frac{\alpha_2 Gb}{1.24 \times 2\pi}[\frac{1}{l_d}\ln(\frac{l_d}{b})] \qquad \textbf{(3.31)}$$

which expresses the Orowan bypass stress proposed by Ashby. In the above equation, α_2 is a constant around one and l_d is particle spacing in the slip plane which can be written as [36, 40]:

$$l_d = 0.8(\sqrt{\pi / f} - 2)r \qquad \textbf{(3.32)}$$

where *f* and *r* are the volume fraction of the particles and their radius, respectively.

B. Microstructure evolution

The principle of scaling (or similitude) is used in the microstructure evolution, which implies that the mircostructural elements scale with each other as follows [25, 38, 40, 41]:

$$\begin{cases} w = q_w \delta \\ \delta = q_c \sqrt{\rho_i} \\ \sqrt{\rho_w} = q_b \sqrt{\rho_i} \end{cases} \qquad \textbf{(3.33)}$$

where q_w, q_c and q_b are scaling constants.

The evolution laws of δ and ρ_i can be summarized as the following simple expressions:

$$\begin{cases} \dfrac{d\rho_i}{d\gamma} = \dfrac{d\rho_i^+}{d\gamma} + \dfrac{d\rho_i^-}{d\gamma} \\ \dfrac{d\delta}{d\gamma} = \dfrac{d\delta^+}{d\gamma} + \dfrac{d\delta^-}{d\gamma} \end{cases} \qquad \textbf{(3.34)}$$

The detailed equations of the evolution laws are available in [25, 38, 40, 41].

3.3 Models for recovery

During ageing at elevated temperature, alloys with prestrain may experience recovery and recrystallisation depending on the ageing temperatures and times. Thereby, the cold-worked material softens. Recovery can be measured by the changes in alloy's properties, such as yield strength, hardness or resistivity [46].

3.3.1 Empirical equations for recovery kinetics

X_R is taken to be a parameter representing a property of the materials (e.g, yield strength, hardness) in a recovered state. Two types of empirical isothermal recovery kinetics are most commonly reported [46].

A. Type 1 kinetics

The type 1 kinetics of recovery is expressed as

$$\frac{dX_R}{dt} = -\frac{\alpha_1}{t} \qquad \textbf{(3.35)}$$

which integrates to

$$X_R = \alpha_2 - \alpha_1 \ln t \qquad \textbf{(3.36)}$$

where α_1, α_2 are constants.

This relationship is considered valid for the middle stages of recovery, but it is invalid during the early stages of recovery ($t \to 0$) when $X_R \to X_0$ or at the end of recovery ($t \to \infty$) when $X_R \to 0$.

B. Type 2 kinetics

The type 2 kinetics of recovery is given by

$$\frac{dX_R}{dt} = -\alpha_1 X_R{}^{j} \qquad \textbf{(3.37)}$$

which integrates to

$$\begin{cases} X_R{}^{-(j-1)} - X_0{}^{-(j-1)} = (j-1)\alpha_1 t & (j > 1) \\ \ln(X_R) - \ln(X_0) = \alpha_1 t & (j = 1) \end{cases} \qquad \textbf{(3.38)}$$

3.3.2 Models for recovery of flow stress based on crystal defects

Recovery of mechanical properties during annealing can also be modelled based on a microstructural representation using two parameters: the cell/subgrain structure represented by size δ and the dislocation density ρ within the subgrains [37]. Thereby, the recovery of flow stress can be obtained by considering the time dependent contributions due to subgrain growth and dislocation network growth. Two types of such models were proposed in the literature [37].

A. Model 1: a fractional approach

In this approach, the microstructure during annealing is treated as a composite structure consisting of a cell/subgrain structure with an average size $\delta(t)$ and dislocation density $\rho(t)$ between the boundaries. Thus, in the model, the instantaneous flow stress during recovery can be expressed by [37]:

$$\sigma(t) = \sigma_i + \alpha_1 MGb\sqrt{\rho(t)} + \alpha_2 MGb\frac{1}{\delta(t)} \quad \textbf{(3.39)}$$

where σ_i is the frictional stress, both α_1 and α_2 are a constant.

The extent of the recovery (R_{rec}) is usually defined in terms of the instantaneous yield strength (or hardness etc.) of the recovered materials ($\sigma(t)$), the yield strength in the deformed state (σ_{wh}) and the yield strength in the undeformed or fully recrystallised state (σ_{rex}) as

$$R_{rec} = \frac{\sigma(t) - \sigma_{rex}}{\sigma_{wh} - \sigma_{rex}} \quad \textbf{(3.40)}$$

R_{rec} is also termed as the fraction residual strain hardening.

Therefore, in terms of the fraction residual strain hardening R_{rec}, equation (3.39) can be written by [37]

$$R_{rec} = f_1\sqrt{\frac{\rho}{\rho_0}} + f_2\frac{\delta_0}{\delta} \quad \textbf{(3.41)}$$

where

$f_1 = \frac{\alpha_1 MGb\sqrt{\rho_0}}{\sigma - \sigma_i}$, $f_2 = \frac{\alpha_2 MGb}{\delta_0(\sigma_{wh} - \sigma_{rex})}$ and $f_1 + f_2 = 1$

ρ_0 and δ_0 are the dislocation density and average cell size at $t=0$, respectively.

B. Model 2: a sequential approach

An alternative possible microstructure evolution during annealing is in the form of a gradual transition from a relatively uniform distribution of dislocations to a cell and subgrain structure [37]. In this case the flow stress can be given by [37]

$$\sigma(t) = \sigma_i + f_n\alpha_1 MGb\sqrt{\rho(t)} + (1 - f_n)\alpha_2 MGb\frac{1}{\delta(t)} \quad \textbf{(3.42)}$$

where f_n is a transition function with the following expression:

$$f_n = \frac{1}{\exp(\frac{t - t^*}{\alpha_3 t^*}) + 1} \quad \textbf{(3.43)}$$

where α_3 is a constant, and t^* is the time at which the flow stress changes from being predominantly determined by the uniformly distributed dislocations to being controlled by subgrain growth.

The fraction residual strain hardening therefore is expressed as [37]

$$R_{rec} = f_n \sqrt{\frac{\rho}{\rho_0}} + (1 - f_n) C^* \frac{\delta_0}{\delta} \qquad \textbf{(3.44)}$$

where

$$C^* = \frac{\alpha_2}{\alpha_1 \delta_0 \sqrt{\rho_0}} \qquad \textbf{(3.45)}$$

The following form for the fraction residual strain hardening was derived and used to model the recovery of Al-Mg alloys by Nes [37]:

$$R_{rec} = 1 - \frac{k_B T}{A} \ln(1 + \frac{t}{\hat{t}}) \qquad \textbf{(3.46)}$$

where A is a constant. $\hat{t}$ has the following form:

$$\hat{t} = \hat{t}_o \exp(\frac{E_{rec}}{k_B T}) \qquad \textbf{(3.47)}$$

where $\hat{t}_0$ is a constant, and E_{rec} is the activation energy of recovery.

Equation (3.46) is a type 1 kinetics. It is commonly used in modelling the kinetics of recovery. For example, it was adopted by Chen et al. in [47] to model the evolution of dislocation density during recovery.

A model with a more detailed description of thermal activation of recovery was proposed by Kuhlmann, by Cottrell and Aytekin and by Friedel [46]. It is based on the assumption that recovery may be controlled by thermally activated glide or cross-slip. In the model, the rate of recovery can be expressed as

$$\frac{d\sigma}{dt} = -k_{rec} \exp[-\frac{E_{rec}(\sigma)}{k_B T}] \qquad \textbf{(3.48)}$$

where k_{rec} is a constant and the activation energy for recovery $E_{rec}(\sigma)$ was suggested to be stress dependent with the following form at low stresses:

$$E_{rec}(\sigma) = E_{rec0} - V_{rec}\sigma \qquad \textbf{(3.49)}$$

where E_{rec0} is a constant and V_{rec} is the activation volume of the elementary recovery events.

Therefore, if recovery is controlled by thermally activated glide, the activation energy decreases linearly with stress σ, or dislocation density. During recovery, the dislocation density decreases, hence the activation energy increases. By measurements of recovery in Al-Mg alloys, E_{rec0} was found to be independent of strain, but to be dependent on the Mg content of the alloy. It ranged from 277 kJ/mol for Al-1%Mg to 231 kJ/mol for Al-5% Mg [46].

Integrating (3.48) gives the following equation:

$$\sigma(t) = \sigma_0 - \frac{k_B T}{V_{rec}} \ln(1 + \frac{t}{\hat{t}}) \qquad \textbf{(3.50)}$$

where σ_0 is the flow stress at *t=0* and $\hat{t}$ is a reference time given by

$$\hat{t} = \frac{k_B T}{k_{rec} V_{rec}} \exp(\frac{E_{rec0} - V_{rec}\sigma}{k_B T}) \qquad \textbf{(3.51)}$$

It is noted that a modified form of the above recovery model was proposed by Verdier et al. [48], which was adopted by Go et al. [49] and by Zurob et al. [50]. This is beyond the scope of the present literature review.

3.4 Models for precipitation hardening

A large number of models have been proposed to predict the strength for precipitation-hardening alloys [50-63]. Shercliff and Ashby [53] made a first attempt to assemble a process model for overall strength for the age hardening aluminium alloys, and it provided a reasonable description of age hardening for some 2XXX and 6XXX alloys. Poole et al. [58, 59] have extended and further developed the Shercliff-Ashby approach to account for the levels of prestrain and recovery involved in the two steps of age-hardening for 7XXX alloys. Deschamps and Brechet [54] have also constructed a comprehensive model for precipitation kinetics integrating nucleation, growth and coarsening, which accounts for the competitive kinetics of heterogeneous and homogeneous precipitation, therefore, it can describe the effect of prestrain on the subsequent ageing behaviour of an Al-Zn-Mg alloy. Myhr and co-workers [55, 56] adopted a precipitation model coupled with classic

nucleation, growth and coarsening based on the method of finite differences to model the age hardening behaviour of Al-Mg-Si alloys. Esmaeili et al. [52, 57] proposed a new precipitation kinetic model for the kinetics of concurrent precipitate formation and cluster dissolution during artificial ageing of an alloy with different levels of natural aging, and the kinetic model is combined with a yield strength model to predict the age hardening behaviour of a naturally aged Al-Mg-Si-Cu alloy. It is beyond the scope of the present literature review to explain all of these models in detail.

Starink and Yan [60, 64, 65] have developed a precipitation model for S phase and clusters in Al-Cu-Mg 2XXX alloys. This model is essentially a model for microstructure development containing the kinetics of nucleation, growth and coarsening of precipitates. The model works well for the description of yield strength evolution during ageing of Al-Cu-Mg 2XXX alloys [60, 64-66]. Hence this model will be adopted in the modelling of yield strength evolution of the alloys studied in this thesis (see Chapter 6). Below, the basic elements of this model are reviewed.

3.4.1 Regular solution model

The solubility limits of Cu and Mg in the matrix for S/clusters (for clusters, the Cu:Mg ratio is assumed to be 1:1) were expressed as [64]

$$(c_e^{Cu})(c_e^{Mg}) = \Delta S_x \exp(-\frac{\Delta H^x}{RT}) \quad (x = S, cluster) \qquad \textbf{(3.52)}$$

where ΔH^x and ΔS are the formation enthalpy and entropy of S/clusters, respectively. The appropriate values can be derived from available solvus of the precipitated phases.

Meanwhile the following relation exists for S/clusters [64]:

$$c_e^{Mg} = c_0^{Mg} - (c_0^{Cu} - c_e^{Cu}) \qquad \textbf{(3.53)}$$

where c_0^{Mg}, c_0^{Cu} are the initial concentrations of Mg and Cu, respectively.

3.4.2 Precipitation model

The Starink-Zahra (SZ) model for precipitation nucleation and growth was used [60, 64-66]:

$$\alpha_x(T,t) = 1 - \{\frac{[k(T)t]^n}{\eta_i} + 1\}^{-\eta_i} \qquad \textbf{(3.54)}$$

where α_x is the transformed fraction of S/cluster, n is the reaction exponent, η_i is the impingement exponent and $k(T)$ is the rate constant expressed by an Arrhenius relation [60, 64-66]:

$$k(T) = k_0 \exp(-\frac{E_{ppt}}{k_B T}) \quad \textbf{(3.55)}$$

where k_0 is a pre-exponent constant, E_{ppt} is the activation energy of the precipitation reaction.

A novel, simple analytical approach is used to model the average size of the precipitates based on the Lifshitz-Slyozov-Wagner (LSW) theory. In this approach, the average precipitate size at nucleation/growth stage is given by [60, 64-66]:

$$\bar{l}_g(t) = \bar{l}_0 \alpha^{1/3} \quad \textbf{(3.56)}$$

where $\bar{l}_0$ is the average size of the precipitates at the start of coarsening.

The average size at coarsening stage is given by the LSW theory [60, 64-66]:

$$\bar{l}_c^{\,3}(t) = \bar{l}_0^{\,3} + k_c(T)t \quad \textbf{(3.57)}$$

with

$$k_c(T) = k_{c0} \exp(-\frac{E_{co}}{k_B T}) \quad \textbf{(3.58)}$$

where E_{co} is the activation energy for coarsening, k_{c0} is a constant.

A simple approach to deal with the transition from growth to coarsening is given by [60, 64-66]:

$$\bar{l}(t) = \bar{l}_g(t) + \bar{l}_c(t) - \bar{l}_0 \quad \textbf{(3.59)}$$

3.4.3 Precipitation hardening model

The cluster strengthening can be expressed by [60, 64, 65]

$$\Delta\tau_{cl} = \frac{\Delta G}{4\pi\sqrt{2}} f_{cl}^{1/2} \quad \textbf{(3.60)}$$

where ΔG is the difference between the shear moduli of the matrix and the clusters and f_{cl} is the volume fraction of the clusters.

The strengthening due to S phase is given by [60, 64, 65]

$$\Delta\tau_s = \frac{0.81Gb}{2\pi(1-\upsilon)^{1/2}}\left[\frac{\ln(d/b)}{0.615d\sqrt{\frac{2\pi}{3f_s}}-d}\right] \qquad \textbf{(3.61)}$$

where υ is the Poisson's ratio for Al, d is the diameter of the cross-section of S phase, and f_s is the volume fraction of S phase.

Figures

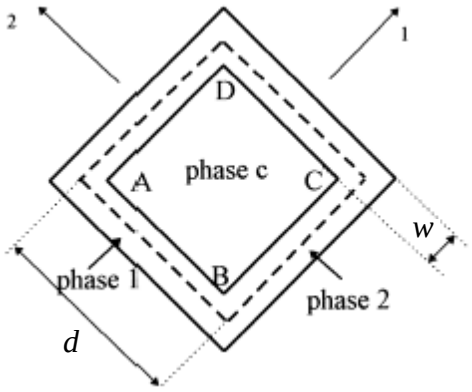

Figure 3.1 A dislocation cell in torsion. The broken line shows the unit cell (from [23])

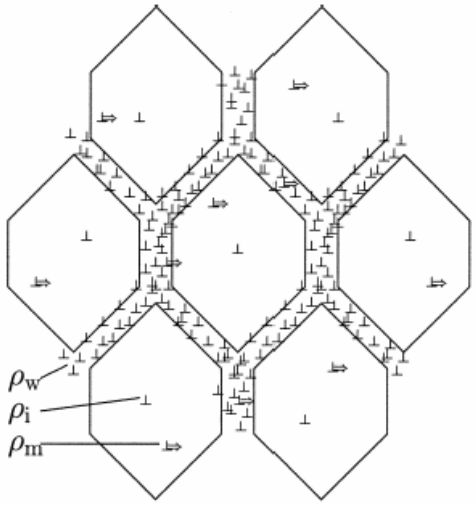

Figure 3.2 Schematic drawings of the arrangement of the three dislocation classes considered in the three-internal-variable model (from [27])

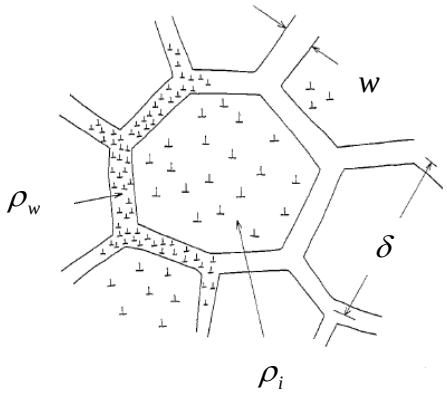

Figure 3.3 A schematic representation of the dislocation microstructure: cell diameter δ, cell wall thickness w, cell wall dislocation density ρ_w and dislocation density within the cells ρ_i (from [25])

References

1. Callister, W.D., ***Materials Science and Engineering: An Introduction*** (5th edition), New York, Wiley, 2000.
2. Altenpohl, D.G., ***Aluminum: Technology, Applications, and Environment–A Profile of a Modern Metal*** (6th edition), Kaufman, J.G. and Das, S.K. (Editors), Warrendale, Pennsylvania, The Aluminum Association Inc. and The Minerals, Metals & Materials Society (TMS), 1998.
3. Sprackling, M.T., ***The plastic deformation of simple ionic crystals***, Materials Science Series, London, Academic Press Inc. Ltd., 1976.
4. Kocks, U.F. and Mecking, H., Prog. Mater. Sci., **48**, 2003, p. 171.
5. Kocks, U.F., Philos. Mag., **13**, 1966, p. 541.
6. Kocks, U.F., J. Eng. Mater.-T. ASME, **98**, 1976, p. 77.
7. Kocks, U.F., ***Constitutive Behavior Based on Crystal Plasticity***, in *Unified Constitutive Equations for Creep and Plasticity*, Miller, A.K. (Editor), London, Elsevier Applied Science, 1987, p. 1.
8. Kocks, U.F., Argon, A.S. and Ashby, M.F., Prog. Mater. Sci., **19**, 1975, p. 1.
9. Mecking, H. and Kocks, U.F., Acta Metall. Mater., **29**, 1981, p. 1865.
10. Mecking, H., Nicklas, B., Zarubova, N. and Kocks, U.F., Acta Metall. Mater., **34**, 1986, p. 527.
11. Mecking, H., ***Strain Hardening and Dynamic Recovery***, in *Dislocation Modelling of Physical Systems*, Ashby, M.F. (Editor), Pergamon Press, Oxford, 1981, p. 197.
12. Estrin, Y. and Mecking, H., Acta Metall. Mater., **32**, 1984, p. 57.
13. Estrin, Y., Sluys, B., Brechet, Y. and Molinari, A., J. Phys. IV, **8**, 1998, p. 135.
14. Kim, H.S., Estrin, Y. and Bush, M.B., Acta Mater., **48**, 2000, p. 493.
15. Braasch, H., Estrin, Y. and Brechet, Y., Scripta Mater., **35**, 1996, p. 279.
16. Brechet, Y., Estrin, Y. and Reusch, F., Scripta Mater., **39**, 1998, p. 1191.
17. Estrin, Y., ***Dislocation-Density-Related Constitutive Modeling***, in *Unified Constitutive Laws of Plastic Deformation*, Krausz, A.S. and Krausz, K. (Editors), Toronto, Academic Press, 1996, p. 69.
18. Estrin, Y., J. Mater. Process. Tech., **80-81**, 1998, p. 33.
19. Estrin, Y., Arndt, S., Heilmaier, M. and Brechet, Y., Acta Mater., **47**, 1999, p. 595.
20. Estrin, Y. and Kubin, L.P., Acta Metall. Mater., **34**, 1986, p. 2455.
21. Estrin, Y. and Brechet, Y., Pure Appl. Geophys., **147**, 1996, p. 745.
22. Estrin, Y. and Mecking, H., Scripta Metall. Mater., **27**, 1992, p. 647.
23. Estrin, Y., Toth, L.S., Molinari, A. and Brechet, Y., Acta Mater., **46**, 1998, p. 5509.
24. Reichert, B., Estrin, Y. and Schuster, H., Scripta Mater., **38**, 1998, p. 1463.
25. Nes, E., Prog. Mater. Sci., **41**, 1997, p. 129.

26. Toth, L.S., Molinari, A. and Estrin, Y., J. Eng. Mater. Technol.-Trans. ASME, **124**, 2002, p. 71.
27. Roters, F., Raabe, D. and Gottstein, G., Acta Mater., **48**, 2000, p. 4181.
28. Goerdeler, M. and Gottstein, G., Mater. Sci. Eng. A, **309**, 2001, p. 377.
29. Karhausen, K.F. and Roters, F., J. Mater. Process. Technol., **123**, 2002, p. 155.
30. Forbord, B., Marthinsen, K. and Nes, E., Mater. Sci. Forum, **331-3**, 2000, p. 557.
31. Furu, T., Orsund, R. and Nes, E., Acta Metall. Mater., **43**, 1995, p. 2209.
32. Furu, T., Orsund, R. and Nes, E., Mater. Sci. Eng. A, **214**, 1996, p. 122.
33. Holmedal, B., Abtahi, S., Marthinsen, K. and Nes, E., Mater. Sci. Forum, **396-4**, 2002, p. 315.
34. Marthinsen, K. and Nes, E., Mater. Sci. Eng. A, **234**, 1997, p. 1095.
35. Marthinsen, K. and Nes, E., Mater. Sci. Forum, **331-3**, 2000, p. 1231.
36. Marthinsen, K. and Nes, E., Mat. Sci. Technol., **17**, 2001, p. 376.
37. Nes, E., Acta Metall. Mater., **43**, 1995, p. 2189.
38. Nes, E. and Marthinsen, K., Mater. Sci. Eng. A, **322**, 2002, p. 176.
39. Nes, E., Marthinsen, K. and Brechet, Y., Scripta Mater., **47**, 2002, p. 607.
40. Nes, E., Marthinsen, K. and Ronning, B., J. Mater. Process. Technol., **117**, 2001, p. 333.
41. Nes, E., Pettersen, T. and Marthinsen, K., Scripta Mater., **43**, 2000, p. 55.
42. Nord-Varhaug, K., Forbord, B., Benestad, J., Pettersen, T., Ronning, B., Bardal, A., Benum, S., Marthinsen, K. and Nes, E., Mater. Sci. Forum, **331-3**, 2000, p. 1387.
43. Ryen, O., Holmedal, B. and Nes, E., Mater. Sci. Forum, **396-4**, 2002, p. 1145.
44. Vatne, H.E., Perocheau, F., Ekstrom, H.E., Poizat, L., Nes, E., Hagstrom, J., Lyttle, M. and Furu, T., J. Phys. IV, **11**, 2001, p. 123.
45. Verdier, M., Saeter, J.A., Janecek, M., Brechet, Y., Guyot, P., Duly, D., Nes, E. and Orsund, R., Mater. Sci. Forum, **217**, 1996, p. 435.
46. Humphreys, F.J. and Hatherly, M., ***Recrystallization and related annealing phenomena*** (2nd edition), Oxford, Elsevier Science Ltd., 2002.
47. Chen, S.P., Kuijpers, N.C.W. and Van der Zwaag, S., Mat. Sci. Eng. A, 2002.
48. Verdier, M., Brechet, Y. and Guyot, P., Acta Mater., **47**, 1998, p. 127.
49. Go, J., Poole, W.J., Militzer, M. and Wells, M.A., ***The interaction between precipitation and recrystallization during annealing of cold rolled AA6111***, in *Thermec'2003, Pts 1-5*, 2003, p. 291.
50. Zurob, H.S., Hutchinson, C.R., Brechet, Y. and Purdy, G., Acta Mater., **50**, 2002, p. 3075.
51. Zurob, H.S., Brechet, Y. and Purdy, G., Acta Mater., **49**, 2001, p. 4183.
52. Esmaeili, S., Lloyd, D.J. and Poole, W.J., Acta Mater., **51**, 2003, p. 3467.
53. Shercliff, H.R. and Ashby, M.F., Acta Metall. Mater, **38**, 1990, p. 1789.

54. Deschamps, A. and Brechet, Y., Acta Mater., **47**, 1999, p. 293.
55. Myhr, O.R. and Grong, ∅., Acta Mater., **48**, 2000, p. 1605.
56. Myhr, O.R., Grong, ∅. and Andersen, S.J., Acta Mater., **49**, 2001, p. 65.
57. Esmaeili, S., Lloyd, D.J. and Poole, W.J., Acta Mater., **51**, 2003, p. 2243.
58. Poole, W.J., Shercliff, H.R. and Castillo, T., Mat. Sci. Technol., **13**, 1997, p. 897.
59. Poole, W.J., Saeter, J.A., Skjervold, S. and Waterloo, G., Metall. Mater. Trans. A, **31**, 2000, p. 2327.
60. Starink, M.J. and Yan, J.-L., ***A model for strengthening of Al-Cu-Mg alloys by S phase***, in *1st International Symposium on Metallurgical Modelling for Aluminum Alloys, ASM Materials Solution 2003*, Tiryakioglu, M. and Lalli, L.A. (Editors), Pittsburgh, Pennsylvania, ASM International, 2003, p. 119.
61. Starink, M.J., Wang, P., Sinclair, I. and Gregson, P.J., Acta Mater., **47**, 1999, p. 3841.
62. Starink, M.J., Wang, P., Sinclair, I. and Gregson, P.J., Acta Mater., **47**, 1999, p. 3855.
63. Starink, M.J., Hobson, A.J. and Gregson, P.J., Mater. Sci. Forum, **331-3**, 2000, p. 1321.
64. Yan, J., ***Strength modelling of Al-Cu-Mg type alloys***, PhD thesis, School of Engineering Sciences, University of Southampton, 2006.
65. Starink, M.J., Gao, N., Davin, L., Yan, J. and Cerezo, A., Philos. Mag., **85**, 2005, p. 1395.
66. Starink, M.J., Gao, N. and Yan, J.L., Mater. Sci. Eng. A, **387-389**, 2004, p. 222.

4 Material Production and Experimental Techniques

4.1 Materials production

The experimental work for the PhD programme involves nine Al-Mg(-Cu)-Mn alloys, which were cast and rolled at Banbury Laboratory UK, of Alcan International Limited. The compositions of the alloys were analysed and the results are listed in Table 4.1.

Table 4.1 The compositions of the nine alloys

Wt.% / Alloy No.	Mg	Cu	Mn	Fe	Si	Zn	Ti	Cr	B
Alloy A1	1.02	<.01	.25	.22	.16	.003	.014	.001	.0018
Alloy A2	1.96	<.01	.25	.20	.15	.003	.013	.001	.0018
Alloy A3	2.95	<.01	.24	.20	.15	.003	.013	.001	.0018
Alloy A4	1.01	.18	.26	.21	.14	.003	.014	.001	.0017
Alloy A5	1.91	.18	.25	.19	.14	.003	.014	.001	.0020
Alloy A6	2.99	.19	.24	.19	.15	.003	.013	.001	.0019
Alloy A7	1.03	.39	.26	.20	.14	.003	.016	.001	.0022
Alloy A8	1.98	.39	.25	.21	.15	.003	.013	.001	.0018
Alloy A9	2.90	.40	.25	.19	.15	.003	.013	.001	.0019

After casting, the ingot was preheated to 540°C at a heating rate of about 50°C/hour and held for four hours for homogenisation treatment. Subsequently the ingot was taken out and it was hot rolled down to 5 mm nominally.

After hot rolling, the plates were solution treated at 500°C for about 20 minutes. Subsequently, they were cold rolled with three different reductions: 90%, 40% and 10%. These three reductions were achieved by multi-pass cold rolling from the 5 mm re-roll gauge to three target thicknesses. The three nominal final thicknesses of the cold-rolled plates are: 4.5 mm for 10% reduction, 3 mm for 40% reduction and 0.5 mm for 90% reduction, respectively. All the procedures of materials processing were conducted at Banbury Laboratory UK. After processing, the cold-rolled plates were stored at room temperature in the laboratory at the University of Southampton.

4.2 Heat treatments

For some samples, solution treatments of the cold-worked samples were performed before experiments or further heat treatment. The solution treatments have been carried out in an air circulated furnace. For the solution treatments, 10% cold-worked samples were selected to be resolutionised at 500°C or 550°C for 30 minutes. The abbreviations STH and STL stand for solution treatment at the higher temperature (550°C) and at the lower temperature (500°C), respectively. After the samples were heated up to the desired solutionising temperature, e.g. 500 or 550°C, the temperature of the furnace was maintained for 30 minutes. Subsequently the samples were taken out and immediately quenched in a bucket of water at room temperature.

For isothermal ageing, some selected samples (e.g., cold-worked samples and solution treated samples) were artificially aged. All of these artificial ageing treatments have been carried out in an air circulating oven. During the heating up of the specimens, their temperature increases slowly. It usually takes 15-30 minutes to heat up to the desired temperature depending on the oven, the size and number of specimens etc. So the actual ageing time is longer than the nominal ageing time. (Note that the nominal ageing time is counted from the moment when the specimens' temperature reaches the desired temperature.) Therefore, an equivalent or effective time is introduced in this study to consider this influence. The temperature evolution during heating needs to be monitored and recorded in order to calculate the equivalent time.

The equivalent time, t_{eq}, is defined as the ageing time at an isothermal temperature, T_{iso}, equivalent to the time at a non-isothermal ageing, based on the condition that the amounts transferred at the two ageing conditions are equal. All the ageing treatments in this study are a non-isothermal ageing heating up to 170°C followed by an isothermal ageing at 170°C. Therefore, the equivalent time can be expressed as follows [1-3]:

$$t_{eq} = \frac{\int \exp(-\frac{E_a}{RT(t)})dt}{\exp(-\frac{E_a}{RT_{iso}})} \qquad \textbf{(4.1)}$$

where t is a time, E_a is the activation energy, which is presumed to be equal to the activation energy of precipitation, i.e. 152 kJ/mol (see Chapter 6), T_{iso} is the (intended or reference) isothermal ageing temperature, and R is the gas constant.

In this study, the equivalent times calculated by equation (4.1) will be used in figures and tables with the results of hardness tests and tensile tests presented in Chapter 5. Time correction is typically in the order of 10 minutes for each incremental ageing.

4.3 Hardness testing

In a preliminary study of recovery and precipitation, samples aged at 170ºC for nominal times between 30 minutes and 56 days were tested by a micro-Vickers hardness tester. Hardness testing was performed on the cold-worked samples of all the nine alloys with three different cold-rolling reductions and the STH samples. Some additional hardness tests were also performed on the STL samples. In the tests, small pieces of plates were cut and ground using #120, 600, 1200 and 4000 grade SiC-grinding paper. These samples were then aged at 170ºC in an oven. Ageing was performed incrementally, i.e., the same samples were aged and tested in several cycles. Each time before hardness tests, the micro-Vickers hardness tester was calibrated using a standard test block. The indentation was conducted with a 1 kg load and held for 15 s. For each ageing condition, five indentations were made on each sample. The mean of the five indentations was used.

4.4 Tensile testing

As the alloys were cold rolled with flat sheet geometry, sheet-type specimens were used for tensile tests. The tensile testing specimens were designed based on the ASTM-E8M standard (see Figure 4.1). To ensure that fracture takes place close to the centre of the samples, a small modification of the design of tensile specimens was adopted (as shown in Figure 4.2). This modification is within the standard's specifications. The figure shows that the smallest cross section area of the specimens in the modified geometry is located in the middle in tensile axis direction. Therefore, a specimen with this geometry is prone to fracture at the middle of the gauge length during tensile testing due to the highest stress occurring in this section. The tensile axis is taken in the longitudinal (L) direction (i.e. the rolling direction). For each alloy with a specific cold-rolling reduction, four conditions were selected for tensile tests: (i) as cold-worked (CW), (ii) aged for 30 minutes, (iii) aged for four hours for 90% and 40% reductions or five days for 10% reduction and (iv) aged for three weeks at 170°C. The three ageing conditions were chosen to represent underaged (30 minutes), peakaged (four hours or five days) and overaged (three weeks) conditions as estimated from the results of hardness testing. Tensile testing was also performed on the freshly solution treated samples solutionised at 500°C to evaluate solution strengthening

due to Mg and Cu. For each condition usually two tests were performed, and in figures (Chapter 5) the test with the highest elongation and/or lowest noise will be presented.

Tensile tests were performed using an 8800 series Instron machine at a constant strain rate of 0.001 s^{-1}. A grip with a hydraulic control unit for a flat specimen was used to clamp the specimens' end. A data acquisition system composed of a data-acquisition software, DASYlab 4.0 and a data-collecting computer was used. An extensometer with 50 mm gauge length was attached to the specimen to measure engineering strain (e) during tensile testing. The true strain (ε) and true stress (σ) were calculated from:

$$\begin{cases} \varepsilon = \ln(1+e) \\ \sigma = \dfrac{F}{S_0}(1+e) \end{cases} \qquad \textbf{(4.2)}$$

where S_0 is the original cross section area of the tensile specimen, and F is the load.

Two types of extensometers were used for tensile testing. Both have a 50 mm gauge length. One has travel range from –5% to +10%, which refers to the old one, and the other has a larger travel range (-10% to +100%), referring to the new one.

For 90% and 40% cold-rolling reductions, all tensile testing was performed using the old extensometer with 50 Hz data acquisition frequency. For 10% reduction, both extensometers were used for tensile testing. One of the two specimens was tested with the same testing setup as that for 90% and 40% reductions, and the other was conducted using the new extensometer with 5 Hz data acquisition frequency. For solution treated samples, tensile testing was performed using the same setup as that for the second specimens for 10% reduction.

During testing it was noticed that different extensometer may require different control parameters for constant strain rate control during tensile tests. Figure 4.3 and Figure 4.4 show examples of the tensile testing results using the old and new extensometer, respectively with the same control parameters. The control system of the Instron testing machine did respond properly when using the old extensometer (see Figure 4.3), whilst the same control parameters resulted in poor control when using the new one (see Figure 4.4). This may be due to the increased sensitivity of the new extensometer, which may require different control parameters for the control system. Appropriate control can be obtained using different control parameters (see Figure 4.5 for an example).

The results measured by the new extensometer when the Instron machine showed poor control (i.e., mainly for the second tests conducted on the samples with 10% reduction) were corrected by removing the dramatic drops in stress from the original data. An example of these corrected data will be presented in Chapter 5 (see Figure 5.31).

4.5 Differential scanning calorimetry (DSC)

For each cold-rolling reduction, DSC experiments were performed on as cold-rolled samples and on aged (two weeks at 170°C) samples. DSC analyses were also conducted on the STH and STL samples. The sample preparation follows general sample preparation methods used in the DSC analysis for aluminium alloys [1]. For 90% reduction, both cold-worked samples and aged samples were punched into small discs (∅5 mm). For all the other DSC specimens, the samples were cut into 8 mm × 8 mm squares and then ground into discs that can be fitted into the sample pan of the Perkin-Elmer Pyris instrument. All DSC samples were ground using #120, 600, 1200 and 4000 grade SiC-grinding paper followed by washing in methanol. The aged samples and solution treated samples were ground and polished again after ageing in order to eliminate the possible oxide film on the surface, which may influence the DSC analyses. The effects of sample preparation (e.g. punching, cutting, grinding etc.) on the data are described in [1]. All of the DSC experiments were conducted on a Perkin-Elmer Pyris 1 DSC, which is a power compensation DSC. It operates under a cryogenic system with the aid of liquid nitrogen to achieve accurate temperature control.

All the experiments were performed at a constant heating rate of 10°C/min. Prior to all experiments, a cleaning run and two baselines were conducted. In order to guarantee that each experimental run has a baseline performed within 4 hours for later correction during data analysis, an extra baseline was conducted between experiments or just before switching off the instrument. The baseline runs were conducted with empty pans and used as reference for analysis. All the results of runs with samples were first corrected by subtracting a baseline run performed within about four hours. This is followed by a second order polynomial correction, which was performed to further correct the combined influence of heat capacity difference and baseline drifts. The detailed correction procedure is presented in [4, 5].

4.6 FEG-SEM / EDS and EBSD

A JSM-6500 multi-purpose high performance field emission gun scanning electron microscope (FEG-SEM) has been used for microstructural analyses. Usually backscattered electron image (BEI) was used for intermetallics analyses. Energy Dispersive Spectroscopy (EDS) at 20 kV was performed to identify the chemical compositions of the coarse intermetallic particles present in the alloys. EDS analyses were run by INCA software. The analyses of grain size, misorientation and texture of the cold-worked alloys were conducted by electron backscattered diffraction (EBSD), using HKL channel 5 software.

For intermetallics analyses, specimens were cut from the cold-rolled plates. Then they were hot mounted and ground to achieve fine surface using 4000 grid SiC paper as final grinding. This is followed by water polishing with 1 μm diamond polishing powder. Finally, oxide polishing suspension (OP-S) polishing was used.

For EBSD study all specimens were cold mounted (to avoid the influence of heating during hot mounting) and subsequently ground to achieve fine surface using 4000 grid SiC paper as final grinding. After grinding, the mould was broken and the specimens were taken out and washed by methanol. After that, they were electrolytically polished by a mixture solution of 67% methanol and 33% nitric acid at -30°C. Finally, the electrolytically polished specimens were used for EBSD study.

10% and 40% cold-rolled samples of alloy A9 were chosen for EBSD analyses. It was found that for 10% cold-rolled samples, a good Kikuchi pattern could be obtained. A reasonably good Kikuchi pattern can be obtained for 40% cold-rolled samples, but it is not as good as that for 10% cold-rolled samples. However, no clear Kikuchi pattern suitable for analysis can be obtained for 90% cold-rolled samples. So there are no EBSD results for 90% cold-rolled alloy A9. Annealing is suggested to eliminate dislocations in the 90% cold-worked samples in order to obtain a clear Kikuchi pattern for EBSD analyses. (This is not conducted in this study.)

4.7 TEM

TEM observations were performed on aged samples of some selected alloys. The aims of TEM observations are mainly the study of precipitates. Due to higher dislocation density in the 90% and 40% cold-worked samples precipitates are difficult to observe, and only

10% cold-worked samples and some solution treated samples were selected for TEM observations. The TEM samples were prepared according to the following procedures.

First, isothermal ageing for selected ageing times at 170°C was conducted in an oven on 10% cold-worked samples and solution treated samples. Solution treated samples were prepared by resolutionising 10% cold-worked samples at 500°C for 30 minutes. After isothermal ageing, the TEM samples were then prepared following standard procedures: a thin slice (~0.3 mm) was cut, ground and polished, then a disk with 3 mm diameter was obtained by punching the slice. Subsequently the disk was ground down to about 0.15 mm in thickness and finally it was electrolytically polished using a twin jet electropolisher operated in a mixed solution of 30% HNO_3 and 70% methanol maintained at a temperature of -30°C. After that, the samples are ready for TEM observations.

The TEM observations were performed using a Jeol JEM 3010 transmission electron microscope operated at an accelerating voltage of 200 kV. Bright field (BF) images and dark field (DF) images were obtained. Some selected area diffraction patterns (SADs) were acquired to identify precipitates present. If the precipitates were large enough and individually discernable, some EDS was conducted to identify the chemical composition of the precipitates, which is also a useful technique to confirm the precipitates in some cases.

Figures

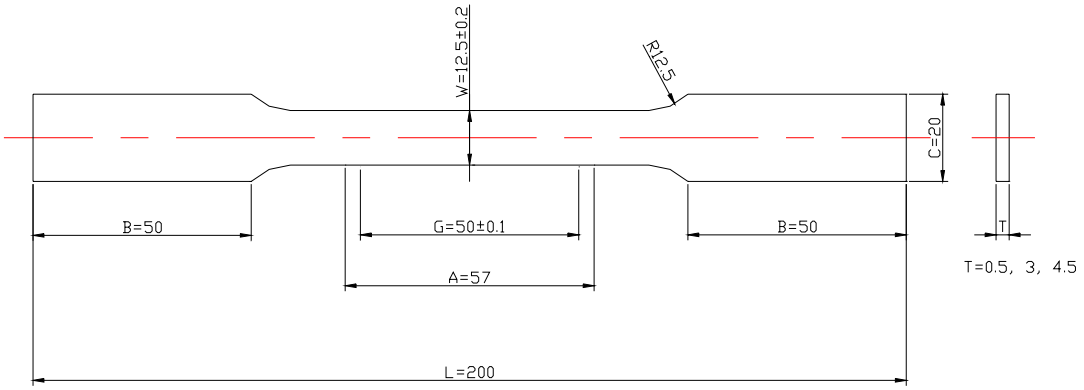

Figure 4.1 Geometry of the ASTM-E8M standard sheet-type tensile test specimens

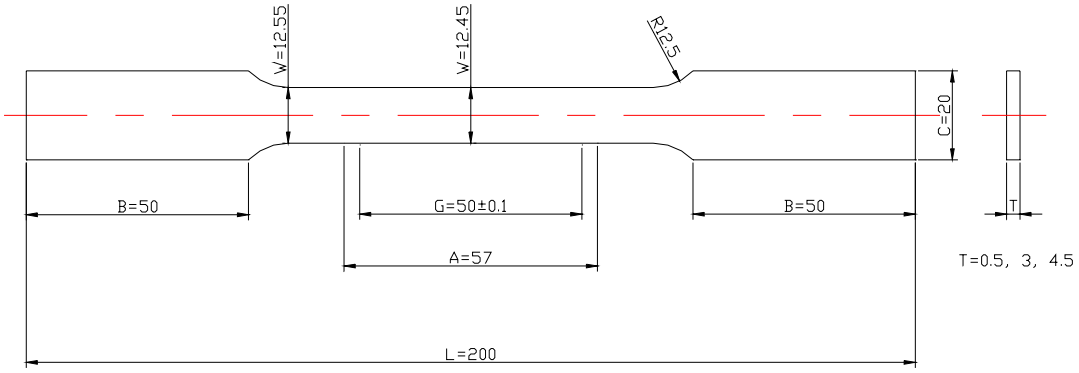

Figure 4.2 Geometry of the designed sheet-type tensile test specimens

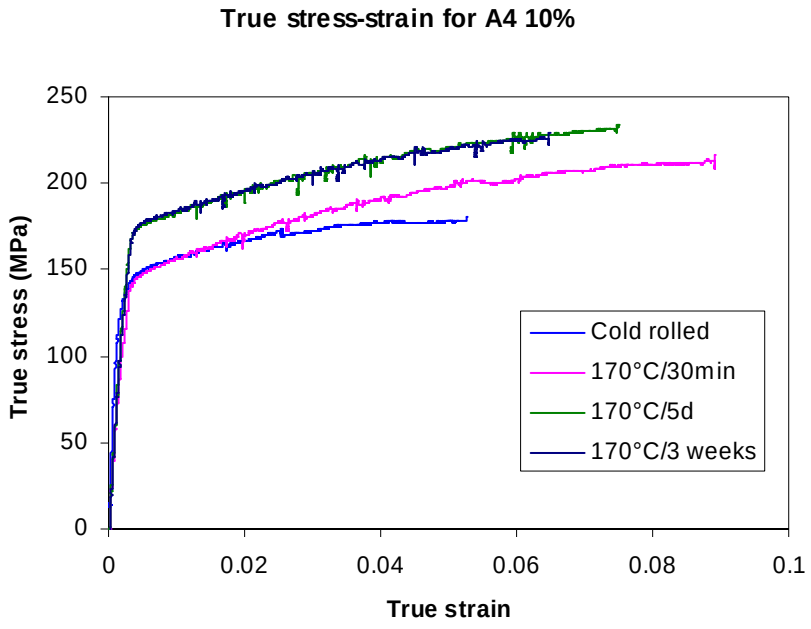

Figure 4.3 An example illustration of tensile testing results using the old extensometer

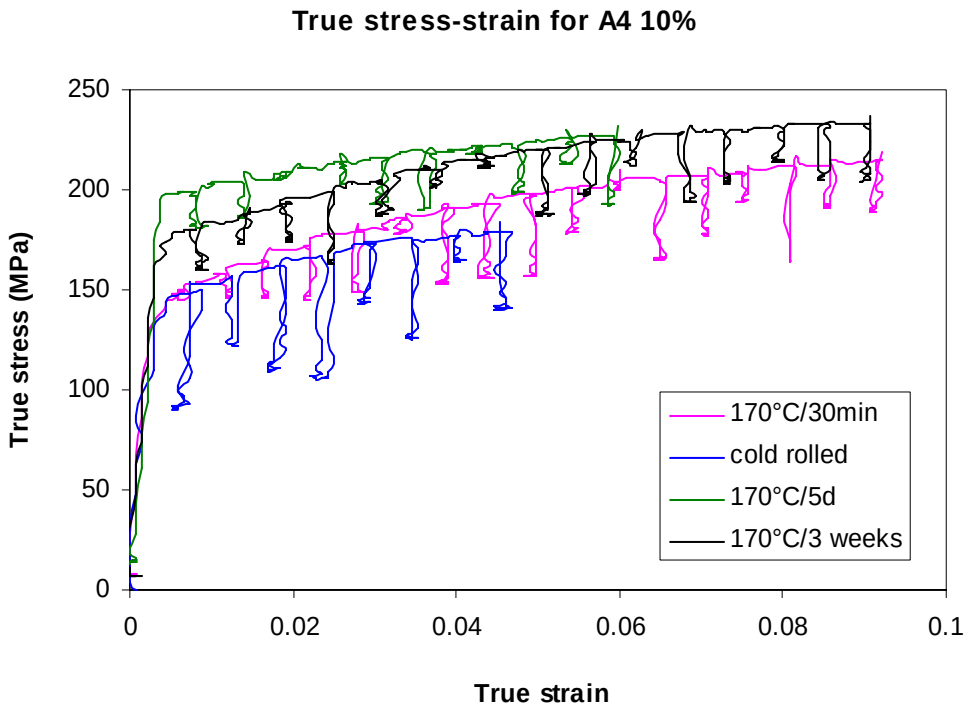

Figure 4.4 An example illustration of tensile testing results using the new extensometer with the same control parameters as those in the tests shown in Figure 4.3

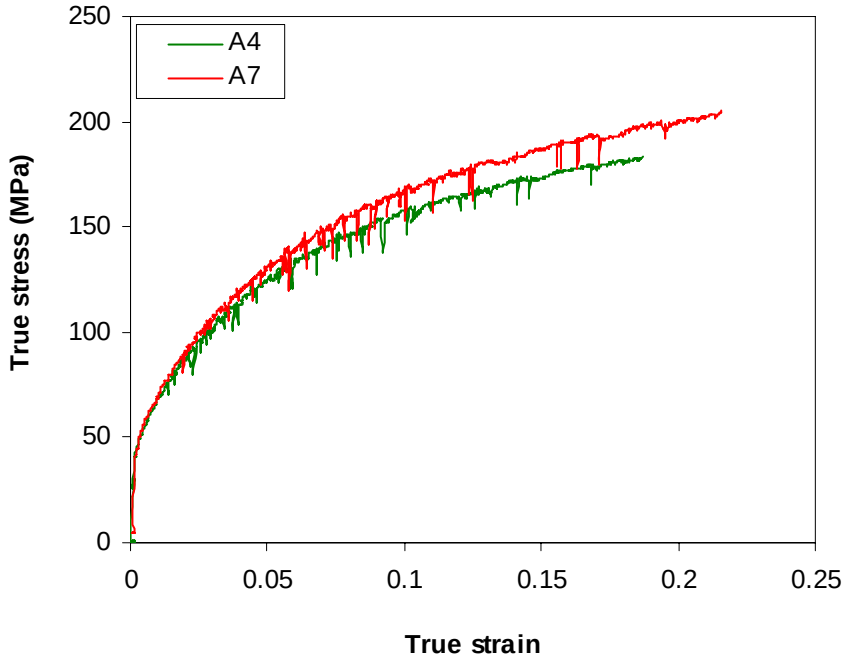

Figure 4.5 An example illustration of tensile testing results for solution-treated samples using the new extensometer with different control parameters than those in the tests shown in Figure 4.3

References

1. Starink, M.J., Int. Mater. Rev., **49**, 2004, p. 191.
2. Yan, J., ***Strength modelling of Al-Cu-Mg type alloys***, PhD thesis, School of Engineering Sciences, University of Southampton, 2006.
3. Kamp, N., ***Toughness-strength relationships in high strength 7xxx aluminium alloys***, PhD thesis, Engineering Materials, School of Engineering Science, University of Southampton, 2002.
4. Starink, M.J. and Zahra, A.M., Thermochim. Acta, **292**, 1997, p. 159.
5. Starink, M.J. and Gregson, P.J., Mater. Sci. Eng. A, **211**, 1996, p. 54.

5 Experimental Results and Analysis

The nano and microstructure evolution and the mechanical properties of nine Al-Mg-Mn alloys with small Cu and Si additions were studied by several techniques. Cold-worked, cold-worked-and-aged as well as solution-treated-and-aged materials were studied.

5.1 Microstructure

The properties of an alloy are strongly determined by the microstructure of the alloy. Hence, in order to understand the properties and service life of the alloy, it is important to analyse its microstructure. In this section, the microstructure including the features of intermetallics, grain structure and texture of the cold-worked alloys will be analysed.

5.1.1 Analysis of intermetallics

Coarse intermetallics are generally detrimental to the properties of an alloy. In addition, due to small additions of Cu and Si in the alloys studied, the formation of Si and/or Cu-containing intermetallic phases (e.g., Mg_2Si, $Al_{12}(Fe,Mn)_3Si$ and Al_2CuMg) may remove Cu and Si from solid solution. Thus the formation of intermetallics during solution treatment will influence the age hardening capability of these alloys during subsequent ageing after cold rolling. Hence it is crucial to understand the formation of these intermetallic particles during thermomechanical processing. In this section, the intermetallic phases present in the cold-worked samples will be first studied by experimental analysis using SEM/EDS. Subsequently, the experimental results will be compared with thermodynamic calculations using MTDATA.

5.1.1.1 Analysis using SEM/EDS

To characterise the intermetallic particles, the cold-rolled alloys were examined in a FEG-SEM. Cold-rolled alloy A9 was selected for detailed intermetallics analyses. The micrographs of intermetallic particle distribution for this alloy with three different reductions are presented in Figure 5.1, Figure 5.2 and Figure 5.3. The section parallel to the L (rolling) and T (transverse) directions was taken for these studies. These micrographs illustrate that the particles are generally aligned in the rolling direction in all the three samples. The particles in 10% cold-rolled sample are usually larger than those in

40% and 90% cold-rolled samples. For 90% cold-rolled samples, the intermetallics were broken up into small particles and they are comparatively homogeneously distributed.

From the overview of the particle distribution in the BEI images (see Figure 5.1, 5.2 and 5.3), the particles appear either brighter or darker compared with the Al matrix. The chemical compositions of the particles were studied using EDS analysis. The EDS results of the brighter particles reveal the presence of Cu, Fe, Mn and Si. A plot of Si:(Fe+Mn+Cu) ratio vs. Al:(Fe+Mn+Cu) ratio (Figure 5.4) shows that these particles can be classified into two groups. In Group I, the Si:(Fe+Mn+Cu) ratio is about 0 and the Al:(Fe+Mn+Cu) ratio is about 5~7.5. The particles in this group are identified to be Al_6(Fe, Mn, Cu). Most of the brighter particles are located in this group. In the other group (Group II), the Si:(Fe+Mn+Cu) ratio is about 0.25~0.3 whilst the Al:(Fe+Mn+Cu) ratio is about 7~8. The particles in group II therefore are identified to be $Al_{12}(Fe,Mn,Cu)_3Si$ (see also section 5.1.1.2). The Al:(Fe+Mn+Cu) ratio obtained from EDS analysis is slightly higher than that in the stoichiometry of $Al_{12}(Fe,Mn,Cu)_3Si$, which is 4. This may be due to the contribution of the surrounding Al matrix when the particles were analysed. Therefore, the brighter particles in the cold-worked alloy A9 can be classified into two categories (as shown in Figure 5.5): one is Si containing $Al_{12}(Fe,Mn,Cu)_3Si$ phase, and the other is Al_6(Fe,Mn,Cu) phase. The third type of particles found in alloy A9 appears darker in the BEI images. The EDS analysis shows that the darker particles contain Mg and Si elements (see Figure 5.6) and they are identified to be Mg_2Si phase. As illustrated in Figure 5.6, a certain amount of oxygen is also revealed by the EDS spectrum. A possible explanation of the occurrence of oxygen in the spectrum will be given later in this section.

Intermetallic analysis using SEM/EDS was also performed on the cold-worked samples of alloys A1, A2, A3, A4 and A5. In these cases L-S sections were studied. Figure 5.7 shows an overview of intermetallic particle distribution in alloy A4, which indicates that only brighter particles are present. This is also the case for alloy A1. In these two alloys, mainly Al-Fe-Mn-Si intermetallic particles were found to be present in the cold-worked samples (see Figure 5.8 for example). Moreover, if the alloy contains Cu, e.g. alloy A4, then Cu is present in the Al-Fe-Mn-Si phase to form Al-Fe-Mn-Cu-Si intermetallic particles, as shown in Figure 5.9. For alloy A3, as illustrated in Figure 5.10, both the brighter and the darker particles are present. EDS analysis indicates that the darker particles are Mg_2Si phase as shown in Figure 5.11. The darker particles identified to be Mg_2Si phase were also

found in alloy A2. Furthermore, for alloy A2, the brighter particles in the BEI images were mainly the Al-Fe-Mn-Si phase. It was observed that the results of alloy A5 were similar to those of alloy A9. The darker particles were identified to be Mg_2Si phase and the bright particles were mainly the Al-Fe-Mn-Cu-Si phase.

Therefore, the following conclusions can be drawn from the intermetallics analysis for alloys A1, A2, A3, A4 A5 and A9:

(1) Mg_2Si particles are present in the cold-worked alloys with Mg>1wt%, i.e. alloys A2, A3, A5 and A9.

(2) The brighter particles in the BEI image were identified to be two types of intermetallic particles: one is an Al-Fe-Mn (or Al-Fe-Mn-Cu if the alloy contains Cu) phase and the other is an Al-Fe-Mn-Si (or Al-Fe-Mn-Cu-Si for Cu-containing alloys) phase. Furthermore, the Al-Fe-Mn-(Cu)-Si phase appears to be more abundant.

As mentioned before, during the identification of Mg_2Si intermetallic particles, the occurrence of oxygen in the EDS spectrum for Mg_2Si phase was noted. The darker particles sometimes had a high amount of oxygen as shown in Figure 5.6, and for other darker particles very limited oxygen is present as shown in Figure 5.11. It has been mentioned in the literature that Mg_2Si phase decomposes in water [1], and it was found that Mg_2Si particles might begin to dissolve during water polishing [2]. The reason why it decomposes or dissolves in water may be explained by the following reaction [3]:

$$Mg_2Si + 4H_2O \rightarrow SiH_4(g) + 2Mg(OH)_2$$

The following reactions may further occur under certain condition:

$$Mg(OH)_2 \rightarrow MgO + H_2O$$

$$SiH_4 + 2O_2 \rightarrow SiO_2 + 2H_2O$$

Therefore, Mg_2Si may be dissolved during water polishing. Variations in the degree of Mg_2Si decomposition during water polishing may explain why the relative O, Mg and Si contents obtained by EDS analyses can be variable. (To avoid the decomposition of Mg_2Si during polishing, alcohol instead of water may be used, but this was not applied in the present work.)

5.1.1.2 Thermodynamic calculations

Prediction of phase diagram can be achieved through computational thermodynamics based on calculating the free energy of co-existing phases present in a system by minimising the Gibbs free energy [4]. If the Gibbs energies of all phases forming a system are described as a function of temperature and pressure, then the amounts and compositions of the phases present can be obtained by minimization of the total Gibbs energy of the system [5]. A variety of commercial software packages, e.g. MTDATA and Thermo-Calc, are widely used for these types of thermodynamic calculations.

In this study, some thermodynamic predictions made by MTDATA software will be used. MTDATA is a software package for the calculation of phase equilibria in multicomponent multiphase systems developed by National Physical Laboratory (NPL). The thermodynamic models necessary to describe the properties of a wide range of phase types are incorporated in the software and database structures [6]. MTDATA calculations for the nine alloys were performed by Innoval Technology using the Alcan Thermodynamic database EURAL3d, which contains data on intermetallic phases commonly observed in Al alloys [7]. Some of the calculation results are presented in Figure 5.12 to Figure 5.15. From the results of the thermodynamic calculations, three types of intermetallics may form during solution treatment at 500°C depending on alloy composition: $Al_6(Fe,Mn)$, $Al_{12}(Fe,Mn)_3Si$ (cubic alpha) and Mg_2Si. The phases predicted to be present in the alloys and their amounts at 500°C and 540°C are listed in Table 5.1, and the experimental observations of the three phases are also illustrated in the table.

Table 5.1 Predicted particles and detected particles in experiments

Alloy	Wt%								
	Al_6Mn			α-Al(Fe,Mn)Si			Mg_2Si		
	540°C	500°C	exp.	540°C	500°C	exp.	540°C	500°C	exp.
A1	0.385	0.060	(-)	0.857	1.349	+	0	0	-
A2	0.500	1.533	(-)	0.773	0	+	0	0.295	+
A3	1.400	1.520	+	0	0	+	0.268	0.357	+
A4	0.697	0.262	(-)	0.672	1.167	+	0	0	-
A5	0.537	1.484	(-)	0.727	0	+	0	0.263	+
A6	1.350	1.473		0	0		0.271	0.358	
A7	0.529	0.137		0.780	1.238		0	0	
A9	1.370	1.502	+	0	0	+	0.263	0.355	+

In the table, + stands for phase detected by EDS, - represents phase not detected, (-) means that limited EDS data did not reveal phase.

General trends noted in these predictions are:

(1) No Mg_2Si particles are predicted to form during solution treatment at 500°C in alloys A1, A4 and A7 (i.e. alloys contain 1wt% Mg), and the amount of Mg_2Si particles is predicted to increase with Mg concentration for other alloys.

(2) The other two types of intermetallic phases predicted to be present in the alloys at 500°C depending on their alloy compositions, are $Al_6(Fe,Mn)$ and cubic alpha ($Al_{12}(Fe,Mn)_3Si$). In the alloys with 1wt% Mg (i.e., alloys A1, A4, A7), mainly cubic alpha phase is predicted to be present, and only a small amount of $Al_6(Fe,Mn)$ phase is predicted to be present. However, for alloys with 2wt% or higher Mg content (i.e., A2, A3, A5, A6, A8, A9), no cubic alpha phase is predicted to be present, but a large amount of $Al_6(Fe,Mn)$ is predicted.

(3) No S phase is predicted to form in any alloy during solution treatment at 500°C.

The MTDATA predictions and SEM/EDS experimental results are consistent with each other in the following aspects:

(1) The only two Fe and Mn containing phases predicted to be present at 500°C are $Al_6(Fe,Mn)$ phase and cubic alpha phase. These are indeed the only two Fe and Mn containing phases observed using SEM/EDS.

(2) MTDATA predicts no Mg_2Si particles are present in the cold-worked alloys with 1wt% Mg content, which is consistent with the experimental observations of these alloys (alloys A1 and A4 were studied).

(3) It is predicted by MTDATA calculations that Mg_2Si particles are present in the alloys with 2wt% or higher Mg content, which agrees with the available experimental observations.

However, there are some differences noticed between the MTDATA predictions and the experimental observations as indicated in Table 5.1:

(1) MTDATA predicts that at 500°C cubic alpha particles are present only in the alloys with 1wt% Mg, and for alloys with higher Mg content, no such particles are predicted. However, cubic alpha phase was detected in all the alloys studied.

(2) $Al_6(Fe,Mn)$ was predicted by MTDATA calculations to be the main type of intermetallic particles in the alloys with 2wt% or higher Mg content. However, very few (or none in some alloys) were detected in the alloys studied.

These differences between equilibrium predictions and measurements may be explained as follows.

Intermetallic particles usually form during solidification. The DC ingots were subjected to preheating at 540°C before hot rolling and solution treated at 500°C prior to cold rolling. According to the MTDATA calculation results shown in Figure 5.12 to Figure 5.15 (and other results available in [7]), both cubic alpha and Al_6Mn phases may form during solidification for all the nine alloys. Whilst the equilibrium amount of cubic alpha at 500°C is predicted to be zero for alloys with two or more wt% Mg, diffusion might be too slow to achieve full transformation or dissolution. Thus cubic alpha could be present as a metastable remnant from solidification or homogenisation at 540°C. For Al_6Mn phase, the situation is also dependent on alloy composition. As illustrated in Figure 5.12, for alloy A1, Al_6Mn phase is not stable at temperatures above 500°C, and it may transform to cubic alpha phase if Si is available. Therefore, the phase transformation from $Al_6(Fe,Mn)$ phase to α-$Al_{12}(Fe,Mn)_3Si$ phase (i.e., the 6-to-α transformation) may occur during preheating at 540°C for alloy A1. So no or limited Al_6Mn particles may be present after preheating. Furthermore, as illustrated in Figure 5.12, the amount of Al_6Mn particles predicted to be stable at 500°C is very low (<0.1wt%). Therefore, after solution treatment, no or very limited Al_6Mn particles may be present in alloy A1. For alloys A4 and A7, the predictions are similar to those of alloy A1. No or very limited Al_6Mn particles are predicted to be present in these two alloys after solution treatment at 500°C. For alloy A2, as shown in Figure 5.13, most of the Al_6Mn formed during solidification is predicted to dissolve during preheating at 540°C, and only about a third of the Al_6Mn particles are predicted to remain after a solution treatment at 500°C. For alloys A5 and A8, the predictions are similar to those of alloy A2. Therefore, for alloys A1, A2, A4, A5, A7 and A8, it would be difficult to detect Al_6Mn particles in the cold-worked samples, which is consistent with the observations that no Al_6Mn particles were detected in alloys A1, A2, A4 and A5. However, for alloy A3 as shown in Figure 5.14, Al_6Mn phase is stable up to about 550°C, hence no 6-to-α transformation could occur during preheating and Al_6Mn phase would not dissolve during solution treatment at 500°C. Thus, as detected by SEM/EDS, Al_6Mn

particles appear in abundance in alloy A3 after solution treatment at 500°C. For alloys A6 and A9, the MTDATA predictions are similar to those of alloy A3. A large amount of Al_6Mn is predicted to be present in these three alloys after solution treatment at 500°C and subsequent cold rolling, which is consistent with the experimental observations of Al_6Mn particles in the cold-worked alloys A3 and A9 shown in Table 5.1 (alloy A6 was not studied by SEM).

As illustrated in Table 5.1, the maximum amount of Mg_2Si particles predicted at 500°C is about 0.36 wt%, which is about 0.38 at%. So the maximum amount of Si removed by the Mg_2Si particles is about 0.13 at%. In all the nine alloys, the gross Si content is about 0.14-0.15 at%. Therefore, when the maximum amount of Mg_2Si particles forms, almost all the Si content may be taken out by Mg_2Si particles according to MTDATA prediction. As indicated in the table, the maximum amount of cubic alpha predicted at 500°C is about 1.35 wt%, which is about 1.12 at%. So the maximum amount of Si removed by $Al_{12}(Fe,Mn)_3Si$ particles is about one sixteenth of 1.12 at% (i.e., about 0.07 at%), which is about 55% of the maximum amount of Si removed by Mg_2Si particles. Furthermore, the available EDS results reveal that $Al_{12}(Fe,Mn)_3Si$ particles are present in all the alloys examined and Mg_2Si particles are not. Hence, to limit unnecessary complexity, only the amount of Si removed by Mg_2Si particles will be taken into account when considering the influence of Si on the subsequent age hardening response of the cold-rolled alloys in later sections and in Chapter 6.

5.1.2 Grain structure and texture analysis

5.1.2.1 Grain structure

EBSD analyses have been performed on L-S sections of alloy A9 with 10% and 40% cold-rolling reductions. The grain boundary maps and deformed/recrystallised maps for alloy A9 with 10% and 40% reductions are shown in Figure 5.16 to Figure 5.19. In the grain boundary maps (Figure 5.16 and Figure 5.17), the dark lines indicate the high angle grain boundaries with misorientation angle greater than 12°, whilst the grey lines represent the low angle grain boundaries with misorientation angle between 2 to 12°. Comparison of the grain maps for the cold-rolled samples with 10% and 40% reductions (see Figure 5.16 and Figure 5.17) shows that generally the grain size in the sample with 10% reduction is larger than that in the sample with 40% reduction. Furthermore, the latter has more low angle grain boundaries. In the deformed/recrystallised maps (see Figure 5.18 and Figure 5.19),

the blue, red and yellow grains represent fully recrystallised grains, deformed grains and substructures, respectively. Comparison of the deformed/recrystallised grain maps for the cold-worked samples with 10% and 40% reductions (see Figure 5.18 and Figure 5.19) shows that the fraction of recrystallised grains is higher in the sample with 10% reduction, whilst the fraction of deformed grains is higher in the sample with 40% reduction. This indicates that recrystallised grains generated during solution treatment may be replaced gradually with deformed grains when the level of cold work increases.

From the EBSD results a wide range of microstructural data can be obtained, such as orientation maps, recrystallised fractions, grain sizes, grain aspect ratios, number of neighbouring grains, misorientation angles, pole figures, inverse pole figure and orientation distribution function (ODF). Grain diameter, grain aspect ratio, deformed, recrystallised and substructure fractions obtained from the EBSD results of cold-rolled alloy A9 with 10% and 40% reductions are given in Table 5.2. From the table, the following observations are made:

(1) The average grain size reduces with increasing cold-rolling reduction.

(2) The grain aspect ratio increases with cold-rolling reduction, indicating that the grains become more elongated during cold rolling.

(3) The fraction of deformed grains increases with increasing cold-rolling reduction, whilst the fraction of recrystallised grains decreases with increasing cold-rolling reduction.

Table 5.2 Microstructure parameters measured by EBSD for alloy A9

Reduction %	Grain diameter (average†) μm	Grain aspect ratio (average†)	Deformation %	Recrystallisation %	Substructure %
10	44.0±35.7*	2.8±1.5*	17	13	70
40	41.0±30.3*	3.0±2.0*	68	19	13

†: for 10%, it is the average of 103 grains, whilst it is the average of 130 grains for 40%.

*: the error is represented by standard deviation.

5.1.2.2 Texture

The texture of the cold-worked alloys can also be analyzed by the EBSD technique. Figure 5.20 and Figure 5.21 show pole figure and inverse pole figure of the cold-rolled alloy A9 with 10% and 40% reduction, respectively. As shown in Figure 5.20, there is only a very weak texture existing in the 10% cold-rolled alloy A9. This may be explained by the

limited deformation experienced for the 10% cold-rolled sample. However, the 40% cold-rolled sample (see Figure 5.21) shows a more distinct texture. The main component of the textures in the 40% cold-rolled sample can be identified to be {110}<211>, which is a Brass texture, one type of rolling texture.

5.2 Mechanical testing

Both hardness testing and tensile testing were used to evaluate the mechanical properties and ageing behaviour of the nine alloys studied. The results obtained will be presented in this section. Hardness testing is a very convenient and commonly used mechanical testing technique to evaluate ageing behaviour of heat treatable alloys and estimate strength. Tensile testing is another commonly used mechanical testing technique to evaluate mechanical properties more accurately. Furthermore, work hardening rate can be evaluated from tensile testing results.

5.2.1 Hardness testing

The results of the hardness evolution during isothermal ageing at 170°C for samples after solutionising at 500°C and subsequent cold rolling with 90%, 40% and 10% reductions are shown in Figure 5.22a, b and c, respectively. Figure 5.22d shows the hardness evolution during isothermal ageing at 170°C for samples with 10% reduction after re-solutionised at 550°C for 30 minutes (i.e. STH samples for abbreviation). In Figure 5.22a-d, an error bar shown in each graph indicates the average of the standard deviations of all tests reported within that graph. The hardness curves for alloys A1 to A9 are shown in Figure 5.23, which shows the overview of the influence of cold-rolling reductions and solutionising temperature on the age hardening behaviour of each alloy. In Figure 5.23, error bars indicating the standard deviations are shown for each testing condition.

As shown in Figure 5.22a, for the alloys with high reduction (90%), almost all Cu-containing alloys, e.g., alloys A4, A5, A7, A8 and A9, show some limited hardening effect during ageing. The Cu-free alloy A1 also shows some precipitation hardening effect, which is not observed in the other two Cu-free alloys A2 and A3. In these two alloys, only recovery was observed. For the age hardening alloys, the hardness reaches a peak relatively quickly (within 1 to 3 hours), and then it drops dramatically after peak hardness, which may be due to the concurrent coarsening of precipitates and recovery. In general, recovery dominates during ageing in the 90% cold-worked samples for all the nine alloys.

For 40% reduction, as illustrated in Figure 5.22b, all Cu-containing alloys and Cu-free alloy A1 show some hardening effect during isothermal ageing at 170°C, and some alloys even show quite pronounced hardening, e.g, alloys A1, A4, A7 and A9. Compared with 90% reduction, for age hardening alloys, the hardness reaches a peak slightly later (at about 4 hours) and it decreases more gently after peak hardness.

For 10% reduction, all Cu-containing alloys and Cu-free alloy A1 show substantial age-hardening (see Figure 5.22c). For these alloys, precipitation dominates during ageing, and it takes about five days to reach peak hardness. Very limited hardness reduction was observed after peak hardness, which may be mainly due to the coarsening of precipitates.

In considering all of the above observations for the cold-worked samples, it is clear that all the Cu-containing alloys are subjected to some precipitation hardening during ageing at 170°C. (The occasional absence of a distinct hardening effect for some alloy/reduction combination might be due to the interactions between recovery and precipitation and/or measurement errors.) For Cu-free alloys, however, the picture becomes slightly more complicated. For all three reductions, as illustrated in Figure 5.23a, the Cu-free alloy A1 shows a distinct precipitation hardening effect. The hardening effect in this alloy during ageing is thought to be due to precipitation hardening due to the β″/β′/β (Mg_2Si) precipitation sequence, which will be discussed in section 5.4.1.1. For the Cu-free alloy A2, as shown in Figure 5.23b, only recovery was observed for 90% reduction and no obvious age hardening effect was detected for 40% reduction. For 10% reduction, very limited hardening effect was observed. For the Cu-free alloy A3, no age hardening effect was observed for all three reductions (see Figure 5.23c). Only recovery was detected in this alloy.

In considering the influence of cold-rolling reduction on ageing behaviour, it is observed that for all alloys, the higher the cold-rolling reduction, the higher the hardness of the as-cold-rolled condition (see Figure 5.23). On extensive ageing, as shown in Figure 5.23, for each alloy, the differences in the hardness due to different cold-rolling reductions become smaller. The differences due to work hardening caused by different cold-rolling reductions will be eliminated gradually due to recovery during ageing. On the other hand, for age hardening alloys, the time to peak hardness of each alloy decreases with increasing cold-rolling reduction. For Cu-containing alloys, it takes about two hours, four hours and five days to reach a hardness peak for 90%, 40% and 10% reductions, respectively. For Cu-

free alloy A1, however, it takes about one hour, four hours and 16 hours to reach a peak hardness for 90%, 40% and 10% reductions, respectively. As will be discussed in section 5.4.1, this is thought to be due to alloy A1 being age hardened by a precipitate phase that is different from the one in the Cu-containing alloys.

In considering the strengthening due to Mg content, for alloys with the same cold-rolling reduction in the as cold-rolled condition, the higher the Mg content, the higher the hardness of the alloy. This may be attributed to two factors: one is solution strengthening due to Mg; the other is the enhancement of work hardening by Mg [8]. Furthermore, for alloys with the same cold-rolling reduction in the as cold-rolled condition, the higher the Cu content, the higher the hardness of the alloy. This increase in hardness may be attributed to the solution strengthening due to Cu.

The hardness testing results of the solution-treated samples (i.e., 10% cold-worked samples resolutionised at 550°C for 30 minutes) shown in Figure 5.22d reveal slightly different trends. Different to the cold-worked samples, which were solutionised at 500°C prior to cold rolling, all the nine alloys show substantial hardening during ageing at 170°C. The hardening effect in each alloy is much stronger than that of the corresponding cold-worked sample. Although the freshly solutionised samples have much lower hardness than cold-worked samples, the hardness at peak ageing for these solution-treated samples usually reaches about same level (or higher) as that for their corresponding 10% cold-worked samples. It is interesting to notice that for some Cu-containing alloys, e.g., alloys A5, A6, A8 and A9, rapid hardening within one hour was observed, which may be due to the formation of GPB zones/clusters. Such rapid hardening was not observed for any of the cold-worked samples. For these solution-treated samples, the time to peak ageing is about eight hours for Cu-free alloys, and it is about 64 hours for Cu-containing alloys, which is even shorter than that for the 10% cold-worked samples. This indicates that the precipitation rate in the solution-treated samples solutionized at the higher temperature (550°C) is enhanced compared with those solutionised at 500°C. This enhanced precipitation rate may be attributed to the greater concentration of vacancies achieved at higher solutionising temperature. The enhanced vacancies can provide more nucleation sites for heterogeneous precipitation, resulting in higher precipitation rate.

Some additional hardness tests were performed on samples with 10% reduction after re-solutionised at 500°C for 30 minutes, which are abbreviated as STL samples. Results are

shown in Figure 5.24. As show in the figure, the ageing behaviour of the STL samples is very similar to their corresponding cold-worked samples. That is, for Cu-free alloys, age hardening decreases with increasing Mg content, whilst all Cu-containing alloys show remarkable age hardening. It is interesting to notice that rapid hardening within 30-minute ageing was detected in the STL samples of alloy A9, which is similar to the STH sample (solutionised at 550°C for 30 minutes) of alloy A9. These hardness results will be further discussed in sections 5.3.2 and 5.4.1.

To some extent, DSC and TEM experimental results may help to assess the kinetics of precipitation reactions responsible for hardening effects discussed above. These DSC and TEM results will be presented and discussed in later sections.

5.2.2 Tensile testing

For each alloy/cold work combination, tensile tests were conducted for four conditions, i.e., as-cold-worked, underaged, peak aged and overaged conditions. Tensile tests were also conducted on the solution-treated alloys to evaluate the solution strengthening contribution due to Mg and Cu. Selected tensile true stress vs. true strain curves are shown in Figure 5.25 to Figure 5.34. The age-hardening trends for the nine alloys observed by the tensile tests are generally consistent with the observations in the hardness tests. That is, alloy A1 and all Cu-containing alloys show some hardening during artificial ageing. As shown in Figure 5.26 to Figure 5.34, the work hardening rate for the cold-rolled conditions is much lower than that for the aged conditions. The work hardening rate of cold-worked samples changes substantially within a short time of ageing (i.e. 30 minutes) at 170°C. The work hardening rate will be further quantitatively studied in Chapter 7.

The 0.2% offset proof strength (PS), ultimate tensile strength (UTS) and elongation (El) were determined from the engineering stress vs. engineering strain curves. The results for solution-treated samples and cold-worked samples are shown in Table 5.3 to Table 5.6. In these tables, generally the average of the results of two or more tests was used. These data listed in the tables are plotted in Figure 5.35 to Figure 5.39.

For solution-treated samples (Figure 5.35 and Figure 5.36) the following trends are observed. Generally, the PS and UTS increase linearly with increasing Mg and Cu contents whilst the elongation decreases with increasing Mg content. This linear increase in PS and UTS may be attributed to the solution strengthening due to Mg and Cu.

For most cold-rolled alloys with 10% reduction, the 0.2% proof strength drops slightly on ageing for 30 minutes (Figure 5.37a), which reveals limited recovery occurring on ageing. The Cu-free alloy A1 and all Cu-containing alloys show substantial hardening during ageing. For the Cu-free alloys A2 and A3, no pronounced hardening was observed. These observations are generally consistent with those obtained from hardness testing. For alloys that do not show substantial age hardening, i.e. alloys A2 and A3, the UTS is nearly constant during ageing. For alloys that show age hardening, the UTS increases slightly up to peak ageing, and then it drops a little after peak ageing (see Figure 5.37b). For the as-cold-rolled samples, both the PS and UTS increase with Mg and Cu contents.

Table 5.3 Tensile data for solution-treated samples

Alloy No.	PS (MPa)	UTS (MPa)	El (%)
A1	49.0	144.6	25.1
A2	64.6	182.0	22.8
A3	80.3	221.1	24.6
A4	50.9	150.6	23.7
A5	65.6	194.9	22.5
A6	87.3	234.7	22.2
A7	53.4	163.4	26.1
A8	66.5	207.0	25.7
A9	84.2	237.9	21.4

For 40% and 90% reductions, similar hardening/softening trends to those for 10% reduction were observed, although in some cases age hardening is very limited or undetected for some Cu-containing alloys, e.g., A5, A6 and A8 with 40% reduction (see Figure 5.38a) and A4, A5 and A8 with 90% reduction (Figure 5.39a). This may be due to the difficulties in accurately determining small changes in 0.2% proof strength.

Analyses of the yield strength of the cold-worked samples and its relation with level of cold work, and Mg and Cu contents were conducted. The results are shown in Figure 5.40 to Figure 5.42. In these figures, the strain or cold-rolling reduction for the solution-treated samples is assumed to be 0.

To convert the cold-rolling reduction to strain, the von-Mises equivalent strain was used. The cold-rolling reduction r_c and the equivalent strain ε are defined respectively as [9]:

$$r_c = \frac{h_0 - h}{h_0} = 1 - \frac{h}{h_0} \qquad \textbf{(5.1)}$$

$$\varepsilon = -\frac{2}{\sqrt{3}}\ln(1-r_c) \qquad \textbf{(5.2)}$$

where h_0 and h are the thicknesses of the plate before and after cold rolling, respectively.

As shown in Figure 5.40, the yield strength increases dramatically with the von Mises equivalent strain at low strains ($\varepsilon \leq 0.2$), and increases more gradually with strain at higher strains. The relation of the yield strength with strain (i.e. work hardening) will be further analysed in Chapter 6.

As shown in Figure 5.41, there is a clear trend that the yield strength increases approximately linearly with Mg content regardless of the level of cold work. Moreover, the strength increment due to Mg addition increases with increasing level of cold work: there is a synergistic effect of Mg addition and cold work. For Cu content, the yield strength increases with Cu content at higher level of cold work, e.g., 40% and 90%, but such trend is not evident at a lower level of cold work (see Figure 5.42). This may be due to small additions of Cu in the alloys.

Table 5.4 Tensile data for 10% cold-rolled alloys

Alloy No.	Ageing time(min)/170°C	PS (MPa)	UTS (MPa)	El (%)
A1	0	138.4	159.4	11.5
	30.4	139.2	183.3	13.5
	7215	154.3	187.5	12.5
	30240	145.0	180.9	12.9
A2	0	170.9	200.2	12.3
	30.4	144.3	207.2	13.6
	7215	140.3	208.6	14.4
	30240	145.6	204.8	14.8
A3	0	184.5	238.6	11.6
	30.4	165.7	237.1	15.3
	7215	157.9	236.3	16.0
	30240	154.1	233.9	16.2
A4	0	146.3	174.2	12.5
	30.4	146.7	199.1	14.4
	7215	183.0	217.5	12.8
	30240	177.0	215.8	12.2
A5	0	175.2	217.8	13.1
	30.4	168.1	236.4	12.3
	7215	187.5	246.6	14.4
	30240	184.9	239.7	12.8
A6	0	187.0	248.7	15.5
	30.4	177.8	257.0	14.4
	7215	187.3	264.4	15.5
	30240	183.5	241.8	14.1
A7	0	142.6	186.9	14.0
	30.4	143.0	207.8	13.0
	7215	184.5	229.3	13.2
	30240	189.9	230.3	12.4
A8	0	178.0	235.5	15.3
	30.4	166.1	253.3	14.5
	7215	200.7	265.1	14.4
	30240	192.2	254.1	12.1
A9	0	215.0	274.4	12.9
	30.4	204.0	285.2	12.4
	7215	229.7	287.7	12.1
	30240	211.9	277.0	12.7

Table 5.5 Tensile data for 40% cold-rolled alloys

Alloy No.	Ageing time(min)/170°C	PS (MPa)	UTS (MPa)	El (%)
A1	0	189.0	205.2	5.9
	34.8	198.7	224.9	8.7
	257.5	200.7	226.6	8.7
	30240	167.2	205.2	8.6
A2	0	220.4	244.4	6.7
	34.8	202.8	253.4	7.3
	257.5	204.3	253.4	8.8
	30240	185.7	236.9	10.1
A3	0	253.3	290.0	7.6
	34.8	230.1	287.8	6.9
	257.5	223.9	282.4	10.1
	30240	208.3	264.2	9.1
A4	0	201.7	218.7	5.8
	34.8	202.5	249.7	7.5
	257.5	211.7	258.3	9.8
	30240	209.2	241.1	8.9
A5	0	235.2	266.9	5.7
	34.8	228.1	289.7	7.9
	257.5	230.6	294.8	9.1
	30240	219.0	263.3	8.8
A6	0	272.7	301.1	7.4
	34.8	250.4	322.5	10.7
	257.5	246.1	324.9	8.8
	30240	222.0	290.0	9.5
A7	0	214.9	239.2	5.6
	34.8	211.2	267.5	8.7
	257.5	224.8	274.9	8.0
	30240	223.7	251.9	8.9
A8	0	252.6	287.1	6.9
	34.8	246.8	311.4	9.4
	257.5	248.7	318.9	8.6
	30240	228.5	275.1	8.2
A9	0	279.3	327.2	7.2
	34.8	263.9	338.3	9.0
	257.5	271.2	347.6	10.6
	30240	245.0	301.3	8.7

Table 5.6 Tensile data for 90% cold-rolled alloys

Alloy No.	Ageing time(min)/170°C	PS (MPa)	UTS (MPa)	El (%)
A1	0	253.8	262.7	3.3
	35.6	246.8	269.6	5.1
	240.8	248.8	266.8	5.5
	30240	208.4	231.3	5.3
A2	0	285.5	300.7	4.0
	35.6	271.9	303.0	5.9
	240.8	266.0	293.5	6.0
	30240	235.7	272.5	7.4
A3	0	334.3	355.7	3.9
	35.6	300.5	340.3	6.5
	240.8	292.5	330.8	6.7
	30240	255.2	305.3	7.6
A4	0	270.0	280.4	4.1
	35.6	267.8	296.7	6.8
	240.8	268.6	296.4	7.7
	30240	241.2	259.2	4.8
A5	0	314.4	328.8	3.5
	35.6	309.0	345.6	6.6
	240.8	298.3	337.0	6.8
	30240	252.9	289.9	6.1
A6	0	352.3	376.6	3.9
	35.6	325.2	371.9	6.4
	240.8	331.0	379.0	7.9
	30240	260.9	312.2	7.1
A7	0	284.8	296.2	3.2
	35.6	279.5	319.0	7.8
	240.8	293.1	327.8	9.1
	30240	233.7	259.2	5.5
A8	0	342.5	358.2	3.4
	35.6	329.3	366.8	6.3
	240.8	325.4	366.2	7.3
	30240	259.8	296.3	5.9
A9	0	371.3	395.2	3.9
	35.6	351.0	399.1	7.2
	240.8	351.1	396.7	6.0
	30240	278.2	329.2	7.6

5.3 Nano and microstructure evolution

For the cold-worked alloys, recovery and precipitation may occur concurrently during ageing. Hence the interactions of recovery and precipitation may influence the microstructure evolution during ageing. The microstructure evolution includes the following two aspects. Dislocations generated during cold deformation will annihilate and a cell structure may form, whilst precipitates will nucleate, grow and coarsen. In this section, the nano and microstructure will be examined by TEM to study the dislocation structure and precipitates. DSC analysis will be further performed to study precipitation and recovery/recrystallisation. Results from both techniques will be used to explain and analyse the hardening/softening effects obtained from hardness tests and tensile tests.

5.3.1 Precipitate analysis by TEM/EDS

TEM can be used to observe dislocation structure and precipitates. Due to the high density of tangled dislocations in the heavily cold-worked samples, it is almost impossible to detect the individual dislocations, especially for samples with higher cold-rolling reduction, e.g. 90% [10]. In this study, TEM was conducted mainly to observe and identify precipitates present in the alloys studied.

Before presenting the TEM results, some difficulties and limitations related to the observation of precipitates in the present alloys need to be discussed. First, due to the small additions of Cu and Si in the alloys, the volume faction of the precipitates is very small compared with that in classical heat treatable Al alloys, e.g. 2XXX, 6XXX and 7XXX alloys. Second, the high dislocation density generated by heavy cold work makes it often difficult or impossible to image precipitates in the TEM. Another difficulty is that many possible precipitates may occur depending on the alloy composition. Furthermore, the diffraction patterns of some precipitates are very similar, which makes it difficult to distinguish them from each other, especially when the volume fractions of the precipitates are very small causing faint different patterns.

5.3.1.1 Literature reported diffraction patterns of precipitates present in Al-Mg-Si(-Cu) alloy system

Some selected TEM observations, especially the diffraction patterns of some precipitates occurring in the Al-Mg-Cu, Al-Mg-Si or Al-Mg-Si-Cu alloy systems reported in the literature will be presented for comparison with experimental results.

The possible precipitates present in the Al-Mg-Cu alloy system are GPBII/S″ and S phases. Micrographs and corresponding diffraction patterns of S phase at [112] and [100] zone axis in an Al-2.81Cu-1.05Mg-0.41Mn (wt%) alloy are illustrated in Figure 5.43. The diffraction patterns of GPBII/S″ and Ω (Al_2Cu) phases and their coexistence with S phase in the same alloy are illustrated in Figure 5.44. Many precipitates were reported in the literature for the Al-Mg-Si or Al-Mg-Si-Cu alloy system. The most commonly reported precipitates are β″, β', β, Q' and Q. Figure 5.45 shows a micrograph of the needle-like β″ precipitates and its corresponding diffraction pattern in an AA6022 alloy (Al-0.58Mg-1.28Si-0.07Cu-0.11Fe-0.08Mn). As illustrated in Figure 5.46, rod-like and lath-like precipitates were present in the same alloy at different condition. The rod-like precipitates were thought to be β' phase and the lath-like precipitates were suggested to be B' or Q phase [11]. The micrograph and the corresponding diffraction pattern in the same alloy shown in Figure 5.47a and b revealed β' and Q' phases, respectively. A simulated diffraction pattern of β' and Q' phases from reference [12] is shown in Figure 5.47c.

5.3.1.2 TEM results

The bright field (BF) image of alloy A1, solution treated and subsequently aged for three weeks at 170°C, unambiguously reveals some rod-like precipitates (see Figure 5.48a). However, the selected area diffraction (SAD) does not show any extra diffraction pattern from precipitates (Figure 5.48b). The absence of extra diffraction spots from precipitates might be due to the low volume fraction of the precipitates and observation zone axis [110] in which the intensity may be not as strong as that in [100] zone axis. For the 10% cold-worked sample of alloy A1 aged for three weeks at 170°C, the BF image shows that some precipitates are present (Figure 5.49a) and the SAD at [100] zone axis reveals some faint extra diffraction spots from the precipitates (circled in Figure 5.49b). The SAD pattern illustrated in Figure 5.49b is consistent with the simulated diffraction pattern of β' phase as shown in Figure 5.47c. Hence the precipitates present in the cold-worked alloy A1 aged for three weeks at 170°C are probably β' phase. It is thought that the precipitates in Figure 5.48a are also β' phase.

For the cold-worked alloy A4 aged for five days at 170°C, no individual precipitate can be unambiguously detected in the BF images (an example shown in Figure 5.50a). However, the SAD pattern illustrated in Figure 5.50b reveals very faint diffraction streaks from precipitates. Such a streak pattern could be due to S phase or β″/β' phase, but due to the

very faint pattern, the precipitates could not be further identified. TEM observations on the cold-worked alloy A4 aged at higher temperature (220°C) are shown in Figure 5.51. The BF image (Figure 5.51a) reveals some larger precipitates marked by spectra 3 and 4. The spectra of both 3 and 4 reveal Mg and Cu in the precipitates (Figure 5.51b shows one example). Furthermore, from the comparison of the SAD of the larger needle shaped precipitate (marked spectrum 4 in Figure 5.51a) shown in Figure 5.51c with the simulated S phase on [112] zone axis (see Figure 5.51d), the larger precipitates can be confirmed to be S (Al_2CuMg) phase. In this sample some small dots marked by white arrows (see Figure 5.51a) were also noted in the BF TEM image. These dots might be an unidentified second type of precipitates, which could be β phase or its precursor.

As shown in Figure 5.52a, the BF image of a cold-worked sample of alloy A7 aged for five days at 170°C reveals some precipitates, whilst the SAD pattern at [100] zone axis reveals some faint streaks from these precipitates (see Figure 5.52b). Again due to the very faint diffraction pattern, these precipitates could not be identified confidently; they could be the precursors of S phase and/or β phase. TEM observations were also made on the cold-worked samples aged for longer time (three weeks) at 170°C. The BF image reveals some precipitates as shown in Figure 5.53a. The SAD is still very faint, but some individual dots rather than the streaks can be discerned in the diffraction pattern shown in Figure 5.53b. They are consistent with the simulated diffraction pattern of S phase shown in Figure 5.43f and hence the precipitates are probably S phase.

The BF TEM observations on a cold-worked sample of alloy A8 aged for three weeks at 170°C reveal some large precipitates on a grain boundary (see Figure 5.54a). The corresponding SAD pattern (see Figure 5.54b) of a large precipitate is consistent with the simulated diffraction pattern of S phase shown in Figure 5.51d, whilst the spectrum marked in Figure 5.54a reveals that Mg and Cu are present in the precipitate (see Figure 5.54c). Hence these precipitates can be identified as S phase.

The BF TEM image of a cold-worked sample of alloy A9 aged for five days at 170°C reveals a high density of dislocations and no precipitates can be unambiguously identified (see Figure 5.55a). However, the SAD pattern shown in Figure 5.55b reveals some extra diffraction spots from precipitates, which are consistent with the simulated diffraction pattern of S phase shown in Figure 5.43f. Thus S phase is likely to be present.

The above discussed TEM results suggest the following. For the overaged samples of cold-rolled alloy A1, β'/β precipitates are likely to be present. For Cu-containing alloys with 1wt% Mg, e.g., alloys A4 and A7, S precipitates and possibly β″/β'/β precipitates are likely to be present in the cold-worked-and-aged samples. For alloys with higher Mg and Cu contents, e.g., alloys A8 and A9, mainly S precipitates are likely to be present in the cold-worked-and-aged samples.

5.3.2 DSC results and analysis

Due to small additions of Cu and Si in the alloys studied, the amount of precipitates in these alloys is very limited compared with that in classical heat treatable alloys. Hence the heat flows measured in DSC experiments are usually very small compared with those in heat treatable alloys. For most heat treatable aluminium alloys, the heat flows due to precipitation reactions are typically around 0.1-0.5 W/g. However, the heat flows for the alloys studied in this project are only around 0.01 W/g or less. Detecting such small heat flows is challenging because equipment noise and baseline instabilities will interfere with the measurement [13]. However, DSC is nevertheless a very useful technique to study precipitation in these Al alloys. Due to the instabilities and drift of the baseline, especially at higher temperatures, it is difficult to determine the baseline accurately. Hence caution should be taken when interpreting the reactions at higher temperatures in the DSC thermograms.

The DSC results of cold-rolled samples, cold-rolled-and-aged samples and solution-treated samples for each of the nine alloys are shown in Figure 5.56. In these figures, cw, 2w and ST represent the DSC traces of as cold-worked samples, cold-rolled-and-aged (two weeks at 170°C) samples and solution-treated samples, respectively. In order to separate the curves of cw, 2w and ST in the figure, the heat flows of the 2w samples and those of ST samples were offset by 30 W/kg and -30 W/kg, respectively.

The DSC results will primarily be used to assess the kinetics of reactions responsible for hardening/softening occurring during isothermal ageing at 170°C. High temperature effects (i.e. peak temperature higher than 400°C) in the DSC runs cannot occur during isothermal ageing at 170°C, and therefore, the analyses will be focused on the effects appearing in the DSC curves in the temperature range of 100-400°C.

The major heat effects for the nine alloys and their probable identifications are summarized and the results are given in Table 5.7. The identifications are discussed below. It should be noted throughout the discussion below that in most cases there is no definite evidence for identification of heat effect. However, from literature review, MTDATA calculations (see section 5.1.1.2) and TEM data (see section 5.3.1) an overview of possible precipitates and temperature ranges for formation can be deduced. As will be shown below the combination of these data with DSC data allows identifications of the major heat effects with a reasonable degree of confidence.

Table 5.7 Major observed effects and probable identifications in the DSC traces

Alloy ID	A/A1	A2	A3	B/B'	C	D/D1	D2
A1 cw	β″ ppt	-	-	Rex	Mn ppt	-	-
A1 2w	-	-	-	Rex	Mn ppt	β″ dissolution	-
A1 STH	β″ ppt	-	-	-	Mn ppt	-	-
A1 STL	β″ ppt	-	-	-	Mn ppt	-	-
A2 cw	β″ ppt	-	-	Rex	Mn ppt	-	-
A2 2w	-	-	-	Rex	Mn ppt	○	-
A2 STH	β″ ppt	-	-	-	Mn ppt	-	-
A2 STL	-	-	-	-	Mn ppt	-	-
A3 cw	-	-	-	Rex	Mn ppt	-	-
A3 2w	-	-	-	Rex	Mn ppt	-	-
A3 STH	β″ ppt	-	-	-	Mn ppt	-	-
A3 STL	-	-	-	-	Mn ppt	-	-
A4 cw	β″ ppt	S′/S ppt	-	Rex	Mn ppt	-	-
A4 2w	-	-	-	Rex	Mn ppt	β″ dissolution	S′/S dissolution
A4 STH	β″+Q' ppt	Q ppt	○	-	Mn ppt	-	-
A4 STL	β″+Q' ppt	○	-	-	Mn ppt	-	-
A5 cw	β″ ppt	S′/S ppt	-	Rex	Mn ppt	-	-
A5 2w	-	-	-	Rex	Mn ppt	β″ or S dissolution	-
A5 STH	β″ ppt	Q ppt	GPB	-	Mn ppt	-	-
A5 STL	S or Q' ppt	Q ppt	-	-	Mn ppt	-	-
A6 cw	S′/S ppt	-	-	Rex	Mn ppt	-	-
A6 2w	-	-	-	Rex	Mn ppt	S′/S dissolution	-
A6 STH	β″ ppt	Q ppt	GPB	-	Mn ppt	-	-
A6 STL	S′/S ppt	-	-	-	Mn ppt	-	-
A7 cw	β″ ppt	S′/S ppt	-	Rex	Mn ppt	-	-
A7 2w	-	-	-	Rex	Mn ppt	β″ dissolution	S′/S dissolution
A7 STH	β″+Q' ppt	Q ppt	GPB	-	Mn ppt	-	-
A7 STL	β″+Q' ppt	○	-	-	Mn ppt	-	-
A8 cw	β″ ppt	S′/S ppt	-	Rex	Mn ppt	-	-
A8 2w	-	-	-	Rex	Mn ppt	β″ or S dissolution	-
A8 STH	β″ ppt	Q ppt	GPB	-	Mn ppt	-	-
A8 STL	S or Q' ppt	Q ppt	-	-	Mn ppt	-	-
A9 cw	○	S′/S ppt	-	Rex	Mn ppt	-	-
A9 2w	-	-	-	Rex	Mn ppt	S′/S dissolution	-
A9 STH	β″ ppt	Q ppt	GPB	-	Mn ppt	-	-
A9 STL	S′/S ppt	○	GPB	-	Mn ppt	-	-

In the table, ppt, Mn ppt and Rex stand for precipitation, precipitation of Mn containing dispersoids and recrystallisation, respectively; cw and 2w represent the cold-worked samples and cold-worked-and-aged samples (two weeks at 170°C), respectively; STH and STL stand for solution-treated samples at higher (550°C) and lower (500°C) solutionising temperature, respectively. GPB means formation of GPB zones or co-clusters. - and ○ mean that reaction is not observed and not identifiable, respectively.

5.3.2.1 Analysis of DSC results of the nine alloys

(1) Alloy A1

For alloy A1, three obvious exothermic effects appear in the DSC curves of cold-worked samples in the temperature range of 150-450°C (Figure 5.56a). They are indicated as A, B and C in the figure. Exothermic effects in DSC may be related to precipitation reaction, recovery or recrystallisation, whilst endothermic effects may be related to dissolution of precipitates. It is noticed that effect B only occurs in the 90% cold-worked specimen, and there is no corresponding effect in 40% and 10% cold-worked specimens. So this effect is considered to be due to recovery or recrystallisation. Moreover, as shown in Figure 5.57, which gathers all the DSC traces of 90% cold-worked samples to illustrate only effect B, all the 90% cold-worked specimens show effect B around the temperature range of 300-350°C. It is interesting to notice that the peak temperature of effect B increases with decreasing Mg content and increasing Cu content. Some of the 40% cold-worked specimens also show a smaller exothermic effect B′ (e.g, B′ in Figure 5.56b, c, e and i), which is also thought to be due to recovery or recrystallisation. However, there is no corresponding effect present in the DSC traces of any of the 10% cold-worked specimens. The observations of effects B and B′ in the DSC runs are also consistent with the fact that the driving force for recovery/recrystallisation increases with increasing deformation or cold-rolling reduction. A further study on the origin of the effect B/B' will be performed (see section 5.3.2.2).

Compared with those of the cold-worked specimens, the traces of the specimens aged for two weeks for alloy A1 (see Figure 5.56a) do not show peak A, but the peaks B and C are still there. Peak B should become weaker or disappear if it is due to recovery, because the specimens could be partially or fully recovered after two-week ageing at 170°C depending on the kinetics of recovery. Actually peak B appears without any sign of weakening in the DSC thermogram after two-week ageing at 170°C. This indicates that peak B could be related to recrystallisation rather than recovery. This can be explained as follows. On annealing at 170°C, no recrystallisation can occur in the cold-worked samples since the annealing temperature is too low to activate recrystallisation. Hence the released energy due to recrystallisation which relates to effect B during DSC runs will not change after ageing for two weeks at 170°C.

The exothermic effect A with a peak temperature around 240°C in Figure 5.56a may be related to precipitation. This effect should be due to the β″/β′/β precipitation sequence since the alloy contains 1wt% Mg, 0.16wt% Si and no Cu. According to literature [14, 15], the maximum rate of β″ (Mg_2Si) precipitation in the DSC experiments at 10°C/min heating rate is around 240-250°C, which is very close to the peak temperature of effect A in this study. Therefore, effect A may be related to β″ precipitation. The dissolution effect D appearing in the aged specimens of alloy A1 (Figure 5.56a) may be attributed to the dissolution of β phase or its precursor formed during ageing prior to the DSC runs.

As shown in Figure 5.56a, an effect C around 400-420°C appears in all the cold-worked samples of alloy A1, and it is also present in the DSC runs of the specimens aged for two weeks at 170°C. Moreover, the effect C appears in the solution-treated samples too. The effect C is thought to be due to the precipitation of Mn containing dispersoids. This interpretation may be supported by two observations. First, this peak appears in all the alloys regardless of the cold-rolling reduction, ageing condition and solutionising temperature. The other supporting factor is that $Al_{12}(Mn,Fe)_3Si_2$ was detected to precipitate in an AA3004 alloy (0.9% Mg, 0.22% Si, 0.98% Mn and 0.46% Fe, which is quite similar to alloy A1 in this study), after ageing for 30 minutes at 455°C [16].

For alloy A1, the occurrence of effect A in the DSC runs of cold-worked samples is consistent with the observation of precipitation hardening of this alloy during ageing at 170°C by hardness testing. The effect A due to β″ precipitation may contribute to the precipitation hardening in alloy A1 during ageing at 170°C.

In the following discussion and later sections, for simplicity, STH and STL samples will be used to indicate the samples re-solution treated at higher temperature (550°C) for 30 minutes and at lower temperature (500°C) for 30 minutes, respectively.

For both STH and STL samples of alloy A1, an exothermic effect A appears in the DSC traces. Its peak temperature is slightly higher (by about 20°C) than that of effect A in the cold-worked samples (see Figure 5.56 a). It is interpreted to be due to β″ precipitation too. It is also consistent with the age hardening observed in both solution-treated samples of alloy A1 (see Figure 5.23a and Figure 5.24).

(2) Alloys A2 and A3

As shown in Figure 5.56b, the DSC traces of the cold-worked samples of alloy A2 show a smaller exothermic effect A due to β″ precipitation than that in alloy A1, but there is no obvious precipitation effect A appearing in the DSC traces of the cold-worked samples of alloy A3 (see Figure 5.56c). This is consistent with the observations by hardness testing that there is no significant precipitation hardening in the cold-worked alloy A2 and that only recovery was detected in the cold-worked alloy A3. The absence of age hardening in the cold-worked alloy A2 may be explained by a concurrent small precipitation hardening effect and recovery occurring during ageing.

The different age hardening response for the cold-worked alloys A1, A2 and A3 may be explained by the SEM microstructure observations and the prediction of thermodynamic calculations. As discussed in section 5.1.1, Mg_2Si particles were detected by SEM/EDS in the cold-worked alloys A2 and A3, but not in the cold-worked alloy A1. According to the MTDATA predictions (see section 5.1.1.2), almost all Si in alloy A3 may be tied up with Mg_2Si particles during solution treatment at 500°C. For alloy A2, limited Si may remain in the matrix after solution treatment at 500°C. However, for alloy A1, very limited Si may be removed from the matrix during the same solution treatment. Therefore, the amount of Si in the matrix available to precipitate during artificial ageing explains the differences in the age hardening response of all the three cold-worked Cu-free alloys.

For alloys A2 and A3, the DSC data indicate that the solutionising temperature may influence the ageing behaviour of solution-treated samples. An exothermic effect A attributed to β″ formation appears in the DSC trace of the STH samples of alloys A2 and A3 (see Figure 5.56b and c). However, as also shown in Figure 5.56b and c, no such effect is detected in the STL samples of alloys A2 and A3. The absence of effect A in the STL samples can also be explained by the SEM observations and thermodynamic calculations. As discussed above, at lower solutionising temperature (500°C), the intermetallic Mg_2Si particles formed during thermomechanical processing remain undissolved in these two alloys. Hence no or very limited Si is available for precipitation during the DSC run. Therefore, the effect A due to β″ precipitation is absent in the STL samples, which is also consistent with the absence of age hardening in the STL samples of alloys A2 and A3 (see Figure 5.24). However, the Mg_2Si particles may be dissolved or partially dissolved at higher solutionising temperature (550°C) according to the MTDATA predictions. Hence

more Si is available for precipitation during the subsequent DSC run. That is consistent with the occurrence of the exothermic effect A in the STH samples, which also agrees well with the observed age hardening in the STH samples of alloys A2 and A3 during ageing (see Figure 5.23b and c).

(3) Alloy A4

For alloy A4, the DSC traces of cold-worked samples become more complicated (see Figure 5.56d). As shown in the plot, effect B appears both in the DSC traces of the 90% cold-worked samples and two-week aged specimens. It is attributed to recrystallisation as discussed before. There are two exothermic effects in the range of 200-300°C for the cold-worked specimens, which are indicated as A1 and A2 in Figure 5.56d, respectively. These two effects disappear after ageing for two weeks at 170°C. They may be related to precipitation reactions, which are responsible for the hardening during ageing observed in this alloy with three cold-rolling reductions. As shown in Figure 5.56d, the effect A1 appears in the 40% and 10% cold-worked samples, and the peak height increases with decreasing cold-rolling reduction. The peak temperature of effect A1 is around 240°C, which is similar to that of effect A in alloy A1. So this effect may be due to β″ precipitation. The effect A2 in Figure 5.56d appears only in the 90% cold-worked samples, and its peak temperature is around 280°C. This may be considered to be due to S′/S precipitation since the alloy contains 0.2wt% Cu, and it also agrees well with the peak temperature for S′/S precipitation observed by other researchers [17, 18]. The endothermic effects D1, D2 present in the two-week aged samples as illustrated in Figure 5.56d are thought to be related to the dissolution of β″ phase and S′/S phase formed during ageing at 170°C, respectively.

In relating the DSC results with hardness testing, the precipitation hardening observed by hardness testing in the cold-rolled alloy A4 with different reductions during ageing at 170°C (see Figure 5.23d) may be caused by different types of precipitates. For 90% reduction, the precipitation hardening effect may be mainly caused by S′/S phases, but β″ precipitation may primarily contribute to the precipitation hardening effect in the cold-rolled alloy with 40% and 10% reductions.

For the solution-treated samples of alloy A4, the DSC data indicate that solutionising temperature has no significant influence on the ageing behaviour of the alloy. As shown in

Figure 5.56d, exothermic effects A1 and A2 appear in both solution-treated samples. These effects are much more prominent in the STH sample than those in the STL sample. The effect A1 occurs in a much broader temperature range of 200-320°C with a peak around 285°C; this wide range could indicate two or more phases forming. According to the precipitation sequence in Al-Mg-Si-Cu alloys suggested in reference [15] (also see section 2.2.2.3), it may be attributed to the formation of β″ phase and Q' phase. The peak temperature of the effect A2 is around 348°C. It is very close to that of Q phase, which has a peak temperature around 345°C during a DSC run [15]. According to SEM analysis and MTDATA predictions, no Mg_2Si particles form either at 500°C or at 550°C for alloys with 1wt% Mg, i.e., most of the Si will be available for precipitation in both STH and STL samples of alloy A4 during DSC runs. The effect A1 and possibly A2 may be attributed to the hardening effect detected both in the STH and STL samples of alloy A4 (see Figure 5.23d and Figure 5.24).

(4) Alloy A5

For the cold-worked samples of alloy A5, the effects A1 and A2 are much smaller than the corresponding effects in the cold-worked samples of alloy A4 (see Figure 5.56e). The small effect A1 due to β″ precipitation appears in the DSC curves of all three cold-worked samples, whilst a possible very small effect A2 due to S′/S precipitation appears in the DSC trace of the 90% and 40% cold-worked samples. An endothermic effect D appears in the two-week aged samples with three different pre-reductions. This may be attributed to the dissolution of β″ phase or S'/S phase formed during ageing prior to the DSC runs. The DSC data indicates that solutionising temperature has a significant influence of the ageing behaviour of the solution-treated samples. As shown in Figure 5.56e, in the STH sample, a small exothermic effect A3 appears in the temperature range about 90-180°C, which may be attributed to the formation of GPB zones or co-clusters containing Mg and Cu or even Si [19]. This effect is consistent with the rapid hardening within 30-minute ageing (referred to as the first stage of age hardening) of the STH sample of alloy A5 (see Figure 5.23e) and thus the formation of GPB zones/clusters may be the origin of the rapid hardening observed. However, such effect is absent in the DSC trace of the STL sample of alloy A5, which is consistent with the absence of rapid hardening in the STL sample of this alloy (see the curve for A5 in Figure 5.24). Exothermic effects A1 and A2 appear in the DSC thermograms of both solution-treated samples, although these effects are much

more marked in the STH sample than those in the STL sample. The peak temperature of effect A1 in the STH sample is around 265°C, whilst that of effect A2 is around 348°C, which suggests that they may be due to the formation of β″ phase and Q phase, respectively. The formation of β″ phase may contribute to the second stage of age hardening of the STH sample of this alloy. In the STL sample, much lower Si or very limited Si is available in the matrix although some Cu is still available, so the effects are much smaller than those in the STH sample. The effect A1 in the STL sample is much broader and quite weak, with a possible peak temperature around 290°C. It might be attributed to the formation of S'/S phase or Q' phase. The effect A2 in the STL sample may be attributed to the formation of Q phase. The effect A1 and possibly effect A2 may be attributed to the age hardening observed in the STL sample of alloy A5 (see the curve for A5 in Figure 5.24).

(5) Alloy A6

As shown in Figure 5.56f, there is no obvious effect A1 due to the formation of β″ phase appearing in any of the DSC traces of the cold-worked specimens of alloy A6, but a very small effect A due to S′/S precipitation appears in the DSC thermogram of the 90% cold-worked sample. A weaker effect A may be present in the DSC runs for the 40% and 10% cold-worked specimens, but that effect is not clear in these samples. The hardening effect observed in the cold-worked alloy A6 with 90% reduction may be related to the precipitation effect A, which is thought to be caused by S′/S precipitation. For 40% and 10% reductions, a small hardening effect was also observed in this alloy by hardness tests (see Figure 5.23f). The absence of effect A in the 40% and 10% cold-worked samples during DSC runs may be due to sluggish S phase formation caused by a combination of lower dislocation density and low levels of Cu. As DSC heating is relatively fast (the potential range for S phase formation is scanned in about 10-20 minutes), no or very little S phase formation may be occurring during DSC.

An endothermic effect D appears in all the three two-week aged samples of alloy A6 (see Figure 5.56f), which may be attributed to the dissolution of S'/S phase formed during ageing prior to the DSC runs.

As indicated in Figure 5.56f, solutionising temperature again influences the ageing behaviour of the solution-treated samples. In the STH sample, three exothermic effects

appear in the range of 100-400°C in the DSC trace. A small exothermic effect A3 occurs in the temperature range of about 100-150°C, which is considered to be due to the formation of GPB zones/clusters. It is consistent with the rapid hardening within 30-minute ageing of the STH sample of this alloy (see Figure 5.23f). A much sharper peak occurs around 240-280°C with a peak around 258°C. This effect (effect A1) may be attributed to the formation of β″ phase, which may contribute to the second stage of age hardening of the STH sample during ageing. Another much smaller effect A2 appearing in the STH sample with a peak around 348°C may be considered to be due to the formation of Q phase. Different to the STH sample, there is no prominent effect A3 appearing in the DSC trace of the STL sample. The absence of effect A3 is consistent with the absence of rapid hardening in the STL sample (see the curve A6 in Figure 5.24). A very small effect A1 (peak temperature around 280°C) may possibly be present, which may be attributed to the formation of S phase. The occurrence of the effect A1 may be supported by the age hardening observed in the STL sample of this alloy (see Figure 5.24). The DSC trace of the STL sample is very similar to those of cold-worked samples. This indicates that the age hardening response of the STL sample is similar to that of the cold-worked samples.

(6) Alloy A7

The DSC traces of alloy A7 are shown in Figure 5.56g. An exothermic effect A1 appears in all the cold-worked samples, but only a small effect A2 appears in the 90% and possibly in the 40% cold-worked sample too. Similar to alloy A1, the effect A1 appears in the cold-worked samples of alloy A7, and the peak height increases with decreasing cold-rolling reduction. Hence effect A1 may be attributed to β″ precipitation. S′/S precipitation may be related to effect A2.

In the two-week aged samples of alloy A7, both effects A1 and A2 disappear and two endothermic effects D1 and D2 appear (see Figure 5.56g), which may be considered to be due to the dissolution of β″ phase and S'/S phase, respectively.

As shown in Figure 5.56g, DSC data indicate that solutionising temperature has a significant influence on the ageing behaviour of the solution-treated samples of alloy A7. For the STH sample, other than effect C, three more exothermic effects are present in the DSC run. The small exothermic effect A3 may be attributed to the formation of GPB zones or clusters, which is consistent with the weak rapid hardening within 30-minute

ageing detected in the STH samples of alloy A7 (see Figure 5.23g). A much broader effect A1 in the range of 230-320°C may be attributed to the formation of two or more phases, which is similar to that of the STH sample of alloy A4. According to the precipitation sequences reported in Al-Mg-Cu-Si alloys [15], it may be considered due to the formation of β″ and Q' phases. The effect A2 with a peak temperature around 348°C may be attributed to the formation of Q phase. For the STL sample, only one broad exothermic effect A1 is prominently present in the DSC trace, which may be attributed to the formation of β″ and Q' phases too. Especially β″ phase would contribute to the age hardening observed in the STL sample of this alloy and the absence of effect A3 is consistent with the absence of rapid hardening within 30-minute ageing in the sample (see the curve A7 in Figure 5.24).

(7) Alloy A8

For the cold-rolled samples of alloy A8, as shown in Figure 5.56h, a small exothermic effect A1 due to the formation of β″ phase appears in the DSC curves for the 40% and 10% cold-worked samples, and an exothermic effect A2 due to the formation of S'/S phase is present in the DSC curves for the 90% and 40% cold-worked samples. For 40% reduction, effect A2 is much stronger than effect A1. Therefore, the precipitation hardening observed by hardness testing could be mainly due to S′/S phase precipitation (i.e. effect A2) for 90% and 40% reductions, whilst mainly β″ phase precipitation may contribute to the hardening for 10% reduction. In the two-week aged samples, both effects A1 and A2 disappear, and a small endothermic effect D appears, which would again be attributed to the dissolution of β″ phase or S′/S phase.

For the solution-treated samples of alloy A8, other than effect C, three prominent exothermic effects appear in the STH sample (see Figure 5.56h). An exothermic effect A3 in the range of 90-180°C may be attributed to the formation of GPB zones or clusters, which may contribute to the rapid hardening within 30-minute ageing detected in the STH sample of this alloy during isothermal ageing (see Figure 5.23h). A sharp exothermic effect A1 occurring in the range of 240-285°C with a peak temperature around 258°C may be attributed to the formation of β″ phase. The exothermic effect A2 with peak temperature around 348°C again may be attributed to the formation of Q phase. For the STL sample, no prominent effect A3 is present. This is consistent with the absence of rapid hardening in the STL sample of this alloy during ageing (see Figure 5.24). A broader

effect A1 is present in the range of 240-320°C with a peak around 280°C, which may be attributed to the formation of S'/S or Q' phase. A very small effect A2 is just about resolvable for the STL sample, which might also be attributed to the formation of Q phase. The effect A1 may be contributed to the age hardening observed in the STL sample of alloy A8 (see Figure 5.24).

(8) Alloy A9

The DSC results of the cold-rolled alloy A9 are somewhat simpler. As shown in Figure 5.56i, no obvious exothermic effect A1 appears in the DSC traces of the cold-worked samples, but an exothermic effect A2 appears in all the cold-worked samples. Moreover, for effect A2, the higher the reduction, the lower the peak temperature and the higher the peak, which is consistent with the observation from other researchers that S′/S precipitation may be facilitated by deformation [17, 18]. The hardening observed in the cold-rolled samples of this alloy by hardness testing therefore can be explained by the precipitation hardening due to the formation of S′/S precipitates.

For the two-week aged samples of alloy A9, again both effects A1 and A2 disappear, and an endothermic effect D appears (see Figure 5.56i). The effect D may be attributed to the dissolution of S′/S phase formed during ageing prior to the DSC runs.

In the solution-treated samples of alloy A9, other than effect C, three more exothermic effects are present in the DSC trace of the STH sample (see Figure 5.56i). The exothermic effect A3 may be attributed to the formation of GPB zones or clusters, which is consistent with the rapid hardening within 30 minutes during isothermal ageing of the STH sample of this alloy (see Figure 5.23i). The exothermic effect A1 with a peak around 258°C may be considered due to the formation of β″ phase. It may contribute to the second stage of age hardening detected in the STH sample. Another exothermic effect (effect A2) with a peak around 348°C may be attributed to the formation of Q phase. Different from the STL samples in other Cu-containing alloys, the exothermic effect A3 is also present in the STL sample of alloy A9 (see Figure 5.56i). This is also attributed to the formation of GPB zones or clusters. It is consistent with the rapid hardening within 30-minute ageing observed in the STL sample of this alloy (see the curve for A9 in Figure 5.24). An exothermic effect A1 with a higher peak temperature around 280°C appears in the DSC trace of the STL sample, which may be considered due to the formation of S'/S phase

since no or very limited Si is available in the STL sample of alloy A9 according to the SEM/EDS analysis. Moreover, the absence of effect A2 due to the formation of Q phase in the DSC trace of the STL sample also supports the conclusion that Si is not available in the matrix for precipitation in the STL sample of alloy A9 during DSC run. The effect A1 may contribute to the second stage of age hardening observed in the STL sample of alloy A9 during ageing (see Figure 5.24).

As shown in Figure 5.56i, exothermic effects B and B′ appear in the DSC traces of 90% and 40% cold-worked samples of the alloy, respectively. No corresponding effect seems to appear in the DSC run of the 10% cold-worked sample. The effects B and B′ are also present in the DSC runs of the specimens aged for two weeks. As discussed before, these effects B and B′ are thought to be due to recrystallisation, which will be further clarified by the experiments presented in the next section.

5.3.2.2 Confirmation of the recrystallisation effect

DSC-size samples of cold-worked alloy A9 with three different cold-rolling reductions were heated incrementally in the DSC calorimeter at a heating rate of 10°C/min, and subsequently rapidly cooled down to room temperature. Samples were taken out from the DSC, and hardness testing was conducted on the samples. The experimental results shown in Figure 5.58 reveal the following. For 90% reduction, recrystallisation starts around 250°C, which is indicated by the hardness beginning to drop dramatically, and it ends at about 350°C, suggested by reaching a near stable hardness value. That agrees well with the temperature range of effect B with a peak temperature at about 320°C in the DSC traces of 90% cold-worked samples of alloy A9 and all the other alloys (see Figure 5.57). For 40% reduction, as illustrated in Figure 5.58, recrystallisation starts around 280°C and ends at about 400°C, which also agrees well with the observation of effect B′ by DSC analyses in the 40% cold-worked sample of this alloy and some other alloys. For 10% reduction, as shown in Figure 5.58, recrystallisation starts around 300°C and ends around 450°C. The DSC curves do not show a clear effect of recrystallisation in any 10% cold-worked samples, which is probably due to the lower stored energy and overlap with other effects (e.g., effect C in Figure 5.56).

The above experiment, therefore, confirms that effects B and B′ in the DSC traces of the cold-worked samples are due to recrystallisation.

5.3.2.3 Summary of DSC results

Taking all the analyses of the DSC results together, the precipitation in the nine alloys is complicated, depending both on alloy composition, level of cold work and solutionising temperature. The above observations and discussion are summarised in Table 5.8.

Table 5.8 Summary of precipitation effects observed in the DSC traces

Alloy No.	Mg wt%	Cu wt%	CW			ST	
			90%	40%	10%	STH	STL
A1	1	0	β	β	β	β	β
A4		0.2	(β)+S	β	β	Q+β	Q+β
A7		0.4	β+(S)	β+(S)	β	GPB, Q+β	Q+β
A2	2	0	(β)	(β)	(β)	β	-
A5		0.2	(β)+(S)	(β)+(S)	(β)	GPB, Q+β	Q+β
A8		0.4	(β)+S	(β)+S	β+(S)	GPB, Q+β	Q+β
A3	3	0	-	-	-	β	-
A6		0.2	(S)	(S)	(S)	GPB, Q+β	S
A9		0.4	S	(β)+S	(β)+S	GPB, Q+β	GPB, S

In the above table, () represents small effect or an effect that cannot be resolved with certainty, - indicates no effect. β means precipitation due to β″/β′/β precipitation sequence, whilst S indicates precipitation due to S″/S′/S precipitation sequence. Q+β means precipitation due to β″+Q'/Q+β precipitation sequences. GPB means formation of GPB zones/co-clusters.

In next section, the results of DSC, TEM and hardness testing will be gathered to consider the precipitation in the alloys studied and the influence of deformation on precipitation and recovery during isothermal ageing of cold-worked samples.

5.4 Discussion

5.4.1 Precipitation in the alloys

For Al-Mg-Cu alloys with low Cu/Mg ratios, during ageing, the following possible precipitation sequence may occur: $\alpha_{ss} \rightarrow$GPB zones (Cu/Mg clusters) $\rightarrow$(S´´)$\rightarrow$S´$\rightarrow$S (Al_2CuMg) [20]. For Al-Mg-Si alloys, the possible precipitation sequence is: $\alpha_{ss} \rightarrow$ GP zones$\rightarrow$β″$\rightarrow$β′$\rightarrow$β (Mg_2Si) [21]. However, currently there are still disputes about the precipitation sequence in both alloy systems. The picture of the precipitation behaviour becomes even more complicated in the Al-Mg-Cu-Si system, as precipitation may strongly depend on the alloy composition. This indicates that the precipitation in the alloys studied may be very complicated due to: 1) the co-existence of small additions of Cu and Si in the Al-Mg-Mn alloys and 2) the possible interactions between precipitation and

recovery for the cold-worked samples. Different age hardening responses can thus be expected in the nine alloys studied.

5.4.1.1 Precipitation in the Cu-free alloys A1-A3

Alloy A1 showed some distinct precipitation hardening during ageing observed by hardness testing and tensile testing. Moreover, the DSC analyses for cold-worked alloy A1 demonstrated an exothermic effect due to precipitation reaction with a peak temperature around 240°C. A cold-worked sample of alloy A2 did not show significant age hardening, which could be caused by concurrent recovery and some limited precipitation hardening. The DSC also detected a small effect due to precipitation reaction in the cold-worked sample of alloy A2. However, there is a total absence of precipitation hardening during ageing of the cold-worked sample of alloy A3, and no precipitation reaction was detected between 100-400°C by DSC analyses for the cold-worked sample of alloy A3. In other words, only recovery was detected in the cold-worked alloy A3 in the experiments.

The microstructure analyses on intermetallic particles by SEM/EDS and the thermodynamic calculations by MTDATA provide an explanation for the different age hardening responses in the cold-worked samples of the three Cu-free alloys. As schematically illustrated in Figure 5.59 and a more detailed Al-Mg-Si phase diagram available in [22], the solubility of Si in Al matrix increases with decreasing Mg content. Therefore, the higher the Mg content in the alloys, the less Si will be available in the matrix after solution treatment at 500°C. This is also consistent with SEM/EDS analyses and thermodynamic calculations. According to the MTDATA predictions, Mg_2Si particles may form during solution treatment at 500°C in alloys A2 and A3, whilst no such particles may form in alloy A1. Hence after solution treatment at 500°C, the amount of Si available in the matrix for precipitation during subsequent ageing is descending in the order: A1, A2 and A3. That is, the higher the Mg content, the lower the amount of Si available in the matrix for precipitation. Therefore, in the cold-worked samples of the three Cu-free alloys, which were solutionised at 500°C, the lower the Mg contents, the higher the precipitation hardening during ageing. In line with this, for the STL samples, which were also solutionised at 500°C, only alloy A1 showed distinct age hardening and no substantial hardening was detected in alloys A2 and A3 by hardness testing (see Figure 5.24). Furthermore, the DSC analysis also confirmed a precipitation reaction due to β″ formation occurring in the STL sample of alloy A1, but not in the STL samples of alloys A2 and A3.

However, the situation changes for the STH samples of the Cu-free alloys. All the STH samples of the three Cu-free alloys show substantial age hardening (see Figure 5.22d). The DSC analysis of the STH samples also confirms the occurrence of a precipitation reaction due to β″ formation in all the three Cu-free alloys (see Figure 5.56a, b and c). In this case, the release of Si from dissolved Mg_2Si particles at higher solutionising temperature (550°C) makes β″ precipitation possible during subsequent DSC runs.

The observed precipitation strengthening in the Cu-free alloys is likely to be due to precipitation following the β″/β′/β (Mg_2Si) precipitation sequence. The TEM study supports the above analysis of precipitation in the Cu-free alloys: the STL sample of alloy A1 aged for three weeks at 170°C (see Figure 5.48a) clearly reveals precipitates. The 10% cold-worked alloy A1 aged for three weeks at 170°C also contains precipitates (see Figure 5.49a) and the SAD shown in Figure 5.49b indicates that possibly β' phase may be present. Thus, with respect to precipitation, the TEM observations, the hardness data and the DSC traces are consistent for the Cu-free alloys.

5.4.1.2 Precipitation in the Cu-containing alloys A4-A9

For the cold-worked samples of the Cu-containing alloys (alloys A4-A9), hardness testing reveals different levels of age hardening depending on alloy composition and cold-rolling reduction. For the solution-treated samples, all the Cu-containing alloys show substantial age hardening (see Figure 5.22d). DSC traces show that the precipitation hardening behaviors in these alloys are quite complex. Precipitation hardening might be due to the precipitation of β″/β′/β and/or S″/S′/S and/or GPB zones/co-clusters, and/or Q precipitation sequence depending on alloy composition, level of cold work and solutionising temperature.

According to the summarized DSC results in Table 5.8, for the STH samples of Cu-containing alloys (i.e. alloys A4-A9), the Q + β precipitation sequence may occur, i.e. the precipitation sequence of clusters/GPB zones → β″ + Q' → Q + β (Mg_2Si). This is similar to the precipitation sequence in an Al-Mg-Si-Cu alloy AA6111 [15] (see section 2.2.2.3 for details). The occurrence of the Q + β precipitation sequence in the STH samples of Cu-containing alloys may be explained as follows. In these samples, all Si or most Si tied up with the Mg_2Si particles will be redissolved at the higher solution temperature of 550°C. Hence both Si and Cu are available in the matrix, which makes the precipitation of the quaternary Q phase possible. The absence of the precipitation of S

phase may be due to the highly reduced dislocation density in the solution-treated samples as compared to the cold-worked samples. As the nucleation of S phase is facilitated by dislocations, the precipitation of S phase will be inhibited by the reduced dislocation density. At the same time, the presence of Si may further inhibit the precipitation of S phase, and facilitate the precipitation of Q phase. As both phases compete for Cu and Mg atoms, this could eliminate S phase formation altogether.

In the case of the STL samples of Cu-containing alloys, the precipitation is slightly different. For alloys with 3wt% Mg, i.e. alloys A6 and A9, most Si is tied up with Mg_2Si particles after solutionising at 500°C and no or very limited Si is available in the matrix. Therefore the S phase precipitation sequence should dominate (see Table 5.8). For the other Cu-containing alloys with lower Mg contents, some or most Si is available in the matrix after solutionising at 500°C, and hence both Si and Cu are available for precipitation. In that case the precipitation sequence of Q phase can be important (see Table 5.8).

For the cold-worked samples of the Cu-containing alloys, precipitation becomes even more complicated, as it may depend on both level of cold work and alloy composition. From the DSC analysis and Table 5.8, the following observations can be obtained. For cold-worked samples, both β and S precipitation sequences may occur in the Cu-containing alloys. The absence of either β or S precipitation sequence in some alloy/cold-rolling reduction combinations might be due to the effects being too small to be detected by DSC. This absence indicates that in addition to alloy composition, cold-rolling reduction or level of cold work has significant effects on precipitation in the alloys. For 90% reduction, the S precipitation sequence dominates in all the Cu-containing alloys, whilst the β precipitation sequence becomes important with decreasing cold-rolling reduction. For a given cold-rolling reduction, S precipitation sequence becomes dominant with increasing Cu and Mg contents. In other words, the following conclusions can be drawn: during ageing, high reduction (90%) facilitates the S precipitation sequence, whilst lower reduction (40% or 10%) promotes the β precipitation sequence. The enhanced S precipitation at higher cold-rolling reduction may be due to the increased dislocation density, which promotes the precipitation of S phase. The reason that β precipitation sequence becomes dominant with decreasing Mg content may be due to a larger amount of Si being available for precipitation in alloys with lower Mg.

As shown in Figure 5.51, for alloy A4, S phase and possibly another unidentified phase (possibly β′ phase) were present in a 10% cold-worked sample aged at 220°C for one week. In addition, as illustrated in Figure 5.53 and Figure 5.54, for alloys A7 and A8, S phase was identified in the 10% cold-worked samples aged for three weeks at 170°C. For alloy A9, S phase was also detected in a 10% cold-worked sample aged for five days at 170°C. These TEM observations are generally consistent with those from DSC analysis discussed above.

5.4.2 The influence of deformation on precipitation and recovery

For age hardening alloys both recovery and precipitation can occur in the cold-worked samples, and their interactions may cause the hardness/strength of the alloys to increase (precipitation hardening effect) or reduce (recovery effect). Two possible sequences of events of recovery-precipitation interactions [23] need to be considered: i) precipitation takes place in fully recovered alloys, and no interactions may occur; ii) precipitation takes place during recovery. In the latter case, interactions may occur. The driving force for recovery is the stored energy of deformation. The higher the deformation, the higher the driving force for recovery. Deformation not only influences recovery, but also affects precipitation because heterogeneous precipitation often occurs on dislocations in the matrix. Hence interactions between precipitation and recovery can occur during ageing. One possible interaction lies in that recovery can delay the progress of precipitation by lowering the number of nucleation sites (i.e. dislocations) available for precipitation [24]. A further possible interaction can occur if the precipitation of fine particles can pin segments of the dislocation network and therefore retards recovery. On the other hand, recovery can be facilitated by precipitation through draining the solute content because alloying elements in solution are thought to retard the progress of recovery through solute-drag effects on dislocation mobility [24]. So in the following, the influence of deformation on recovery and precipitation during ageing for the cold-worked samples of age hardening alloys studied in this project (i.e., alloys A1 and A4-A9) will be briefly discussed.

As shown in section 5.2.1, for alloys with the highest level of deformation, e.g. 90% cold-rolling reduction, the hardness increases immediately on ageing and it reaches a peak at about 2 hours. Then it starts to drop very quickly and dramatically (see Figure 5.22a). However, the hardening effect represented by the maximum hardness increment is very weak. Similar trends with slightly stronger hardening effect were observed for alloys with

medium deformation, e.g. 40% cold-rolling reduction. For medium deformation, the increase in hardness is slower, and the hardness also reduces relatively slowly after it reaches a peak at about four hours (see Figure 5.22b). For alloys with low deformation, e.g. 10% cold-rolling reduction, as shown in Figure 5.22c, the hardness increases very slowly, and it takes about five days for the Cu-containing alloys to reach a peak (about 16 hours for alloy A1). Subsequently hardness decreases very slowly too. However, the hardening effect becomes much stronger than that for 40% and 90% reductions.

The above observations can be discussed in terms of the influences of deformation on precipitation and recovery. Firstly, the reduced time to peak hardness with increasing cold-rolling reduction suggests that deformation facilitates precipitation, i.e. the kinetics of precipitation is enhanced at higher deformation. Secondly, the reduced hardening effect with increasing cold-rolling reduction indicates that the driving force for recovery is enhanced with increasing deformation. The decreased hardness drop after peak hardness with decreasing cold-rolling reduction has a more convoluted origin, which may be explained as follows. Severe deformation provides high initial driving force for recovery and more heterogeneous nucleation sites (i.e. dislocations) for precipitation as well. For 90% reduction, since a large amount of dislocations caused by heavy deformation act as nucleation sites for heterogeneous precipitation, precipitation may be facilitated at the early stage of ageing (within 1-3 hours) and occur very fast, and thus it may suppress recovery, which then dominates further ageing after peak hardness. Therefore, for 90% reduction, the rapid and dramatic drop in hardness after peak hardness is likely due to rapid recovery and the coarsening of precipitates. For 10% reduction, due to the lowest driving force for recovery, recovery may be retarded by precipitation, which is the dominant mechanism during ageing. The slow decrease in hardness after peak hardness is likely mainly due to the coarsening of precipitates. Effects for 40% reduction are intermediate between those for 90% and 10% reductions.

5.4.3 Solution strengthening due to Mg and Cu

Mg and Cu can strengthen aluminium alloys by solid-solution strengthening, which is proved by the yield strength data in this study (see Figure 5.41 and Figure 5.42). The hardness also increases with increasing Mg and Cu contents as shown in Figure 5.22. As shown in Figure 5.41 and Figure 5.42, the slope in the plots of the yield strength vs. Mg/Cu content increases with increasing cold-rolling reduction, which indicates that the

amount of strengthening due to Mg and Cu contents increases with increasing cold-rolling reduction. Hence, the substantial increase in hardness due to Mg and Cu additions (see Figure 5.22a, b and c) is not only attributed to the enhanced solid solution strengthening, but also to the increased work hardening resulting from Mg and Cu additions.

5.5 Concluding remarks

In this chapter, the microstructure of cold-worked samples which includes intermetallic particles and their distribution, grain structure and texture was studied and the yield strengths of cold-worked samples and their evolution during isothermal ageing were measured. The results of microstructure studies from SEM/EDS, thermodynamic calculations, TEM and DSC will be used to construct a precipitation model, which will be presented in Chapter 6. The yield strength data will be used to determine a work hardening model. A yield strength model will be devised to predict the yield strength evolution of cold-worked samples during isothermal ageing. The yield strength model will be calibrated and tested using the yield strength data presented in this chapter.

Work hardening can be studied using tensile testing data. Work hardening rate will be derived from stress-strain data and analysis of work hardening rate as functions of level of cold work, Mg and Cu contents and ageing time will be further conducted. Finally existing work hardening models will be utilized to explain main trends observed in experiments. These will be discussed in Chapter 7.

Figures

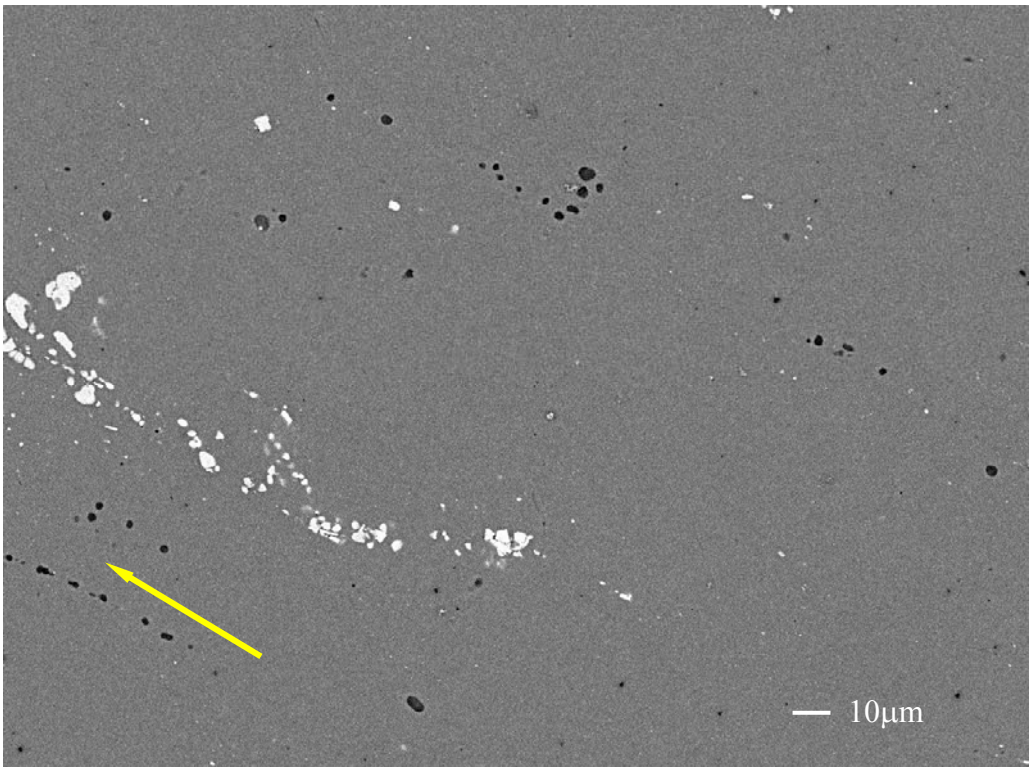

Figure 5.1 SEM backscattered electron image (BEI) of LT polished section of 10% cold-worked alloy A9 (Arrow indicates the rolling direction)

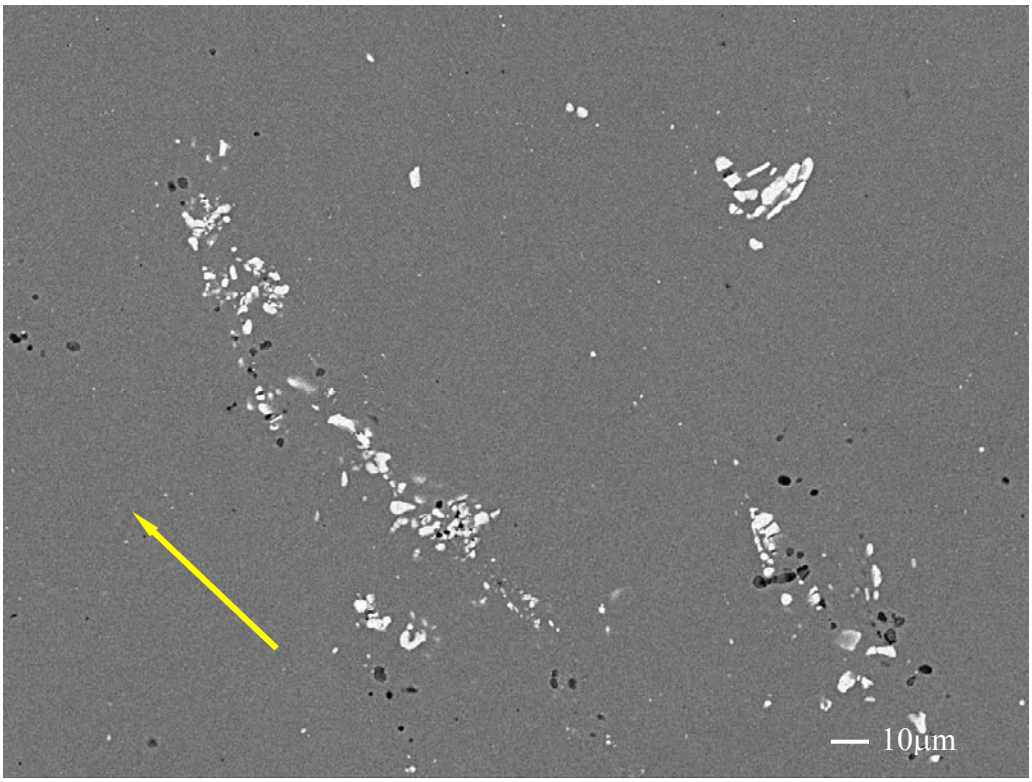

Figure 5.2 SEM backscattered electron image (BEI) of LT polished section of 40% cold-worked alloy A9 (Arrow indicates the rolling direction)

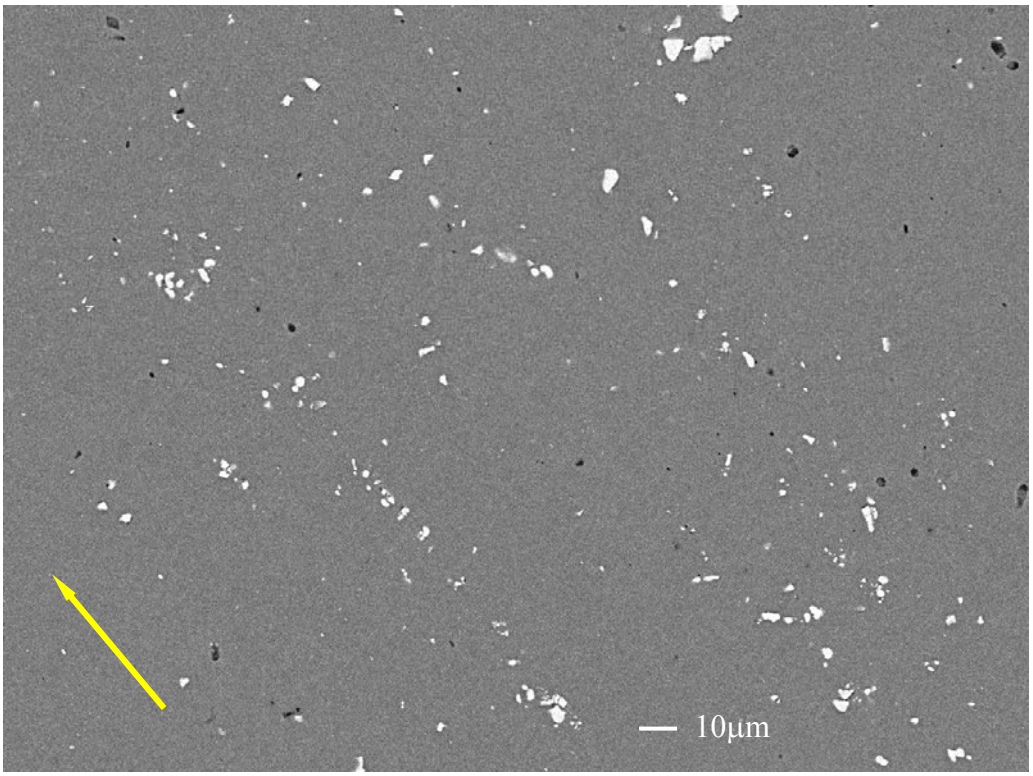

Figure 5.3 SEM backscattered electron image (BEI) of LT polished section of 90% cold-worked alloy A9 (Arrow indicates the rolling direction)

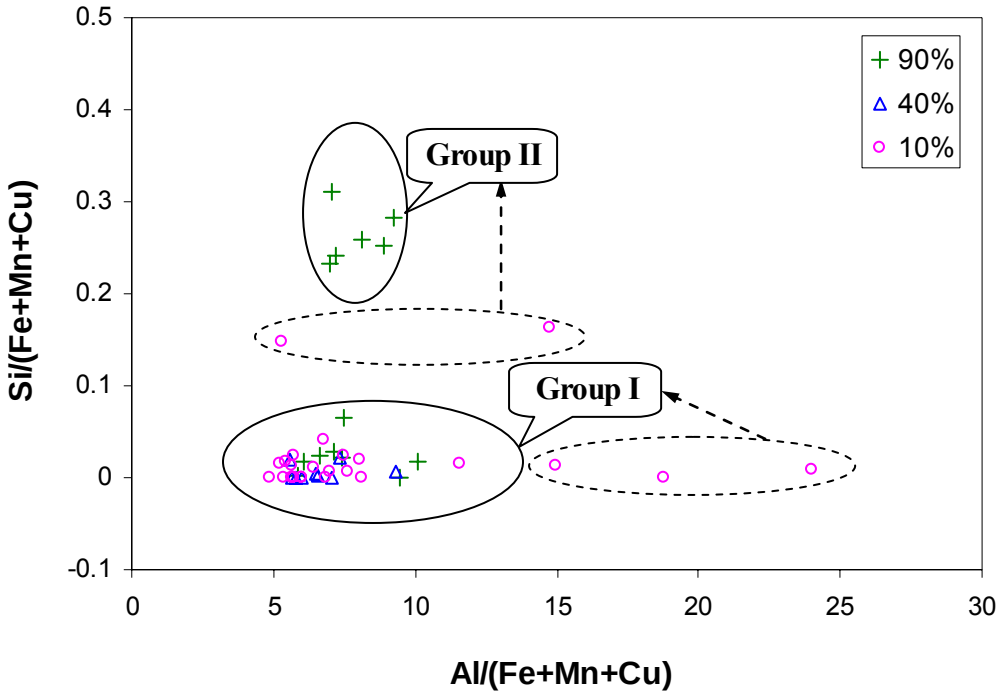

Figure 5.4 The Si:(Fe+Mn+Cu) ratio vs. the Al:(Fe+Mn+Cu) ratio for the bright particles in alloy A9

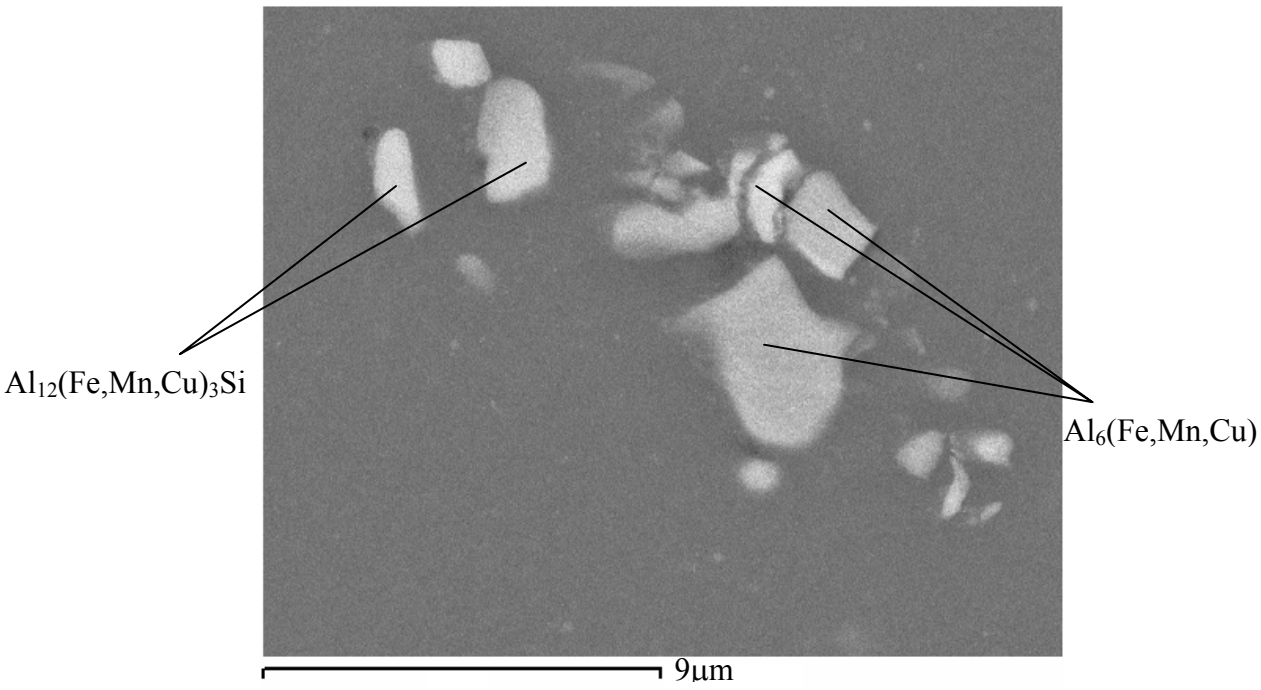

Figure 5.5 SEM micrograph of the bright particles identified in the cold-rolled alloy A9 (BEI mode)

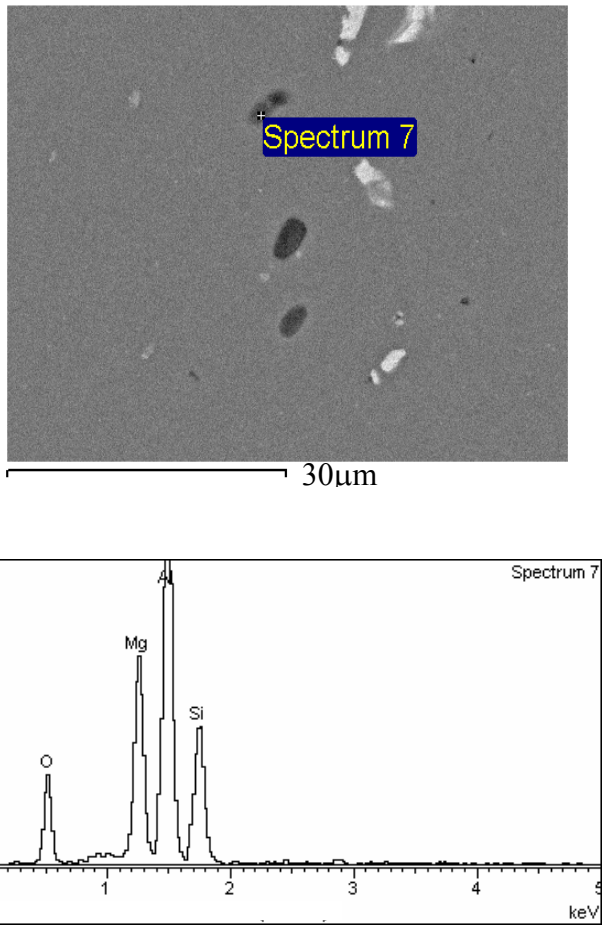

Figure 5.6 SEM BEI image and EDS spectrum obtained from indicated position (alloy A9). The spectrum indicates that the particle is Mg_2Si

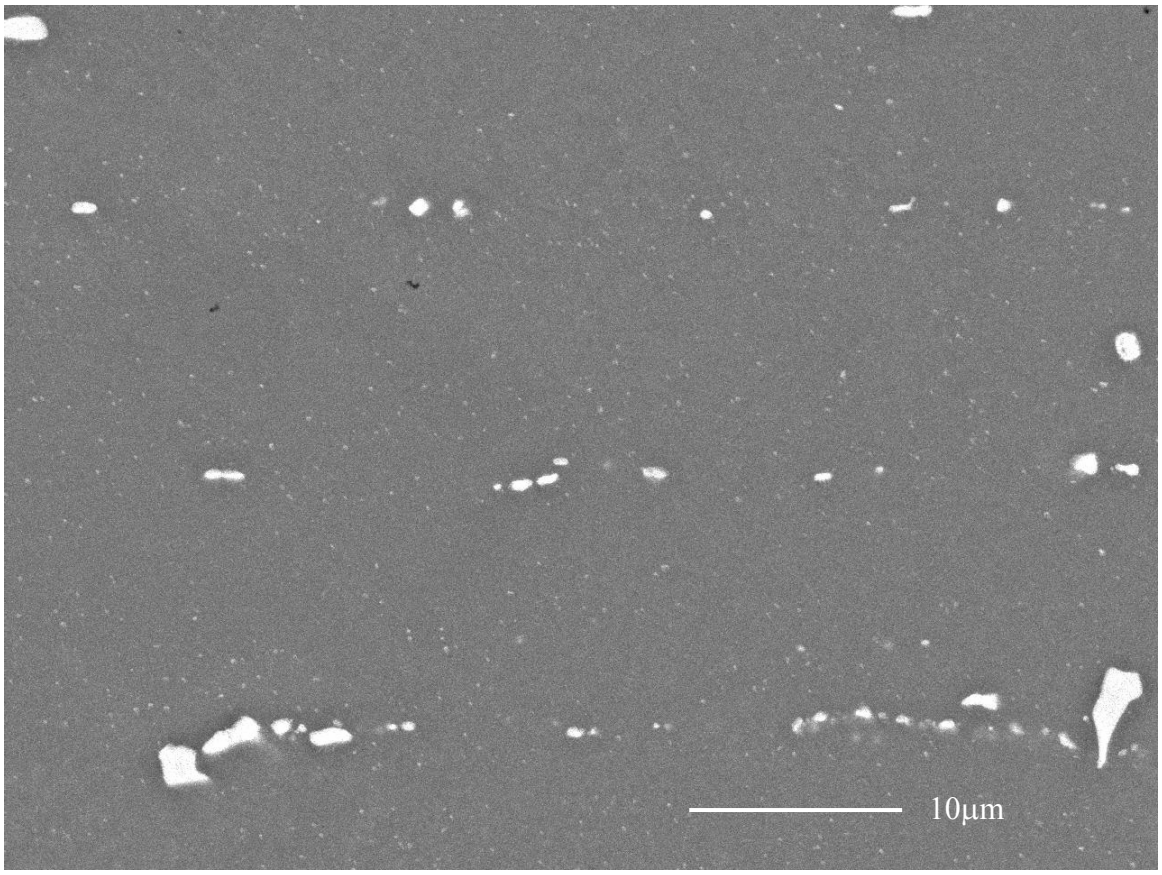

Figure 5.7 Overview of intermetallics distribution in alloy A4 (BEI mode)

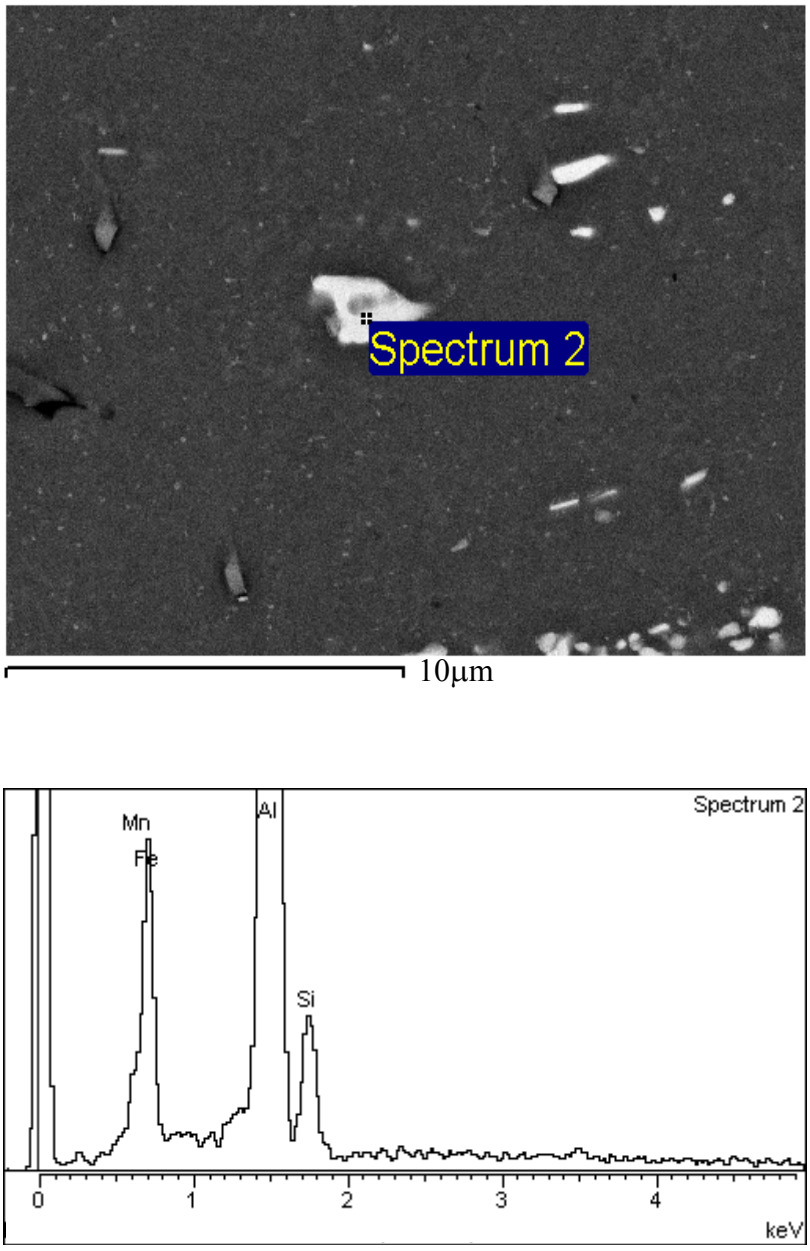

Figure 5.8 SEM BEI image and EDS spectrum obtained from indicated position (alloy A1). The spectrum indicates that the particle is $Al_{12}(Fe,Mn)_3Si$

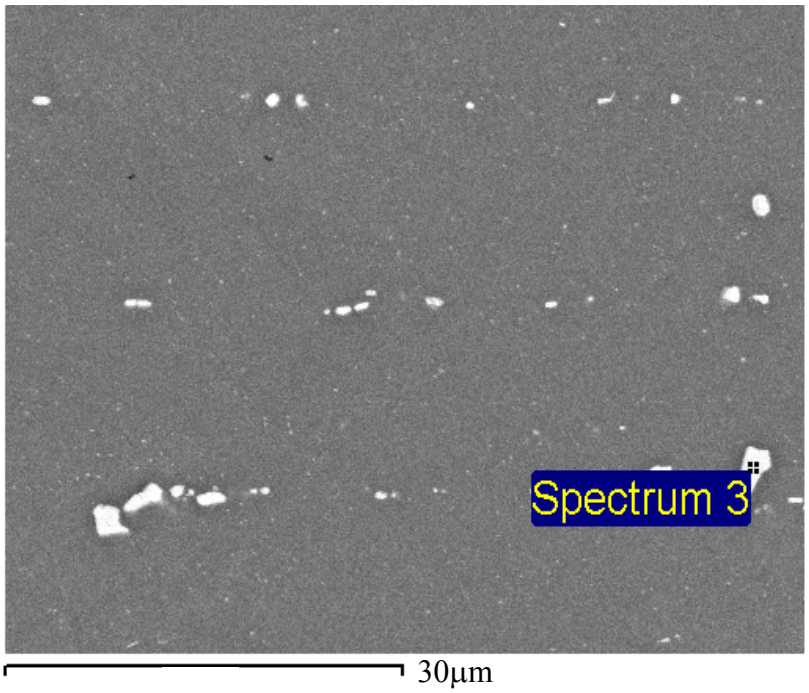

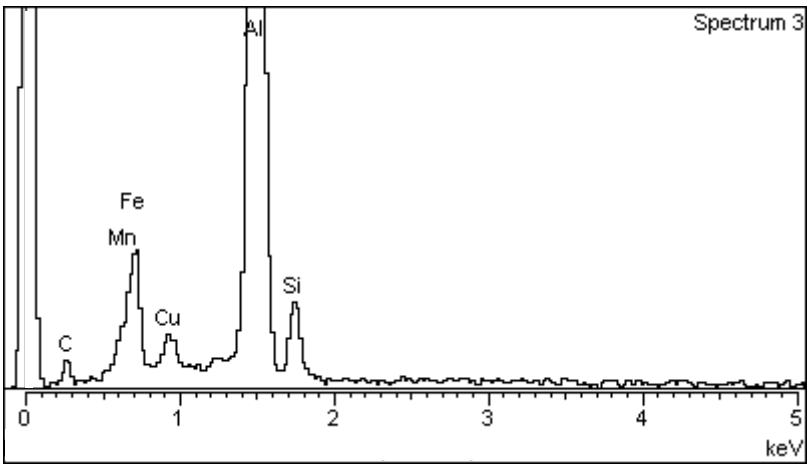

Figure 5.9 SEM BEI image and EDS spectrum obtained from indicated position (alloy A4). The spectrum indicates that the particle is $Al_{12}(Fe,Mn,Cu)_3Si$

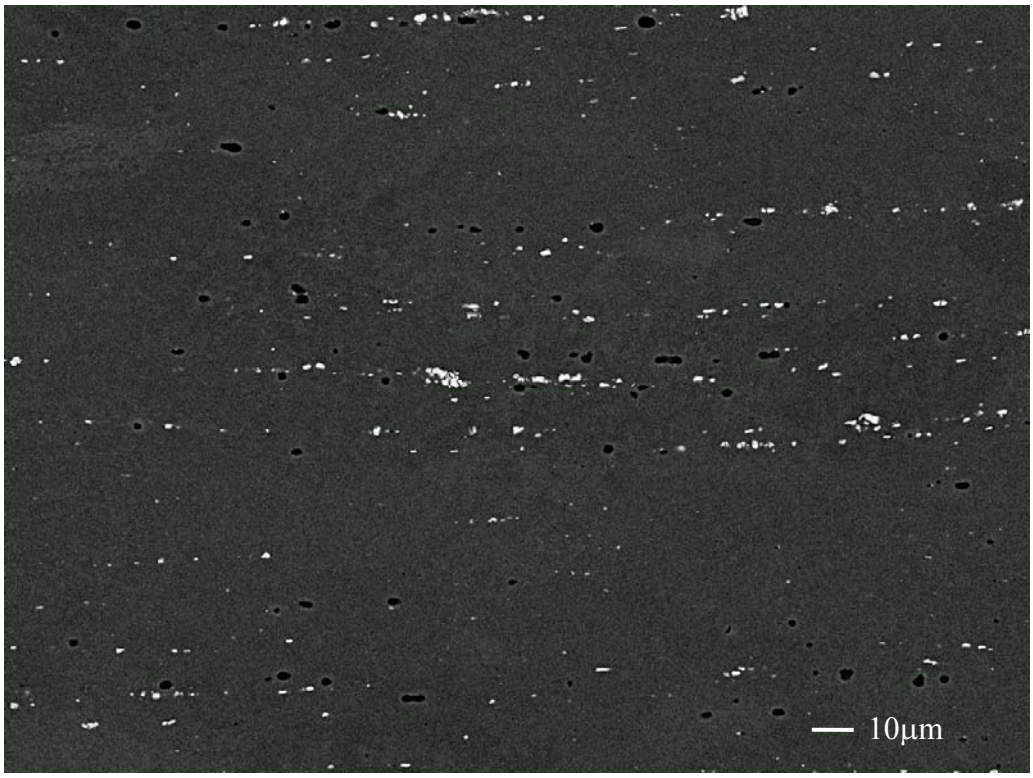

Figure 5.10 Overview of intermetallics distribution in alloy A3 (BEI mode)

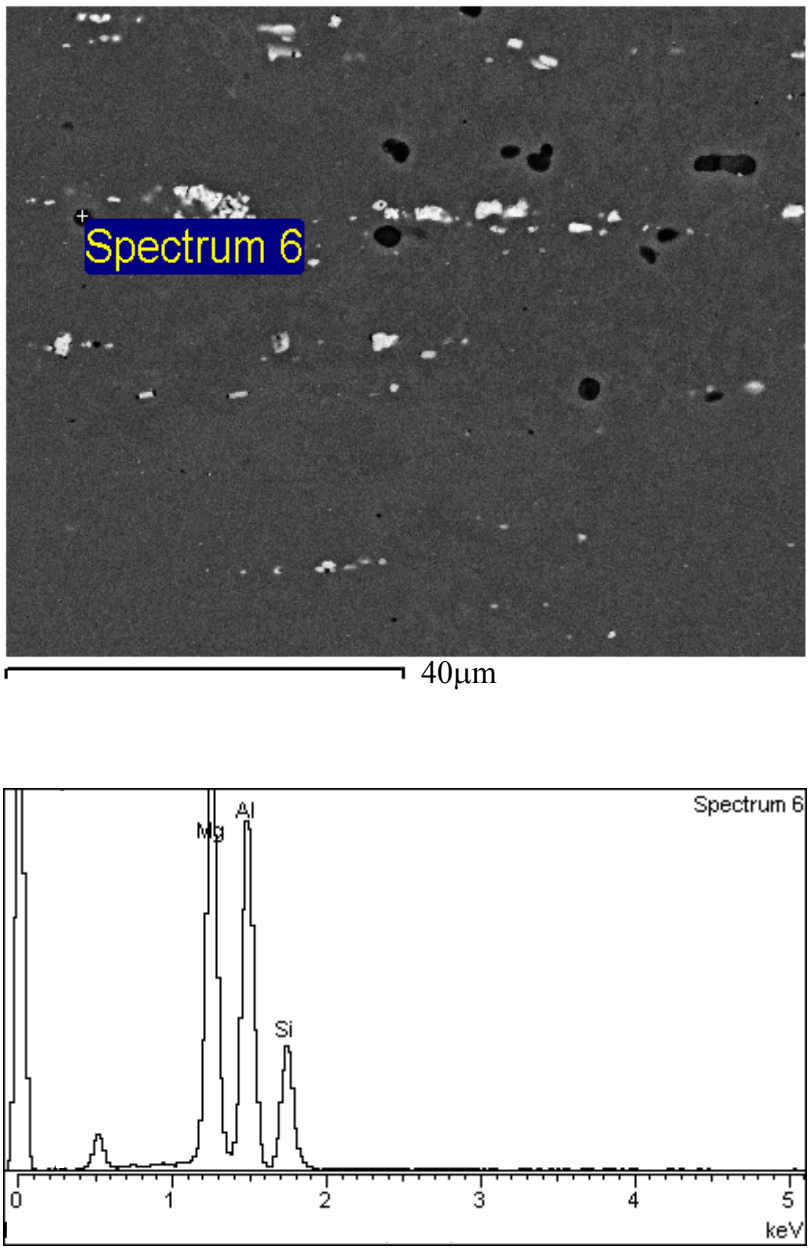

Figure 5.11 SEM BEI image and EDS spectrum obtained from indicated position (alloy A3). The spectrum indicates that the particle is Mg_2Si

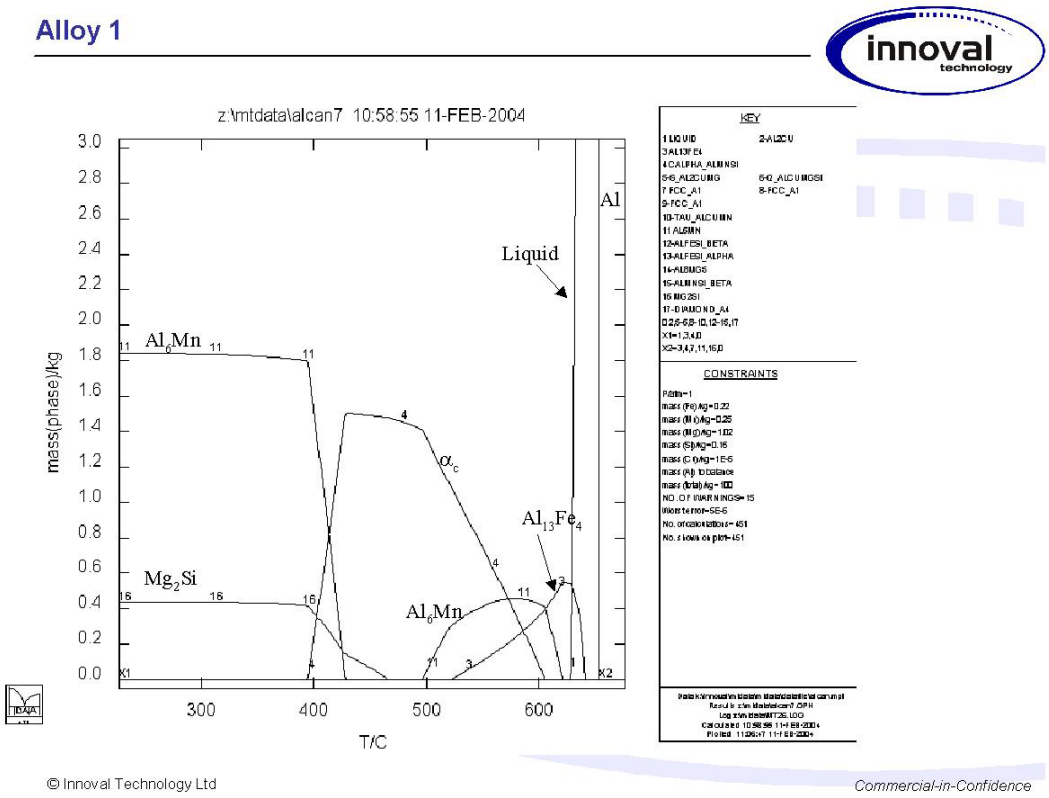

Figure 5.12 MTDATA multiphase calculation results for alloy A1 [7]

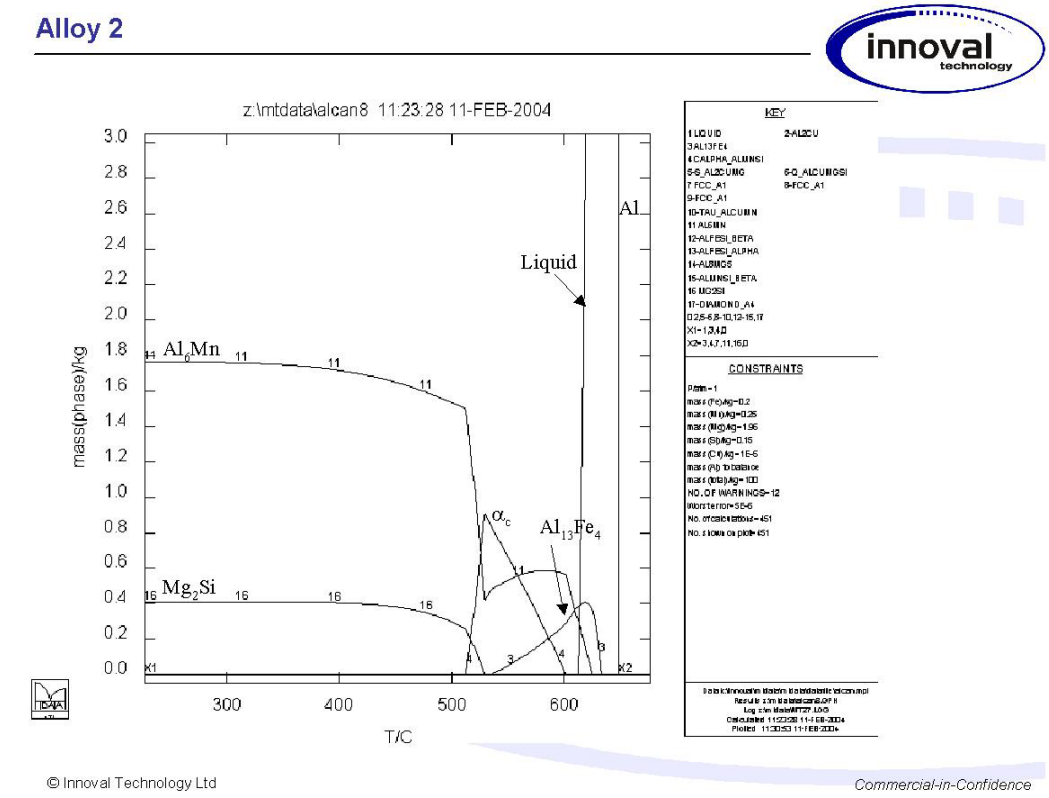

Figure 5.13 MTDATA multiphase calculation results for alloy A2 [7]

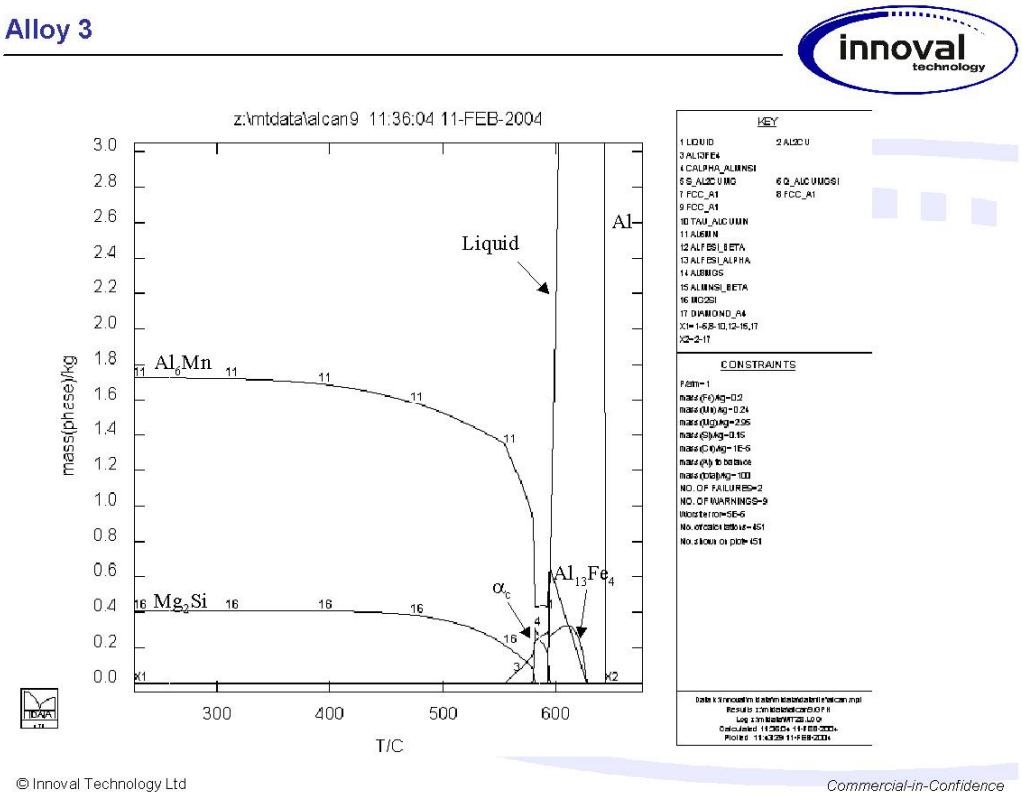

Figure 5.14 MTDATA multiphase calculation results for alloy A3 [7]

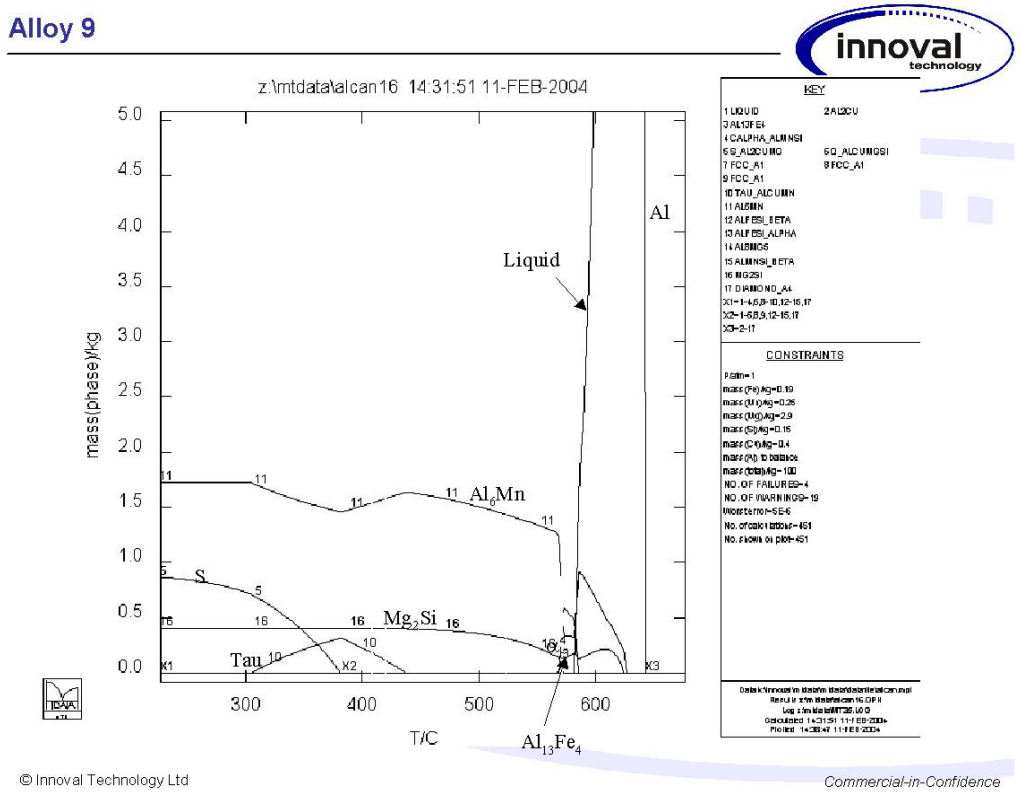

Figure 5.15 MTDATA multiphase calculation results for alloy A9 [7]

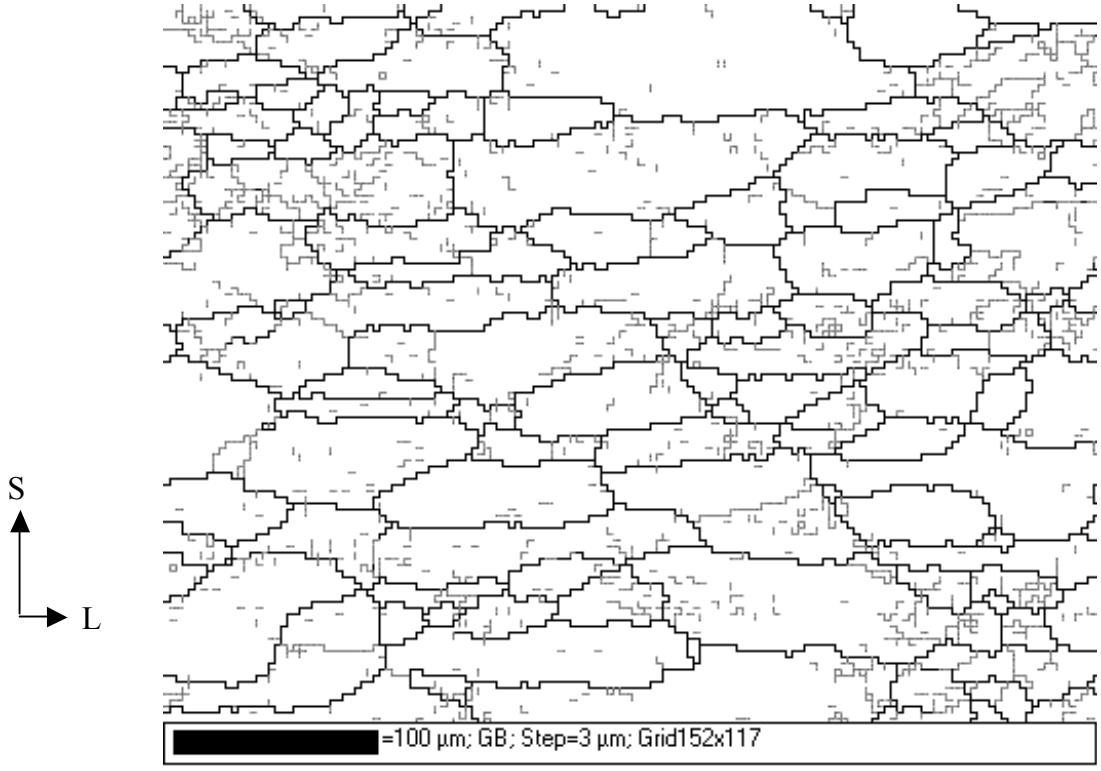

Figure 5.16 Grain boundary map for alloy A9 with 10% reduction (dark lines: >12°, grey lines: 2-12°)

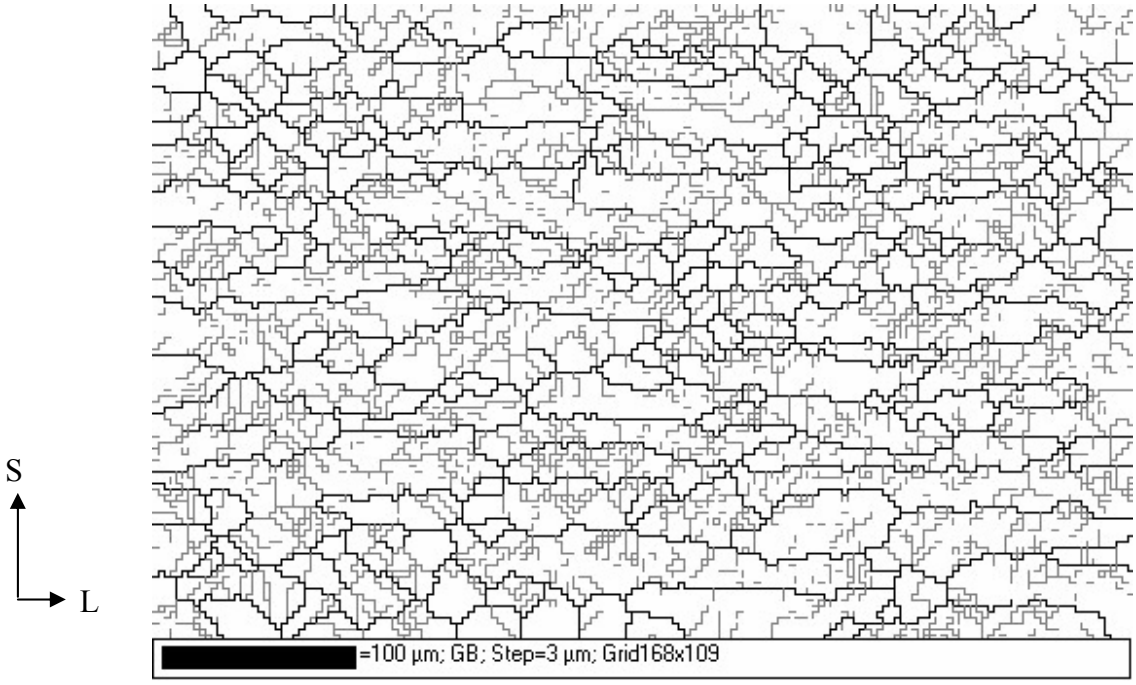

Figure 5.17 Grain boundary map for alloy A9 with 40% reduction (dark lines: >12°, grey lines: 2-12°)

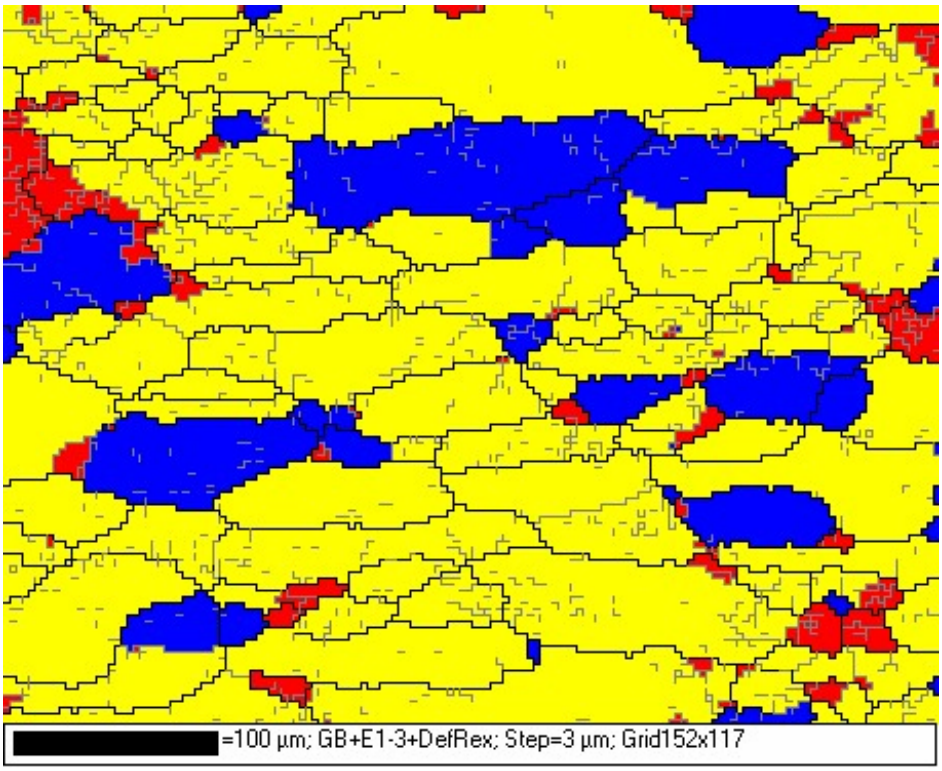

Figure 5.18 Deformed/recrystallised grain map for alloy A9 with 10% reduction (Blue: fully recrystallised, Red: deformed, Yellow: substructure)

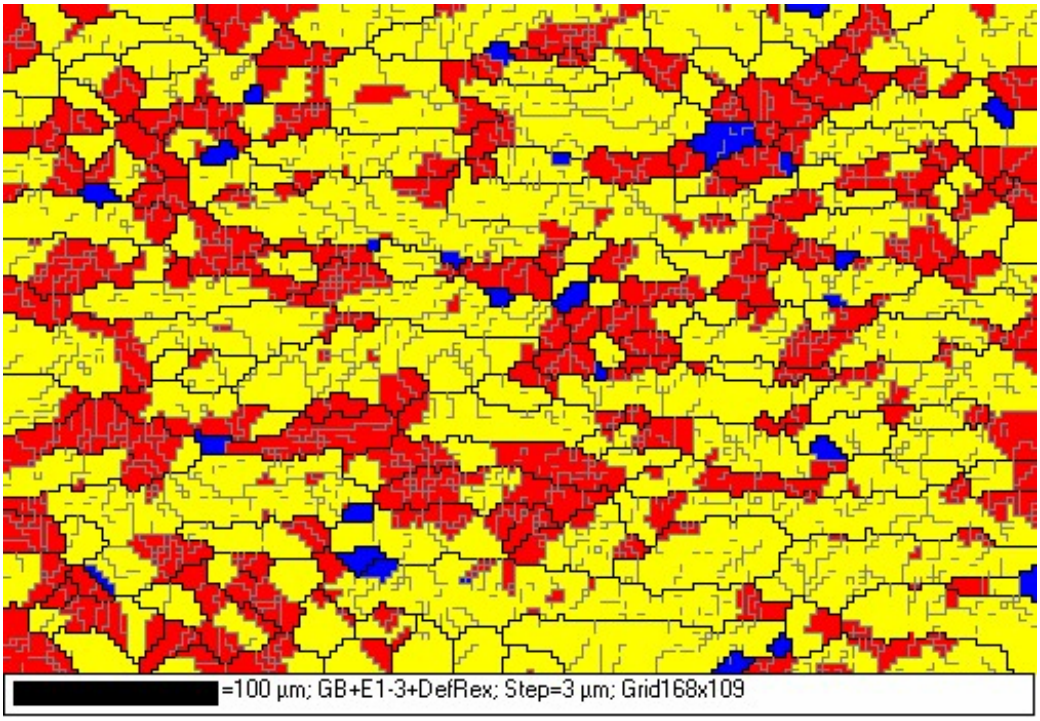

Figure 5.19 Deformed/recrystallised grain map for alloy A9 with 40% reduction (Blue: fully recrystallised, Red: deformed, Yellow: substructure)

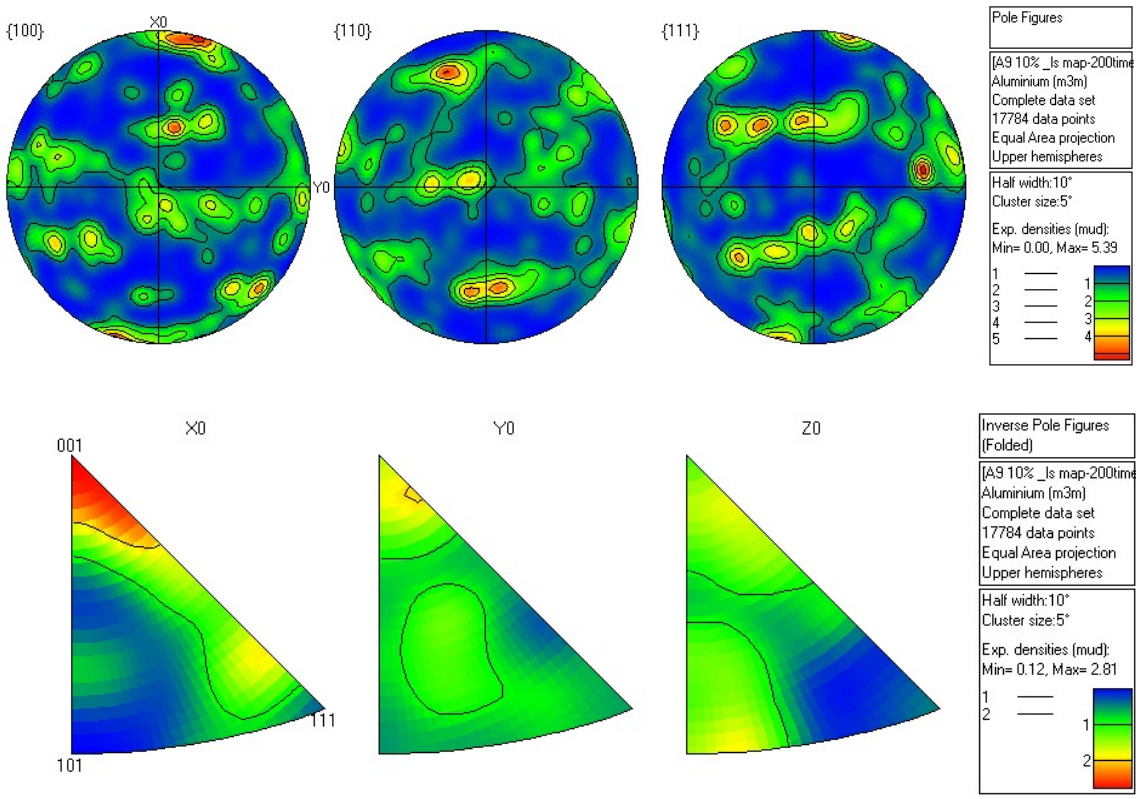

Figure 5.20 Pole figures and inverse pole figures for alloy A9 with 10% reduction

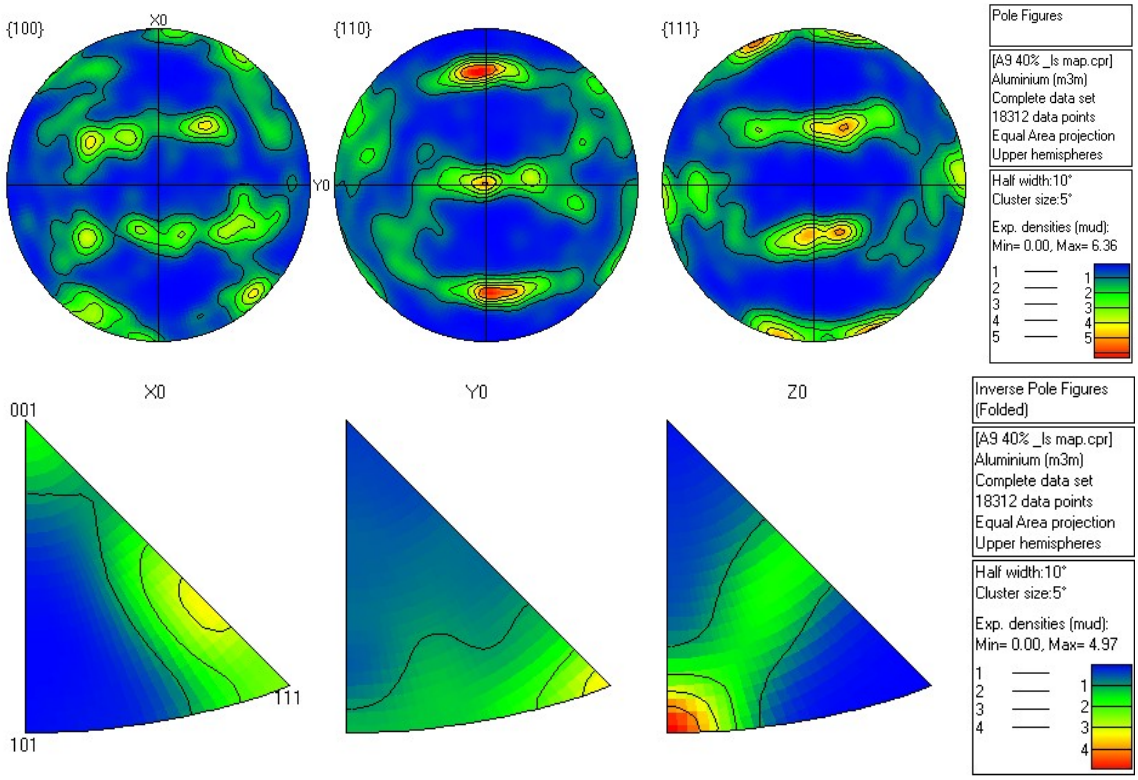

Figure 5.21 Pole figures and inverse pole figures for alloy A9 with 40% reduction

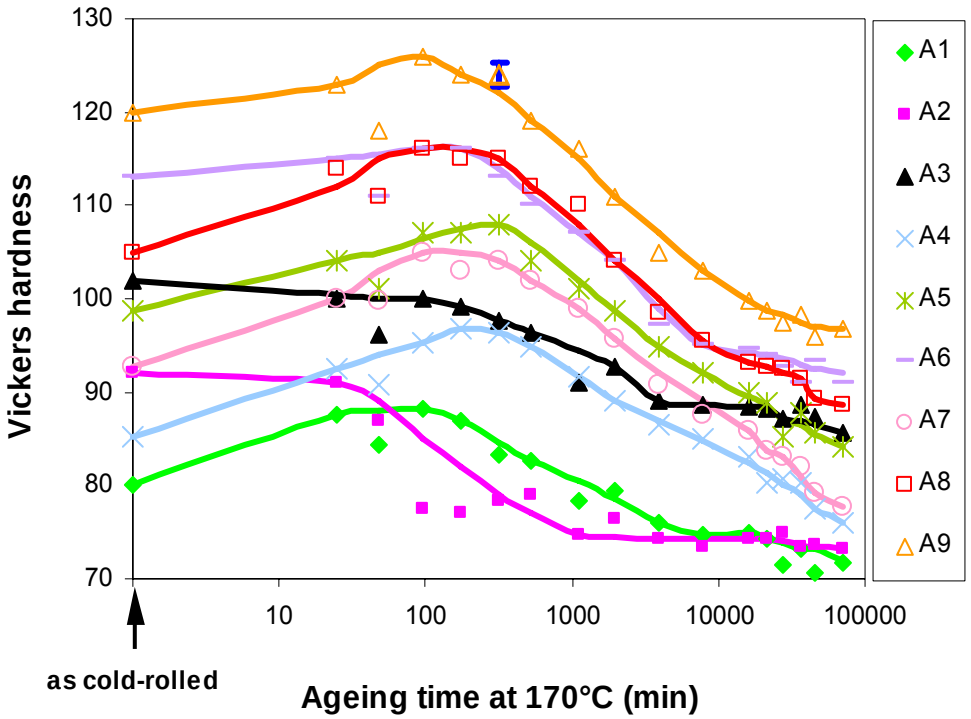
130
120
110
100
90
80
70
Vickers hardness
10
100
1000
10000
100000
as cold-rolled
Ageing time at 170°C (min)
A1
A2
A3
A4
A5
A6
A7
A8
A9

a.

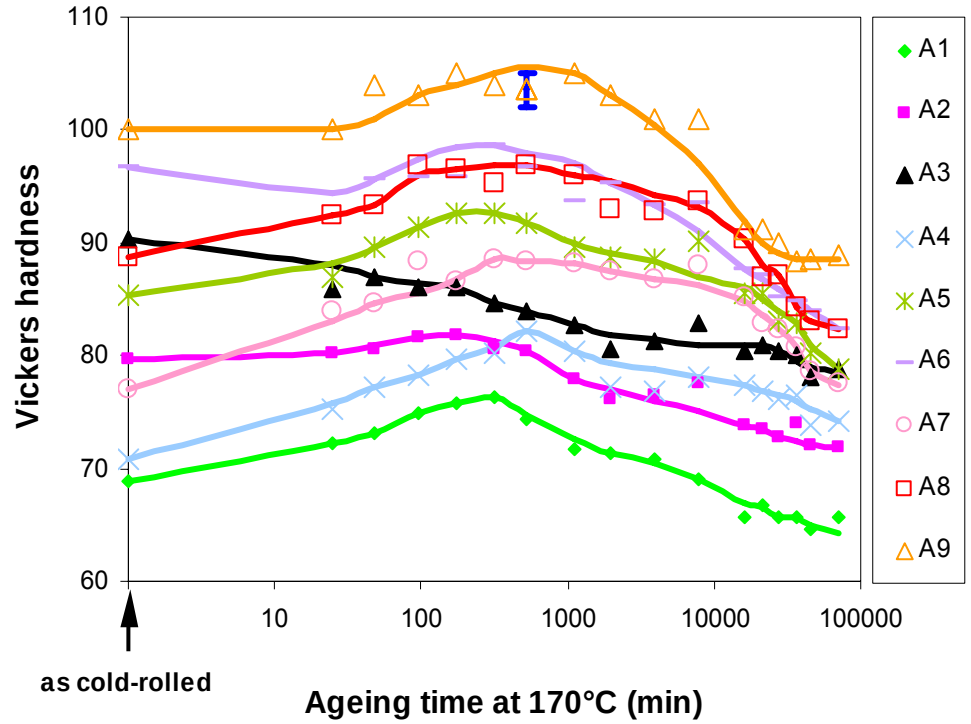
110
100
90
80
70
60
Vickers hardness
10
100
1000
10000
100000
as cold-rolled
Ageing time at 170°C (min)
A1
A2
A3
A4
A5
A6
A7
A8
A9

b.

c.

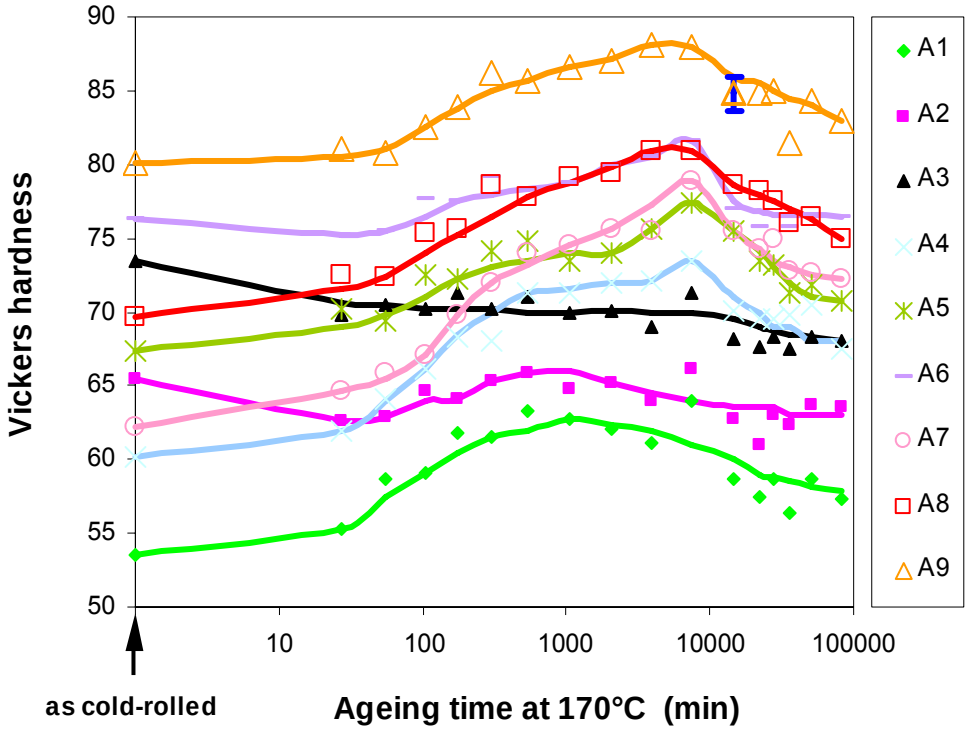

d.

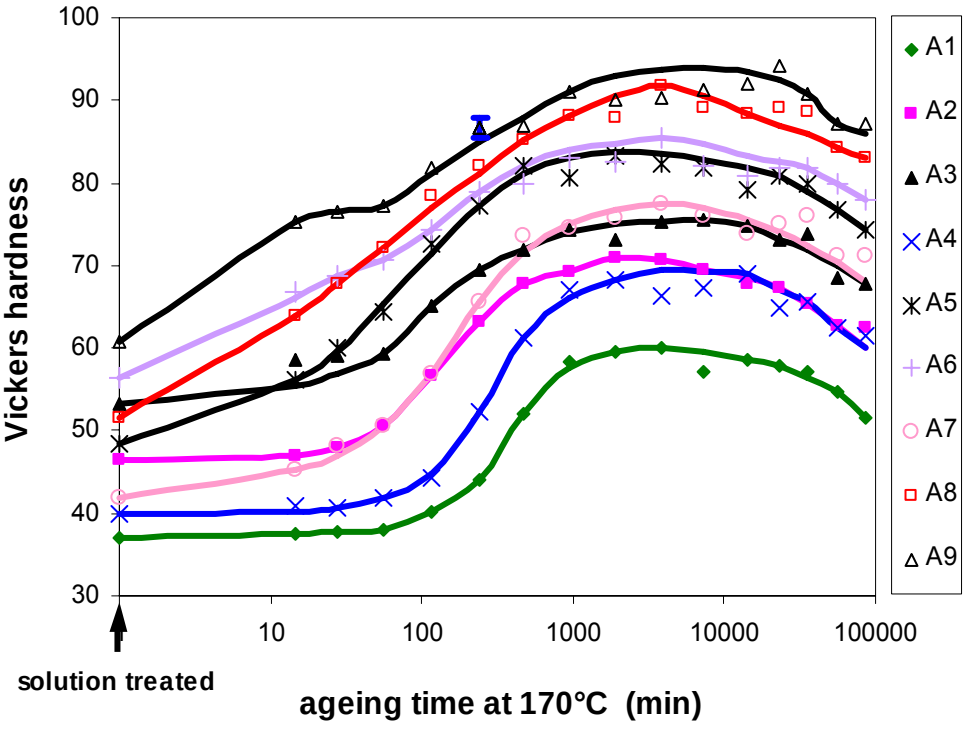

Figure 5.22 Hardness during isothermal ageing at 170°C: a. cold-worked samples with 90% reduction; b. cold-worked samples with 40% reduction; c. cold-worked samples with 10% reduction; d. solution-treated samples solutionised at 550°C for 30 minutes

a.

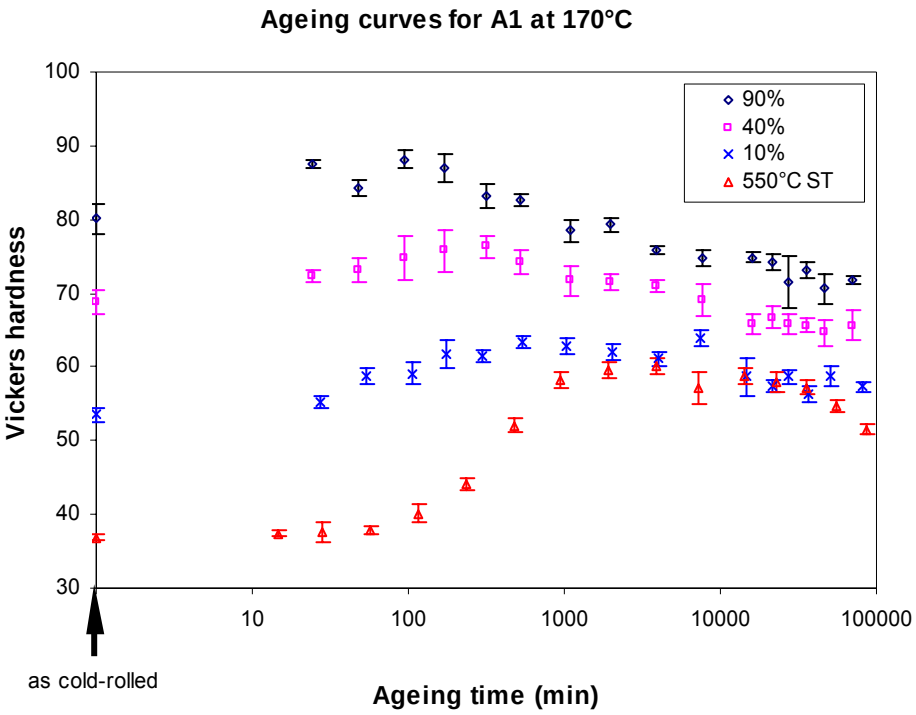
Ageing curves for A1 at 170°C
Vickers hardness
Ageing time (min)
90%
40%
10%
550°C ST
as cold-rolled
100
90
80
70
60
50
40
30
10
100
1000
10000
100000

b.

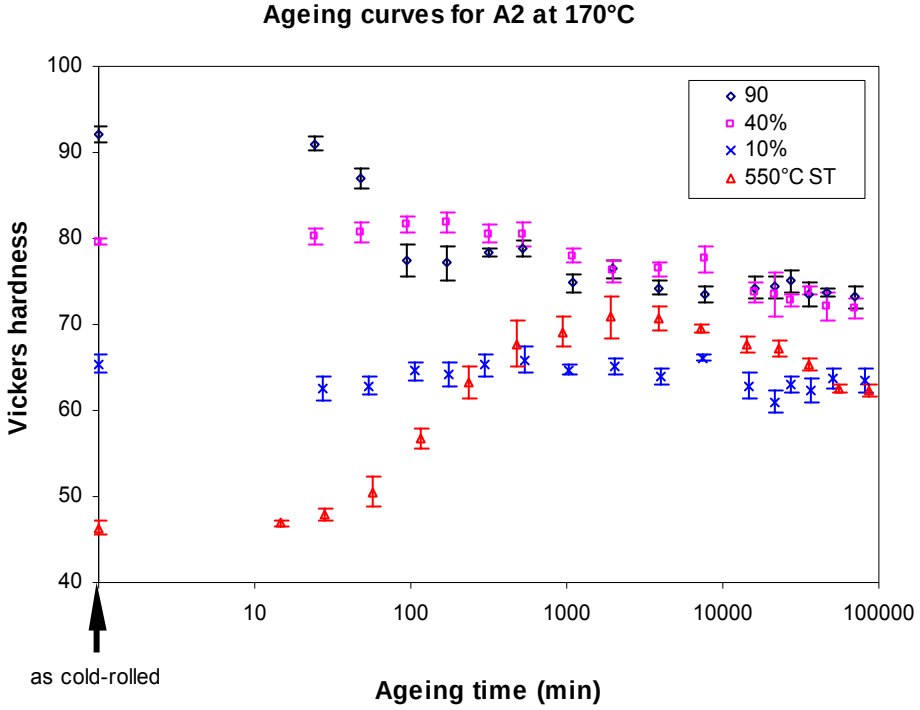
Ageing curves for A2 at 170°C
Vickers hardness
Ageing time (min)
90
40%
10%
550°C ST
as cold-rolled
100
90
80
70
60
50
40
10
100
1000
10000
100000

c.

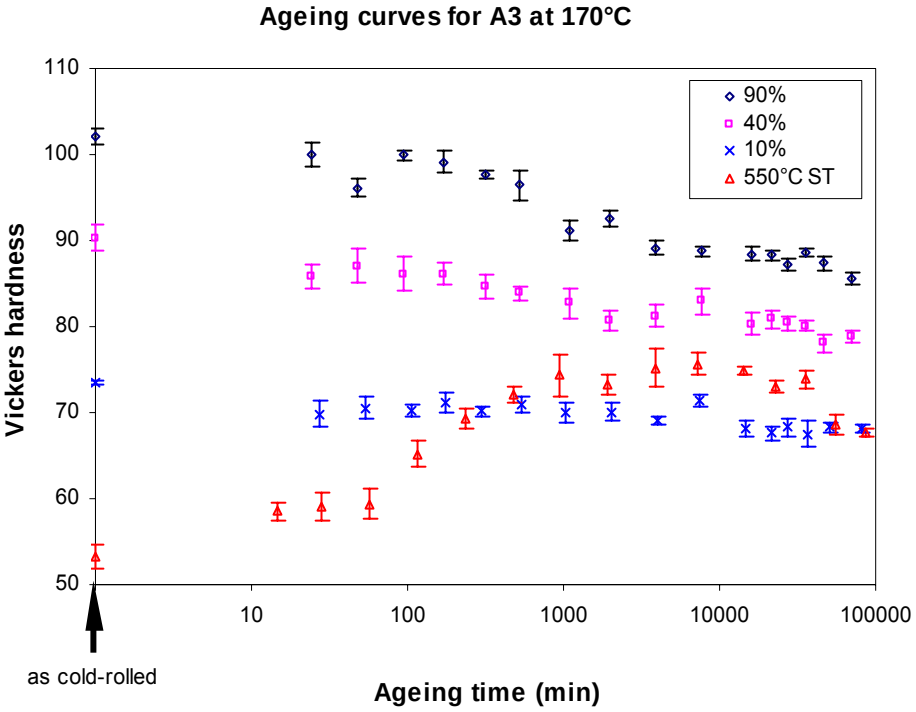
Ageing curves for A3 at 170°C
Vickers hardness
110
100
90
80
70
60
50
90%
40%
10%
550°C ST
10
100
1000
10000
100000
as cold-rolled
Ageing time (min)

d.

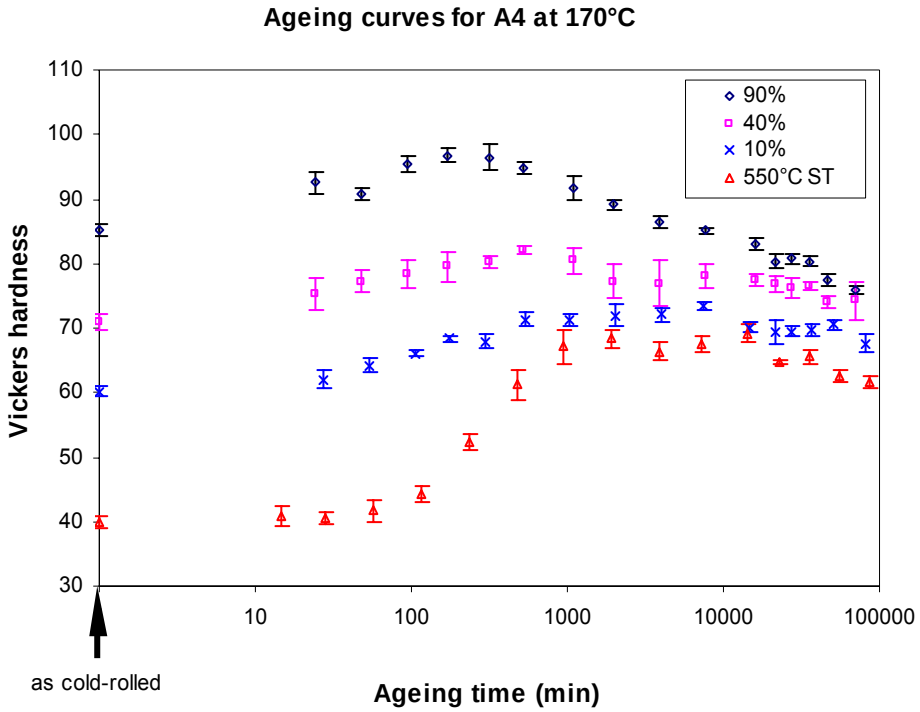
Ageing curves for A4 at 170°C
Vickers hardness
110
100
90
80
70
60
50
40
30
90%
40%
10%
550°C ST
10
100
1000
10000
100000
as cold-rolled
Ageing time (min)

e.

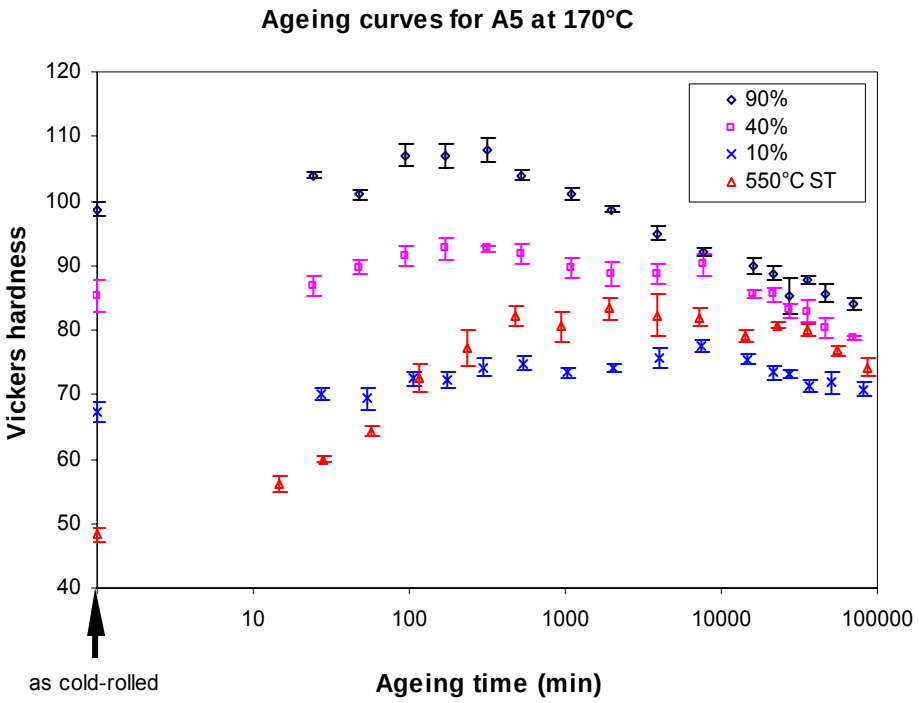
Ageing curves for A5 at 170°C
Vickers hardness
120
110
100
90
80
70
60
50
40
90%
40%
10%
550°C ST
as cold-rolled
10
100
1000
10000
100000
Ageing time (min)

f.

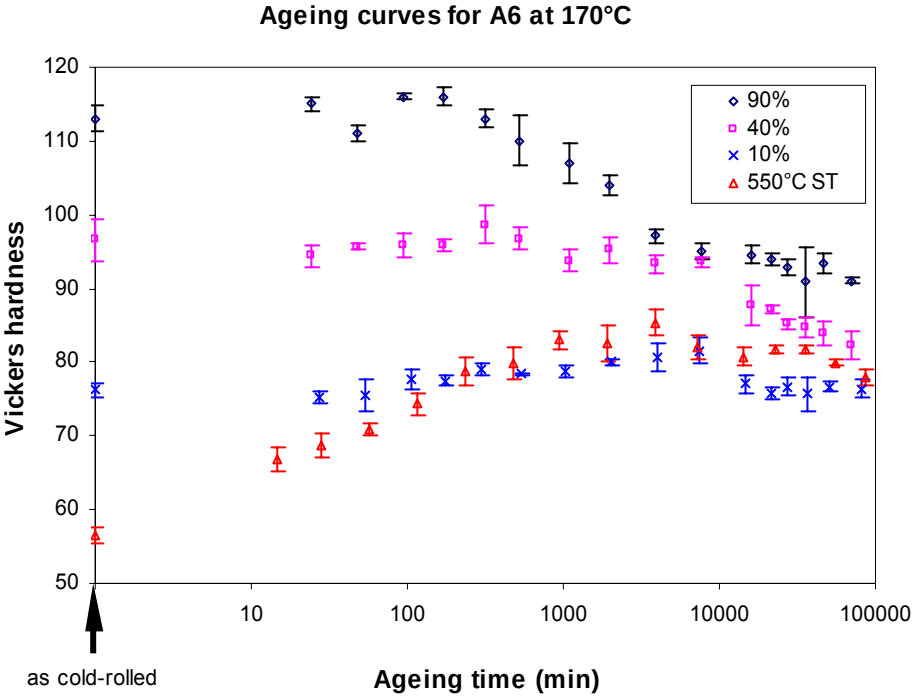
Ageing curves for A6 at 170°C
Vickers hardness
120
110
100
90
80
70
60
50
90%
40%
10%
550°C ST
as cold-rolled
10
100
1000
10000
100000
Ageing time (min)

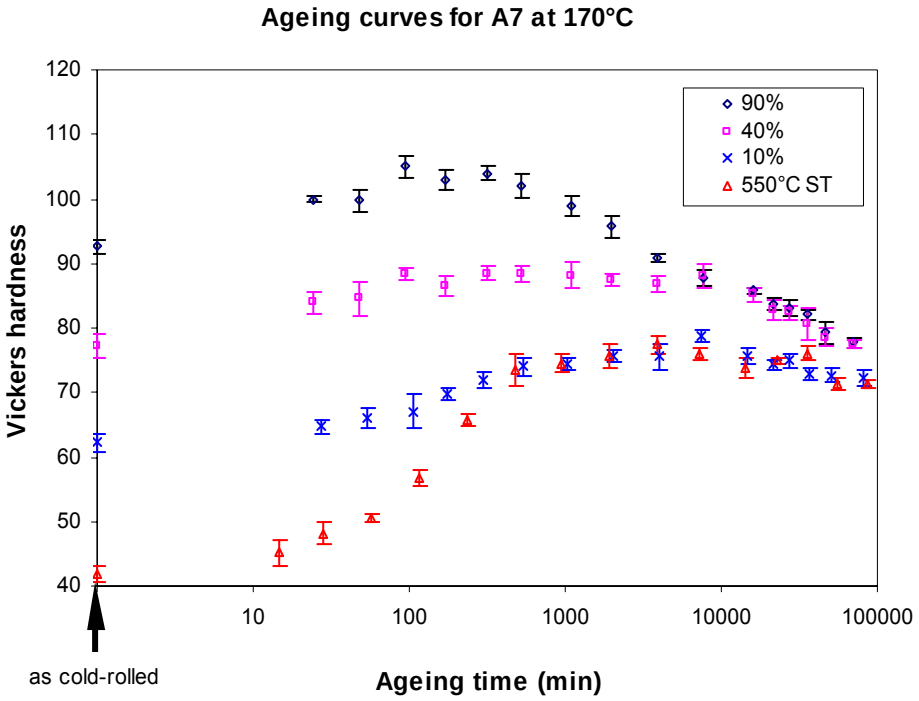
Ageing curves for A7 at 170°C
Vickers hardness
Ageing time (min)
90%
40%
10%
550°C ST
as cold-rolled
120
110
100
90
80
70
60
50
40
10
100
1000
10000
100000

g.

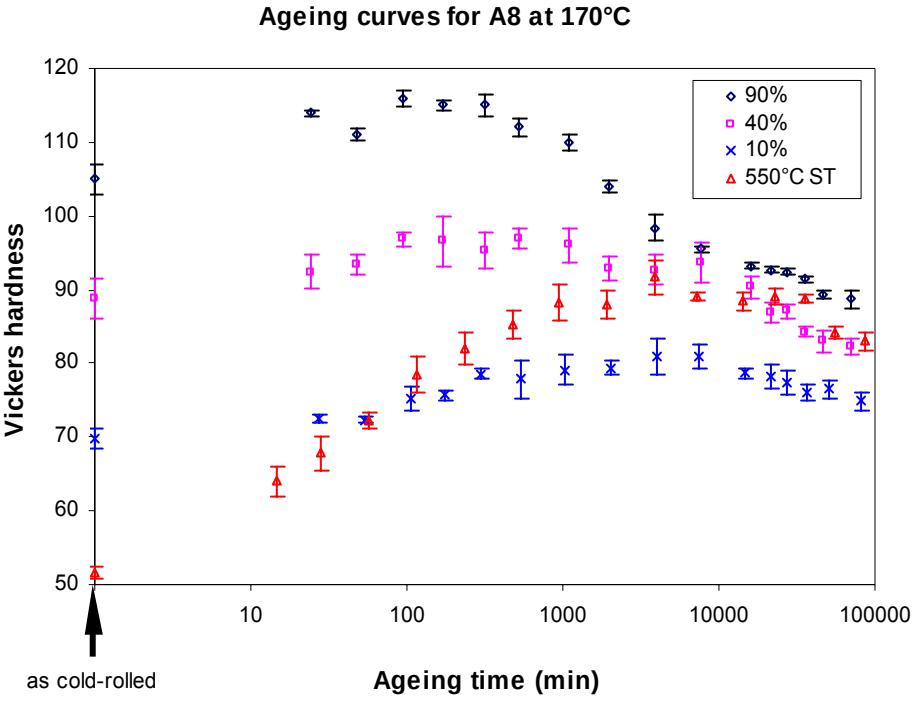
Ageing curves for A8 at 170°C
Vickers hardness
Ageing time (min)
90%
40%
10%
550°C ST
as cold-rolled
120
110
100
90
80
70
60
50
10
100
1000
10000
100000

h.

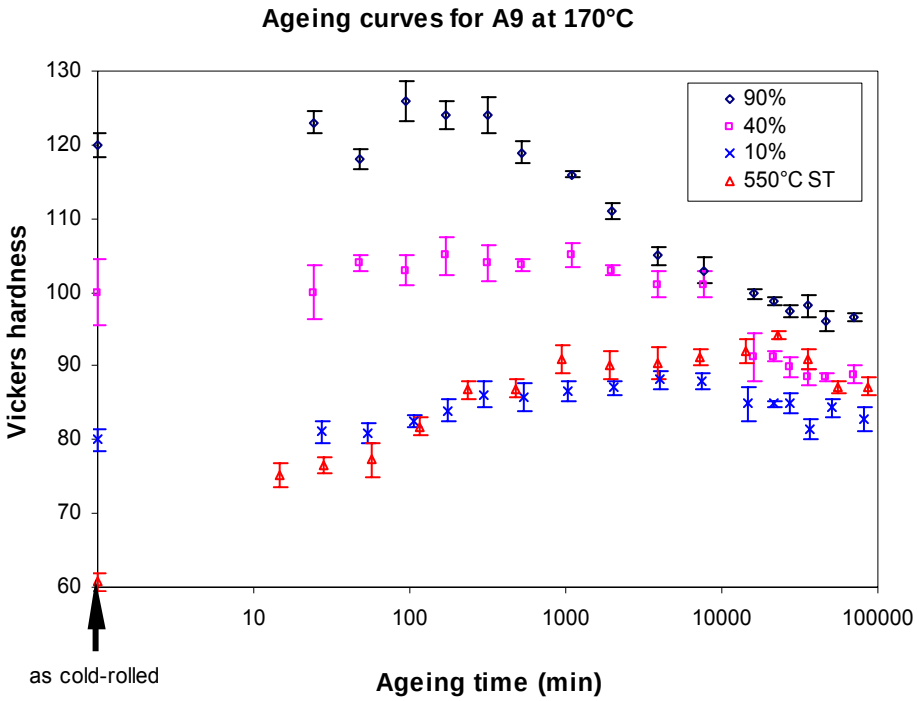

i.

Figure 5.23 Hardness during isothermal ageing at 170°C: a. A1, b. A2, c. A3, d. A4, e. A5, f. A6, g. A7, h. A8, i. A9 (In the figure, 550°C ST stands for samples solution treated at 550°C for 30 minutes and 10%, 40% and 90% stand for cold-worked samples with 10%, 40% and 90% reductions, respectively.)

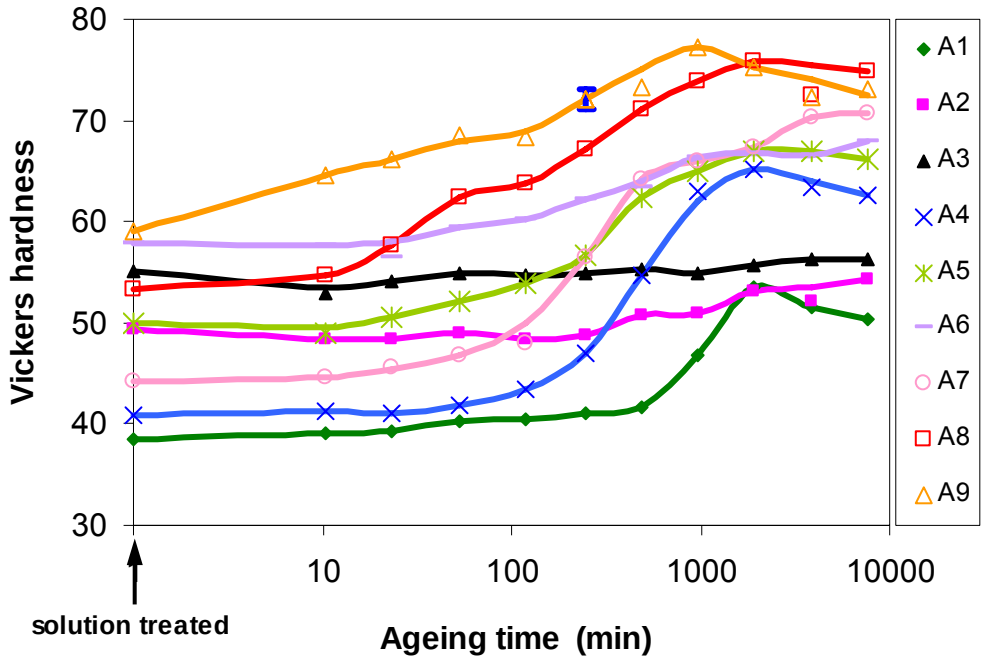

Figure 5.24 Hardness during isothermal ageing at 170°C for solution-treated samples solutionised at 500°C for 30 minutes

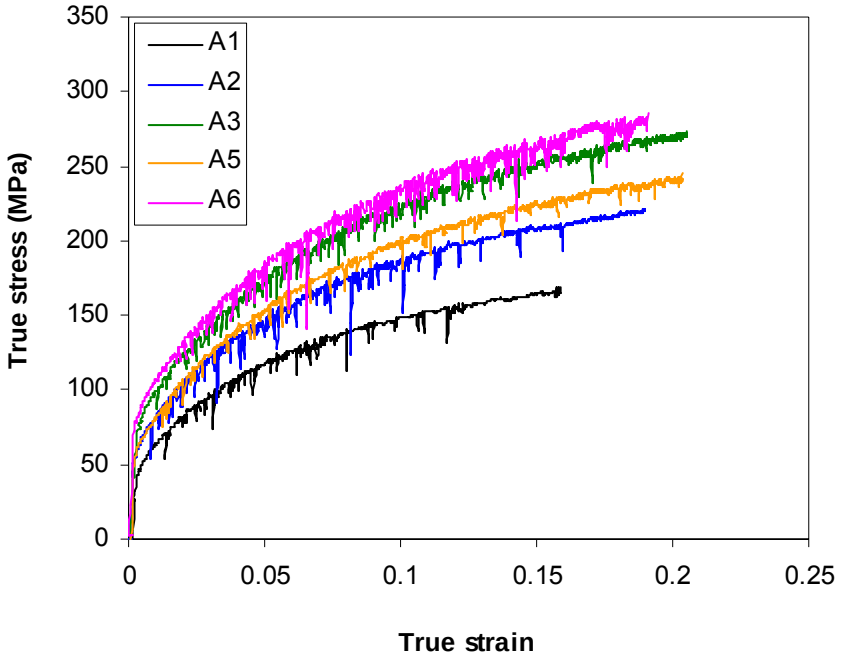

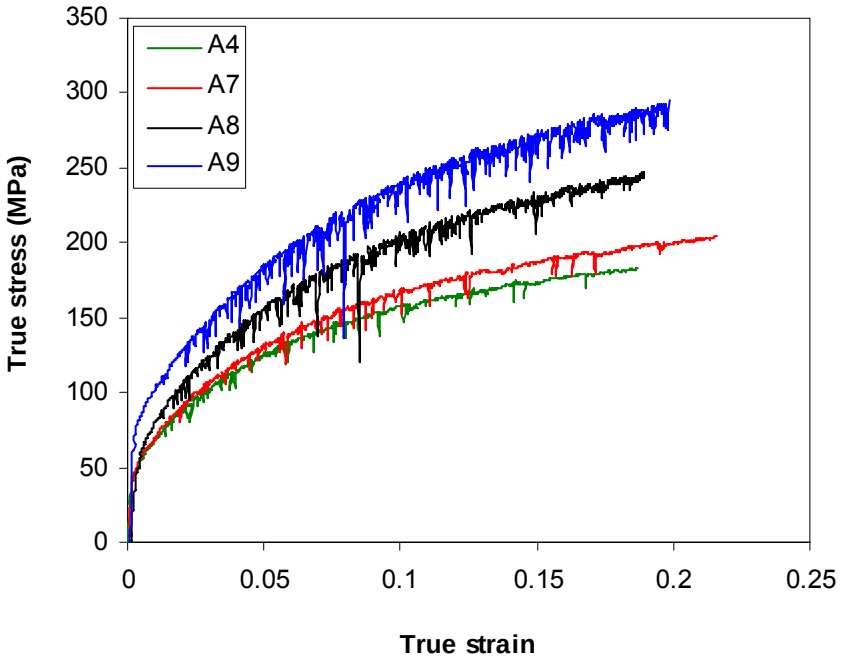

Figure 5.25 Tensile true stress vs. true strain for solution-treated samples (for clarity, the results are presented in two graphs)

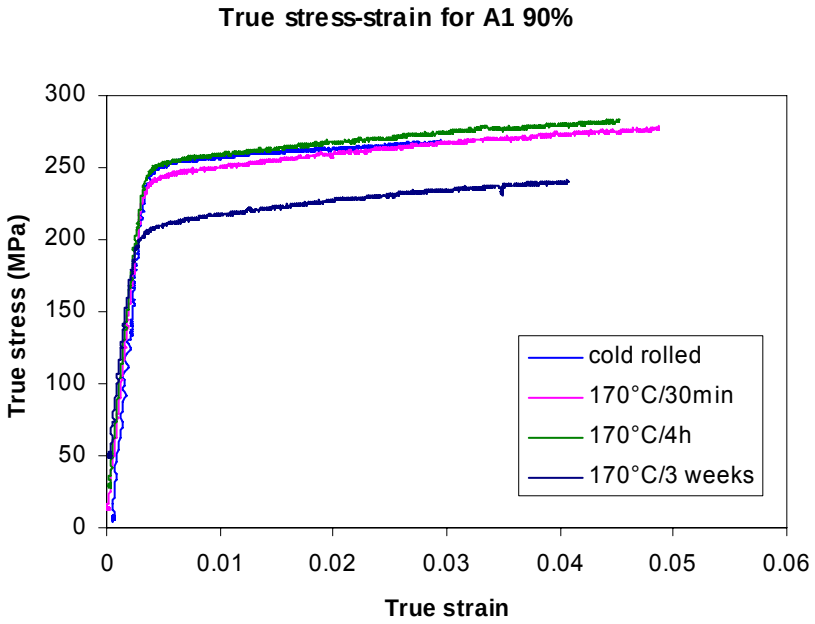

Figure 5.26 Tensile true stress vs. true-strain for alloy A1 with 90% reduction

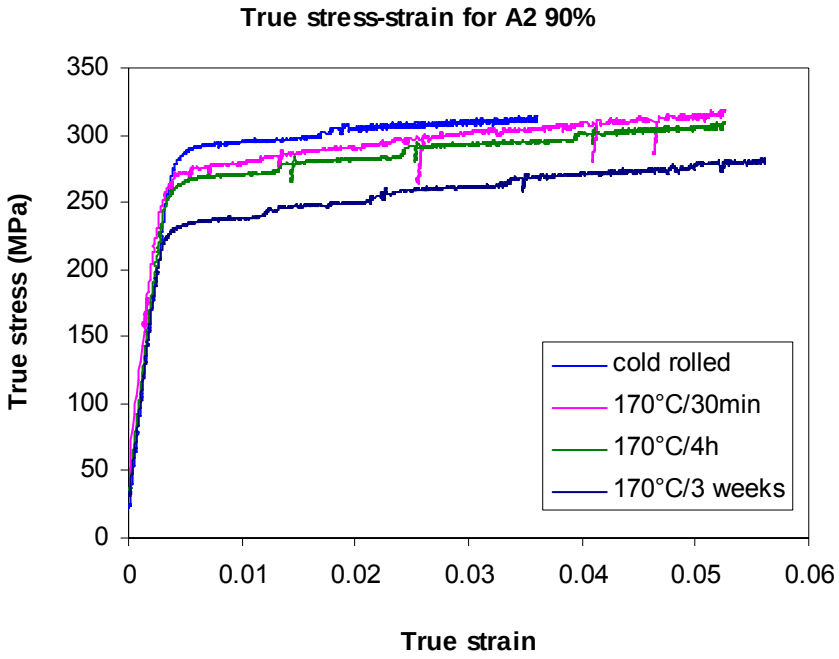

Figure 5.27 Tensile true stress vs. true-strain for alloy A2 with 90% reduction

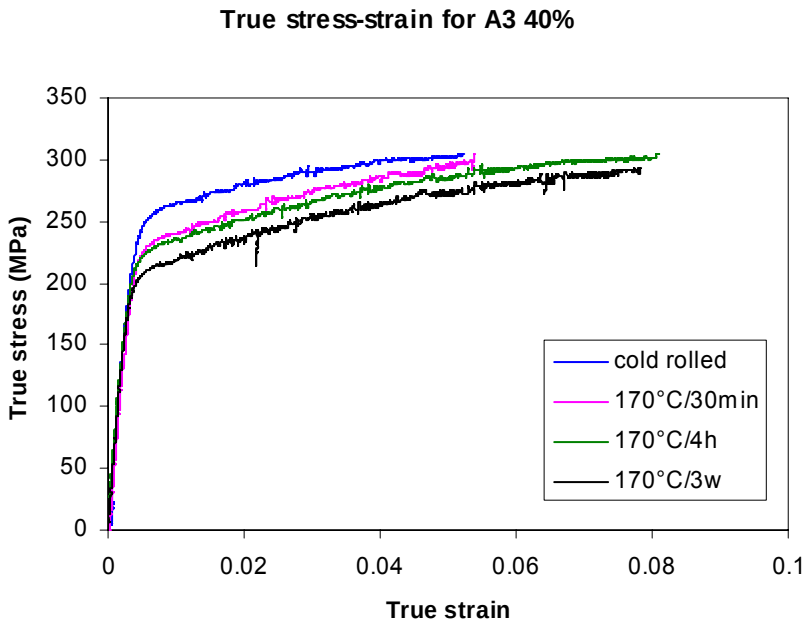

Figure 5.28 Tensile true stress vs. true-strain for alloy A3 with 40% reduction

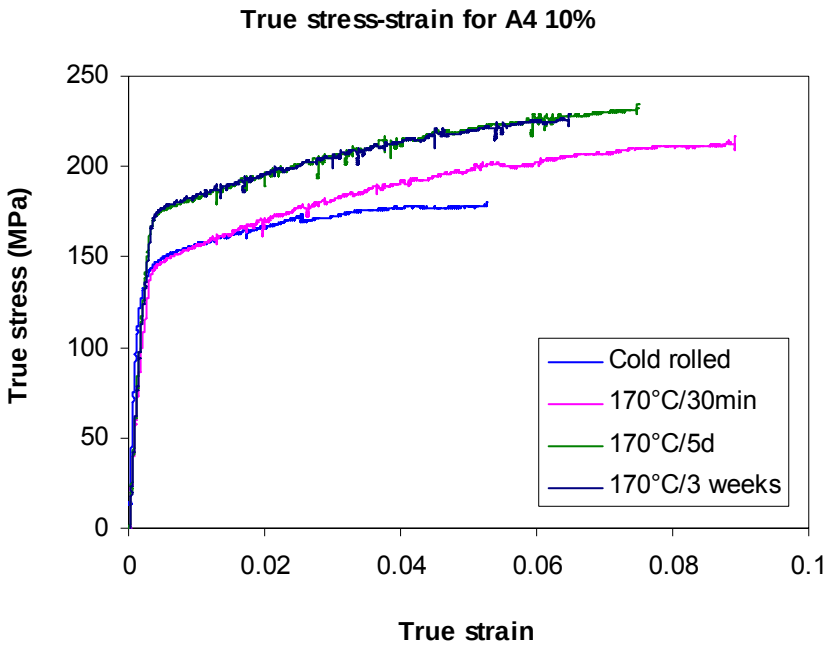

Figure 5.29 Tensile true stress vs. true-strain for alloy A4 with 10% reduction

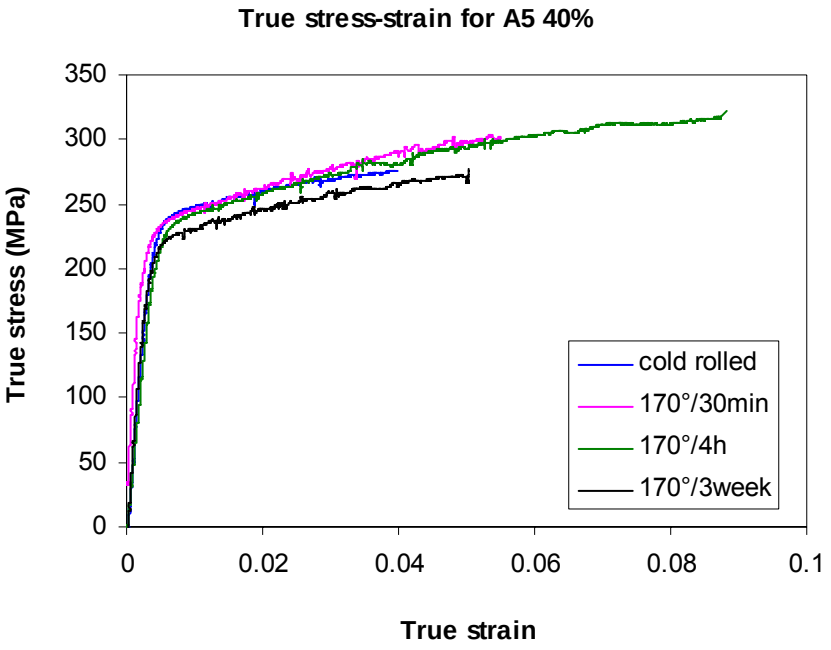

Figure 5.30 Tensile true stress vs. true-strain for alloy A5 with 40% reduction

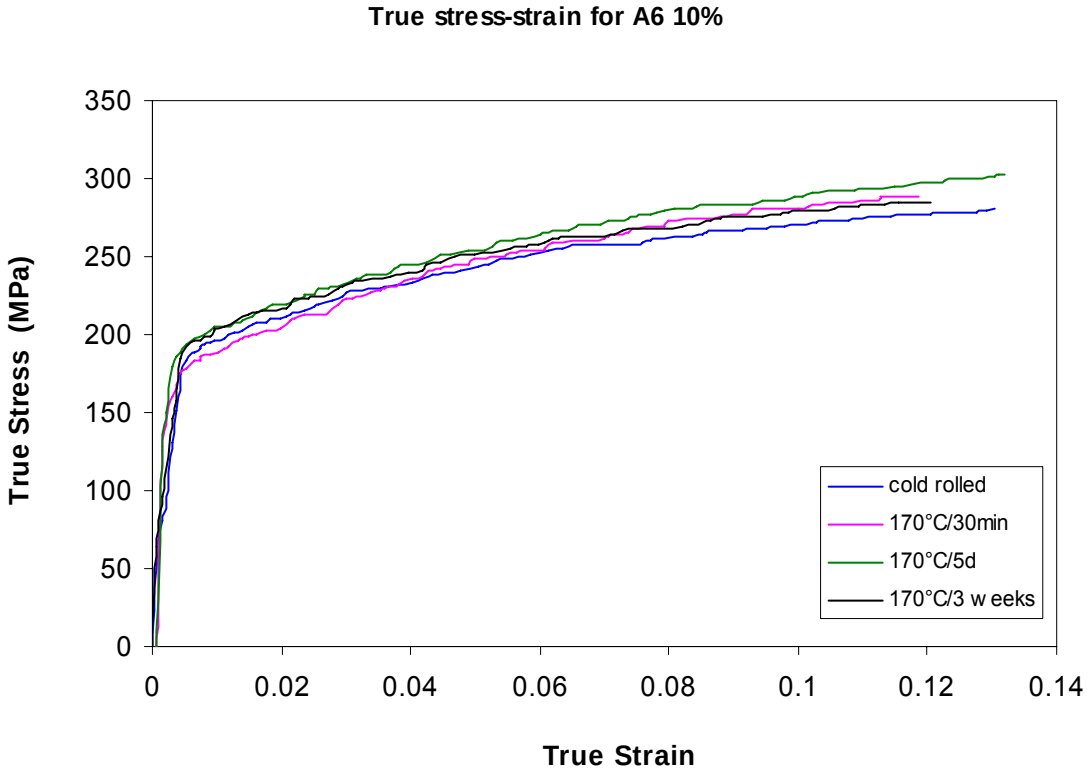

Figure 5.31 Tensile true stress vs. true-strain for alloy A6 with 10% reduction

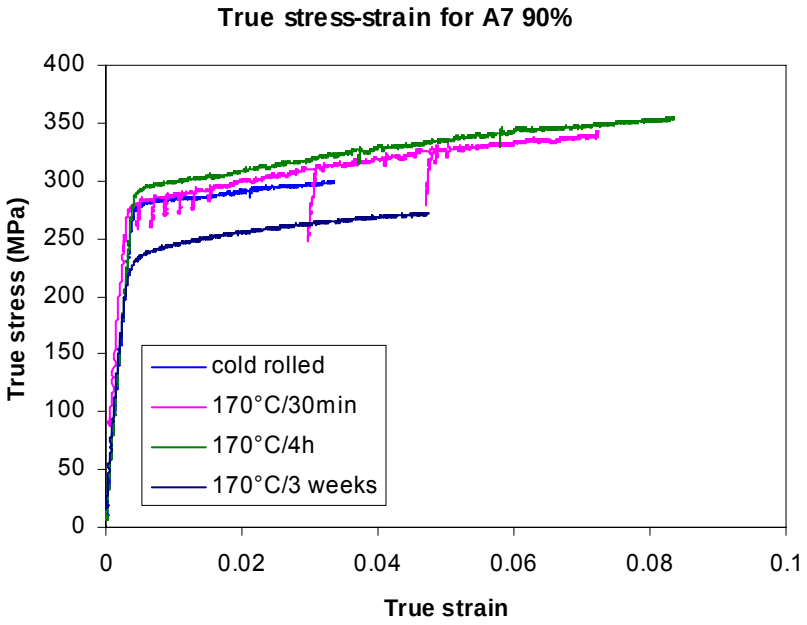

Figure 5.32 Tensile true stress vs. true-strain for alloy A7 with 90% reduction

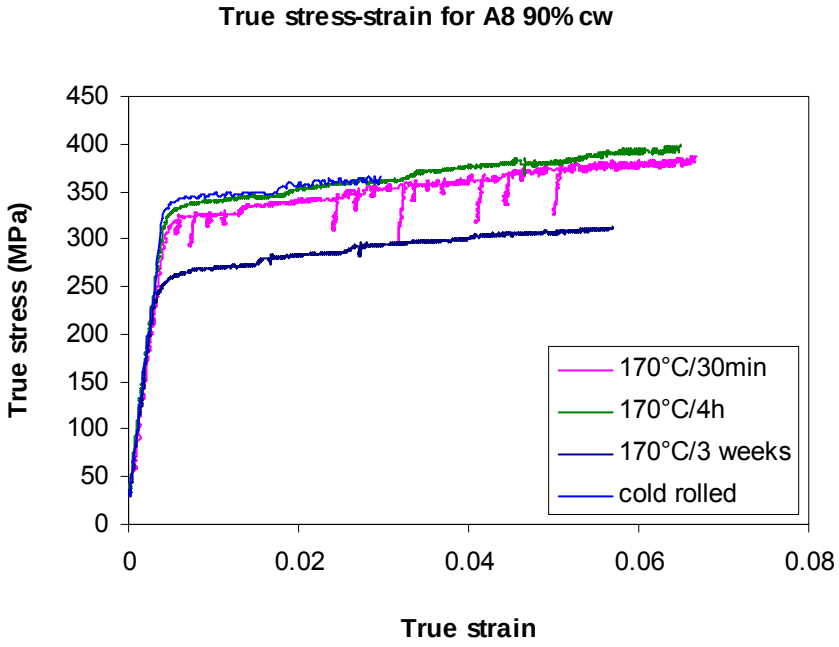

Figure 5.33 Tensile true stress vs. true-strain for alloy A8 with 90% reduction

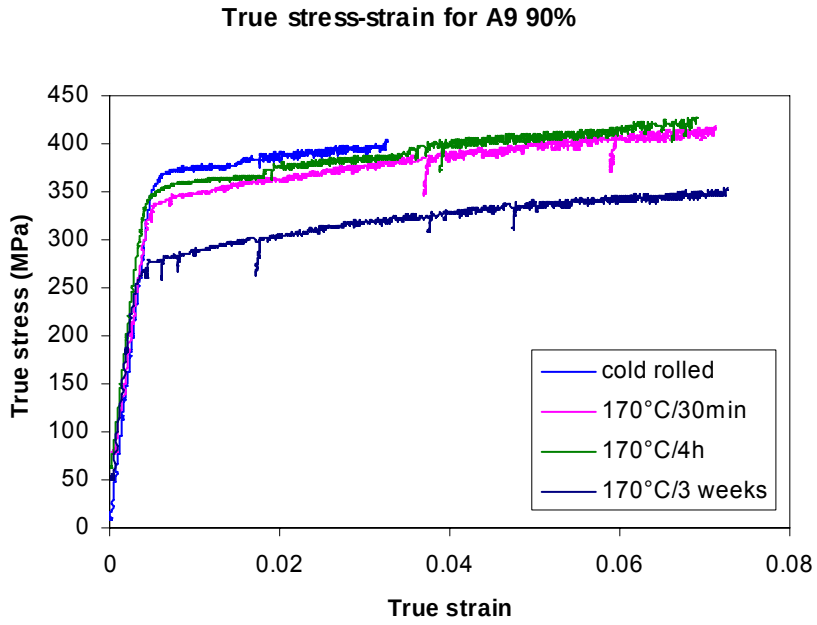

Figure 5.34 Tensile true stress vs. true-strain for alloy A9 with 90% reduction

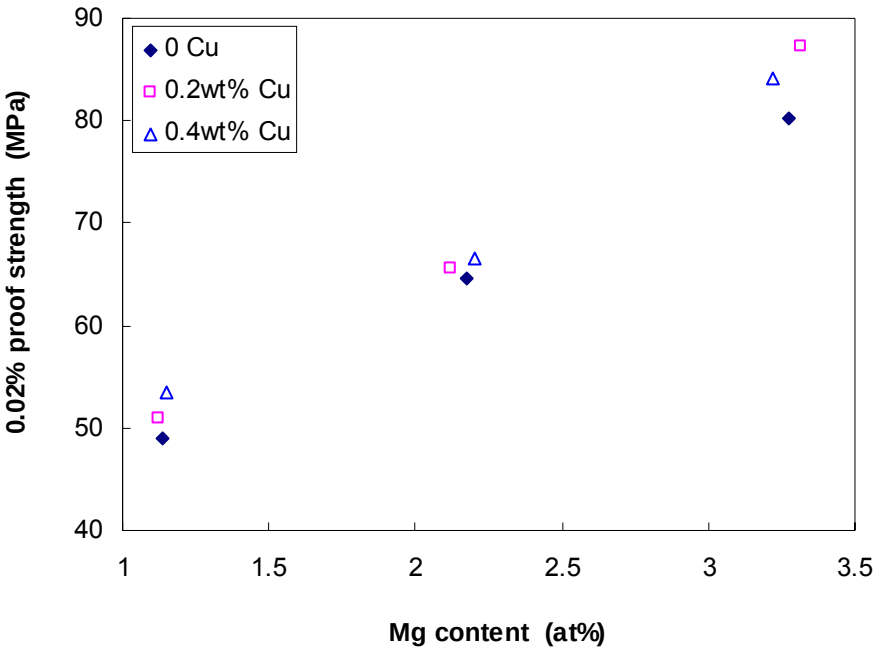

a.

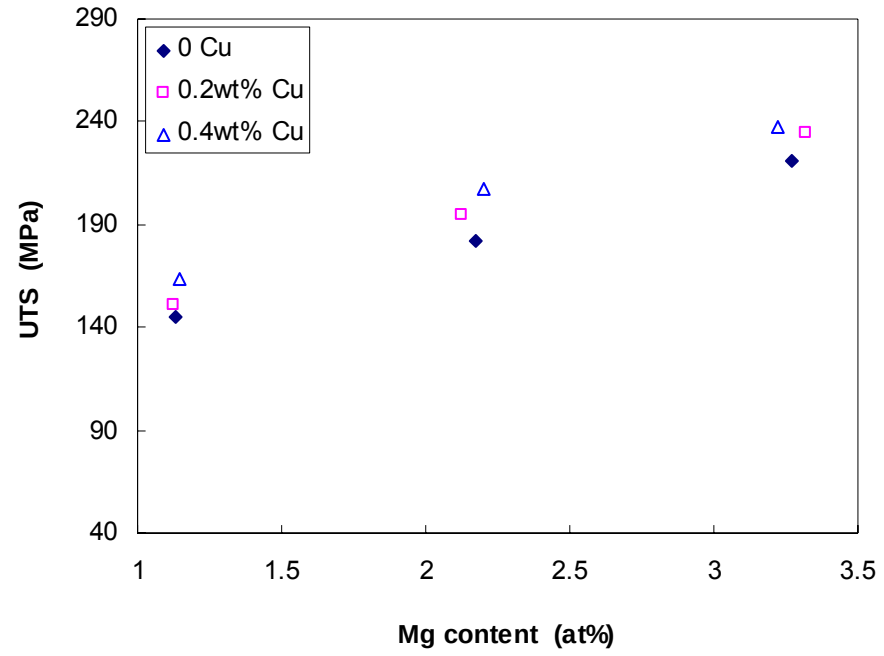

b.

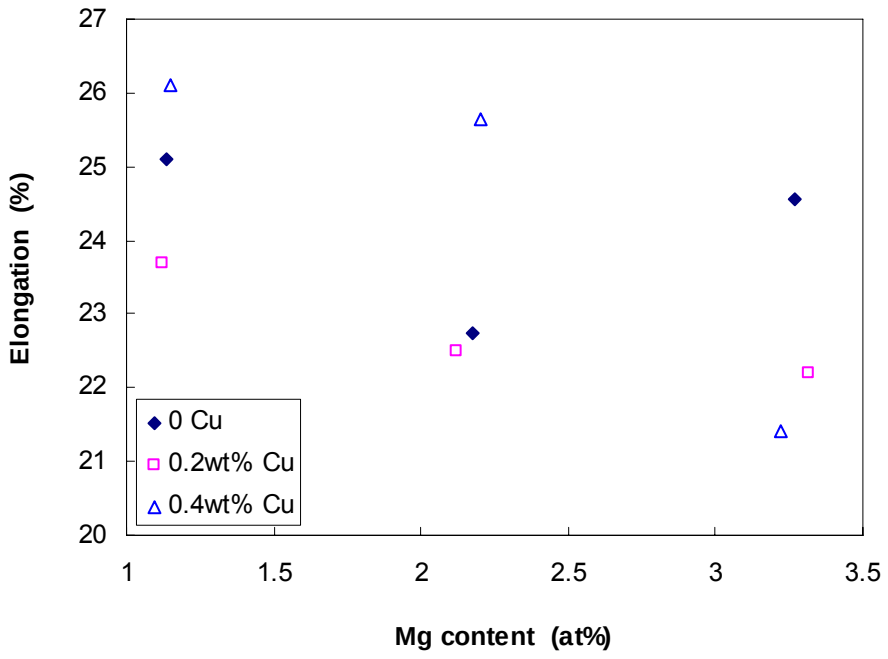

c.

Figure 5.35 Tensile test data vs. Mg contents for solution-treated samples: a. 0.2% PS, b. UTS, c. elongation

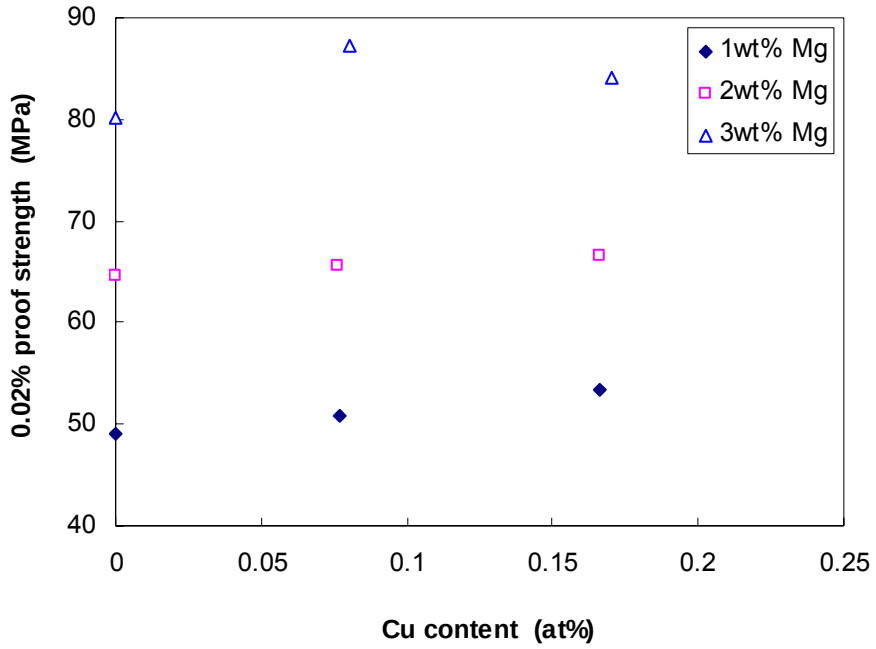
90
80
70
60
50
40
0.02% proof strength (MPa)
0
0.05
0.1
0.15
0.2
0.25
Cu content (at%)
1wt% Mg
2wt% Mg
3wt% Mg

a.

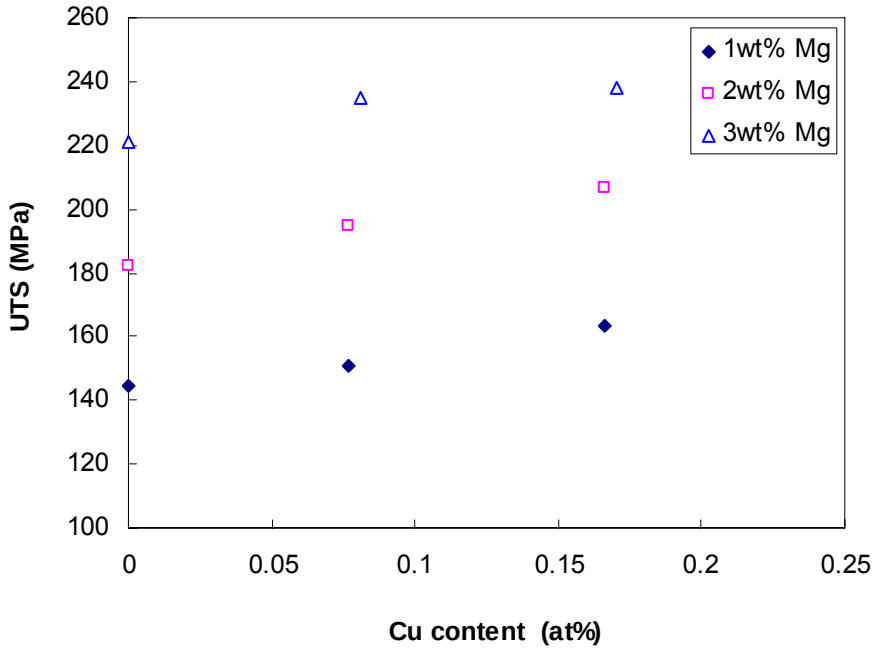
260
240
220
200
180
160
140
120
100
UTS (MPa)
0
0.05
0.1
0.15
0.2
0.25
Cu content (at%)
1wt% Mg
2wt% Mg
3wt% Mg

b.

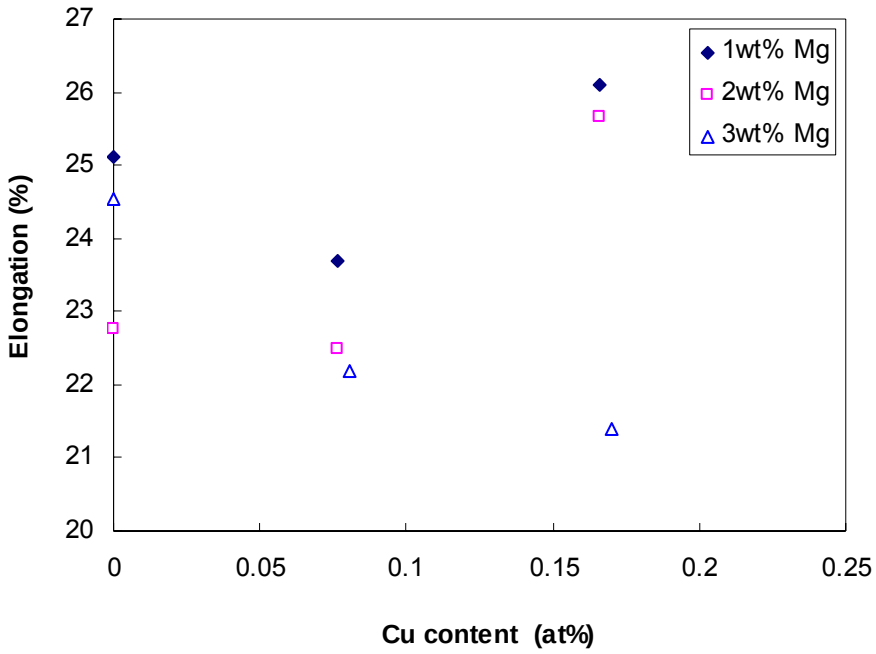

c.

Figure 5.36 Tensile test data vs. Cu contents for solution-treated samples: a. 0.2% PS, b. UTS, c. elongation

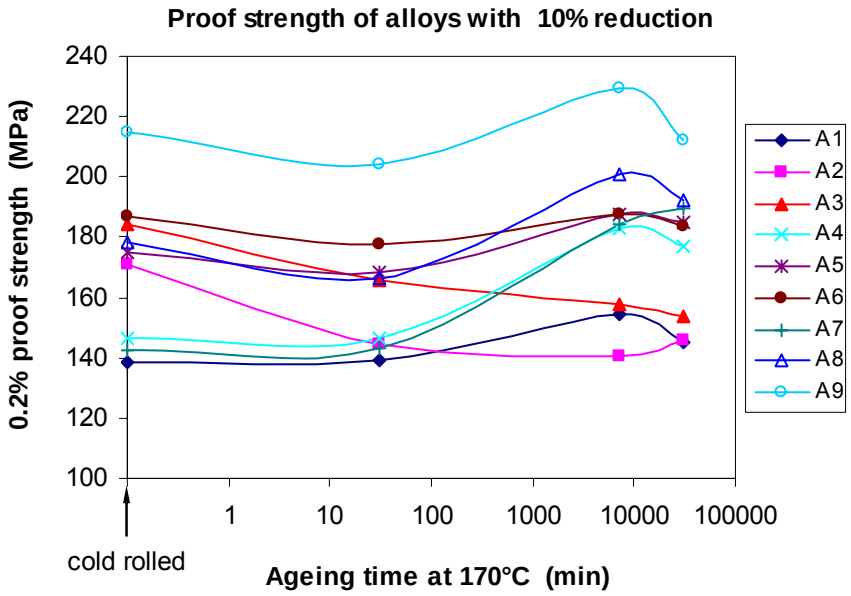

a.

b.

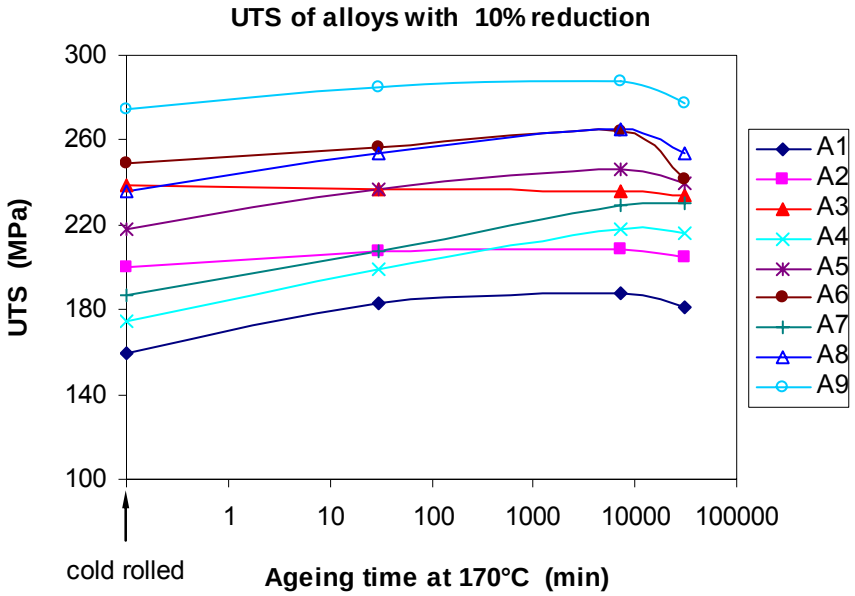

c.

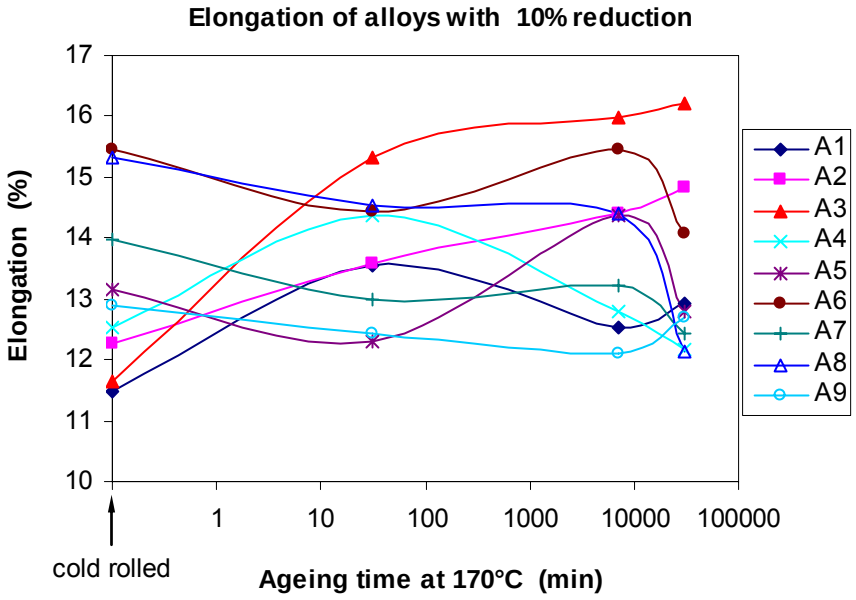

Figure 5.37 Tensile test data vs. ageing time at 170°C for 10% cold-rolled samples: a. 0.2% PS, b. UTS, c. elongation. Lines are added as guide only.

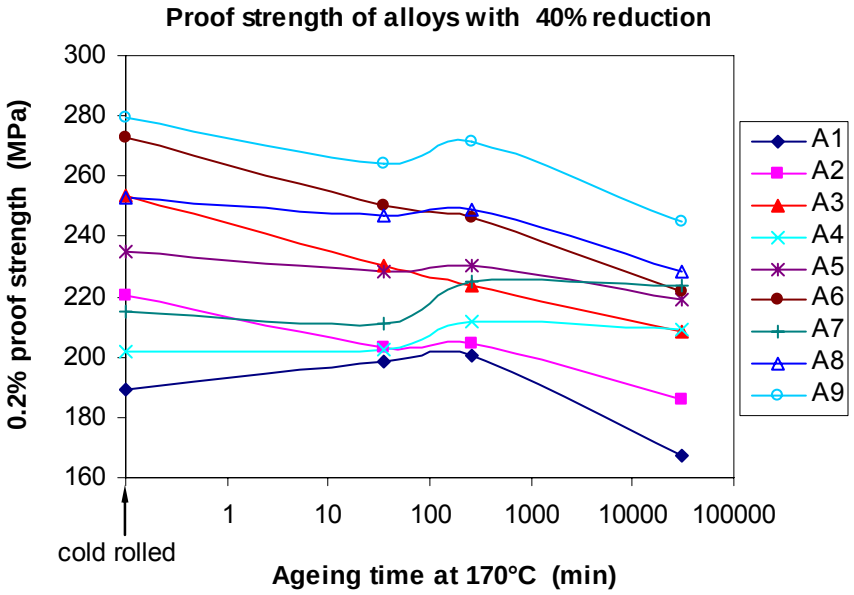
Proof strength of alloys with 40% reduction
0.2% proof strength (MPa)
300
280
260
240
220
200
180
160
1
10
100
1000
10000
100000
cold rolled
Ageing time at 170°C (min)
A1
A2
A3
A4
A5
A6
A7
A8
A9

a.

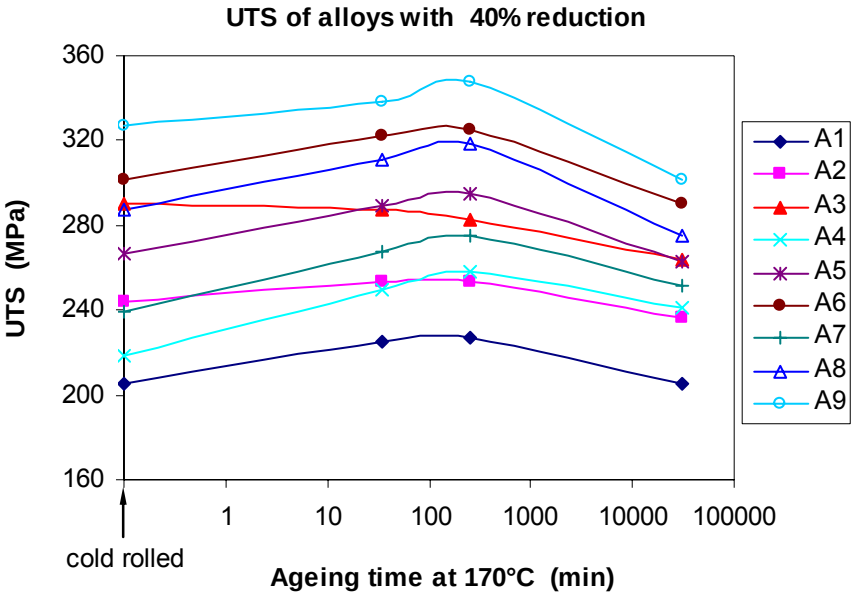
UTS of alloys with 40% reduction
UTS (MPa)
360
320
280
240
200
160
1
10
100
1000
10000
100000
cold rolled
Ageing time at 170°C (min)
A1
A2
A3
A4
A5
A6
A7
A8
A9

b.

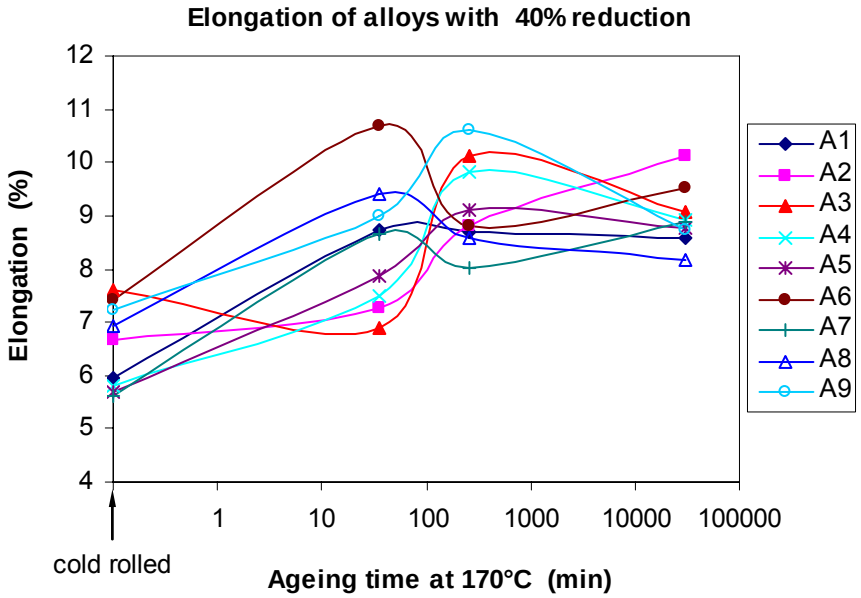

c.

Figure 5.38 Tensile test data vs. ageing time at 170°C for 40% cold-rolled samples: a. 0.2% PS, b. UTS, c. elongation. Lines are added as guide only.

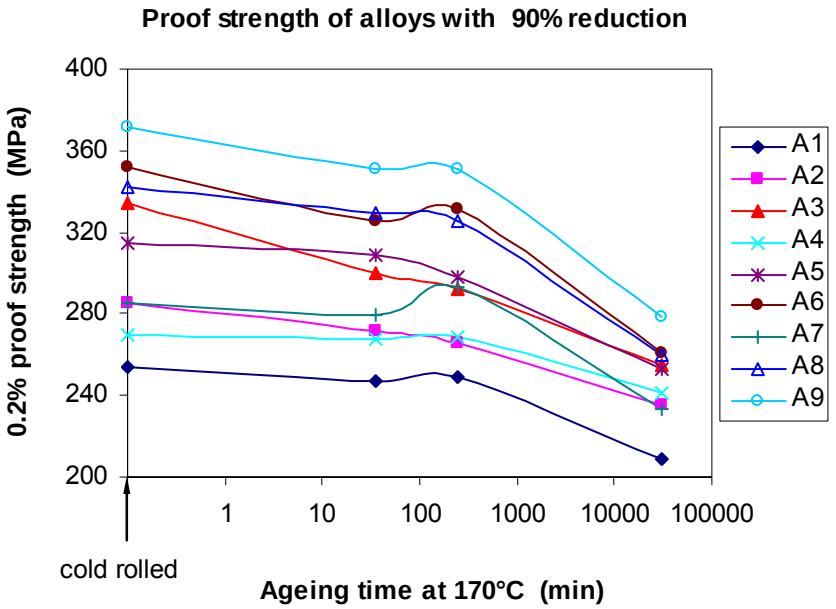

a.

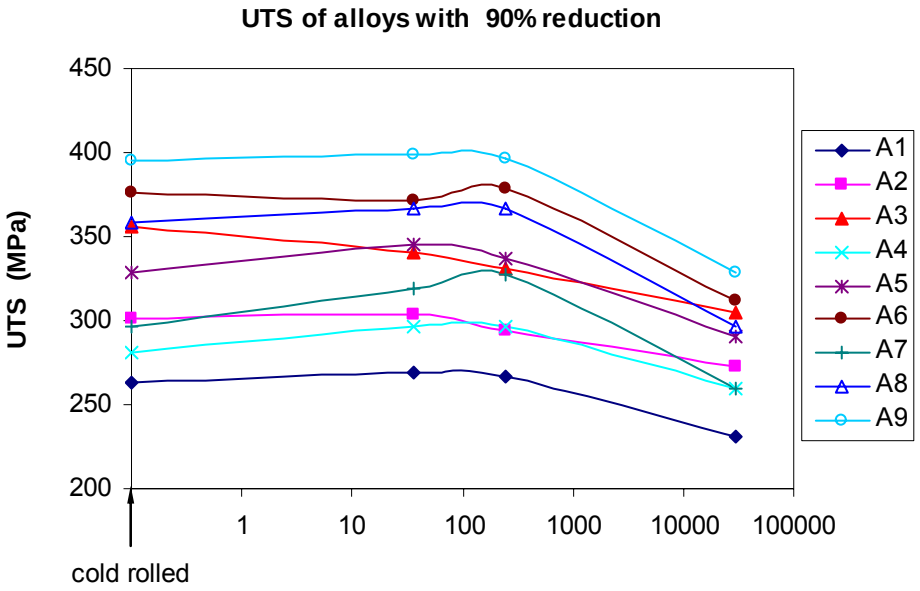

b.

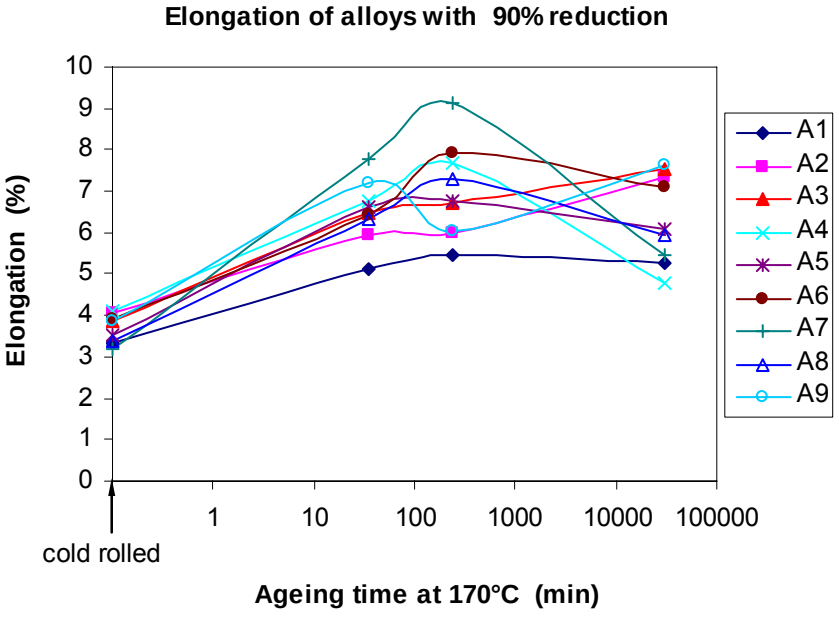

c.

Figure 5.39 Tensile test data vs. ageing time at 170°C for 90% cold-rolled samples: a. 0.2% PS, b. UTS, c. elongation. Lines are added as guide only.

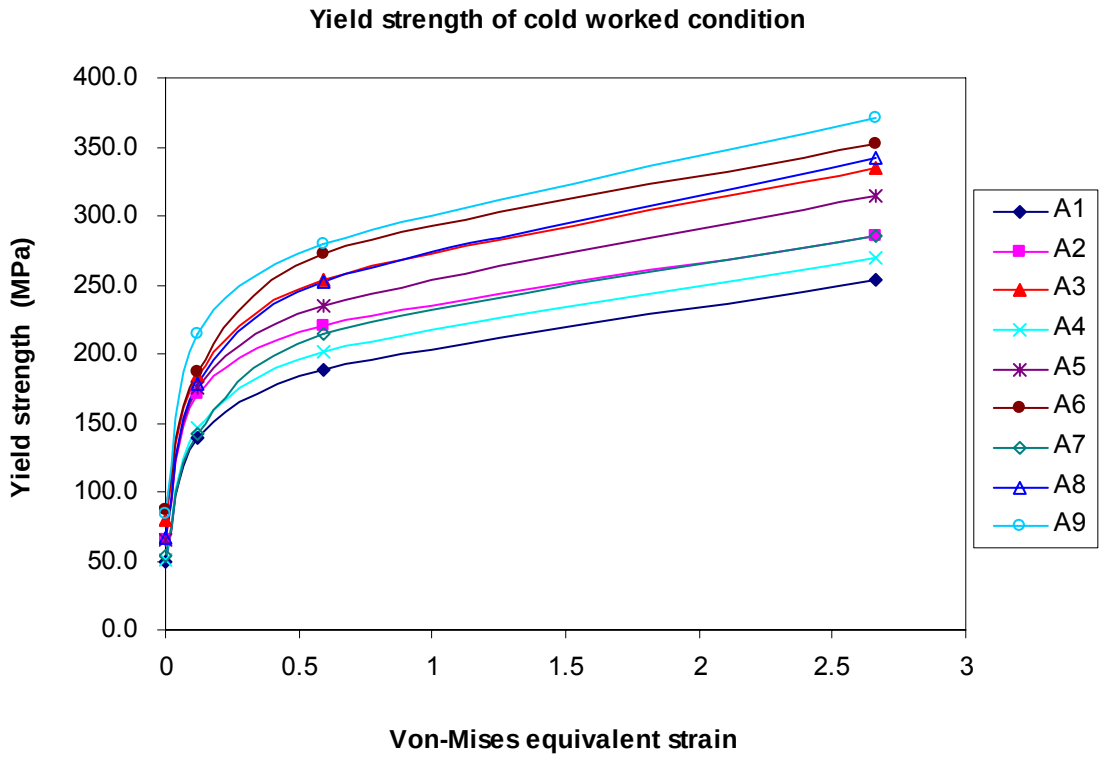

Figure 5.40 Yield strength of cold-worked samples vs. von-Mises equivalent strain ε resulting from cold rolling. Lines are added as guide only.

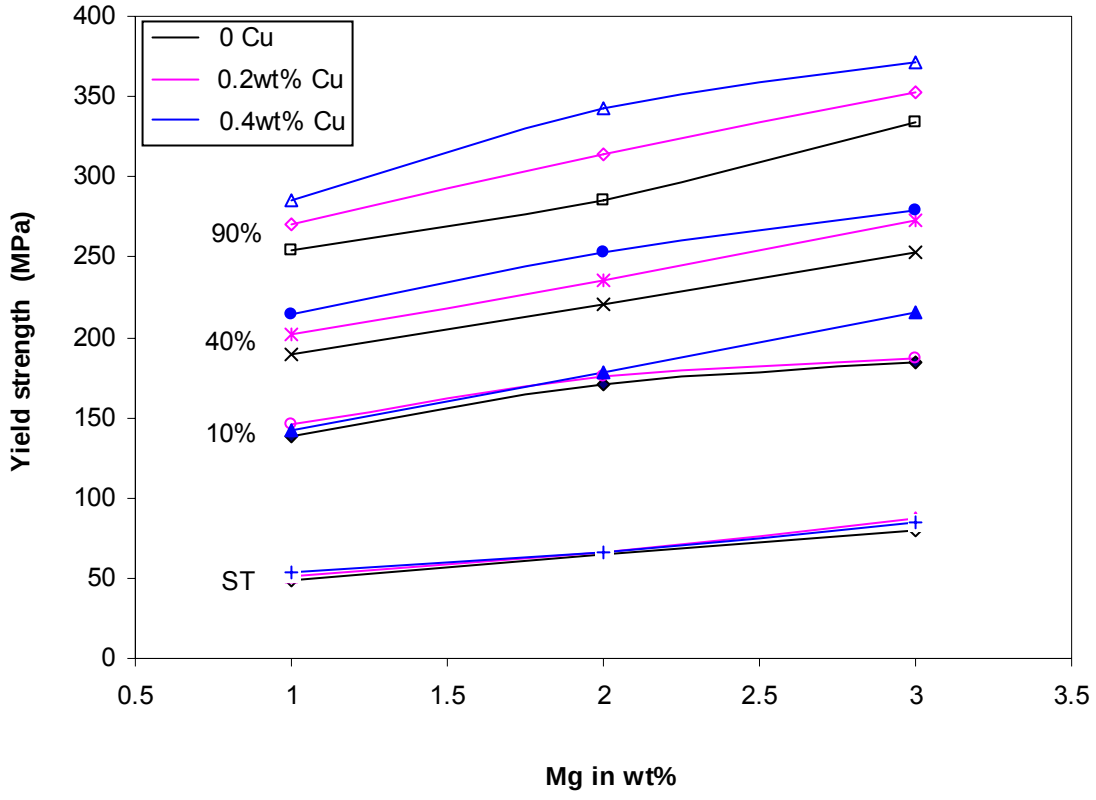

Figure 5.41 Yield strength of cold-worked samples vs. Mg content. Lines are added as guide only.

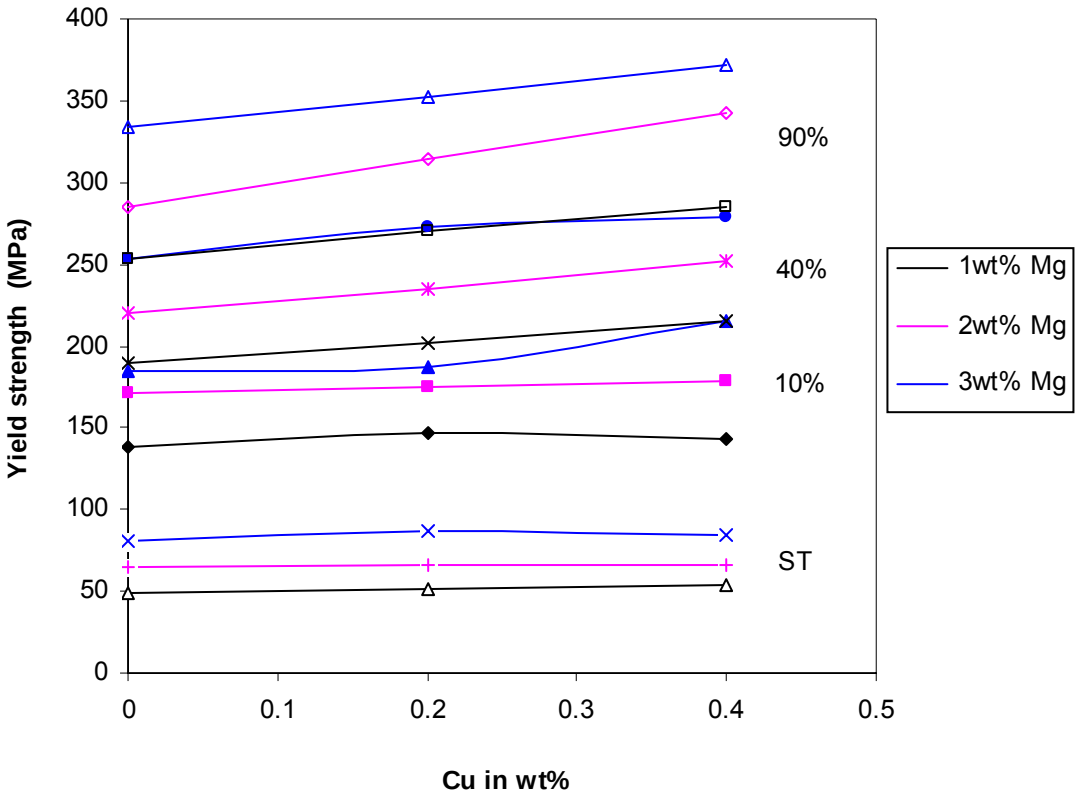

Figure 5.42 Yield strength of cold-worked samples vs. Cu content. Lines are added as guide only.

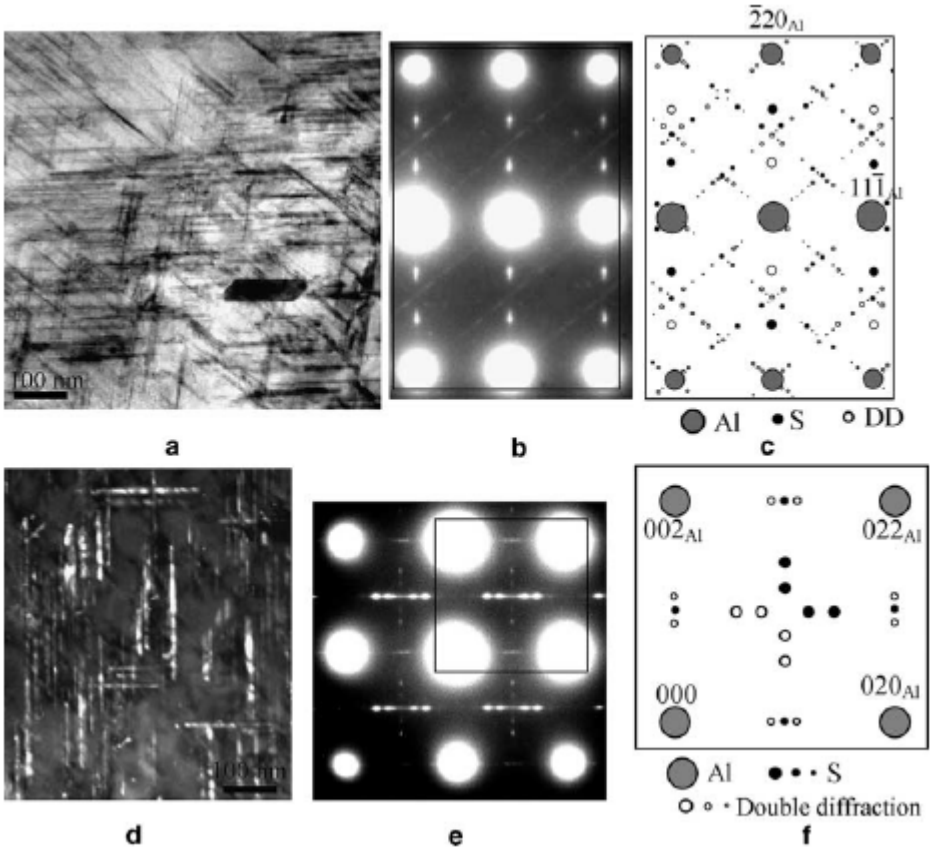

Figure 5.43 TEM micrographs and corresponding diffraction patterns of an Al-2.81Cu-1.05Mg-0.41Mn (wt%) alloy quenched, stretched and subsequently aged at 190°C for (a-c) 6h; (d-f) 12h. a. bright field, B=$[112]_{Al}$, b. SAD at $[112]_{Al}$ zone axis, c. simulated SAD pattern corresponding to (b), d. dark field, B=$[100]_{Al}$, e. SAD, B=$[100]_{Al}$, f. simulated SAD pattern corresponding to e (from reference [25])

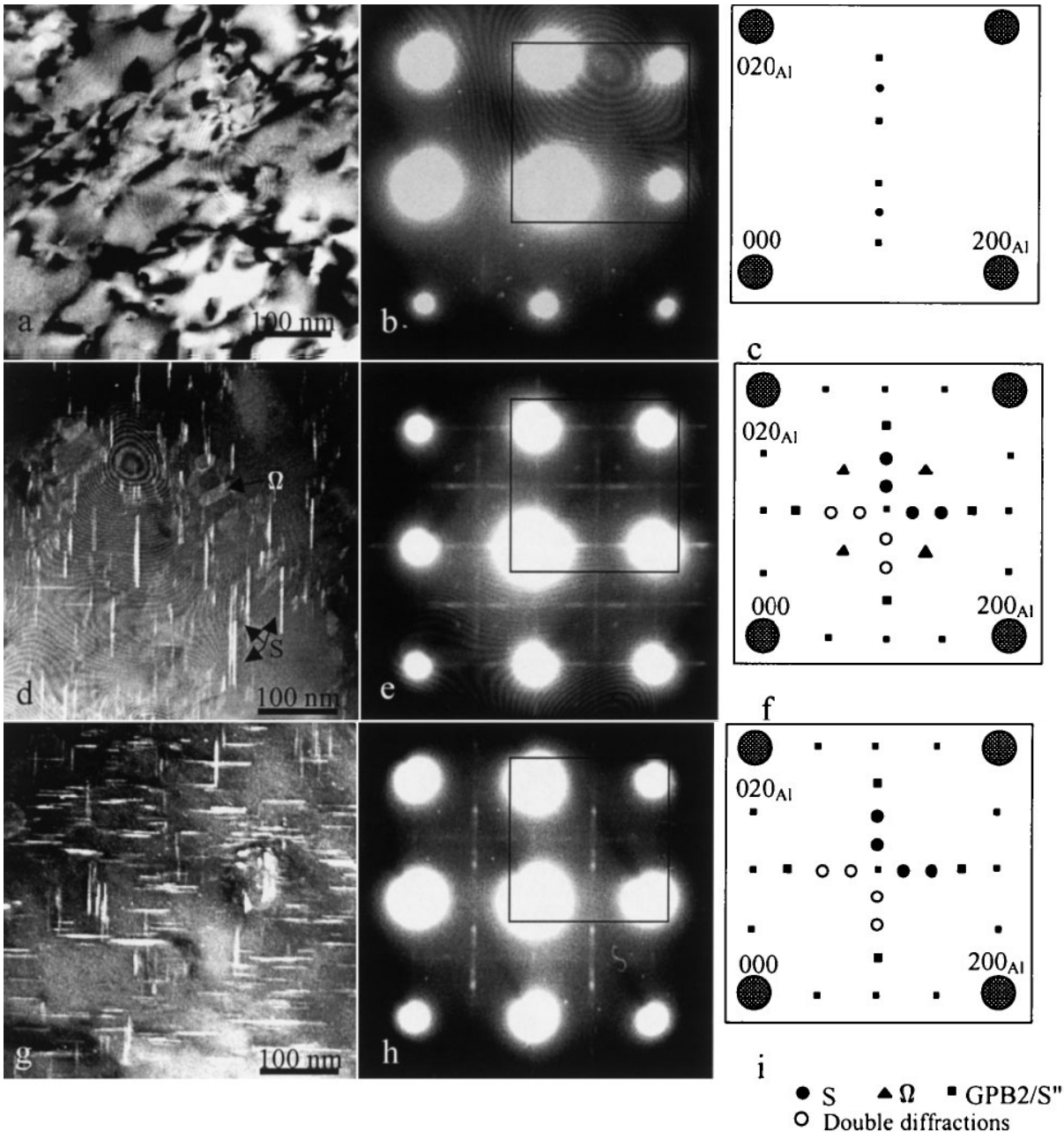

Figure 5.44 TEM dark field images and corresponding diffraction patterns of an Al-2.81Cu-1.05Mg-0.41Mn (wt%) alloy aged for different times at 150°C: a-c 24h, d-f 48h, g-i 72h (from reference [26])

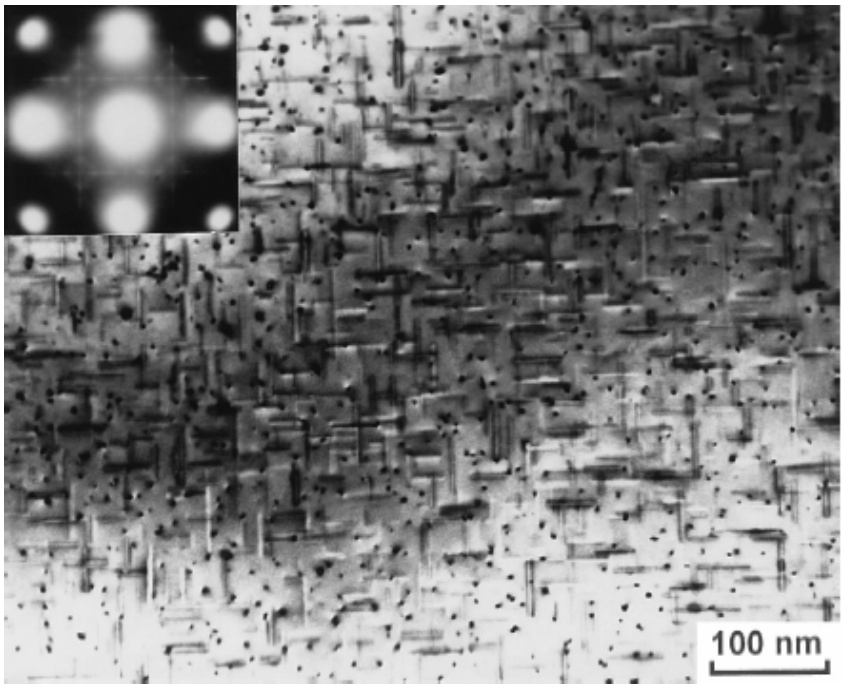

Figure 5.45 Bright-field TEM micrograph ($[001]_{Al}$ zone axis) of the sample of an AA6022 alloy heated to 260°C at 10°C/min immediately after solutionising and quenching. Needle-like β″ precipitates oriented along $<010>_{Al}$ directions are observed (from reference [11])

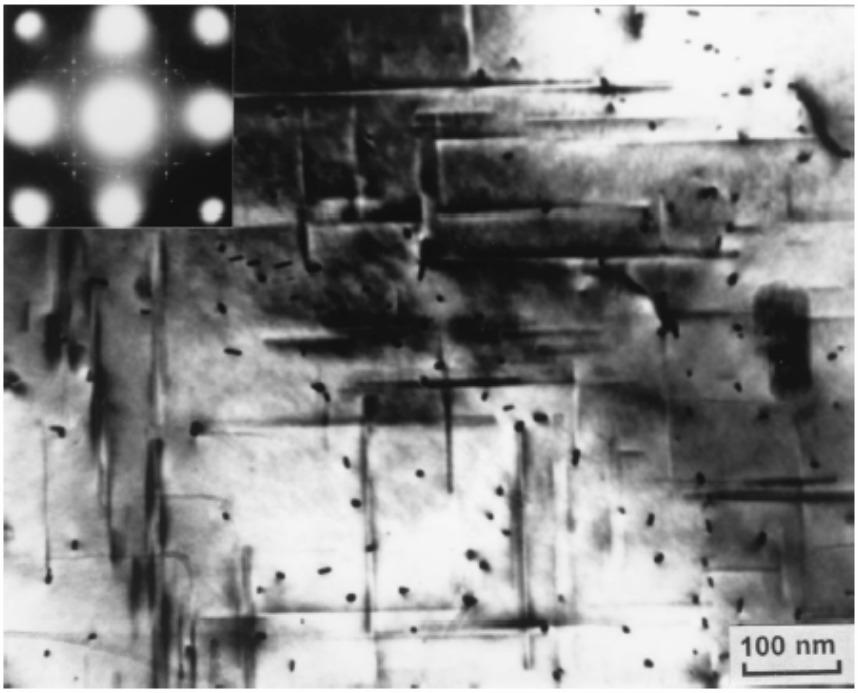

Figure 5.46 Precipitate morphology ([001]Al zone axis) of the sample of an AA6022 alloy heated to 300°C at 10°C/min immediately after solutionising and quenching. At this stage, rod-like and lath-like precipitates predominate (from reference [11])

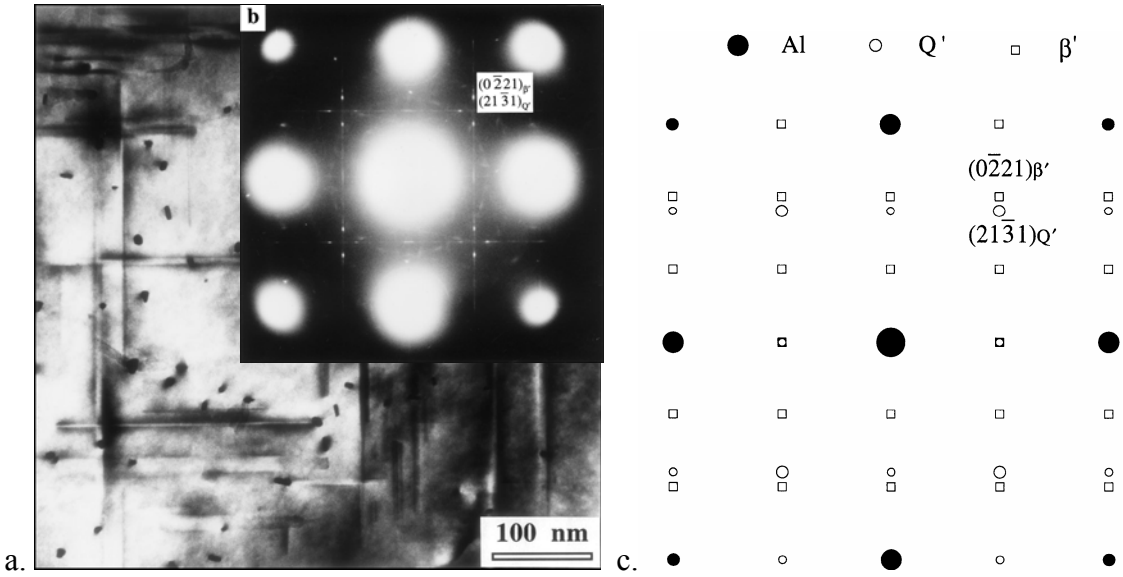

Figure 5.47 a. bright-field TEM micrograph of an AA6022 alloy heated at 10°C/min to 260°C, revealing the rectangle and round shapes when the precipitates are viewed end-on, b. SAD at [001] zone axis corresponding to TEM micrograph in a, c. a simulated diffraction pattern of β' and Q' in Al matrix with the orientation relationships of $[100]_{Al}//[0001]_{\beta'}$, $(020)_{Al}//(0220)_{\beta'}$ and $[100]_{Al}//[0001]_{Q'}$, $(020)_{Al}//(2130)_{Q'}$ (from reference [12])

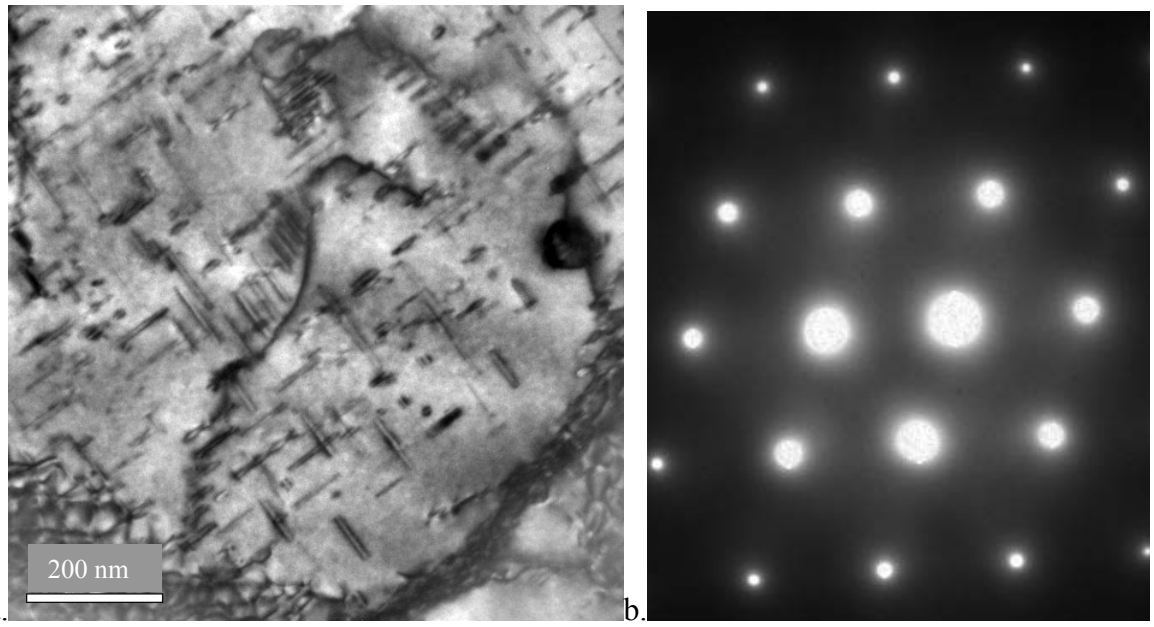

Figure 5.48 TEM results of alloy A1 solution treated at 500°C and subsequently aged for three weeks at 170°C: a. BF image at [110] zone axis, b. corresponding SAD

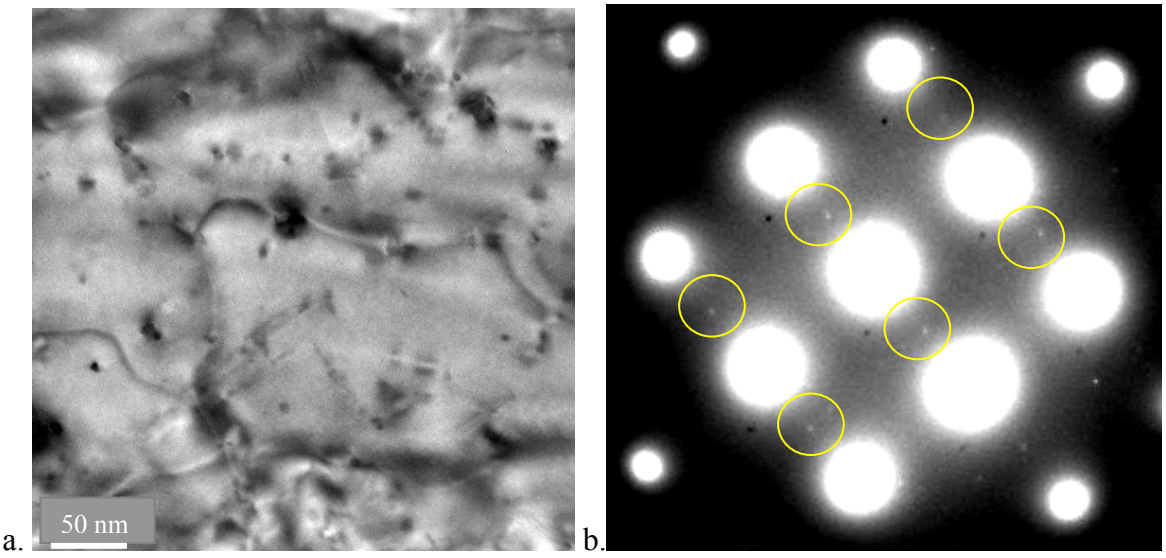

Figure 5.49 TEM results of alloy A1 cold-rolled at 10% reduction and subsequently aged for three weeks at 170°C: a. BF image at [100] zone axis, b. corresponding SAD

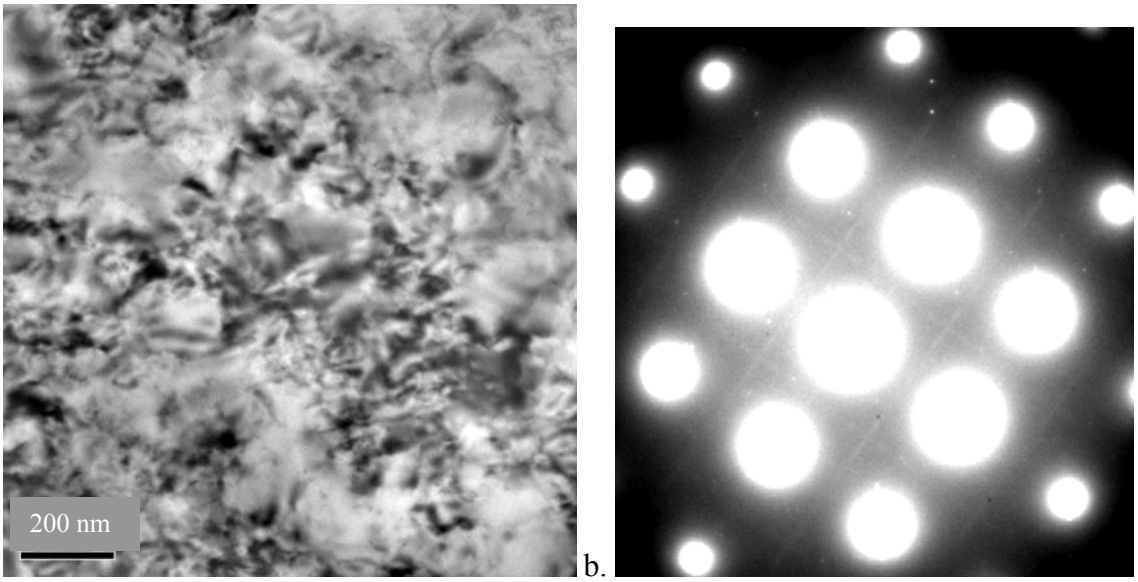

Figure 5.50 TEM results of alloy A4 cold-rolled at 10% reduction and subsequently aged for five days at 170°C: a. BF image at [100] zone axis, b. corresponding SAD

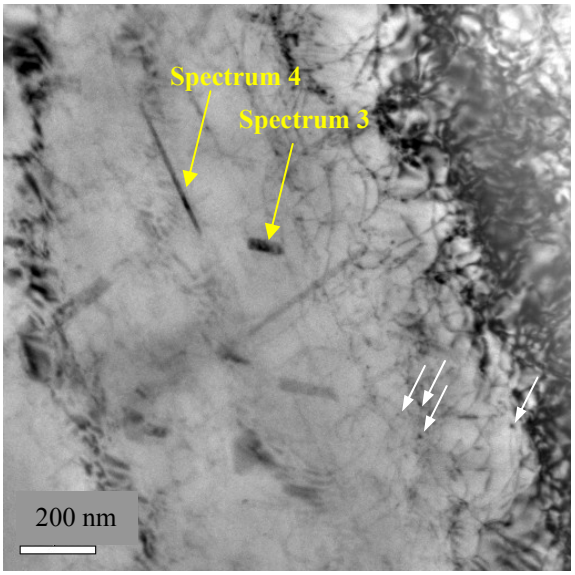

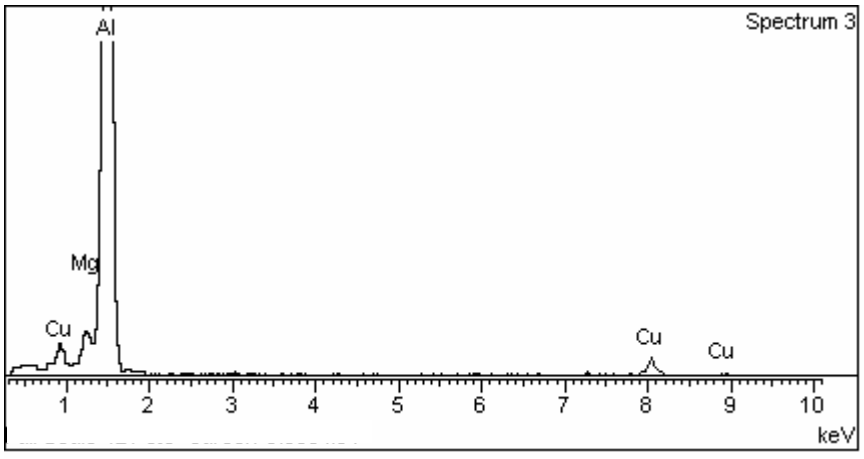

c. 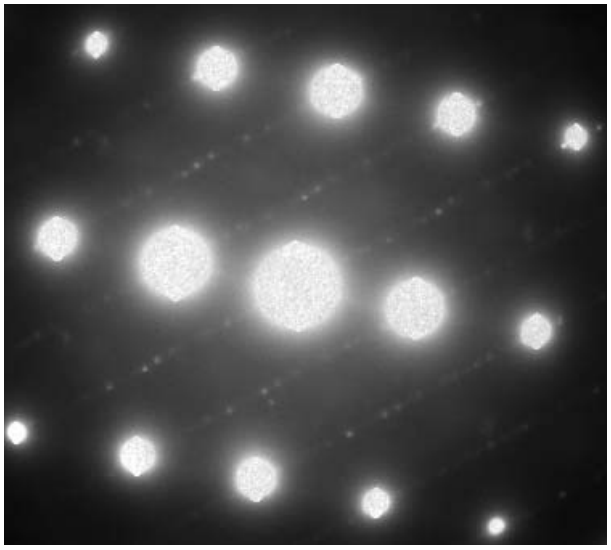

d. 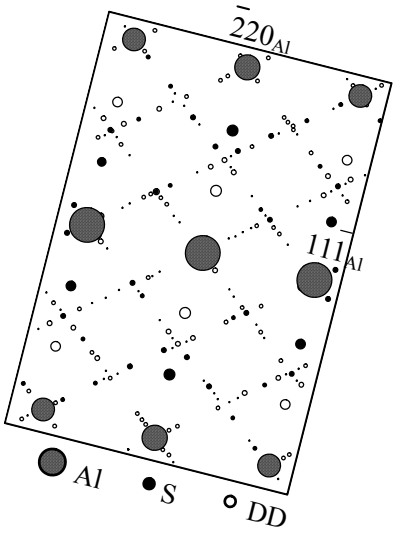

Figure 5.51 TEM results of alloy A4 cold-rolled at 10% reduction and subsequently aged for one week at 220°C: a. BF image at [112] zone axis, b. EDS spectrum from position 3 marked in a, c. corresponding SAD at [112] zone axis, d. simulation of diffraction pattern for S phase at [112] zone axis (from reference [25])

a. 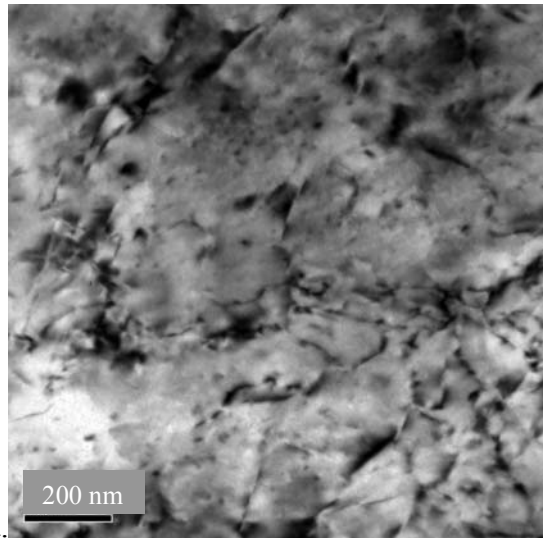

b. 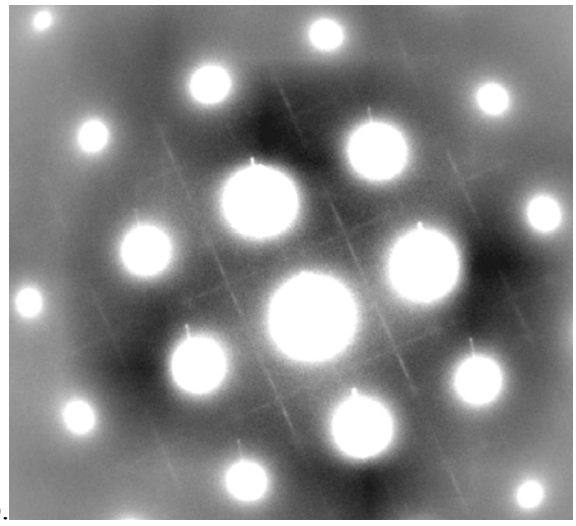

Figure 5.52 TEM results of 10% cold-rolled alloy A7 aged for five days at 170°C: a. BF image close to [100] zone axis, b. corresponding SAD at [100] zone axis

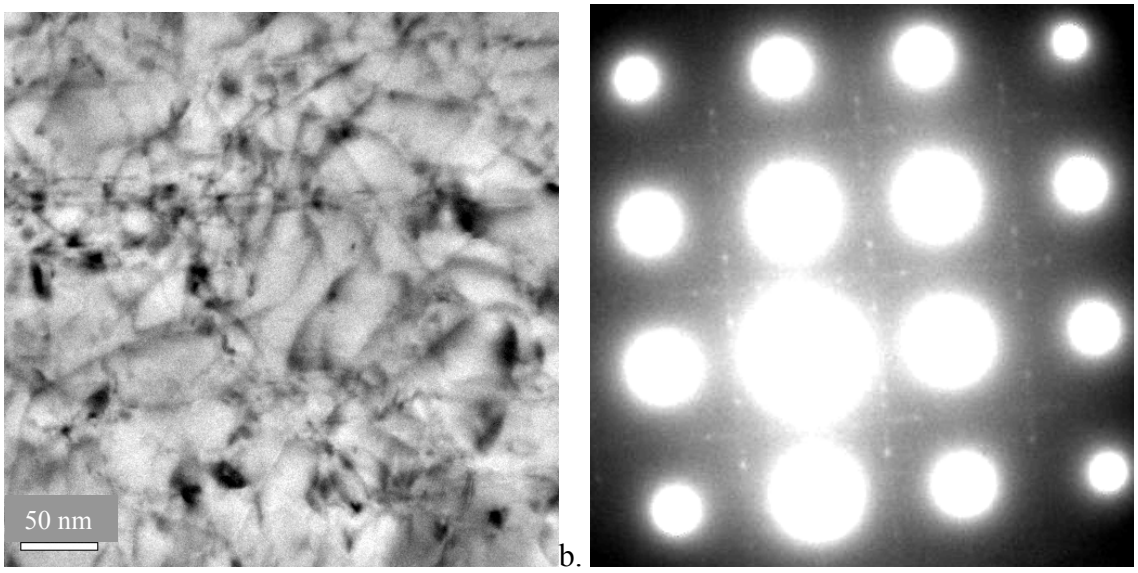

Figure 5.53 TEM results of alloy A7 cold-rolled at 10% reduction and subsequently aged for three weeks at 170°C: a. BF image at [100] zone axis, b. corresponding SAD

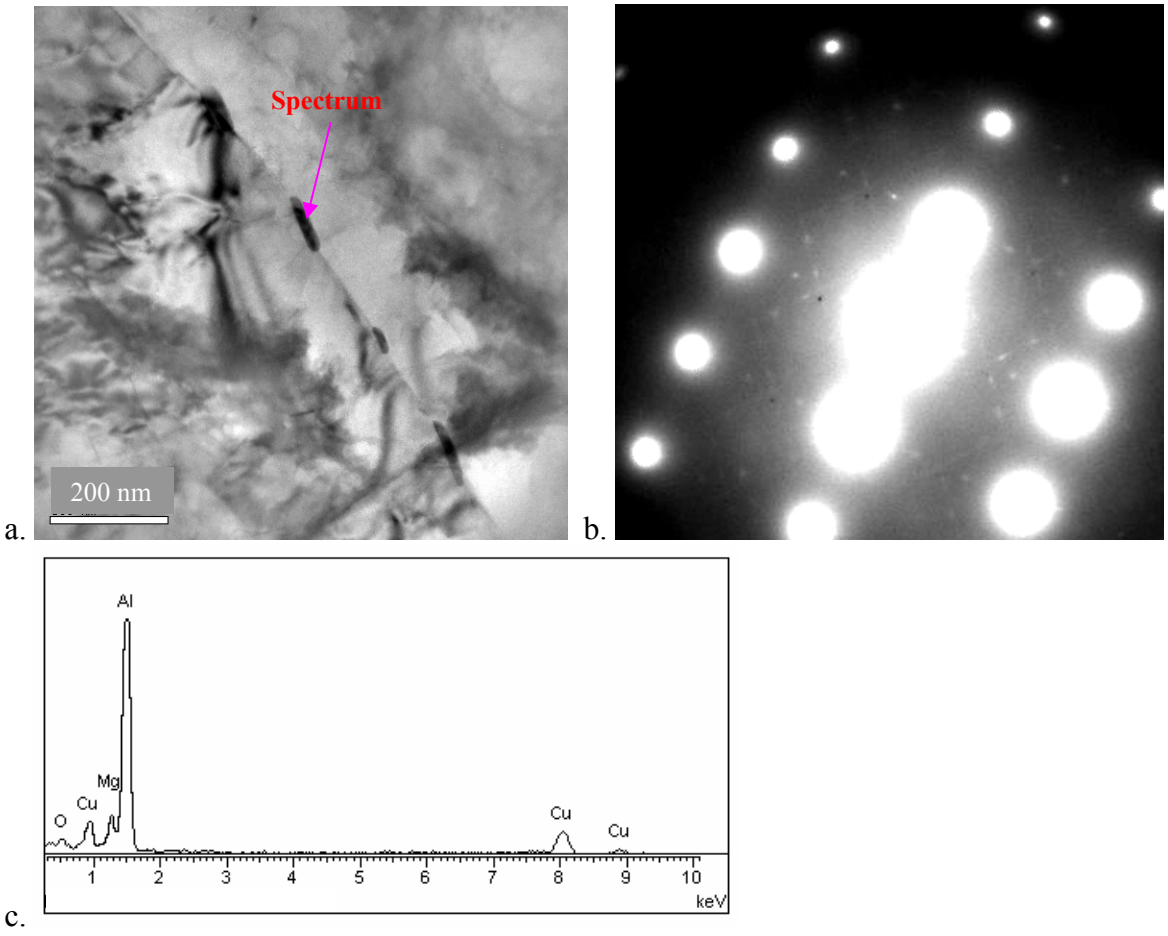

Figure 5.54 TEM results of alloy A8 cold-rolled at 10% reduction and subsequently aged for three weeks at 170°C: a. BF image at [112] zone axis, b. corresponding SAD, c. spectrum of the large precipitate on the boundary marked in a

a. 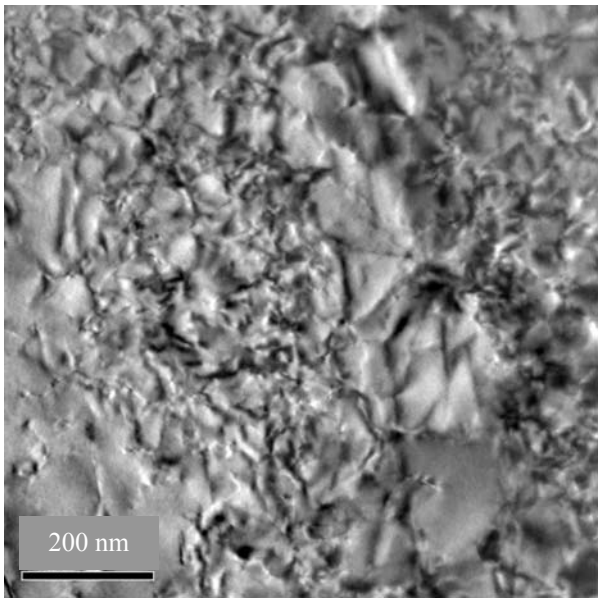

b. 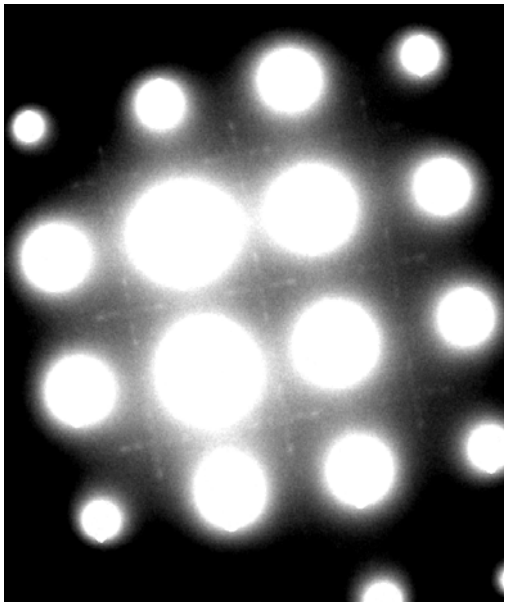

Figure 5.55 TEM results of 10% cold-rolled alloy A9 and subsequently aged for five days at 170°C: a. BF image at [100] zone axis, b. corresponding SAD

a.

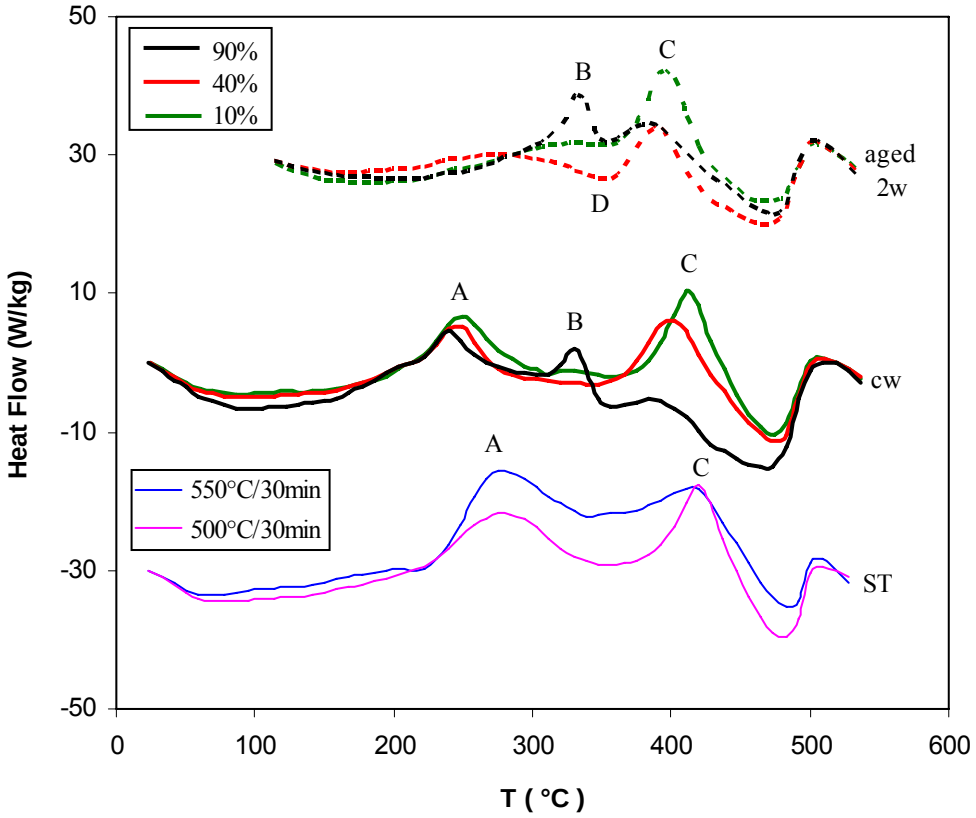
90%
40%
10%
B
C
D
aged
2w
A
B
C
cw
550°C/30min
500°C/30min
A
C
ST
Heat Flow (W/kg)
T (°C)
50
30
10
-10
-30
-50
0
100
200
300
400
500
600

b.

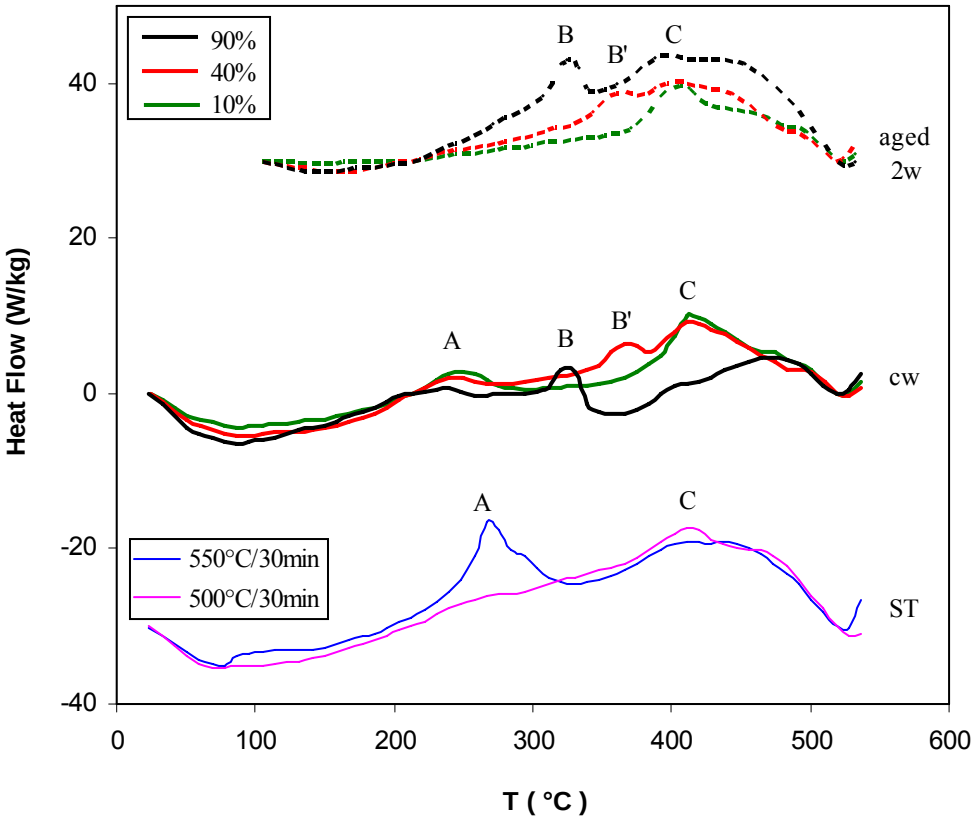
90%
40%
10%
B
B'
C
aged
2w
A
B
B'
C
cw
550°C/30min
500°C/30min
A
C
ST
Heat Flow (W/kg)
T (°C)
40
20
0
-20
-40
0
100
200
300
400
500
600

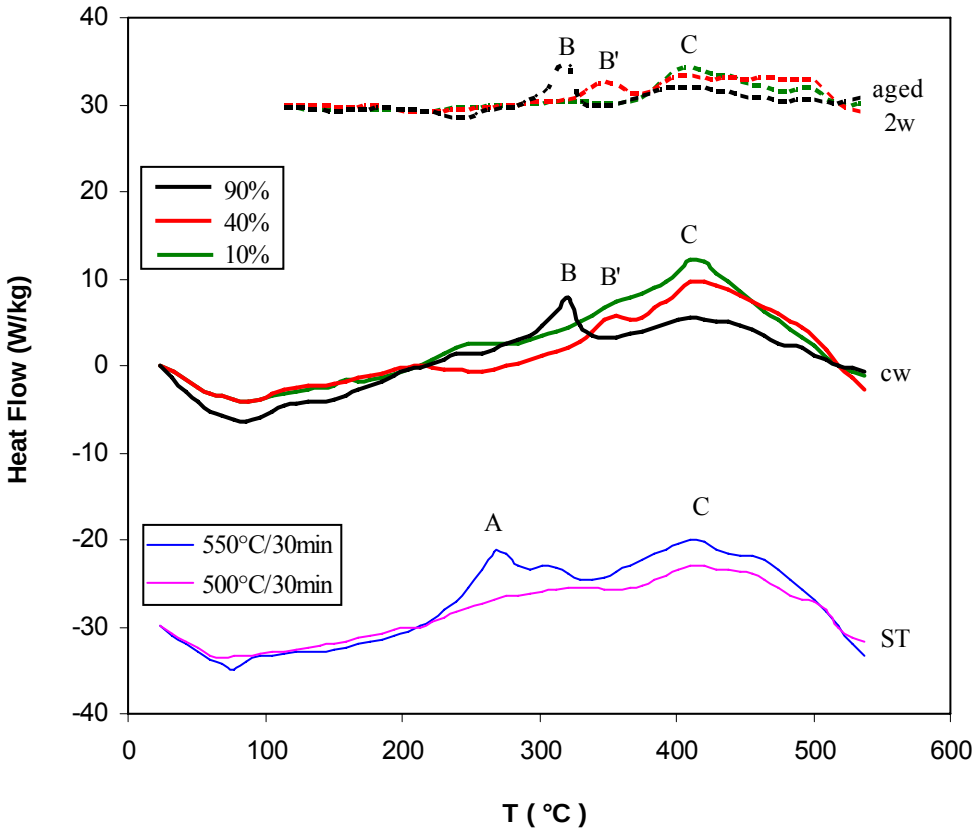
Heat Flow (W/kg)
T (°C)
B
B'
C
aged
2w
90%
40%
10%
cw
A
550°C/30min
500°C/30min
ST

c.

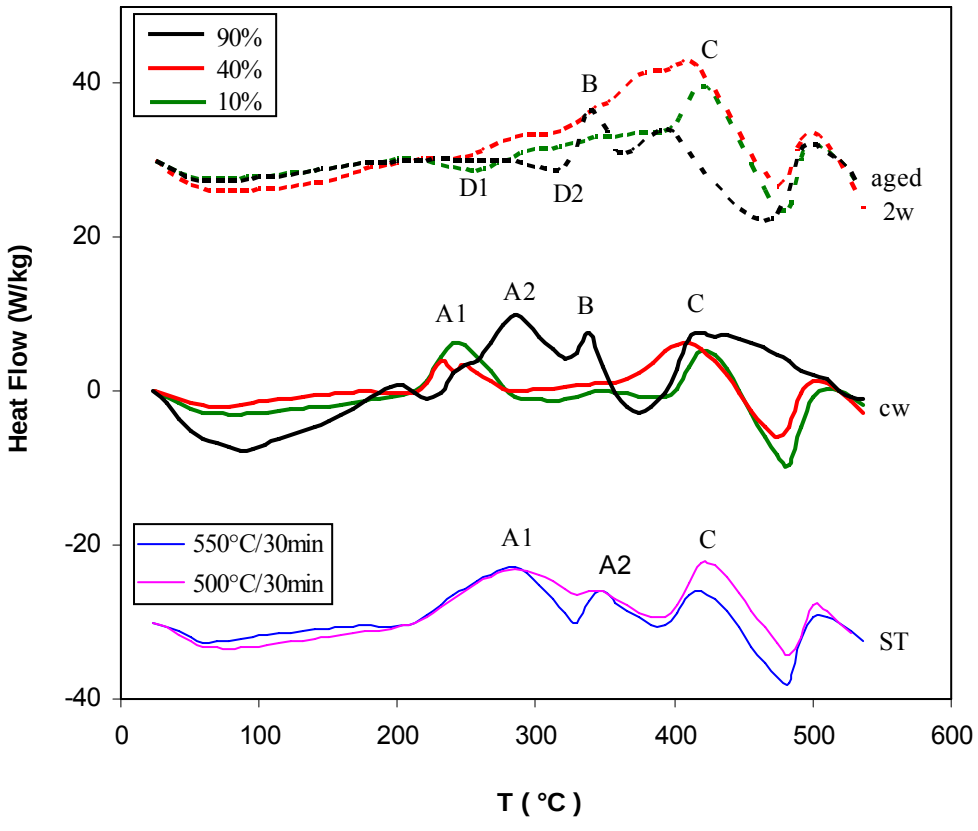
Heat Flow (W/kg)
T (°C)
90%
40%
10%
C
B
D1
D2
aged
2w
A1
A2
cw
550°C/30min
500°C/30min
ST

d.

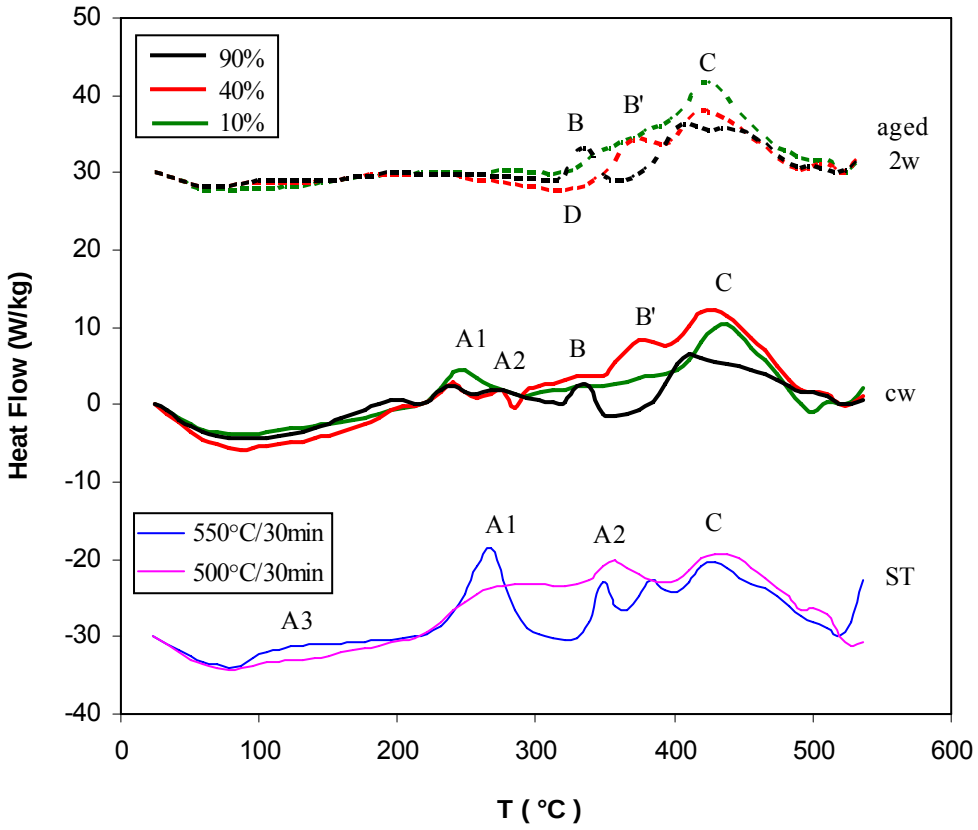
90%
40%
10%
aged 2w
cw
ST
550°C/30min
500°C/30min
A1
A2
A3
A
B
B'
C
D
Heat Flow (W/kg)
T (°C)

e.

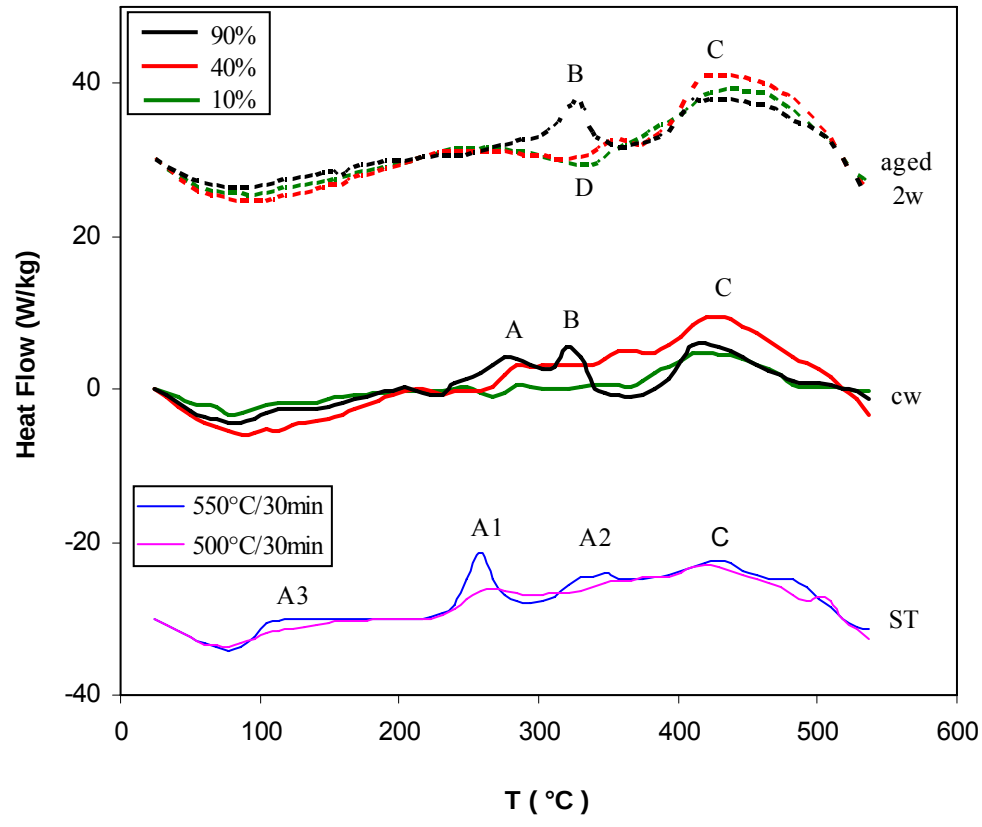
90%
40%
10%
aged 2w
cw
ST
550°C/30min
500°C/30min
A1
A2
A3
A
B
C
D
Heat Flow (W/kg)
T (°C)

f.

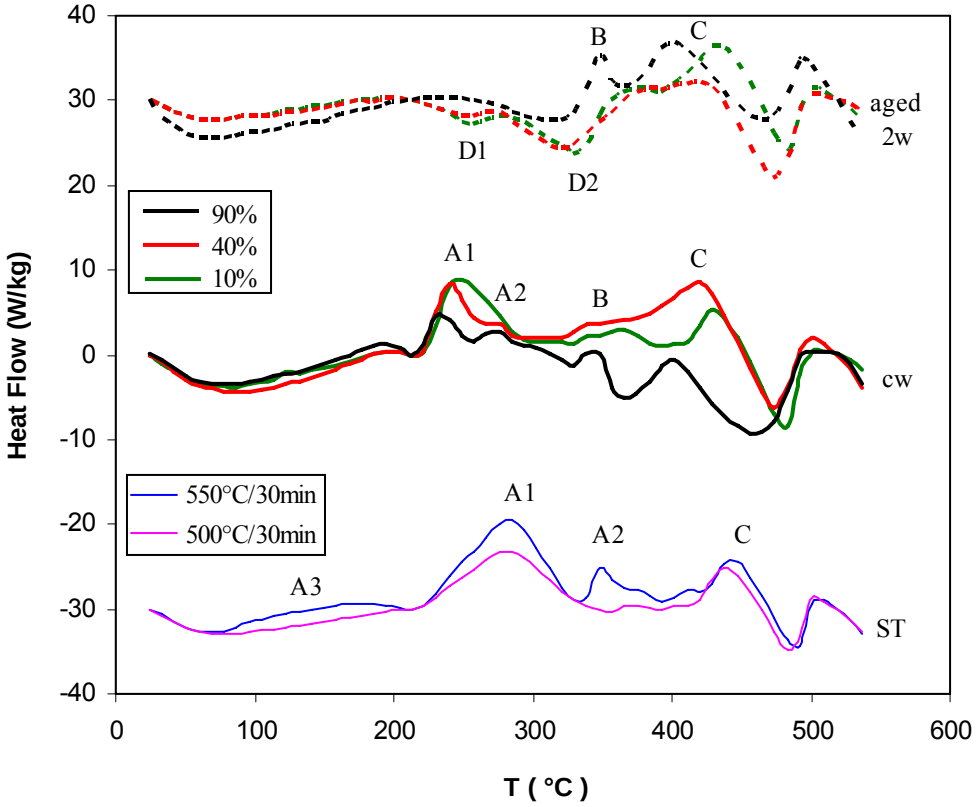
Heat Flow (W/kg)
T (°C)
90%
40%
10%
550°C/30min
500°C/30min
aged 2w
cw
ST
A1
A2
A3
B
C
D1
D2
D

g.

h.

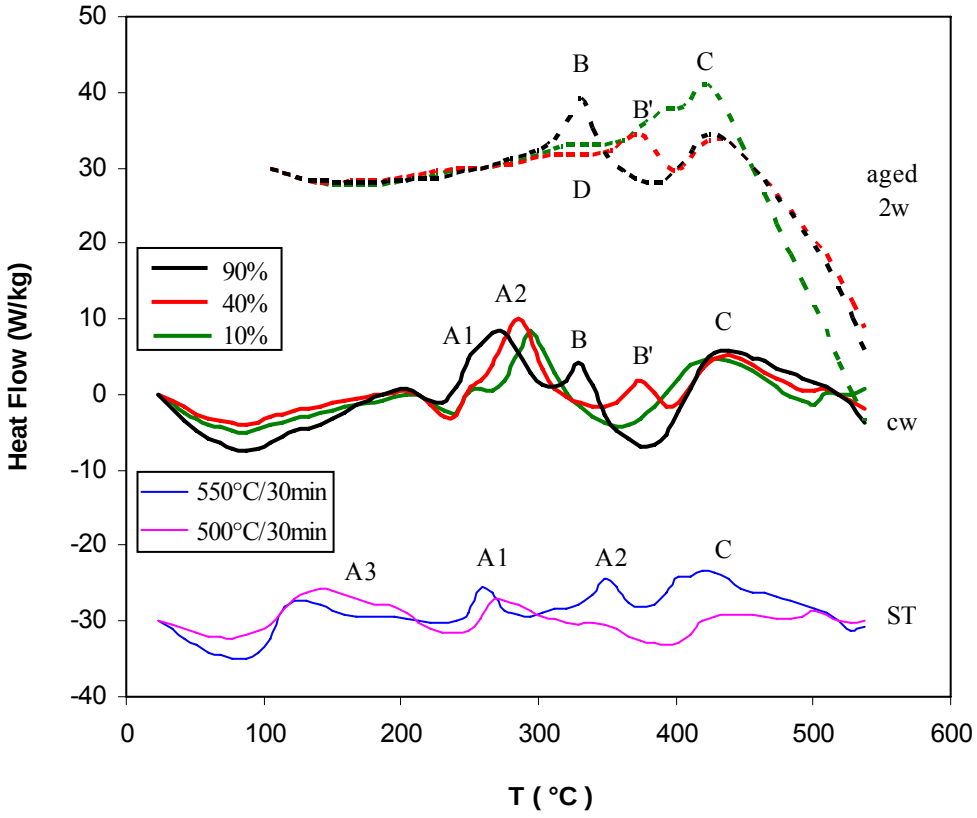

i.

Figure 5.56 DSC curves: a. Al, b. A2, c.A3, d.A4, e. A5, f. A6, g. A7, h. A8, i. A9

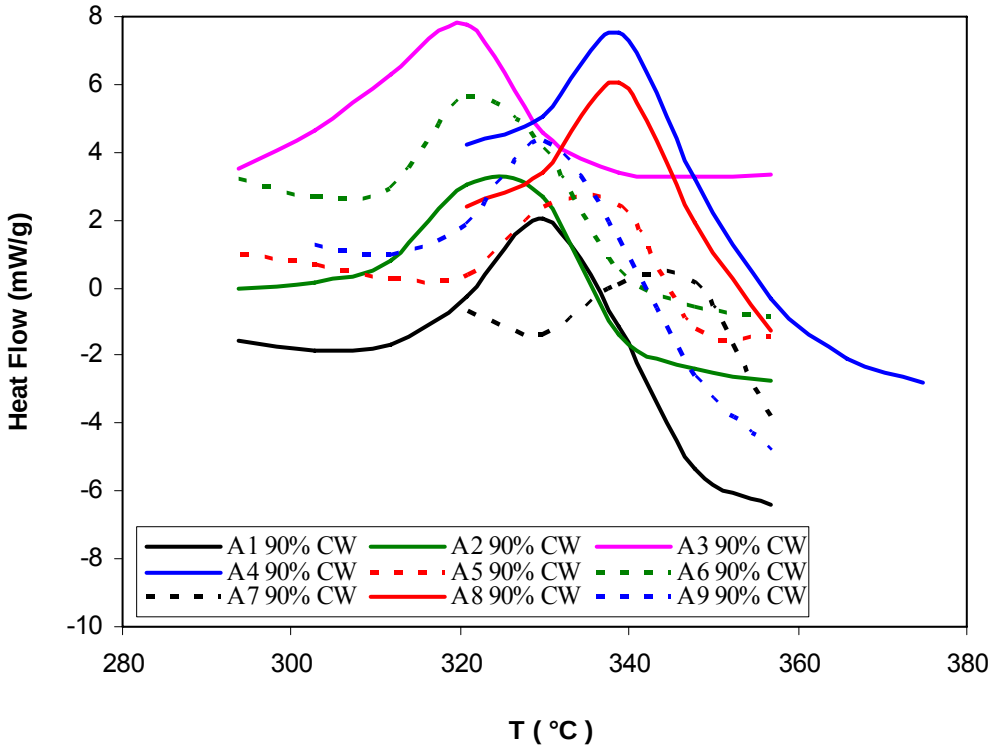

Figure 5.57 DSC curves of all the 90% cold-rolled alloys showing effect B

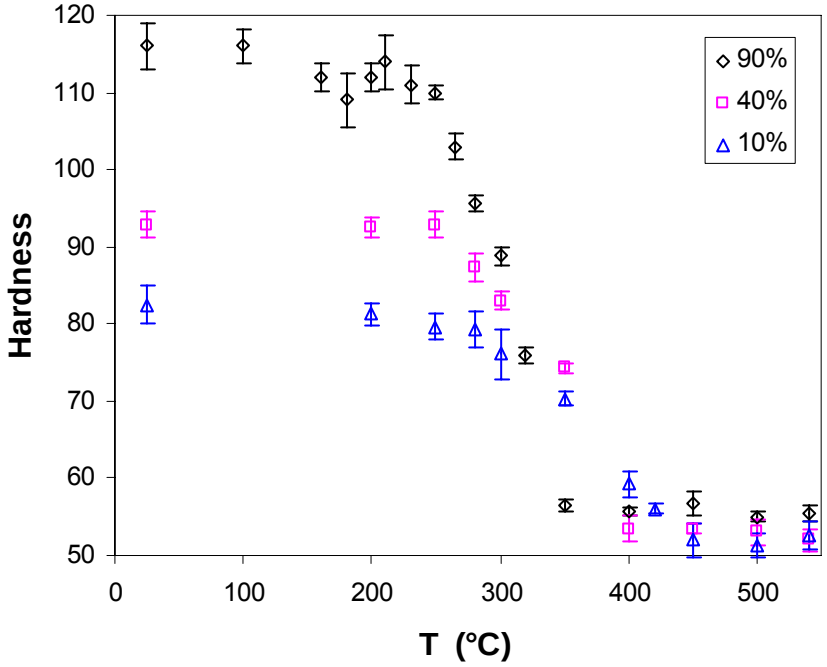

Figure 5.58 Hardness of alloy A9 heated in the DSC at a heating rate of 10°C/min

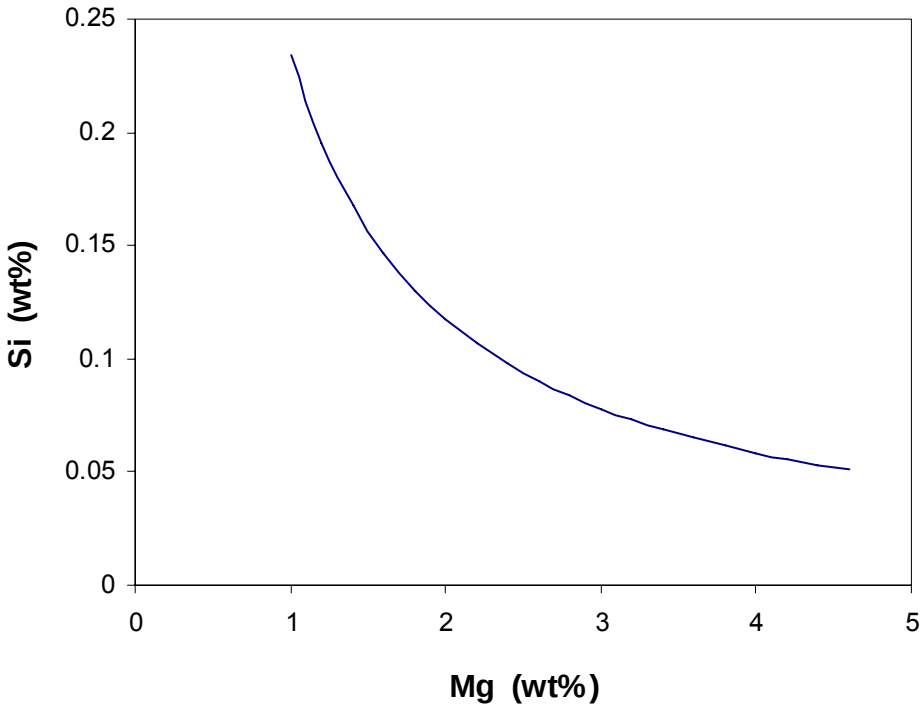

Figure 5.59 Estimation of the solvus of Mg_2Si in an Al-Mg-Si phase diagram at 500°C based on a regular solution model approach (see equation (6.4))

References

1. Lange, N.A. and Forker, G.M., ***Lange's Handbook of Chemistry*** (10th edition), New York, McGraw-Hill Book Company, 1967.
2. Blanc, C., Roques, Y. and Mankowski, G., Corrosion Sci., **40**, 1998, p. 1019.
3. Sneed, M.C. and Brasted, R.C., ***The elements and compounds of group IVA (Vol.7)***, Comprehensive inorganic chemistry, New York, D. Van Nostrand Company, INC., 1958.
4. Starink, M.J. and Mellor, B., ***Advanced Materials I, Part III/IV Course***, Univerisity of Southampton, 2002.
5. Ansara, I., Int. Mater. Rev., **24**, 1979, p. 20.
6. Davies, R., Dinsdale, A., Gisby, J., Robinson, J. and Martin, S., Calphad, **26**, 2002, p. 229.
7. Cama, H., ***MTDATA calculations for alloys cast for Southampton University***, Innoval Technology Ltd., Banbury, 2004.
8. Sanders, R.E., Baumann, S.F. and Stumpf, H.C., ***Wrought Non-Heat-Treatable Aluminum Alloys***, in *Aluminium Alloys---Contemporry Research and Applications*, Vasudevan, A.K. and Doherty, R.D. (Editors), London, Academic Press, Inc., 1989.
9. Go, J., Poole, W.J., Militzer, M. and Wells, M.A., Mat. Sci. Technol., **19**, 2003, p. 1361.
10. Wang, S.C., Zhu, Z. and Starink, M.J., J. Microsc.-Oxf., **217**, 2005, p. 174.
11. Miao, W.F. and Laughlin, D.E., Scripta Mater., **40**, 1999, p. 873.
12. Miao, W.F. and Laughlin, D.E., Metall. Mater. Trans. A, **31**, 2000, p. 361.
13. Starink, M.J. and Dion, A., Thermochim. Acta, **417**, 2004, p. 5.
14. Yao, J.Y., Graham, D.A., Rinderer, B. and Couper, M.J., Micron, **32**, 2001, p. 865.
15. Esmaeili, S., Wang, X., Lloyd, D.J. and Poole, W.J., Metall. Mater. Trans. A, **34**, 2003, p. 751.
16. Chen, L. and Morris, J.G., Scripta Metall Mater, **18**, 1984, p. 1365.
17. Ratchev, P., Verlinden, B., De Smet, P. and Van Houtte, P., Acta Metall. Mater., **46**, 1998, p. 3523.
18. Yan, J., ***Strength modelling of Al-Cu-Mg type alloys***, PhD thesis, School of Engineering Sciences, University of Southampton, 2006.
19. Kovarik, L., Miller, M.K., Court, S.A. and Mills, M.J., ***Atom probe tomography study of GPB zones in Al-Mg-Cu(-Si) alloys***, in *International conference on solid-solid phase transformations in inorganic materials 2005*, Howe, J. (Editor), Phoenix, Arizona, USA, TMS (The Minerals, Metals & Materials Society), 2005.
20. Gouma, P.I., Lloyd, D.J. and Mills, M.J., Mater. Sci. Eng. A, **319**, 2001, p. 439.
21. Marioara, C.D., Andersen, S.J., Jansen, J. and Zandbergen, H.W., Acta Mater., **51**, 2003, p. 789.

22. Hutchinson, C.R. and Ringer, S.P., Metall. Mater. Trans. A, **31**, 2000, p. 2721.
23. Lee, K.J., Scripta Mater., **40**, 1999, p. 759.
24. Zurob, H.S., Hutchinson, C.R., Brechet, Y. and Purdy, G., Acta Mater., **50**, 2002, p. 3075.
25. Wang, S.C., Starink, M.J. and Gao, N., Scripta Mater., **54**, 2006, p. 287.
26. Wang, S.C. and Starink, M.J., Int. Mater. Rev., **50**, 2005, p. 193.

6 A Yield Strength Model for Ageing Behaviour of Cold-Worked Al-Mg(-Cu)-Si-Mn Alloys

6.1 Introduction

In the previous chapter, the artificial ageing behaviour of nine Al-Mg(-Cu)-Si-Mn alloys have been investigated using hardness tests, tensile tests, DSC analysis, SEM/EDS and TEM. In order to understand them quantitatively, a model will be developed. Thus in this chapter, a physical framework including models for the microstructure evolution during artificial ageing, which includes a precipitation model and a dislocation evolution model, and a strengthening model combining the contributions of solid-solution strengthening, dislocation strengthening (i.e. work hardening & recovery) and precipitation hardening, will be developed.

In the model for microstructure evolution, a precipitation model will be developed based on the SZ model to describe precipitate evolution (including volume fraction and mean precipitate size) during ageing. Subsequently, a dislocation evolution model will be proposed for dislocation generation due to work hardening and dislocation annihilation due to static recovery occurring during ageing. After that, a yield strength model will be established to quantitatively elucidate various contributions to yield strength. The model will be calibrated by available experimental data, and tested using independent (unseen) data. Finally, the modelling results will be presented followed by a discussion.

To limit the model complexity some simplifications will be made. For example, for work hardening, a one-parameter (effective dislocation density) model will be utilized. An accuracy of about 8.6 MPa will be achieved over a range of 212 MPa, which is about 4.1% of the total range of strengths. The good performance of the model indicates that the simplifications do not influence the accuracy significantly, whilst providing some benefits such as model transparency and reduced programming and computing time.

6.2 Microstructure evolution

During isothermal ageing the microstructure of the cold-worked samples changes. The main changes include: the nucleation, growth and coarsening of precipitates; the annihilation of dislocations generated during previous cold work prior to ageing and cell

formation and evolution due to recovery. In this study, a precipitation model will be developed to describe the nucleation, growth and coarsening of precipitates. A dislocation evolution model will be proposed to treat dislocation annihilation due to recovery during ageing. The initial dislocation density right before ageing will be obtained from a work hardening model, which will be incorporated into the dislocation evolution model. To keep the model relatively simple, the formation of cells and their evolution will not be considered in the model.

6.2.1 Precipitation model

The alloys studied in this project contain Al, Mg, Cu and Si with Cu/Mg ratios (wt%) at 0-0.4 and Si/Mg ratios (wt%) at 0.05-0.15. Therefore, as discussed in literature review, the precipitation sequences in these alloys are complicated, and depend on the alloy's composition and pre-strains. In the present precipitation model, based on the experimental results from mechanical testing, SEM/EDS, TEM and DSC, the following simplifying assumptions were used:

(1) No clusters/zones form during artificial ageing of the cold-worked alloys.

(2) Since the alloys have substantial Mg but small additions of Cu and Si, both the S and β″ phases may form depending on alloy composition during artificial ageing. There is no competition between the formation of S and β″ phases due to a large amount of Mg available in the matrix.

(3) S phase has a fixed stoichiometry of Al_2CuMg and the fixed stoichiometry for β″ phase is Mg_2Si.

(4) All precipitation hardening is caused by these two phases: S and β″.

Therefore, the precipitation model simplifies the microstructure evolution and strengthening of these alloys by only considering the formation and dissolution of two types of precipitates: S and β″, which in most alloys exist concurrently during artificial ageing. The components of the precipitation model include:

- A thermodynamic model for prediction of the solvi boundaries for the strengthening phases S and β″, based on the solubility product (this is essentially a regular solution model).

- A kinetic model for prediction of the fraction transformed, the average precipitate size and volume fraction of precipitates (S and β″) as a function of alloy composition, ageing temperature, time and prestrain (i.e. cold-rolling reduction).

The output of the precipitation model, e.g, the average precipitate size and volume fraction of precipitates will be used as the input of the precipitation strengthening model. This will be discussed in section 6.3.

6.2.1.1 Thermodynamic model for solvi prediction

6.2.1.1.1 Solvi prediction of S and β″ phases

The regular solution model will be used to calculate the solvi of S and β″ phases in the Al-rich matrix. In general, it can be expressed as follows.

The solvus of a phase i (intermetallic phase or precipitate phase) with fixed stoichiometry of $M_mA_aB_b$ (M is the main constituent of the alloy and A, B are the alloying elements) is given by [1-3]:

$$(c_e^A)^a (c_e^B)^b = \Delta S_i \exp(-\frac{\Delta H^i}{RT}) \qquad \textbf{(6.1)}$$

where ΔH^i is the standard formation enthalpy per unit of phase i, c_e^A and c_e^B are the solubilities of alloying elements *A* and *B* (in atomic fraction), respectively and ΔS_i is the standard formation entropy which is assumed to be a constant.

Meanwhile, when the phase i dissolves, the concentration of elements A and B in solid solution is fixed by the stoichiometry of the reaction, hence the following relation exists [1]:

$$c_e^A = c_0^A - \frac{a}{b}(c_0^B - c_e^B) \qquad \textbf{(6.2)}$$

where c_0^A and c_0^B are the initial concentrations of the alloying elements *A* and *B* dissolved in the matrix at the start of ageing, respectively.

Thus, by solving equations (6.1) and (6.2), c_e^A and c_e^B can be determined.

Using the concepts discussed above, the solvi for S and β″ phases can be predicted by the following two sets of equations:

$$\begin{cases} (c_e^{Cu})(c_e^{Mg}) = c_{0,S}\exp(-\dfrac{\Delta H^S}{RT}) \\ c_e^{Mg} = c_0^{Mg} - (c_0^{Cu} - c_e^{Cu}) \end{cases} \quad \textbf{(6.3)}$$

$$\begin{cases} (c_e^{Mg})^2(c_e^{Si}) = c_{0,\beta}\exp(-\dfrac{\Delta H^\beta}{RT}) \\ c_e^{Mg} = c_0^{Mg} - 2(c_0^{Si} - c_e^{Si}) \end{cases} \quad \textbf{(6.4)}$$

(In the above equations, all concentrations are in atomic fractions.)

The superscripts *S* and β represent S and β″ phases, respectively.

These two sets of equations lead to a quadratic and cubic equation which can be solved by standard solution equations.

In the above solvi prediction models, the values of the parameters can be obtained from literature for both phases. For β″ phase, ΔS_β and ΔH^β were obtained from [4]:

$$\begin{cases} \Delta S_\beta = \exp[112\ \text{kJ/(mol.K)}/R] = 7.09\times10^5 \\ \Delta H^\beta = 95.9\ \text{kJ/mol} \end{cases}$$

For S phase, ΔS_S and ΔH^S can be obtained from [3]:

$$\begin{cases} \Delta S_S = 5.0\times10^5 \\ \Delta H^S = 77\ \text{kJ/mol} \end{cases}$$

6.2.1.1.2 Prediction of undissolved particles

During solidification, depending on the alloy composition, some insoluble intermetallic phases will form, which might not be dissolved during subsequent solution treatment depending on the solutionising temperature and time. These undissolved intermetallics will influence the initial solute concentration dissolved in the matrix, which is available for the formation of precipitate phases during ageing.

In the alloys studied in this project, as shown in chapter 5, intermetallic phases Mg_2Si, $Al_{12}(Fe,Mn)_3Si$ and $Al_6(Fe,Mn)$ were detected by SEM/EDS in the cold-worked samples. Only the phases containing Mg, Si or Cu will influence the formation of the strengthening phases S and β″. Since there is substantial Al and Mg in the matrix, the three intermetallic phases do not significantly influence the formation of S precipitates. However, the formation of the two Si containing intermetallic phases (Mg_2Si and $Al_{12}(Fe,Mn)_3Si$) will influence the formation of β″ phase during subsequent ageing. The formation of Mg_2Si

and $Al_{12}(Fe,Mn)_3Si$ undissolved particles during solidification and subsequent solution treatment involves a competition for solute element Si. The fraction of Si in the $Al_{12}(Fe,Mn)_3Si$ phase (i.e, 1/16) is much lower than that in the Mg_2Si phase (i.e., 1/3), hence, for evaluation of the amount of Si available in the matrix for precipitation during ageing, only the formation of the intermetallic phase Mg_2Si is considered in the model for simplicity.

Using the regular solution model, the amount of intermetallic phase Mg_2Si formed during solution treatment can be calculated by:

$$x_{Mg_2Si} = 3(c_g^{Si} - c_e^{Si}) \qquad \textbf{(6.5)}$$

where c_g^{Si} is the gross concentration of Si content of a alloy and c_e^{Si} is the solubility of Si in the matrix at the solutionising temperature, T_s.

Meanwhile, the amount of undissolved S phase formed during solution treatment can be evaluated by:

$$x_{Su} = 4(c_g^{Cu} - c_e^{Cu}) \qquad \textbf{(6.6)}$$

where c_g^{Cu} is the gross concentration of Cu content of the alloy and c_e^{Cu} is the solubility of Cu in the matrix at the solutionising temperature, T_s. However, for the present alloys, the amount of Cu is too low to cause undissolved S phase intermetallics.

Consequently, the effective solute concentration or the initial concentration of alloying elements Cu, Mg and Si (c_0^{Cu}, c_0^{Mg} and c_0^{Si} in (6.3) and (6.4)) dissolved in the matrix can be expressed by:

$$\begin{cases} c_0^{Cu} = \dfrac{c_g^{Cu} - \dfrac{1}{4}x_{Su}}{1 - x_{Su} - x_{Mg_2Si}} \\ c_0^{Mg} = \dfrac{c_g^{Mg} - \dfrac{2}{3}x_{Mg_2Si} - \dfrac{1}{4}x_{Su}}{1 - x_{Su} - x_{Mg_2Si}} \\ c_0^{Si} = \dfrac{c_g^{Si} - \dfrac{1}{3}x_{Mg_2Si}}{1 - x_{Su} - x_{Mg_2Si}} \end{cases} \qquad \textbf{(6.7)}$$

where c_g^{Mg} is the gross concentration of Mg content in the alloy.

6.2.1.2 Kinetic model for microstructure evolution

A kinetic model based on the SZ model (see section 3.4.2 and reference [3]), is applied in the present model to describe the microstructure development including mean size and volume fraction of the precipitates.

6.2.1.2.1 Volume fraction of the precipitates

According to the SZ model [5, 6], the fraction transformed for the precipitate phases S and β″ during isothermal ageing can be expressed as:

$$\alpha_S(T,t) = 1 - \left(\frac{[k_S(T,\varepsilon)t]^{n_S}}{\eta_i} + 1\right)^{-\eta_i} \quad \textbf{(6.8)}$$

$$\alpha_\beta(T,t) = 1 - \left(\frac{[k_\beta(T,\varepsilon)t]^{n_\beta}}{\eta_i} + 1\right)^{-\eta_i} \quad \textbf{(6.9)}$$

where n_S and n_β are the reaction exponent (or Avrami exponent) for the precipitation of S and β″ phases, respectively. η_i is the impingement exponent. $k_S(T,\varepsilon)$ and $k_\beta(T,\varepsilon)$ are temperature and pre-strain dependent factor for the formation of S and β″ phases, respectively. They are given in an Arrhenius form as follows:

$$k_S(T,\varepsilon) = k_{0,S}(\varepsilon)\exp\left(-\frac{E_{ppt}^S}{RT}\right) \quad \textbf{(6.10)}$$

$$k_\beta(T,\varepsilon) = k_{0,\beta}(\varepsilon)\exp\left(-\frac{E_{ppt}^\beta}{RT}\right) \quad \textbf{(6.11)}$$

where E_{ppt} is the activation energy for the precipitation reaction, the superscripts S and β stand for phase S and β″, respectively. $k_{0,S}(\varepsilon)$ and $k_{0,\beta}(\varepsilon)$ are pre-exponential factors for the precipitation of S and β″ phase depending on the pre-strain of the alloy subjected to during cold work before ageing.

In equations (6.8) to (6.11), some of the parameters can be obtained from literature. Following literature [3], n_S is taken as 2.5 throughout the model. n_β is chosen as the same value as n_s, i.e., n_β is also fixed at 2.5 throughout this study. $\eta_i = 1$ is used in this model following literature [3, 5]. According to literature [3], the activation energy for S phase formation is taken as 152 kJ/mol. Precipitation is a diffusion controlled process, so the activation energy for diffusion may influence the activation energy for precipitation. The precipitation of β″ phase involves the diffusion of Mg and Si atoms in Al, whilst the

precipitation of S phase involves the diffusion of Mg and Cu atoms in Al. The activation energies for diffusions of Mg, Cu and Si atoms in Al are 130.4, 136.0 and 137.0 kJ/mol respectively [7], which are very close to each other. Hence the activation energy for β″ precipitation is presumed to be identical to that of S formation, i.e. 152 kJ/mol.

In order to determine $k_{0,S}(\varepsilon)$ and $k_{0,\beta}(\varepsilon)$, the influence of pre-deformation on the precipitation during ageing is to be described mathematically first. Dislocations formed during pre-deformation will provide heterogeneous nucleation sites for precipitation [8, 9], hence precipitation will generally be facilitated by deformation. In order to determine the relation between $k_{0,S}(\varepsilon)$ or $k_{0,\beta}(\varepsilon)$ and pre-strain ε, the following assumptions are made:

- All dislocations are potential S and β″ phases nucleation sites;
- Both the number of S phase nuclei, N_S, and the number of β″ phase nuclei, N_β, are proportional to the initial dislocation density, ρ_0, at the start of ageing;
- There are enough dislocations available for S phase and β″ phase nucleation, i.e., there is no significant competition for the available nuclei in the process of the nucleation of the two phases;
- The pre-exponential factors, $k_{0,S}(\varepsilon)$ and $k_{0,\beta}(\varepsilon)$, are proportional to the number of nuclei.

These assumptions lead to the following proportionality:

$$k_{0,i}(\varepsilon) \propto N_i \propto \rho_0 \qquad (i = S, \beta)$$

Meanwhile, the following relation exists [10]:

$$\Delta\tau_d^0 = \alpha_\rho G b \rho_0^{1/2} \qquad \textbf{(6.12)}$$

where α_ρ is a dimensionless constant, and following analysis in the literature [11, 12] it is here taken as 0.3.

So, the initial dislocation density ρ_0 is proportional to the square of the critical resolved shear stress (CRSS) increment due to dislocation strengthening, $\Delta\tau_d^0$, at work hardening state, i.e.,

$$\rho_0 \propto (\Delta\tau_d^0)^2$$

As to be discussed later (in section 6.2.2.1) in the work hardening model, the following relation exists:

$$\Delta\sigma_d^0 = M\Delta\tau_d^0 = K_{wh}\varepsilon^{n_{wh}} \qquad \textbf{(6.13)}$$

where $\Delta\sigma_d^0$ is the stress contribution due to dislocation strengthening, and M is the Taylor factor. The meanings of the other variables in the equation are referred to section 6.2.2.1.

Hence the relation between $\Delta\tau_d^0$ and strain for the alloys studied can be expressed by:

$$\Delta\tau_d^0 \propto \varepsilon^{n_{wh}}$$

Hence

$$\rho_0 \propto (\varepsilon)^{2n_{wh}}$$

Thereby, the following proportionality exists for the relation between $k_{0,S}(\varepsilon)/k_{0,\beta}(\varepsilon)$ and ε:

$$k_{0,i}(\varepsilon) \propto (\varepsilon)^{2n_{wh}} \qquad (i = S, \beta)$$

Subsequently, the following expression can be obtained:

$$k_{0,i}(\varepsilon) = k_{\varepsilon,i}\varepsilon^{2n_{wh}} + k_{ND,i} \quad (i = S, \beta) \qquad \textbf{(6.14)}$$

where k_ε and k_{ND} are constants.

This relation can be justified by DSC data. The justification is explained as follows.

As shown in Chapter 5, for cold-rolled alloy A9, for all three reductions (10%, 40% and 90%), DSC data showed that mainly S phase precipitation occurs in the temperature range up to 300°C during DSC runs. Moreover, the peak of S formation shifts to higher temperature with decreasing cold-rolling reduction (see Figure 6.1). Using the concept of equivalent time described in [13], the temperature to reach a particular stage (e.g. peak temperature T_p) in the formation of a phase at constant heating rate can be converted to a time (i.e. equivalent time t_p) to reach the same stage at an isothermal temperature. Hence, the change of T_p with the level of cold work during DSC is directly related to a change of t_p with cold work.

According to the DSC results, a different precipitation sequence to that for cold-worked samples may occur for the solution-treated (at 500°C/30 min or 550°C/30 min) samples of alloy A9. In the solution-treated samples, clusters/GPB zones, β″ and Q precipitation may

occur, which may suppress the precipitation of S phase during the DSC runs, especially for 550°C/30 min solution-treated specimen (see Figure 6.1). Hence the precipitation sequence of solution-treated samples may be completely different from that of cold-worked samples. Therefore, the solution-treated condition (0%) will not be considered here.

From the DSC data, the peak temperatures (T_p) for each cold-rolling reduction can be determined. They are 294.9, 286.4 and 271.8°C for 10%, 40% and 90% reductions, respectively. Subsequently, the following equation (from [13]) was used to calculate the equivalent time, t_p, corresponding to the peak in the DSC thermograms:

$$t_p \approx 0.786 \frac{T_p}{\beta_{hr}} \left(\frac{RT_P}{E^S_{ppt}}\right)^{0.95} \exp\left[\frac{E^S_{ppt}}{R}\left(\frac{1}{T_{iso}} - \frac{1}{T_p}\right)\right] \qquad \textbf{(6.15)}$$

where β_{hr} is the heating rate used during the DSC scan; T_{iso} is the isothermal ageing temperature used (170°C in this study). The values of t_p obtained for alloy A9 are shown in Figure 6.2.

According to (6.8), at a certain α_S the following relation holds:

$$k_{0,S}(\varepsilon) \propto 1/t_p(\varepsilon)$$

The calculated values of $1/t_p(\varepsilon)$ from DSC data have the following relation:

$$1/t_p(\varepsilon) = g_1 \varepsilon^{2n_{wh}} + g_2 \qquad \textbf{(6.16)}$$

In the equation, n_{wh} is the work hardening exponent. It is obtained from work hardening model (see section 6.2.2.1). Hence its value is fixed. g_1 and g_2 are constants, but their values will change depending on the fitting to the measured $1/t_p(\varepsilon)$ values used.

The fit to the measured $1/t_p(\varepsilon)$ values using equation (6.16) is shown in Figure 6.2. As shown in the figure, the prediction agrees well with the measured results from DSC data, which, to some extend, justifies that equations (6.14) and (6.16) provide a reasonable description of the relation of $1/t_p$ and $k_{0,S}/k_{0,\beta}$ with ε.

As shown in Figure 6.3, for cold-worked samples of alloy A1, only β″ precipitation occurs in the temperature range up to 300°C during DSC runs, and the higher the cold-rolling reduction, the lower the peak temperature. The same calculation procedures as discussed above can be performed on alloy A1, and the results are shown in Figure 6.4. Since for the

solution-treated samples only β″ precipitation occurs in the temperature range up to 300°C too, the solution-treated condition (i.e. strain is 0) is considered in this case. As shown in the figure, the prediction results using equation (6.16) are not so good over the whole strain range, especially in the low strain range. This may be explained as follows.

According to literature, β″ not only forms on dislocations, but can also form in the matrix free of dislocations [14-16]. However, equation (6.14) was derived based on the assumption that precipitates form exclusively on dislocations. This may explain the limitation of equation (6.16) when it is applied to β″ phase formation. There may also be another reason, i.e., in the DSC runs, β′ formation usually follows β″ formation for Al-Mg-Si alloys [17-22]. In some cases, overlap between β″ formation and β′ formation occurs during the DSC run. In that case, a broader exothermic peak instead of a narrow and sharp one may be observed. As shown in Figure 6.3, both solution-treated specimens show a broader exothermic peak as compared to the cold-worked specimens. This indicates that the overlapping of the peaks may occur during the DSC runs, and the measured peak temperature of the overlapping β″/β′ effect in the solution-treated specimens for alloy A1 would be higher than the actual peak temperature of β″ formation only. The DSC results of solution-treated alloy A3 show a comparatively narrow and sharp formation peak of β″ (see Figure 5.55c). The peak temperature for β″ formation for solution-treated alloy A3 is lower than that in the solution-treated alloy A1. Using the peak temperature obtained from DSC results of solution-treated alloy A3, the fitting results using equation (6.16) are slightly improved (see Figure 6.5). However, it is interesting to note that there are some data on the peak temperatures for β″ formation at various strains (0-5%) for an AA6111 alloy (typical composition Al-0.75Mg-0.85Si) from literature [23]. In [23], the peak temperatures measured by DSC at a heating rate of 10°C/min (same heating rate as that in this study) are 254.7, 251.7 and 246.5°C for 0, 2 and 5% cold work, respectively. Using 254.7°C as the peak temperature for zero strain from [23] and the measured data for alloy A1 with 10%, 40% and 90% cold work, based on equation (6.16), a much better fit is obtained, as shown in Figure 6.6a. The fitting results are almost same if all three data points from [23] were included in the fitting, as shown in Figure 6.6b. It is noted that excluding the solution-treated condition, the prediction for 10%, 40% and 90% cold-worked conditions can be very close to the measured results as shown in Figure 6.7. In this study, only the ageing behaviour of cold-

worked samples is considered. Hence, the relation expressed in equation (6.16) is thought to be valid for the cold-worked conditions.

Therefore, as discussed above, the relation between $k_{0,S}/k_{0,\beta}$ and ε expressed by (6.14) is thought to be reasonable and applicable in the scope of this study.

After determining the transformed fraction, the amount of S and β″ phase formed during ageing can be given by:

$$x_S(T,t) = 4\alpha_S(T,t)(c_0^{Cu} - c_e^{Cu}) \qquad \textbf{(6.17)}$$

$$x_\beta(T,t) = 3\alpha_\beta(T,t)(c_0^{Si} - c_e^{Si}) \qquad \textbf{(6.18)}$$

Then, the volume fraction of the precipitates can be expressed as [3]:

$$f_i(T,t) = \frac{x_i V_{at}^i}{x_S V_{at}^S + x_\beta V_{at}^\beta + (1 - x_S - x_\beta)V_{at}^m} \approx x_i \frac{V_{at}^i}{V_{at}^m} \qquad (i = S, \beta) \qquad \textbf{(6.19)}$$

where V_{at} is the mean atomic volume, the superscripts *S*, β and *m* stand for S phase, β″ phase and the Al-rich matrix, respectively. From the respective crystal structures, it can be shown that $V_{at}^S \approx V_{at}^m$ [3]. Therefore, for S phase, the volume fraction, f_S , can be approximated by its atomic fraction, x_S , i.e., $f_S \cong x_S$.

For β″ phase different crystal structures have been reported in the literature. The crystal structure of β″ phase was generally reported to be monoclinic, however, its lattice parameters reported were different (see [24]). Hence due to the uncertainty of the crystal structure, it is difficult to calculate the mean atomic volume for β″ phase. A simplified treatment is used instead.

In the β″ (Mg_2Si) phase, there are two Mg atoms and one Si atom, totalling three atoms. Double diameters of Mg atom (2×0.32 nm) plus one diameter of Si atom (0.234 nm) are equal to 0.874 nm, which is close to triple diameters of Al atom (3×0.286 nm=0.858 nm). Hence, the mean atomic volume of β″ phase, V_{at}^β , should be nearly equal to that of the matrix, V_{at}^m . Thus, the following relation is used*:

* Using this simplified treatment, the approximation, $V_{at}^S \approx V_{at}^m$, can also be derived. This is shown as follows. In S phase, there are four atoms in total (two Al atoms, one Mg atom and one Cu atom). Two diameters of Al atom (2×0.286 nm), one diameter of Cu atom (0.256 nm) and one diameter of Mg atom (0.32 nm) amount to 1.148 nm, which is very close to quadruple diameters of Al atoms (i.e. 1.144 nm). Hence, the following approximation is valid: $V_{at}^S \approx V_{at}^m$.

$$f_\beta \cong x_\beta \qquad \textbf{(6.20)}$$

6.2.1.3 Precipitate sizes

In the present model, a simple analytical approach proposed in the literature [3, 25] is applied to model the average size of the precipitates. In this approach, assuming new nuclei grow in three dimensions and retain their initial shape, the average size of precipitates in a particular direction during the nucleation and growth stage, $\bar{l}_g$, grows according to [3, 26]:

$$\bar{l}_{g,i}(t) = \bar{l}_{0,i}\alpha_i^{1/3} \quad (i = S, \beta) \qquad \textbf{(6.21)}$$

where $\bar{l}_0$ is the average precipitate size at the start of coarsening, and the subscripts *S* and β stand for phase S and β″, respectively.

Assuming that the coarsening of the precipitates complies with the classical LSW coarsening theory, the average size at coarsening stage, $\bar{l}_c$, is given by [3]:

$$[\bar{l}_{c,i}(t)]^3 = (\bar{l}_{0,i})^3 + k_{c,i}(T,\varepsilon)t \qquad (i = S, \beta) \qquad \textbf{(6.22)}$$

where

$$k_{c,i}(T,\varepsilon) = k_{c0,i}(\varepsilon)\exp(-\frac{E_{co}^i}{RT}) \qquad (i = S, \beta) \qquad \textbf{(6.23)}$$

where E_{co} is the activation energy for coarsening. To limit the number of fitting parameters in the model, the activation energy for coarsening is taken identical to the activation energy for precipitation, i.e., 152 kJ/mol is used throughout the model; k_{c0} is a pre-exponential factor depending on pre-strain, ε. It is assumed to have a similar dependence on strain as $k_0(\varepsilon)$ does and hence it follows:

$$k_{c0,i}(\varepsilon) = p_{k,i}k_{0,i}(\varepsilon) \qquad (i = S, \beta) \qquad \textbf{(6.24)}$$

where p_k is a constant, subscripts *S* and β stand for S and β″ phases, respectively.

There is a transition from growth to coarsening, but this transition can not be captured by the SZ and JMAK type models [2]. However, a simple approximation is devised to deal with the transition by taking [3]:

$$\bar{l}_i(t) = \bar{l}_{g,i}(t) + \bar{l}_{c,i}(t) - \bar{l}_{0,i} \qquad (i = S, \beta) \qquad \textbf{(6.25)}$$

At the coarsening stage, $\bar{l}_g$ in equation (6.25) is equal to $\bar{l}_0$, thus equation (6.25) is reduced to $\bar{l}(t) = \bar{l}_c(t)$. Hence at the coarsening stage, equation (6.25) is essentially the same as equation (6.22). At the nucleation and growth stage, the approximation $\bar{l}_c(t) \approx \bar{l}_0$ is valid. Hence equation (6.25) can be used to describe both the nucleation/growth and coarsening stage under certain conditions [3]. This simple, analytical approach is applied in the present model for the evolution of precipitate size without considering the finer details of the transition.

Combining the thermodynamic model and kinetic model discussed above, the microstructure development including the evolution of volume fraction and mean precipitate size for S precipitates and β″ precipitates can be analytically modelled.

6.2.2 Dislocation evolution model

Dislocation evolution of the cold-worked samples during ageing involves two parts:

- Dislocation generation due to work hardening during cold deformation, which determines the initial dislocation density prior to ageing;
- Dislocation annihilation due to recovery during ageing.

In this section, models for dislocation generation and dislocation annihilation will be proposed to describe dislocation evolution during isothermal ageing.

6.2.2.1 Dislocation generation: work hardening model

In this section, several work hardening models will be used to fit the experimental data on yield strength of cold-worked samples. The model which gives the best fit will be selected.

The strength of a material increases with strain due to dislocation strengthening, and this phenomenon is known as work/strain hardening. The yield strength of a cold-worked alloy, σ_{wh}, can be expressed as

$$\sigma_{wh} = \sigma_{rex} + \Delta\sigma_{wh} \qquad \textbf{(6.26)}$$

where σ_{rex} is the strength of recrystallised material, which can be expressed by (6.48), and $\Delta\sigma_{wh}$ is the strength increase due to work hardening.

In this study, three types of stress-strain relation (work hardening) were used to fit the experimental data. These three types of stress-strain relation are:

- Hollomon equation, which is a simple power law equation expressed as

$$\sigma_{wh} = \sigma_{rex} + K_{wh}\varepsilon^{n_{wh}} \quad \textbf{(6.27)}$$

where K_{wh} is strength coefficient, n_{wh} is the strain hardening exponent and ε is the von-Mises equivalent strain in the case of cold rolling processing. The Hollomon equation is a commonly used empirical work hardening model.

- Voce equation, which can be derived from the KM model (see section 3.2.2.1) and is expressed as [27]

$$\sigma_{wh} = \sigma_1 + (\sigma_s - \sigma_1)[1 - \exp(-\frac{\varepsilon - \varepsilon_1}{\varepsilon_c})] \quad \textbf{(6.28)}$$

where σ_1 and ε_1 represent the initial stress and strain at the start of the test, σ_s represents saturation stress at which the strain hardening rate becomes zero, ε_c is a characteristic strain for the material. ε_1 is generally set as zero, hence the above equation reduces to [27]

$$\sigma_{wh} = \sigma_s - (\sigma_s - \sigma_1)\exp(n_v\varepsilon) \quad \textbf{(6.29)}$$

where $n_v = -1/\varepsilon_c$.

- A modified Voce equation, which is given by [28]

$$\sigma_{wh} = \sigma_s - (\sigma_s - \sigma_1)\exp(n_v\varepsilon^{n_{wh}}) \quad \textbf{(6.30)}$$

where n_{wh} is a constant.

Equations (6.29) and (6.30) can be rewritten as

$$\sigma_{wh} = \sigma_{rex} + K_{wh}[1 - \exp(n_v\varepsilon^{n_{wh}})] \quad \textbf{(6.31)}$$

where $\sigma_{rex} = \sigma_1$ and $K_{wh} = \sigma_s - \sigma_1$. When $n_{wh} = 1$, the above equation reduces to the Voce equation (6.29). If $n_{wh} \neq 1$, it is equivalent to the modified Voce equation (6.30).

As shown in Figure 5.40 in Chapter 5, taking 0.2% proof strength as yield strength, the yield strength of these cold-rolled alloys with different rolling reductions (0, 10%, 40% and 90%) can be well presented by the power law work hardening model, i.e. the Hollomon equation. Moreover, as shown in Figures 5.41 and 5.42, the yield strength

increases with increasing Mg and Cu concentrations and as shown in Figures 7.33 and 7.34, the work hardening rate also increases with Mg and Cu concentrations. Within the Hollomon power law description, these observations show that the strength coefficient, K_{wh}, increases with increasing Mg and Cu contents. Through quantitatively analysing these yield strength data, the following relation between K_{wh} and Mg/Cu contents was obtained:

$$K_{wh} = K_{wh}^{Mg} c_{Mg} + K_{wh}^{Cu} c_{cu} + K_{wh}^{0} \qquad \textbf{(6.32)}$$

where K_{wh}^{Mg}, K_{wh}^{Cu} and K_{wh}^{0} are constants.

Replacing K_{wh} in equations (6.27) and (6.31) with equation (6.32) and fixing n_{wh} as a constant for all the nine alloys, the yield strengths of the cold-worked samples of the nine alloys are used to fit both equations (6.27) and (6.31). The obtained root mean squared errors (RMSEs) are 5.6 MPa, 22.0 MPa and 4.8 MPa for the Hollomon equation (6.27), Voce equation (6.31) ($n_{wh} = 1$) and modified Voce equation (6.31) ($n_{wh} \neq 1$), respectively.

From the above analyses, the following conclusions can be drawn. First, the Voce equation which can be derived from the KM model is not a good representation of the work hardening behaviour of the cold-worked alloys studied in this project. Secondly, the Hollomon equation and the modified Voce equation give similar accuracy (5.6 MPa vs. 4.8 MPa) for the available experimental data. Hence, either can be used to describe the work hardening behaviour of the cold-worked alloys. In this study, the Hollomon equation will be used for the simplicity.

In the following section, a one-parameter dislocation strengthening model will be applied.

According to the one-parameter dislocation strengthening theory, $\Delta\sigma_{wh}$ in (6.26) can be given by the following equation:

$$\Delta\sigma_{wh} = \Delta\sigma_d^0 = M\Delta\tau_d^0 = M\alpha_\rho Gb\sqrt{\rho_0} \qquad \textbf{(6.33)}$$

whilst in the Hollomon equation, $\Delta\sigma_{wh}$ is expressed by

$$\Delta\sigma_{wh} = K_{wh}\varepsilon^{n_{wh}} \qquad \textbf{(6.34)}$$

Hence, the following relation exists

$$\Delta\sigma_{wh} = M\alpha_{\rho}Gb\sqrt{\rho_0} = K_{wh}\varepsilon^{n_{wh}} \quad \textbf{(6.35)}$$

Therefore the initial dislocation density, ρ_0, can be given by

$$\rho_0 = (\frac{K_{wh}\varepsilon^{n_{wh}}}{M\alpha_{\rho}Gb})^2 \quad \textbf{(6.36)}$$

6.2.2.2 Dislocation annihilation: recovery model

The yield strength of a work-hardened alloy will decrease when it is artificially aged or annealed. This phenomenon is recovery or recrystallisation, which depends on the annealing temperature and time. The softening of a cold-worked alloy is due to dislocation annihilation and rearrangement, which leads to the formation of a cell and subsequently to cell growth. During isothermal ageing at 170°C, only recovery will occur, as recrystallisation can not be activated at such low temperature. Therefore, only recovery is considered in the present model. (Note that recrystallisation was observed at higher temperatures during DSC scans, see section 5.3.2.)

Based on a detailed survey on the evidence regarding recovery, Nes [29] found that the fraction residual strain hardening, R_{rec}, defined by equation (3.40), can be commonly presented in terms of a logarithmic time decay law as follows [29]:

$$R_{rec} = 1 - S_{th}(T,\varepsilon)\ln[1+\frac{t}{t_r(T,\varepsilon)}] \quad \textbf{(6.37)}$$

This recovery time law was widely observed for a range of metals, including various cold-rolled Al-Mg alloys with low to very high cold work levels [29, 30].

$S_{th}(T,\varepsilon)$ and $t_r(T,\varepsilon)$ depend on the rate-controlling recovery mechanisms, which include thermally activated glide and solute drag [29]. In the present model, the recovery mechanism in the alloys isothermally aged at 170°C is assumed to be thermally activated glide. Therefore, S_{th} and the relaxation time t_r can be expressed as follows [29]:

$$S_{th} = p_1 T\frac{\sqrt{\rho_0}}{\sigma_{wh} - \sigma_{rex}} \quad \textbf{(6.38)}$$

$$t_r = [p_2\sqrt{\rho_0}\exp(\frac{p_3}{k_B T})]^{-1} \quad \textbf{(6.39)}$$

where p_1, p_2 and p_3 are constants, σ_{wh} and σ_{rex} are the yield stress in work hardened state and fully recrystallised state, respectively. k_B is Boltzmann's constant.

For constant temperature experiments, S_{th} and t_r can be simplified as:

$$S_{th} = p_1^{'} \frac{\sqrt{\rho_0}}{\sigma_{wh} - \sigma_{rex}} \quad \textbf{(6.40)}$$

$$t_r = (p_2^{'} \sqrt{\rho_0})^{-1} \quad \textbf{(6.41)}$$

Meanwhile, the following proportional relation exists according to the work hardening model:

$$\sqrt{\rho_0} \propto \Delta\tau_d^0 \propto (\sigma_{wh} - \sigma_{rex})$$

and thus, the following simplified expressions can be obtained at constant temperature:

$$S_{th} = p_1^{''} \quad \textbf{(6.42)}$$

$$t_r = p_2^{''} (\sigma_{wh} - \sigma_{rex})^{-1} \quad \textbf{(6.43)}$$

σ_{rex} and σ_{wh} can be determined from the solution strengthening model and work hardening model, respectively, and hence R_{rec} can be predicted by combining equations (6.37), (6.42) and (6.43). On the other hand, from the definition of the fraction residual strain hardening, R_{rec}, and dislocation strengthening equation, the following derivation can be obtained in the absence of precipitation:

$$R_{rec} = \frac{\sigma_{rec}(t) - \sigma_{rex}}{\sigma_{wh} - \sigma_{rex}} = \frac{M\alpha_\rho Gb\sqrt{\rho(t)}}{M\alpha_\rho Gb\sqrt{\rho_0}} = \sqrt{\frac{\rho(t)}{\rho_0}} \quad \textbf{(6.44)}$$

where $\sigma_{rec}(t)$ and $\rho(t)$ are the yield strength and the dislocation density at a time, *t*, during recovery in the absence of precipitation, respectively.

Hence the dislocation density evolution during the recovery process can be given by

$$\rho(t) = \rho_0 (R_{rec})^2 \quad \textbf{(6.45)}$$

Subsequently, the dislocation strengthening contribution during recovery can be expressed by

$$\Delta\tau_d(t) = \alpha_\rho Gb\sqrt{\rho(t)} = R_{rec}\Delta\tau_d^0 \quad \textbf{(6.46)}$$

6.3 Strengthening model

In order to model the yield strength of these cold-worked-and-aged alloys, the following contributions have to be considered in the yield strength model:

- Solid-solution strengthening, which is mainly due to Mg and Cu
- Dislocation strengthening, i.e. work hardening & recovery
- Precipitation hardening
- Base strength, covering all minor hardening mechanisms (e.g., intrinsic strength, grain boundary strengthening)

All these contributions are considered, and they will be discussed in detail in this section.

6.3.1 Solid-solution hardening

In the case of multicomponent alloys, a number of models [31-35] have been proposed to determine the strengthening effect due to dissolved alloying elements. A general form can be given as follows:

$$\Delta\tau_{ss} = \sum k_j c_j^{n_{ss}} \quad \textbf{(6.47)}$$

where k_j is a constant related to the properties of the related solute j, c_j is the solute concentration. Theoretical treatments indicate n_{ss} could equal 2/3, 1 or 1/2 [33].

For the nine alloys studied in this project, time dependence of solution strengthening due to Mg and Cu elements is considered and the solid solution hardening due to other elements, e.g., Fe, Mn and Si and grain boundary strengthening are all included in the base strength, σ_b. The yield strength of solution-treated or fully recrystallised alloys, σ_{rex}, is written as

$$\sigma_{rex} = \sigma_b + M\Delta\tau_{ss} \quad \textbf{(6.48)}$$

where M is the Taylor factor. The self-consistent modelling of the plastic deformation of FCC polycrystals gives $M \cong 2.6$ [36]. Therefore, $M = 2.6$ was used throughout the model. $\Delta\tau_{ss}$ is given by:

$$\Delta\tau_{ss} = k_{Mg}(c_{Mg})^{n_{ss}} + k_{Cu}(c_{Cu})^{n_{ss}} \quad \textbf{(6.49)}$$

where k_{Mg} and k_{Cu} are the solid solution strengthening coefficients due to Mg and Cu, respectively; c_{Mg} and c_{Cu} are the concentrations of Mg and Cu, respectively.

In the above equation, the instantaneous concentration of Mg and Cu, c_{Mg} and c_{Cu} during ageing, can be obtained from the precipitation model using the following equations:

$$c_{Mg} = c_0^{Mg} - \frac{2}{3}x_\beta(t) - \frac{1}{4}x_S(t) \quad \textbf{(6.50)}$$

$$c_{Cu} = c_0^{Cu} - \frac{1}{4}x_S(t) \quad \textbf{(6.51)}$$

6.3.2 Dislocation strengthening

Dislocation strengthening includes two contributions, work hardening and recovery, which can be derived from the dislocation evolution model. First, the initial dislocation density, ρ_0, which can be obtained from the work hardening model, is expressed by equation (6.36). Then from the recovery model, the dislocation density evolution during ageing can be derived, which is given by equation (6.45). Hence the dislocation strengthening evolution can be further calculated by equation (6.46).

6.3.3 Precipitation hardening

Both S and β″ precipitates have a very high aspect ratio (S precipitates are generally rod/lath-shaped particles, whilst β″ precipitates are generally reported to be needle/lath-shaped). In this study, both are considered to be nonshearable and by-passed by the Orowan bowing mechanism. This assumption is reasonable and can be supported by literature. For instance, in the study of Starink and co-workers [25, 37], S precipitates were considered to be nonshearable and by-passed by the Orowan looping mechanism and good modelling results were achieved. According to the TEM observations by Donnadieu and Dirras et al. [38, 39], β″ precipitates are predominately by-passed by dislocations. Hence β″ precipitates are also considered to be nonshearable. Since both types of precipitates are not spherical, in order to describe their morphology accurately, two or three parameters (length, width and thickness for lath shape, length and diameter for rod shape) are needed for the three dimensions of the precipitates. In the present model, for simplicity, only one parameter, i.e., the equivalent diameter is used to describe the precipitates. The equivalent

diameter is the diameter of a circle occupying the same area of a non-circular cross section. Using this treatment, the contribution of the precipitates to strengthening can be evaluated by the following equation [3, 37]:

$$\Delta\tau_i = \frac{0.81Gb}{2\pi(1-\upsilon)^{1/2}}\left[\frac{\ln(d_i/b)}{0.615d_i\sqrt{\frac{2\pi}{3f_i}}-d_i}\right] \qquad (i=S,\beta) \qquad \textbf{(6.52)}$$

where υ is the Poisson's ratio for Al, d and f are the equivalent diameter and the volume fraction of the precipitates, respectively. The subscripts S and β represent phases S and β″, respectively.

The obstacle strength of S and β″ precipitates to dislocation movements is at about same order of magnitude and hence a superposition rule should be applied to consider the strengthening contribution due to the two types of precipitates. For two types of obstacles with similar strength, they are usually superposed according to the quadratic addition law [2, 25, 37, 40-42]. Thus, the contribution of the precipitation strengthening, $\Delta\tau_{ppt}$, is taken as:

$$(\Delta\tau_{ppt})^2 = (\Delta\tau_S)^2 + (\Delta\tau_\beta)^2 \qquad \textbf{(6.53)}$$

6.3.4 Combined yield strength model

In the overall yield strength model, the following contributions are considered:

- solid-solution strengthening, $\Delta\tau_{ss}$
- dislocation strengthening, $\Delta\tau_d$, which includes work hardening and recovery
- precipitation hardening, $\Delta\tau_{ppt}$
- base strength, σ_b, which covers all minor hardening mechanisms

In these heavily cold-worked Al-Mg alloys, due to small additions of Cu and Si in the alloys, precipitation hardening may occur during ageing. In this study, dislocations introduced by cold work and precipitates (i.e. S phase and β″ phase) are considered to be strong obstacles to dislocation movement. Therefore, the obstacle strengths responsible for dislocation strengthening, $\Delta\tau_d$ and precipitation hardening, $\Delta\tau_{ppt}$ are of a similar magnitude and the quadratic superposition is applied here [2, 3, 25, 40-42]:

$$(\Delta\tau_{d\&ppt})^2 = (\Delta\tau_d)^2 + (\Delta\tau_{ppt})^2 \quad \textbf{(6.54)}$$

where $\Delta\tau_{d\&ppt}$ is the combined contribution of dislocation strengthening and precipitation hardening.

The obstacle strength due to solid solution hardening is much weaker than that for precipitation and dislocation hardening, and hence a linear addition rule is applied:

$$\Delta\tau_{tot} = \Delta\tau_{ss} + \Delta\tau_{d\&ppt} \quad \textbf{(6.55)}$$

where $\Delta\tau_{tot}$ is total resolved shear stress. Thus the overall yield strength can be given by:

$$\sigma_y(t) = \sigma_b + M\Delta\tau_{tot} \quad \textbf{(6.56)}$$

6.4 Calibration and testing of the model

Throughout sections 6.2 and 6.3, the values of parameters that are known from literature have been indicated; several other parameters will need to be obtained through model calibration. In this section, the methods used to calibrate and test the model will be discussed in detail.

6.4.1 Methods of calibration

In principle, a range of procedures for calibrating and testing can be devised. Two different methods of calibration and testing of the model (see Figure 6.8) will be discussed in this section. Both methods test the accuracy of the model using independent (unseen) data not included in calibration. The solid-solution hardening model will be first calibrated using the tensile testing data of solution-treated (ST) alloys. This is the common calibration step in the two methods. In the subsequent procedures, two different methods are used. The first method (Method I) is a step-by-step calibration and testing of the model. The following steps are included in this method:

① The work hardening model will be calibrated and tested using tensile data of ST alloys and cold-worked alloys with three different cold-rolling reductions (e.g., 10%cw, 40%cw and 90%cw). ②Then the recovery model will be first assessed by using yield strength data of alloy A3. ③Subsequently, the precipitation model will be calibrated together with the recovery model, which includes two steps. First, the recovery model together with β" precipitation model will be calibrated using tensile data of alloys A1-A3 and then the S

precipitation model will be calibrated using the tensile data of alloys A4-A9. At this stage, all parameters are calibrated and the model is ready for testing. ④ Finally, the model will be tested using hardness data, prior to which the conversion of micro-Vickers hardness to yield stress will be performed. The procedures of calibration and testing the model in Method I are shown in Figure 6.8. Thus, in essence, all the parameters in the model are calibrated by fitting tensile data step by step, and the model is tested by using hardness data (see Figure 6.9 for a simplified sketch). In method I, all the tensile data are used for calibration.

In method II, as schematically shown in Figure 6.10, the tensile data will be separated into two parts and only part of tensile data (about 50%) will be used for calibration or training of the model, the remaining tensile data will be used for testing the model. This is a train and test method [2, 40]. Method I is a gradual and progressive process, whilst method II is conducted in a single step. Each method has its own benefits, which will be discussed later after the results of the methods are described.

6.4.2 Calibration of solid-solution hardening model

In (6.48) and (6.49), σ_b, k_{Mg}, k_{Cu} and n_{ss} need to be determined by experimental data. This is achieved as follows.

Tensile specimens of alloys A1-A9 with 40% cold work were re-solution treated at 500°C/30min and subsequently tensile tested. The measured 0.2% proof strengths, $\sigma_{0.2}$, are listed in Table 6.1. These data are used to calibrate the solid-solution hardening models and determine the above-mentioned parameters.

Table 6.1 0.2% PS of solution-treated alloys (unit: MPa)

Alloys	A1	A2	A3	A4	A5	A6	A7	A8	A9
$\sigma_{0.2}$	49.0	64.6	80.3	50.9	65.6	87.3	53.4	66.5	84.2

Taken n_{ss} as 1, 2/3 and 1/2 respectively, using the 0.2% proof strength as yield strength, three sets of parameters σ_b, k_{Mg} and k_{Cu} can be determined by the Least Square Method (LSM). Comparing the root mean squared error (RMSE) using different n_{ss} values, the lowest RMSE can be achieved when $n_{ss}=1$. An analysis of literature data from handbook for aluminium alloys [43] by Yan [3] also indicates that $n_{ss}=1$ best describes data. Therefore, in the solid solution strengthening model, the exponent n_{ss} is taken as 1. The other parameters were determined by the LSM and their values are listed in Table 6.2.

Table 6.2 Calibrated values of parameters in solution strengthening model

Parameter	Value
n_{ss}	1
σ_b	31.5 MPa
k_{Mg}	590 MPa
k_{Cu}	780 MPa

After these parameters were determined, the yield strength of the solution-treated alloys can be modelled using equations (6.48) and (6.49), and the predicted results and experimental results are shown in Figure 6.11. As shown in the figure, the predicted results reflect the experimental results very well with RMSE about 1.4 MPa.

As discussed previously, the base strength σ_b includes the following contributions:

- Intrinsic strength which reflects the yield strength of pure aluminium. According to the ASM aluminium handbook [43], the yield strength of 99.999% Al is 15-20MPa.
- Solid solution strengthening from elements other than Mg and Cu, e.g, mainly Mn and Si in the alloys studied. The solid-solution effects on the yield strength of Mn and Si in super-purity Al are 30.3 MPa/wt% and 9.2 MPa/wt%, respectively [43]. In the alloys studied, Mn and Si contents are about 0.25 wt% and 0.15 wt%, respectively. Therefore, the overall solid solution strengthening from the two elements are about 9 MPa. For Fe, another major impurity in the alloys (about 0.2 wt%), its contribution to the strength can be ignored since its solid solubility in aluminium is very low (about 0.052 wt% [43]).
- Grain size contribution to strength. According to the analysis in [12], these contributions are negligible in the present recrystallised samples.

The estimated σ_b can be obtained by summing up the above contributions, which is about 25-35 MPa. This supports that the calibrated $\sigma_b = 31.5$ MPa is reasonable.

The above calibrated values for k_{Mg}, k_{Cu} can be compared with literature data. According to Lloyd and Court's work on Al-Mg alloys [44], the solution hardening is linear with Mg level and its hardening coefficient is about 16 MPa/wt%Mg, which equals about 14 MPa/at%Mg for the contribution to the macroscopic stress. Considering $M=2.6$, it follows k_{Mg}=540 MPa, which is close to the calibrated value (590 MPa). The analysis of literature data from the ASM Handbook [43] by Wang et al. [12] showed that the values for k_{Mg} and k_{Cu} are 500 and 1050 MPa, respectively. A different M value for the Taylor factor was

used to derive these two values. In [12], the M value used was calculated according to Taylor model (M=3.07), whilst in this study M value is obtained according to a self-consistent model (M=2.6). The k_{Mg} and k_{Cu} obtained from the ASM handbook by Wang et al. are equivalent to 570 and 1270 MPa respectively when M=2.6 is used. Using these two values in the solid solution strengthening model, the value for σ_b obtained at the best fit is 31.7 MPa with RMSE=1.7 MPa. Comparing the values obtained from the two methods for the three parameters, for σ_b and k_{Mg}, the two sets of corresponding values are very close, whilst the two values for k_{Cu} have some difference. However, this would not make much difference since there is only a small amount of Cu (≤0.4wt%) in the alloys. Moreover, the RMSEs obtained from the two methods are also very close. Through the comparison, therefore, it can be concluded that the values calibrated here (see Table 6.2) and the values obtained from Wang et al.'s analysis of data in the handbook are consistent. Thus the parameters calibrated in Table 6.2 will be used and these parameters will be fixed throughout calibrations and modelling in subsequent sections.

6.4.3 Method I — Step-by-step calibration and testing of the model

6.4.3.1 Work hardening model calibration and testing

In the work hardening model, there are four parameters that need to be determined: K_{wh}^{Mg}, K_{wh}^{Cu}, K_{wh}^{0} and n_{wh}. The yield strength of solution-treated ($\varepsilon = 0$) and cold-worked alloys with three cold-rolling reductions: 10% ($\varepsilon = 0.12$), 40% ($\varepsilon = 0.59$) and 90% ($\varepsilon = 2.66$) were used to calibrate the work hardening model. The measured 0.2% proof strengths are listed in Table 6.3. As indicated in the table, there are 36 data points in the database for work hardening model calibration and testing. In order to calibrate and test the work hardening model, the concept of train and test method [2, 40] will be used here. Following this method the data are split into two subsets: about 50% of the data will be used to calibrate the work hardening model, and the other 50% of the data will be used to test the accuracy of the model. The subset data for calibration of the model will be selected randomly so that the data are well spread. The selected subset data for calibration/training of the model are listed in Table 6.4. By fitting the selected experimental data listed in the table using the LSM, the four parameters in the work hardening model were determined and their values are shown in Table 6.5. The fitting error represented by RMSE is 5.5 MPa.

Table 6.3 0.2% PS of solution-treated alloys and cold-worked alloys (unit: MPa)

Alloys	A1	A2	A3	A4	A5	A6	A7	A8	A9
ST	49.0	64.6	80.3	50.9	65.6	87.3	53.4	66.5	84.2
10%	138.4	170.9	184.5	146.3	175.2	187.0	142.6	178.0	215.0
40%	189.0	220.4	253.3	201.7	235.2	272.7	214.9	252.6	279.3
90%	253.8	285.5	334.3	270.0	314.4	352.3	284.8	342.5	371.3

Table 6.4 Selected data for calibration the work hardening model (+ means the related data have been selected, otherwise the data are not selected)

	0%	10%	40%	90%
A1	+		+	
A2		+		+
A3	+		+	
A4	+			+
A5		+		+
A6		+	+	
A7	+			+
A8	+	+		
A9			+	+

Table 6.5 Calibrated values of parameters in the work hardening model

Parameter	Value
K_{wh}^{Mg}	1861 MPa
K_{wh}^{Cu}	14643 MPa
K_{wh}^{0}	136 MPa
n_{wh}	0.27

In the literature [45], values of n_{wh} from 0.257 to 0.281 are given for Al-Mg alloys. It is 0.276, 0.281 and 0.257 for Al-5.5Mg (T4), Al-5.5Mg (artificially aged at 180°C/30min) and Al-6.6Mg (artificially aged at 180°C/30min) alloy, respectively. The mean of the values of n_{wh} is 0.271, which is almost the same as the calibrated results ($n_{wh} = 0.27$) in this work.

After the parameters in the work hardening model are determined, they will be fixed. Then the other subset of remaining data will be used to test the accuracy of the model. The test of the model shows that the accuracy of the model is 6.2 MPa (RMSE error).

The fitting and testing results using the values listed in Table 6.5 and the experimental results are shown in Figure 6.12. As shown in the figure, the predicted results describe the work hardening behaviour of all the alloys well. Therefore, the work hardening model can be regarded as applicable and the parameters calibrated using the above method were fixed throughout later calibration and modelling.

6.4.3.2 Calibration of recovery model

Having determined the parameters in Table 6.5, the next two parameters, p_1'' and p_2'', in the recovery model are to be determined. As cold-rolled alloy A3 shows no precipitation, its 0.2% proof strength data will be used to calibrate the recovery model. By fitting the experimental data using the LSM, the two parameters were determined. When calibrating the recovery model, the predicted values for σ_{wh} and σ_{rex} in equation (6.43) instead of the measured data were used. The calibrated values for p_1'' and p_2'' are 0.021 and 360 s.MPa, respectively. The measured and predicted ageing curves for alloy A3 are shown in Figure 6.13. The RMSE for fitting of these data is about 6.5 MPa. As shown in the figure, the ageing curves for 90% and 40% reduction were fitted well, but for 10% reduction the prediction slightly overestimates the data. It is thought that small inaccuracies in the measured percentage of cold-rolling reduction could be the cause of this. As discussed above, precipitation is ignored when using the recovery model to fit the experimental data for alloy A3, which may also cause some inaccuracy. Although there was no precipitation hardening detected during ageing of the cold-rolled alloy A3 using tensile tests and hardness tests, very weak precipitation may still occur during ageing. This weak precipitation hardening may be offset by recovery, which leads to only softening being observed in experiments. Therefore, this calibration of the recovery model can only be considered to be a first assessment. The final calibration of the recovery model has to be performed together with precipitation model, which will be discussed below.

After the recovery model was first assessed, the remaining part of the model to be calibrated is the precipitation model. There are two sets of parameters for the two types of precipitates: β" and S. For convenience of description, the precipitation model will be divided into a β" precipitation model and a S precipitation model to refer to the precipitation model due to β" and S phase, respectively. The former will be calibrated first with recovery model using tensile data from alloys A1, A2 and A3. The S precipitation model will finally be calibrated using tensile data from alloys A4-A9 (see Figure 6.8). In the following, these two steps will be discussed in detail.

6.4.3.3 Calibration of recovery and β″ phase precipitation model

In the β″ phase precipitation model, the following parameters need to be determined: $k_{\varepsilon,\beta}$, $k_{ND,\beta}$, $\bar{l}_{0,\beta}$ and $p_{k,\beta}$.

These parameters for microstructure prediction need to be calibrated by fitting the experimental data obtained from tensile tests. Alloys A1-A3 are Cu-free alloys, and hence only the β precipitation sequence occurs in these alloys. Therefore, the proof strength data of these alloys can be used to calibrate the β″ phase precipitation model. The recovery model will be calibrated together with the β″ precipitation model since recovery and β″ precipitation may occur in the cold-rolled alloys A1-A3. The rate of β″ precipitation reaction is controlled by parameter $k_{\varepsilon,\beta}$, which determines the time to peak ageing. As shown in Chapter 5, it is almost impossible to determine the time to peak ageing from the available tensile data gathered in this study. However, the hardness data have enough information to determine the time to peak ageing. Hence $k_{\varepsilon,\beta}$ will be adjusted to fit the time to peak hardness of alloys A1-A3, especially alloy A1, which has the strongest precipitation hardening in the three Cu-free alloys. In this way, parameter $k_{\varepsilon,\beta}$ is determined to be 4.0×10^{14} s^{-1} and is fixed at this value. After that, the other parameters in the β″ precipitation and the recovery model will be determined using the LSM to fit the experimental 0.2% proof strength data of alloys A1-A3. The fitting error in this case presented by RMSE is 6.5 MPa. The experimental results and the predicted results are shown in Figure 6.14 (a)-(c). The six parameters determined are listed in Table 6.6. After the six parameters were determined, they will be fixed throughout the further calibration and modelling in the Method I.

Table 6.6 Determined values of parameters in recovery and β″ precipitation model

Parameter		Value
recovery	p_1''	0.018
	p_2''	177.5 s.MPa
β'' precipitation	$k_{\varepsilon,\beta}$	4.0×10^{14} 1/s
	$k_{ND,\beta}$	5.0×10^{8} 1/s
	$\bar{l}_{0,\beta}$	4.2 nm
	$p_{k,\beta}$	1.4

6.4.3.4 Calibration of S phase precipitation model

After the parameters in the recovery model and β″ precipitation model were determined, the only set of parameters to be calibrated is the parameters in the S precipitation model. These include the following parameters: $k_{\varepsilon,S}$, $k_{ND,S}$, $\bar{l}_{0,S}$ and $p_{k,S}$.

Parameters for microstructure prediction also need to be calibrated by the experimental results from tensile testing. In all the Cu-containing alloys, S precipitation may occur. Therefore, the tensile data from cold-rolled alloys A4-A9 will be used to calibrate the parameters in the S precipitation model. Similar to the β precipitation model, the rate of the S precipitation reaction is controlled by parameter $k_{\varepsilon,S}$, which determines the time to peak ageing. As discussed in Chapter 5, mainly S phase precipitation occurs in the cold-worked Cu-containing alloy A9. Hence, parameter $k_{\varepsilon,S}$ can be determined to be 7.5×10^{13} s^{-1} by fitting the time to peak hardness of alloy A9. $k_{\varepsilon,S}$ is fixed at this value and then the other three parameters for microstructure prediction for S phase precipitation will be determined using the LSM to fit the experimental 0.2% proof strength of alloys A4-A9. The predicted results and measured results are shown in Figure 6.14 (d)-(i). As shown in these figures, the predicted results agree reasonably well with the measured results, with the overall fitting error of 12.5 MPa (RMSE). The determined parameters are listed in Table 6.7.

Table 6.7 Determined values of parameters in S precipitation model

Parameter		Value
S precipitation	$k_{\varepsilon,S}$	7.5×10^{13} 1/s
	$k_{ND,S}$	5.0×10^{8} 1/s
	$\bar{l}_{0,S}$	4.4 nm
	$p_{k,S}$	1.3

In this section, all the parameters used in the yield strength model were obtained by fitting the experimental 0.2% proof strength data using the LSM. After all the parameters were calibrated, the model can be used to predict unseen data. In the following section, the model will be tested through application to hardness tests.

6.4.3.5 Testing of the model

In order to use the results of hardness tests to test the model that has been calibrated by Method I, the relation between hardness and 0.2% proof strength has to be determined first. In the following the conversion relation between hardness and 0.2% proof strength obtained from experimental results will be discussed prior to the discussion of the modelling results.

6.4.3.5.1 Conversion of hardness to yield strength

All the tested hardness and corresponding 0.2% proof strength for the alloys studied is shown in Figure 6.15. As shown in the figure, the correlation between hardness and 0.2% proof strength ($\sigma_{0.2}$) is reasonable, but by no means strictly linear. For each separate cold work level, there is a very clear linear relation between Vickers hardness (H_v) and $\sigma_{0.2}$. The slope of the straight line depends on the level of cold work (see Figure 6.16 to Figure 6.19), thus the following relation holds:

$$\sigma_{0.2} = f_{\sigma-Hv}(\varepsilon) H_v \qquad \textbf{(6.57)}$$

where $f_{\sigma-Hv}$ is a function of strain ε. The term of $f_{\sigma-Hv}$ can be approximated by the following equation:

$$f_{\sigma-Hv}(\varepsilon) = 1.41\varepsilon^{0.13} + 1.35 \qquad \textbf{(6.58)}$$

Using equation (6.57) together with (6.58), hardness can be converted to 0.2% proof strength. For thermomechanical processing conditions by which both hardness testing and tensile testing have been conducted, the converted 0.2% proof strength and the measured 0.2% proof strength are shown in Figure 6.20. As shown in the figure, the converted results agree reasonably well with the tested results with RMSE=11.5 MPa. Hence, the hardness can be converted to 0.2% proof strength with good accuracy. Using this, the converted hardness data can be used to validate the modelling results.

6.4.3.5.2 Modelling results

The model discussed in sections 6.2 and 6.3 with the parameters calibrated in sections 6.4.2 and 6.4.3 is applied to model the ageing behaviour of the cold-rolled alloys, and its results will be compared with the measured hardness results. The modelling results and the hardness testing results are shown in Figure 6.14. For comparison, the tensile results are also shown in the figure. In general, the modelling results agree reasonably well with the hardness testing results for all the nine alloys. For example, the model predicts the magnitude of age hardening achievable in each of the nine alloys quite accurately. The overall RMSE is 14.3 MPa (test error). Considering that the range of $\sigma_{0.2}$ is about 120 to 400 MPa, the RMSE is 5% of the total range of $\sigma_{0.2}$ data. The testing RMSEs are 11.7, 15.0, 7.9, 15.2, 18.9, 11.3, 14.6, 16.2, 15.1 MPa for alloys A1 to A9, respectively. Figure 6.21 shows an overview of correlation between modelling results and the measured results.

In summary, it has been shown that Method I calibrates and tests the model step by step and it is easy to understand. The hardness data can be used to test the model obtained, which is very helpful since it is relatively easy to obtain. However, this method has one drawback, i.e., the test error obtained from this method is not the actual test error due to the model, because the error of the conversion of hardness to $\sigma_{0.2}$ data superposed on it. Hence, the test error obtained from this method (i.e., 14.3 MPa) is an overestimation.

6.4.4 Method II — Training and testing of the model

The second method, Method II uses two separate subsets from the database of tensile data for calibration and testing of the model. In this method, all parameters except the parameters for solid solution strengthening will be calibrated in a single step by randomly selecting part of $\sigma_{0.2}$ data, and the remaining $\sigma_{0.2}$ data will be used to test the model. No hardness data will be used in this method (with the exception of the determination of $k_{\varepsilon,i}$ with $i = \beta, S$). In the following, the method will be discussed.

6.4.4.1 Calibration of the model

As discussed in section 6.4.3, the available experimental tensile test data gathered in this study can not provide enough information to determine peak ageing. However, the hardness data can provide more accurate information to determine the time to peak ageing. Hence, the parameters $k_{\varepsilon,\beta}$ and $k_{\varepsilon,S}$ have to be determined from the hardness data. Therefore, these two parameters will be taken as the identical values from Method I. So in this method, the following parameters will be determined:

- Parameters for work hardening: K_{wh}^{Mg}, K_{wh}^{Cu}, K_{wh}^{0} and n_{wh}.
- Parameters for recovery: $p_1^{"}$ and $p_2^{"}$.
- Parameters for microstructure prediction for β" phase: $k_{ND,\beta}$, $\bar{l}_{0,\beta}$ and $p_{k,\beta}$.
- Parameters for microstructure prediction for S phase: $k_{ND,S}$, $\bar{l}_{0,S}$ and $p_{k,S}$.

In order to calibrate the model, some alloy/reduction combinations will be selected to train the model. The subset database for calibration is listed in Table 6.8.

After the selection of the database for the calibration, the model will be calibrated by fitting the selected experimental data using the LSM. The determined values of the parameters are listed in Table 6.9. The fitting RMSE using this method is 8.6 MPa. The fitting results together the modelling results to be discussed later are shown in Figure 6.22.

In this method, the fitted value of n_{wh} is 0.275, which is slightly higher than that in Method I (0.27) and the average of the measured values for Al-Mg alloys in [45] (0.271).

Table 6.8 Selected data for training the model (+ indicates that data are selected)

pre-reduction	10%				40%				90%			
ageing condition	cw	30min	5d	3w	cw	30min	4h	3w	cw	30min	4h	3w
A1	+	+	+	+					+	+	+	+
A2												
A3	+	+	+	+	+	+	+	+	+	+	+	+
A4												
A5	+	+	+	+	+	+	+	+	+	+	+	+
A6												
A7	+	+	+	+	+	+	+	+	+	+	+	+
A8												
A9	+	+	+	+					+	+	+	+

Table 6.9 Determined values of all the parameters in the model using Method II

Parameter		Value
work hardening	K_{wh}^{Mg}	1689 MPa
	K_{wh}^{Cu}	15118 MPa
	K_{wh}^{0}	140.32 MPa
	n_{wh}	0.275
recovery	p''_1	0.035
	p''_2	53806.8 s.MPa
β'' precipitation	$k_{\varepsilon,\beta}$	4.0×10^{14} 1/s (from Method I)
	$k_{ND,\beta}$	5.0×10^{8} 1/s
	$\bar{l}_{0,\beta}$	5.9 nm
	$p_{k,\beta}$	0.1
S precipitation	$k_{\varepsilon,s}$	7.5×10^{13} 1/s (from Method I)
	$k_{ND,s}$	5.0×10^{8} 1/s
	$\bar{l}_{0,\beta}$	4.8 nm
	$p_{k,s}$	0.8

6.4.4.2 Testing of the model

After the model has been calibrated using part of the $\sigma_{0.2}$ data, it can be applied to predict the remaining data (the unseen data), providing a true test of the accuracy of the model. The modelling results are shown in Figure 6.22. The overall tested accuracy of the model represented by RMSE is 8.6 MPa, which is identical to the fitting error. The predicted $\sigma_{0.2}$

data vs. measured $\sigma_{0.2}$ data are shown in Figure 6.23. As shown in the figure, a good accuracy has been achieved by the model prediction.

The Method II has the following advantages:

- There is only one single calibration step involved;
- No hardness conversion has been used, hence the test error reflects the actual accuracy of the model.

However, it has some drawbacks too.

- Since more parameters have to be calibrated in one step, optimisation requires robust software which can avoid local minima in RMSE. (Some problems were encountered with the software employed, the 'solver' routine in Microsoft Excel);
- Sufficient data are required to train and test the model independently. It takes longer time to obtain the experimental data through tensile tests compared with hardness tests.

(It is noticed that the values of the fitting parameters calibrated from Method I provide very good starting values for the fitting parameters in the training and testing Method II, which makes the optimisation in Method II run efficiently and effectively.)

6.5 Discussion

In the early sections of this chapter, the yield strength model has been developed. Two methods of calibration and test of the model have been applied. A good agreement between the predictions and experimental results has been achieved for each method when applied to predict the ageing behaviours of the nine cold-rolled alloys with three reductions. In this section, some comparisons of model predictions with experimental observations will be discussed and some fitting parameters will be compared with literature data.

6.5.1 Comparison with microstructure

6.5.1.1 Intermetallics

Using the thermodynamics model described in section 6.2.1.1, the undissolved intermetallics can be predicted. The model correctly predicts that there is no undissolved S particle formed during solutionising, whilst there are non-soluble Mg_2Si particles formed

depending on the composition of the alloy. According to the model prediction, during solutionising at 500°C, the amount of Mg_2Si particles formed increases with increasing gross Mg content. As discussed in Chapter 5, some Mg_2Si particles were detected in the cold-rolled specimens of alloys A2 and A3, whilst no Mg_2Si particles were detected in the cold-rolled alloy A1. Accordingly, the model prediction agrees well with these experimental observations. The results of the model prediction for the amount of the particles formed during solutionising can also be compared with the thermodynamic calculations using MTDATA performed by Innoval Technology. The comparison is shown in Figure 6.24 to Figure 6.32. In these figures, "modelled" represents the results from the model prediction in this study, whilst "MTDATA" stands for the results from the thermodynamic calculations using MTDATA software. In general, the predictions from the simple regular solution model used in this study give similar results as compared to the more complex thermodynamic calculations using MTDATA software. The prediction of intermetallics formed at solutionising temperature and the amount of precipitates at ageing temperature is very critical to the accuracy of the predictions of ageing curves, and therefore, the predictions at these two particular temperatures are essential to the accuracy of the model. As shown in the figures, for all alloys, the modelled results from this study are very close to the MTDATA calculation results, and sometimes the two results are virtually identical both at the solutionising temperature (500°C or 773K) and ageing temperature (170°C or 443K). This indicates that the accuracy of the present simple regular solution model is sufficient. In this sense, the regular solution model and the parameters involved in the solvi prediction used in this model can be regarded as applicable and reliable. This comparison also indicates that for the present alloys the much more detailed CALPHAD thermodynamic modelling (here achieved by the MTDATA software with commercially available databases) can be used as the basis for a microstructure development and strength model. This could provide a model that makes predictions for compositions where other phases apart from the ones considered here remain undissolved.

6.5.1.2 Strengthening phases

In the model, only two strengthening phases are considered: S and β″. Their formation during ageing depends on the alloy's composition. There are three possibilities during ageing: only β″ phase formation may occur, or S phase formation may occur, or the

formation of both phases may occur. According to the model prediction, in the Cu-free alloys (alloys A1-A3), β″ is the only strengthening phase which causes precipitation hardening in the alloys during ageing. The precipitation of β″ phase in the Cu-free alloys can be supported by DSC analyses and hardness testing presented in Chapter 5. The model predicts that the precipitation hardening due to β″ phase formation decreases with increasing Mg content, which was observed by hardness tests and was also supported by DSC data (see Chapter 5). According to the model prediction, this is attributed to the formation of non-soluble Mg_2Si particles during solution treatment at 500°C. The model predicts that the higher the Mg content in the alloy, the higher the amount of Mg_2Si particles formed during solutionising at 500°C. This prediction agrees well with the results of the SEM/EDS intermetallics examinations discussed in Chapter 5. The predicted precipitation in the Cu-free Al-Mg alloys with small Si additions can also be supported by TEM results. As shown in Figure 5.48, in a sample of 10% cold-worked alloy A1, subsequently aged for three weeks at 170°C, the bright field (BF) image shows some precipitates, and the corresponding selected area diffraction (SAD) shows faint additional reflections from the precipitates, which are consistent with the simulated diffraction pattern of β' phase. The model also predicts that, in the Cu-containing alloys with 3wt% Mg (i.e., alloys A6 and A9), S phase is the main strengthening phase because most of the Si is removed from the solid solution due to the formation of Mg_2Si particles during solutionising and hence little Si is available for precipitation during subsequent ageing. This prediction is also supported by the results of DSC and TEM experiments. As shown in Figure 6.1, for all the cold-rolled specimens of alloy A9, mainly the effect due to the formation of S phase is detected during DSC runs. For 90% cold-rolling reduction, only the formation of S phase was detected by DSC. There might be some formation of a small amount of β″ phase compared with the strong formation of relatively large amount of S phase during DSC run for the 10% cold-rolled specimen. TEM results for 10% cold-worked alloy A9, subsequently aged for five days at 170°c, show a high density of dislocations and no precipitates could be unambiguously identified in the BF image (Figure 5.54a). However, the SAD (Figure 5.54b) shows a pattern consistent with S phase. For alloys other than those mentioned above, i.e., alloys A4, A5, A7 and A8, the formation of both β″ and S phase may occur according to the model prediction. Microstructure study by TEM observations for these cold-rolled-and-aged samples is difficult. Compared with typical heat treatable alloys, e.g., 2XXX, 6XXX and 7XXX, the

volume fraction of precipitates in all alloys studied is very small. Combined with the high density of dislocations (due to heavy cold work), this makes the identification of precipitates very difficult. Hence, precipitates present in the samples might sometimes not be revealed in BF or dark field (DF) images due to the high density of dislocations and/or low volume fraction of precipitates and the influence of dislocations on the diffraction pattern. As discussed in Chapter 5, S phase and an unidentified second type of precipitates were detected in the cold-worked alloy A4 aged for one week at 220°C (see Figure 5.51). TEM results also reveal the presence of S phase in the cold-worked samples aged for three weeks at 170°C of alloy A7 (see Figure 5.53) and alloy A8 (see Figure 5.54), respectively. No second type of precipitates is detected, but this can not be taken as evidence that no second type of precipitates is present in these two alloys. In this sense, the model prediction for alloys A4, A5, A7 and A8 is generally consistent with TEM results discussed in Chapter 5.

6.5.2 Comparison of fitted parameters with literature

In section 6.4, some calibrated/fitted parameters were compared with literature data, e.g., k_{Mg}, k_{Cu} and n_{wh}. In this section, fitted parameters which determine the size of precipitates during ageing will be compared with literature data, e.g., the size of precipitates at the start of coarsening and the parameters controlling the coarsening rate of precipitates.

6.5.2.1 The size of precipitates at the start of coarsening

The size of precipitates at the start of coarsening (e.g., $\bar{l}_{0,\beta}$ and $\bar{l}_{0,S}$) has a strong influence on the peak strength of the alloys during ageing. In a slightly overaged AA2024 sample, the measured radii of the S rods from the edge on variants range from about 2.5 nm to 6 nm with an average of 4.4 nm [25]. Moreover, $\bar{l}_{0,S} = 4.7$ nm provides a best fit for Al-Cu-Mg alloys [3, 25]. Hence, 4.7 nm is considered as a reasonable value for $\bar{l}_{0,S}$. In an Al-Mg-Si alloy [4], the mean precipitate radius in terms of an equivalent radius of sphere with identical volume were evaluated based on the mean precipitate volume from TEM micrographs. The results are plotted in Figure 6.33. The measured radius of precipitates at peak strength is about 4.9 ± 1.5 nm, i.e., $\bar{l}_{0,\beta}$ is around 4.9 ± 1.5 nm.

In method I, the calibrated values for $\bar{l}_{0,\beta}$ and $\bar{l}_{0,S}$ parameters are 4.2 nm and 4.4 nm, respectively. In method II, they are 5.9 nm and 4.8 nm, respectively. Comparing with the

literature data discussed above, the values of the fitted parameters from both methods are close to the measured size of both types of precipitates: β" and S. This observation provides important further support for the model.

6.5.2.2 The coarsening rate of precipitates

$k_{c,i}(T,\varepsilon)$ ($i = \beta$, S) determines the coarsening rate of the precipitates, which can be determined by measuring the precipitate size at different times of coarsening stage using TEM. There are some limited literature data on the coarsening rate of S phase, which were reviewed by Rainforth and Jones [46] (see Table I and Figure 1 in [46]). In non-stretched alloys, these measured data varied by quite a large magnitude (5 orders of magnitude) depending on alloy composition and temperature. Moreover, none of these data were measured at 170°C. Two independent data series from Sen et al. [47] and Cho [48] may be used to extrapolate a value of $k_{c,S}(T,\varepsilon = 0)$ at 170°C, as illustrated in Figure 6.34. The extrapolated values of $k_{c,S}(T,\varepsilon = 0)$ at T=443K (or 170°C) for the coarsening rate of S phase are 4.4×10^{-4} nm^{-3}/s (extrapolated from Sen et al.'s data) and 1.8×10^{-4} nm^{-3}/s (extrapolated from Cho's data).

In method I, the predicted values for $k_{c,S}(T,\varepsilon)$ are 0.37, 0.88 and 1.98×10^{-4} nm^{-3}/s for 10%, 40% and 90% pre-reduction, respectively, whilst in method II they are 0.24, 0.56 and 1.26×10^{-4} nm^{-3}/s for 10%, 40% and 90% pre-reduction, respectively. The predicted values for $k_{c,S}(443K,\varepsilon > 0)$ in this model seem slightly lower than those extrapolated values for $k_{c,S}(443K,\varepsilon = 0)$ from literature. As discussed in [46] due to the differences in alloy composition and the methods used to evaluate $k_{c,S}(T,\varepsilon = 0)$, the measured results varied over five orders of magnitude (see Table I in [46]). Taking this into account and considering the influence of the dilute alloy composition and cold work in this study on the coarsening rate of precipitates, the predicted values in this study, which are slightly lower than the extrapolated values, are thought to be quite reasonable.

In method I, the predicted values for $k_{c,\beta}(T,\varepsilon)$ are 2.1, 5.0 and 11.3×10^{-4} nm^{-3}/s for 10%, 40% and 90% reduction, respectively. They are 0.15, 0.36 and 0.81×10^{-4} nm^{-3}/s in method II for 10%, 40% and 90% reduction, respectively. From the substantial difference it can be deduced that these coarsening rates have a limited direct influence on model predictions, presumably because variations are compensated for by changes in predicted recovery rates. In method I, the predicted coarsening rates of β" phase are about one magnitude higher than those of S phase, whilst in method II, the predicted coarsening rates of β" phase are

slightly lower than those of S phase. However, considering the fact that measured coarsening rates of S phase reported in literature show five orders of magnitude difference, the predicted coarsening rates of both β" and S phases are consistent with the limited available evidence.

6.5.3 Limitations of the model and sources of test error

In this work, a model was developed and applied to predict the ageing behaviour of the cold-rolled alloys. In general, a good agreement between the modelling results and experimental results has been achieved. In method I, the test error on unseen data is slightly higher (about 14.3 MPa) due to the superposition of the conversion error from hardness data to $\sigma_{0.2}$ data. In method II, the accuracy of the model is about 8.6 MPa based on the prediction accuracy for unseen data. Although a good accuracy is achieved using the model, there are some limitations for the present model.

First, the interactions between recovery and precipitation are not considered. These interactions are complex, which includes the following three possibilities [8, 9, 49, 50]:

- Recovery may delay the progress of precipitation by reducing the number of nucleation sites available for precipitation since the dislocation density will be annihilated/ reduced through recovery;
- Precipitation may retard recovery through pinning segments of dislocation network by the precipitation of fine particles;
- Recovery may be facilitated by precipitation through draining the solute content because alloying elements in solution are thought to retard the progress of recovery through solute-drag effects on dislocation mobility.

So far, no model which considers all the three interactions between recovery and precipitation has been proposed in literature. Only the first interaction listed above was considered in the only model considering the interactions proposed in the literature by Zurob et al. [8, 9, 49], which was applied to steels. This model also has some limitations. It underestimated the effect of precipitation on recovery at higher temperatures, and this was thought to be due to the formation of well-developed substructures when the sample is annealed at higher temperatures [49].

As shown both in Figure 6.14 and Figure 6.22, the modelling results for some alloys are less satisfactory than others. There are several sources leading to the deviations:

- Measurement error. Sometimes, the test error is large due to measurement inaccuracies. For example, in method I, the test error for alloy A2 is about 15.0 MPa. As shown in Figure 6.14 (b), there is larger difference between the predicted results and the results of hardness tests for 90% reduction, which is thought due to the measurement error. This is supported by the dramatic and unexplained hardness drops, which are not consistent with the observations in other alloys. Such dramatic drop is also not consistent with the results of tensile tests of the same alloy.
- M is fixed at a constant value (M=2.6) throughout the modelling. Actually, M is related to texture. In the cold-rolled alloys with different pre-reductions, the texture will change. Hence, M should also change with cold-rolling reduction (In fact, it will increase with reduction.). This may be one reason that in the same alloy, model accuracy depends on cold-rolling reduction.
- As indicated before, for Method I, the conversion of hardness to 0.2% proof strength will also cause some error, which will lead to further error towards the predictions of the ageing behaviour of cold-rolled alloys.
- Some assumptions in the model may cause some error. For example, in the precipitation model, k_{c0} is assumed to be proportional to k_0 as expressed by equation (6.24). This may not be accurate enough. Nevertheless, it is thought that there is no theory that can provide a better relation at present.

6.5.4 Variations of the model

6.5.4.1 Superposition rule

As discussed in section 6.3.5, for the overall yield strength model, a quadratic superposition rule has been applied for the summation of the contributions of dislocation strengthening and precipitation hardening. A linear superposition of the two contributions has also been attempted. The accuracy of the model on unseen data using the train and test method (method II) is not significantly affected, but the fitted values for $\bar{l}_{0,\beta}$ and $\bar{l}_{0,S}$ parameters changed to 12.6 nm and 9.1 nm, respectively, both of which are much higher than the available literature data. Based on these results, the quadratic superposition rule is thought to represent the physics of precipitation hardening better.

6.5.4.2 Fixing $\bar{l}_{0,\beta}$ and $\bar{l}_{0,S}$ using data from literature

According to the discussion in section 6.5.2.1, from the available literature data on the size of precipitates, $\bar{l}_{0,\beta}$ and $\bar{l}_{0,S}$ may be thought to be 4.9 nm and 4.7 nm, respectively. If these two parameters are fixed at these two values, slightly different fitted parameters can be obtained using the train-and-test method II. The training and test errors are 8.8 MPa and 8.3 MPa. The training error is slightly higher than its corresponding value when the two parameters of precipitate sizes are not fixed. On the contrary, the test error is slightly lower than its corresponding value when the two parameters of precipitate sizes are not fixed. This indicates the model can work well when the sizes of the precipitates are fixed based on literature data and the accuracy will not be significantly affected.

6.5.4.3 Activation energy of β" phase

The study on the effect of cold work on the precipitation kinetics of AA6111 alloy by Quainoo and Yannacopoulos [23] reveals that the activation energy of β" formation decreases with the level of cold work from 146.9 (0%), 119.9 (2%) to 114 kJ/mol (5%). The measured activation energy for β" formation at 0% cold work (146.9 kJ/mol) is very close to the one used in this model (152 kJ/mol). In order to investigate the flexibility of the model to the change of the activation energy, the activation energy is changed to 114 kJ/mol. Since the activation energy is changed, the value for $k_{\varepsilon,\beta}$ will change significantly to compensate. Using method II, both the training and testing errors are 8.5 MPa, which are practically identical to those values when using 152 kJ/mol as activation energy. This shows that the change of activation energy does not change the accuracy of the model. This should come as no surprise as all experiments were performed at one temperature, which means that the activation energy has no influence on the model.

6.5.5 HV/$\sigma_{0.2}$ reduction during ageing for the cold-rolled alloys

As shown in Figure 6.14 and Figure 6.22, the model predicts that there is an initial reduction in the yield strength/hardness at short ageing times (up to 15 minutes) for each cold-rolled alloy. The higher the cold work level, the larger the hardness/yield strength reduction. This reduction also depends on the alloy's composition. The lower the Mg contents in the alloy, the higher the reduction. Hence, the alloys A1, A4 and A7 have larger hardness/$\sigma_{0.2}$ reduction, especially for sheet with 90% pre-reduction. In the three alloys, alloy A7 with 90% cold work has the largest hardness/$\sigma_{0.2}$ reduction during ageing.

According to the prediction, the time to the dip in hardness/$\sigma_{0.2}$ is at several minutes, which is difficult to catch by experimental techniques when the specimens are aged at 170°C. The reactions (both recovery and precipitation) will be slowed down when the specimens are aged at lower temperatures. Therefore, in order to observe the reduction in hardness, ageing at lower temperature (140°C) was performed on specimens of alloys A1, A4 and A7 with 90% and 40% cold work. The results of hardness tests for lower ageing temperature are shown in Figure 6.35. As shown in the figure, for 90% cold work, all three alloys have a slight hardness decrease at very short ageing times. For 40% cold work, only alloy A7 shows a slight hardness decrease whilst the other two alloys have almost no hardness change in the very early ageing. Since the decrease in hardness is very small (the maximum is about five Vickers hardness number change according to the model prediction), it is difficult to detect this small change by hardness testing. However, the experimental results shown in Figure 6.35 confirm that there is a small hardness drop in the very early ageing. This further supports the model.

This local minimum is due to the interactions between recovery and precipitation, which occur simultaneously upon ageing. The level of the hardness reduction depends both on the driving force for recovery and precipitation hardening in the alloys. The higher the level of cold work, the higher the driving force for recovery, which results in larger softening during ageing. On the other hand, the stronger the precipitation hardening, the larger the hardness/yield strength increases during ageing. Therefore, the softening or the reduction in hardness/yield strength is most pronounced for samples with high level of cold work and weak precipitation hardening. That is why the hardness reduction can be detected in the 90% cold-worked specimens (higher driving force for recovery/softening), whilst there is no hardness reduction observed for the specimens with lower level of cold work.

6.6 Summary

In this chapter, a model for yield strength of cold-rolled Al-Mg(-Cu)-Si-Mn has been developed. The model is based on analytical equations. Two methods of calibration and testing of the model have been discussed. In Method I, all $\sigma_{0.2}$ data have been used to calibrate the model step by step, and then the hardness data have been used to test the model. In general, the model describes the hardness data of all the nine cold-rolled Al-Mg(-Cu)-Si-Mn alloys aged at 170°C well. For Method II, some of the $\sigma_{0.2}$ data have

been used to calibrate the method, whilst the remaining $\sigma_{0.2}$ data have been used to test the model. In general, for either method, good model accuracy has been achieved. The discussion of the limitations of the model and the sources of the test error indicates some possible future improvement of the model and highlights inherent limitations in achievable accuracy.

Figures

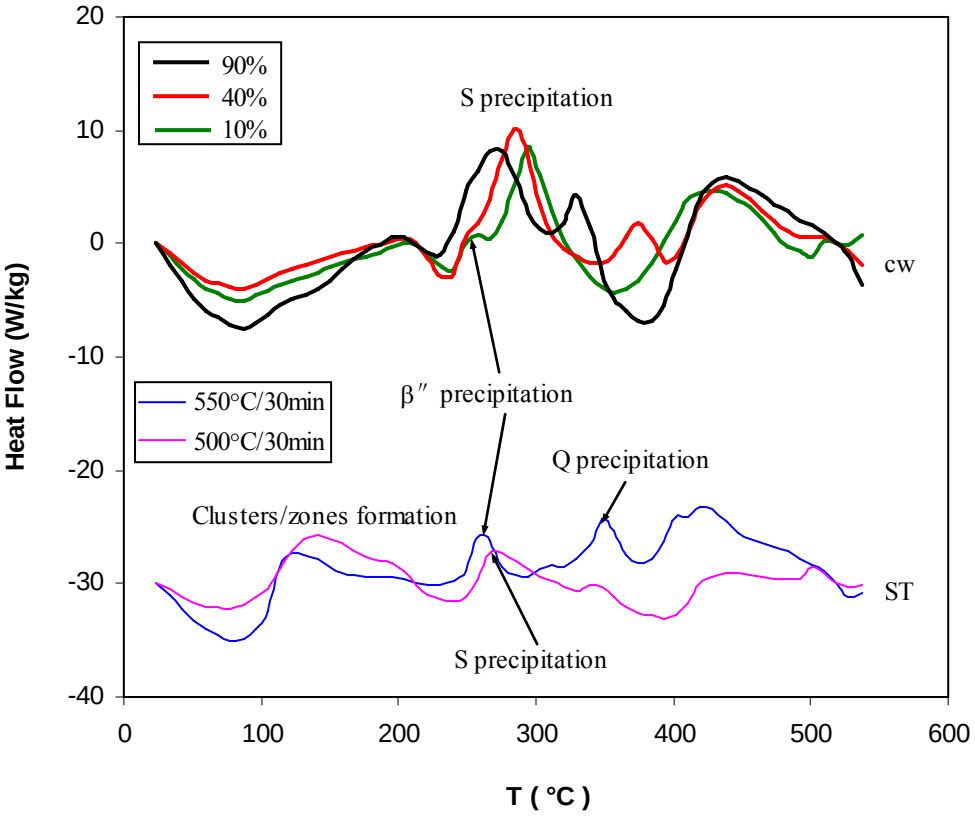

Figure 6.1 DCS data for alloy A9

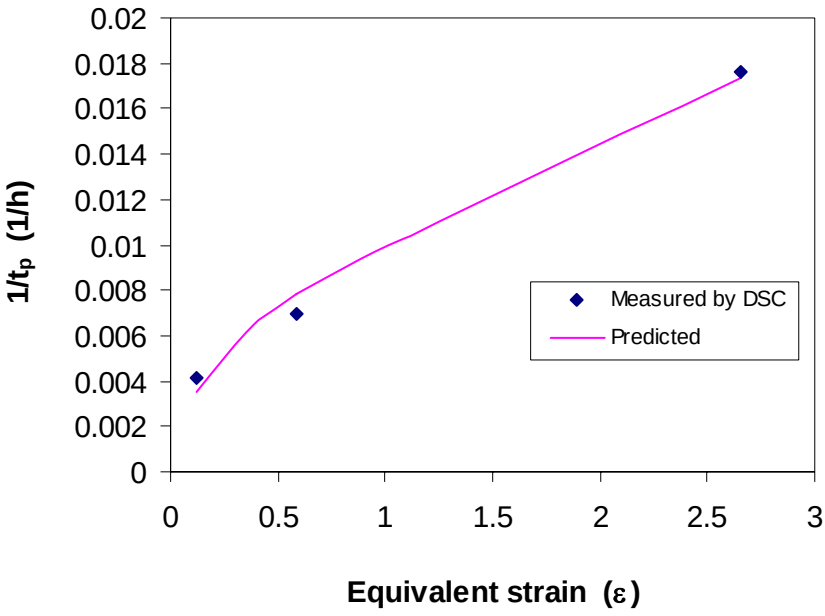

Figure 6.2 Measured and fitted $1/t_p$ for S formation in alloy A9

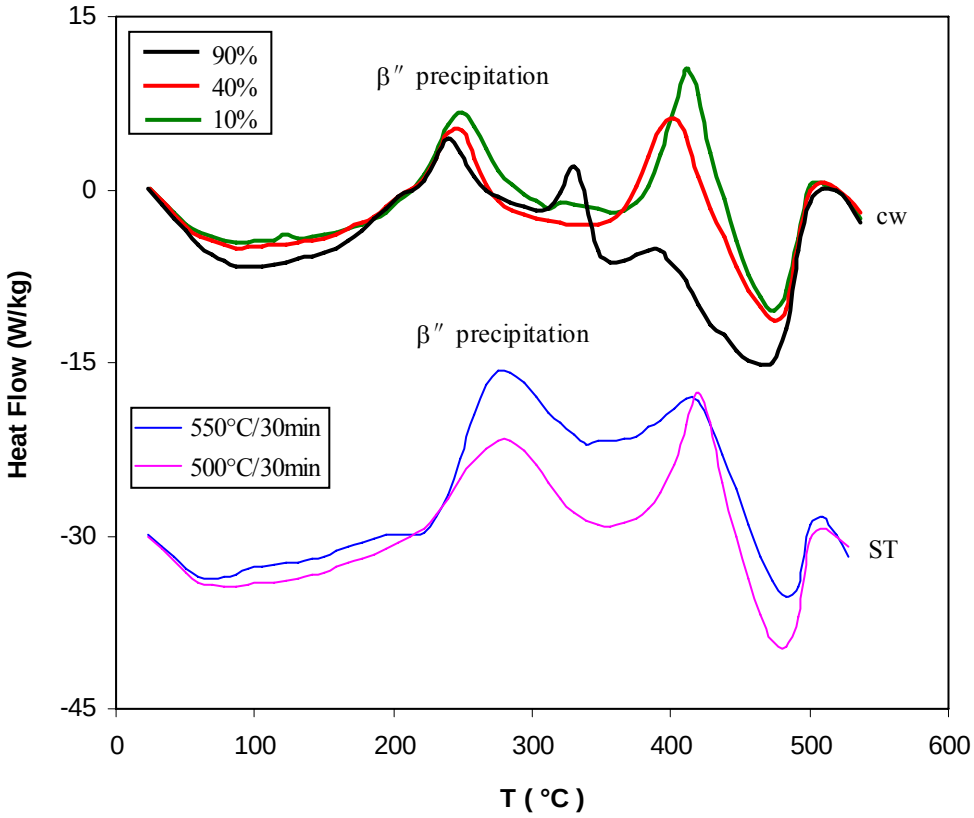

Figure 6.3 DSC data for alloy A1

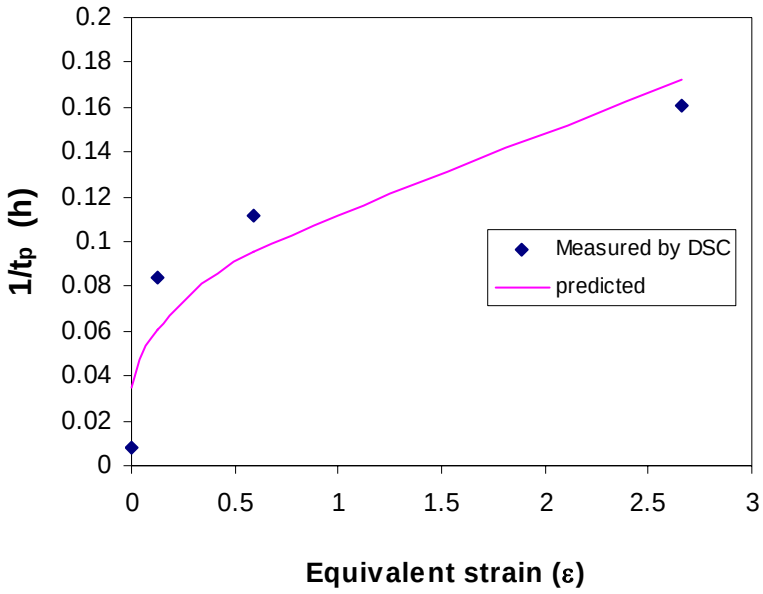

Figure 6.4 Measured and fitted $1/t_p$ for β″ formation in alloy A1

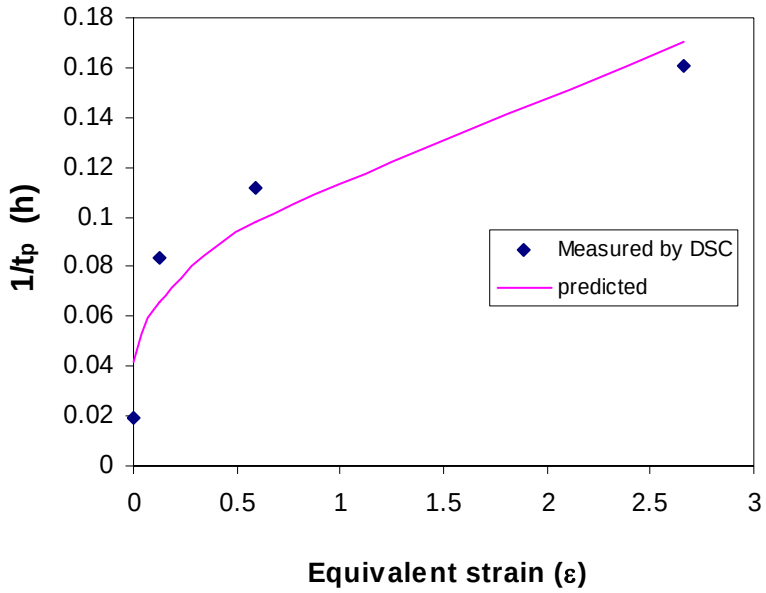

Figure 6.5 Measured and fitted $1/t_p$ β″ formation (using t_p from solution-treated specimen of alloy A3 replacing the one from solution-treated specimen of alloy A1)

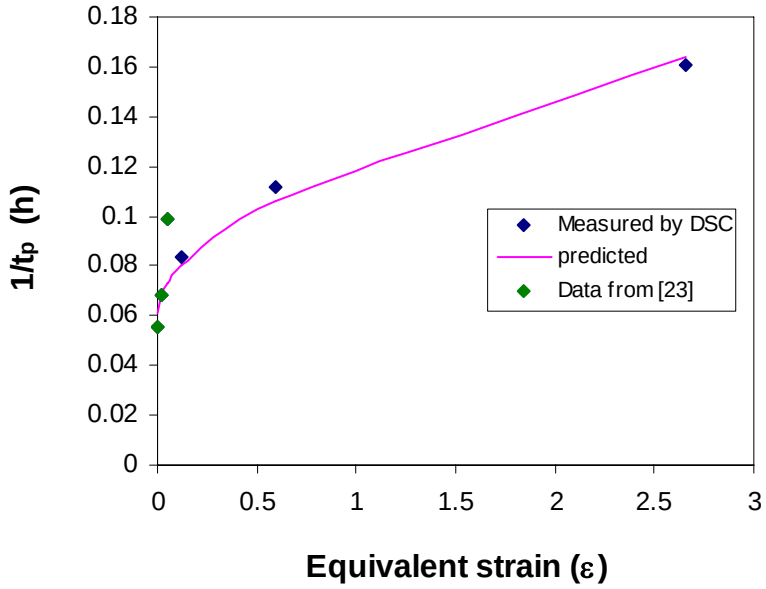

(a) Data at ε=0 from an AA6111 alloy [23] and at 10%, 40% and 90% from alloy A1 were used for fitting

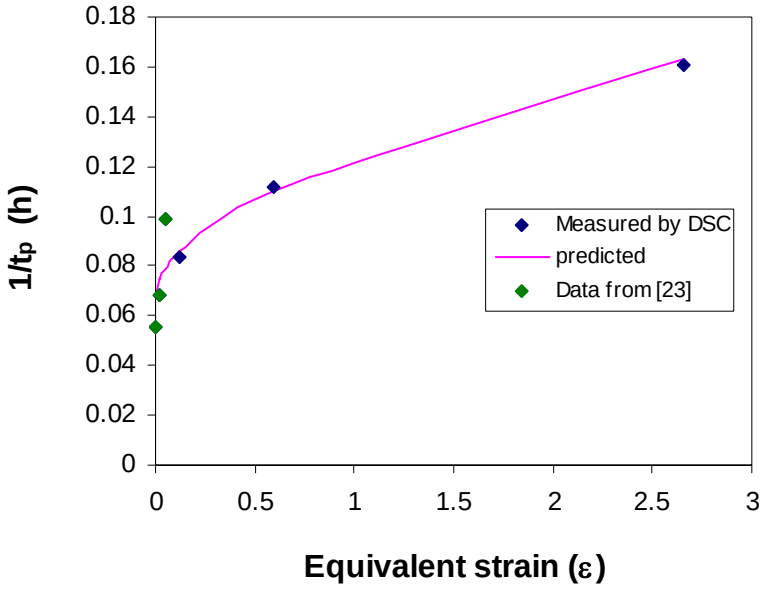

(b) Data at 0, 2% and 5% from an AA6111 alloy [23] and at 10%, 40% and 90% from alloy A1 were used for fitting

Figure 6.6 Measured and fitted $1/t_p$ for β″ formation

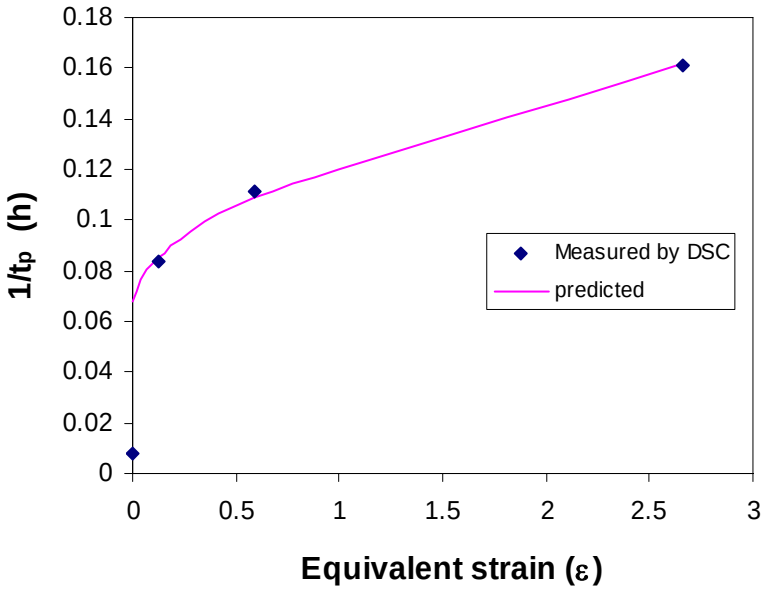

Figure 6.7 Measured and fitted $1/t_p$ for alloy A1 (fit to data for cold-worked conditions only)

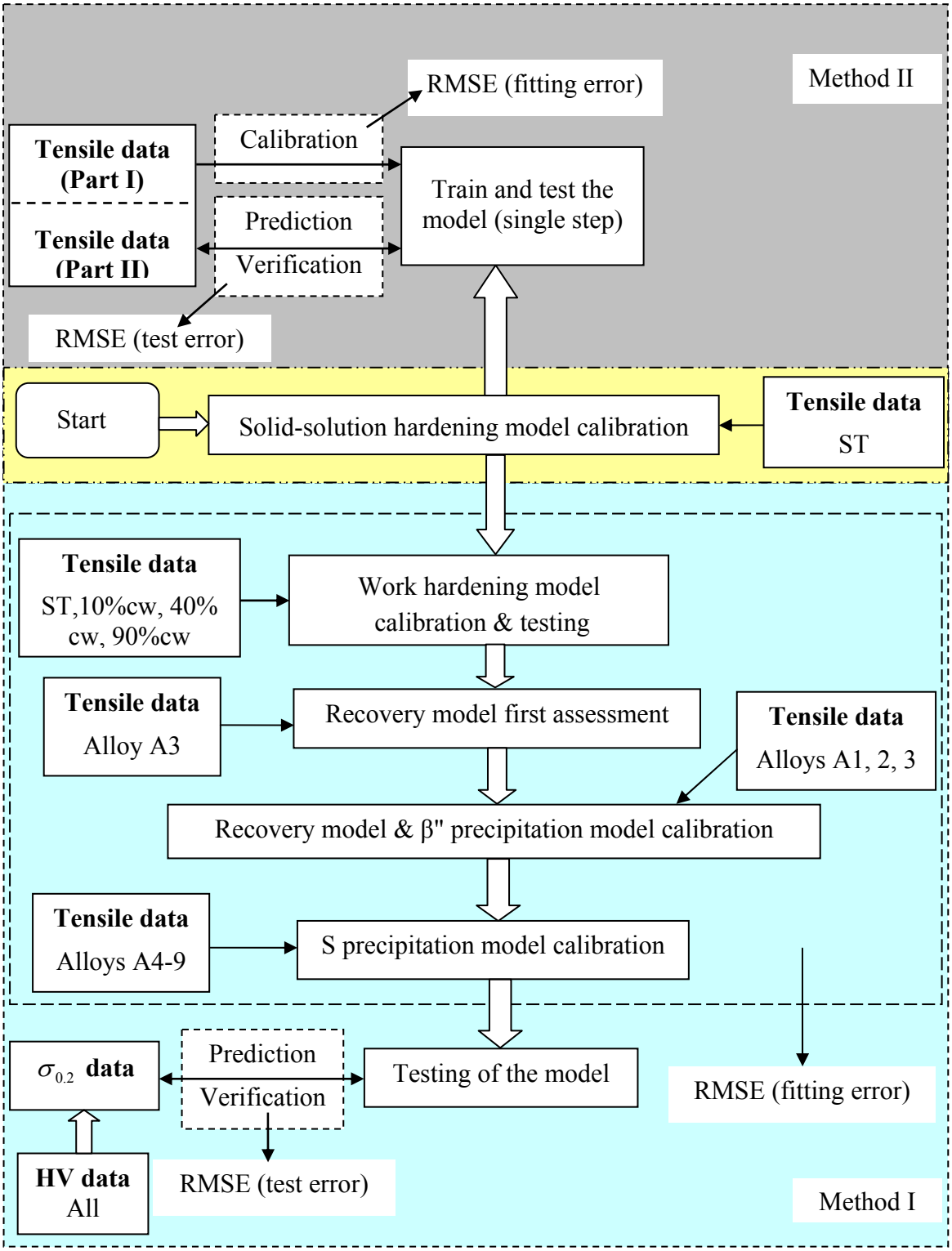

Figure 6.8 Flow chart of the procedures of calibration and testing the model

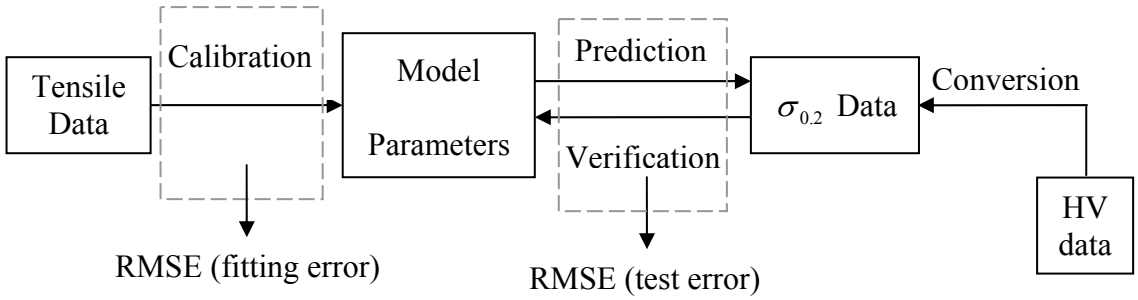

Figure 6.9 Flow chart of calibration and testing the model using method I

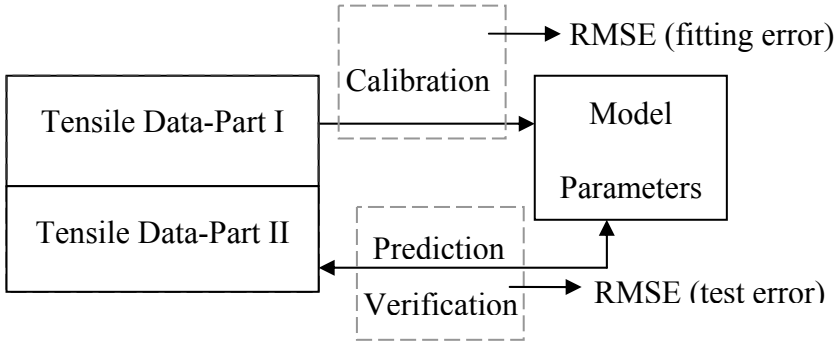

Figure 6.10 Flow chart of calibration and testing the model using method II

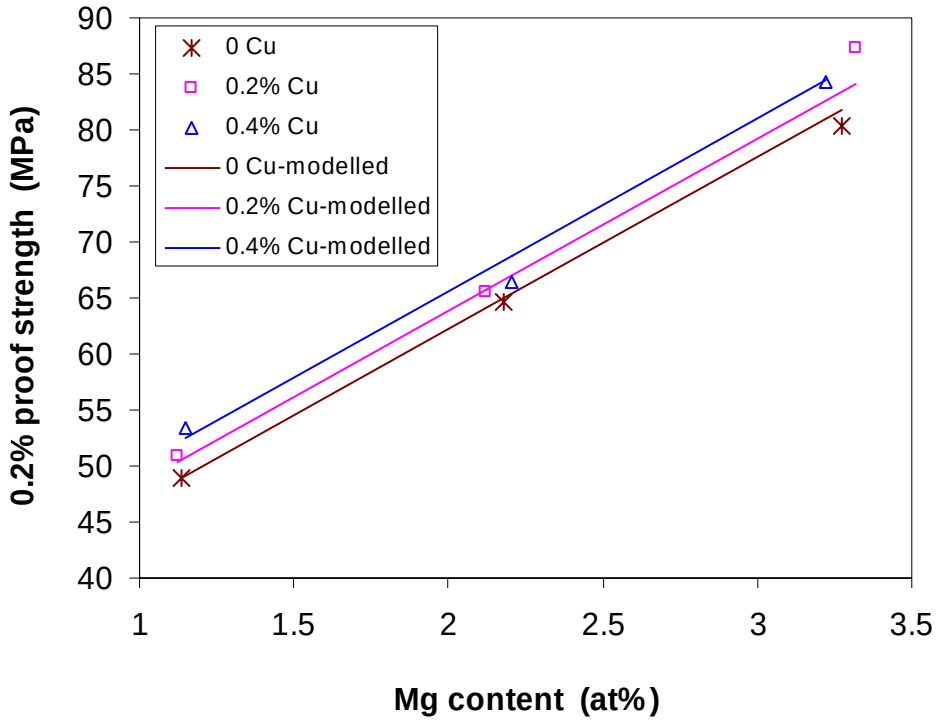

Figure 6.11 Measured 0.2% PS of solution-treated alloys and the prediction

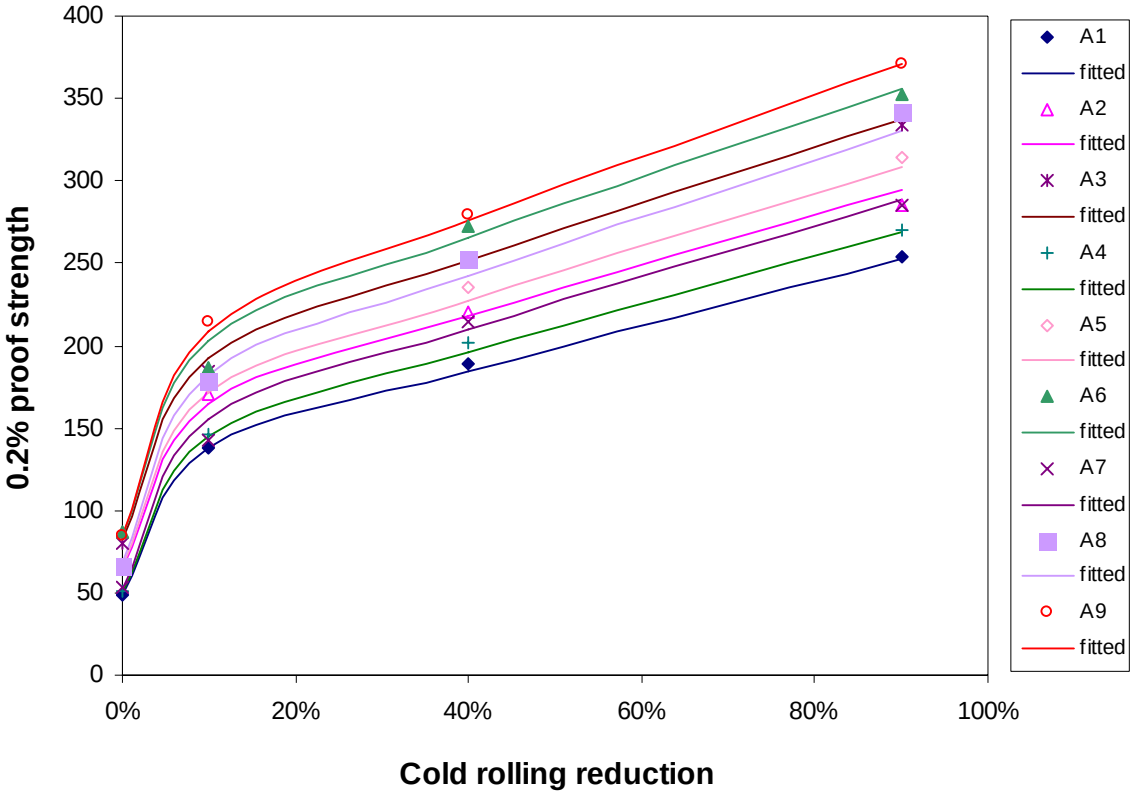

Figure 6.12 The results of work hardening model calibration and testing

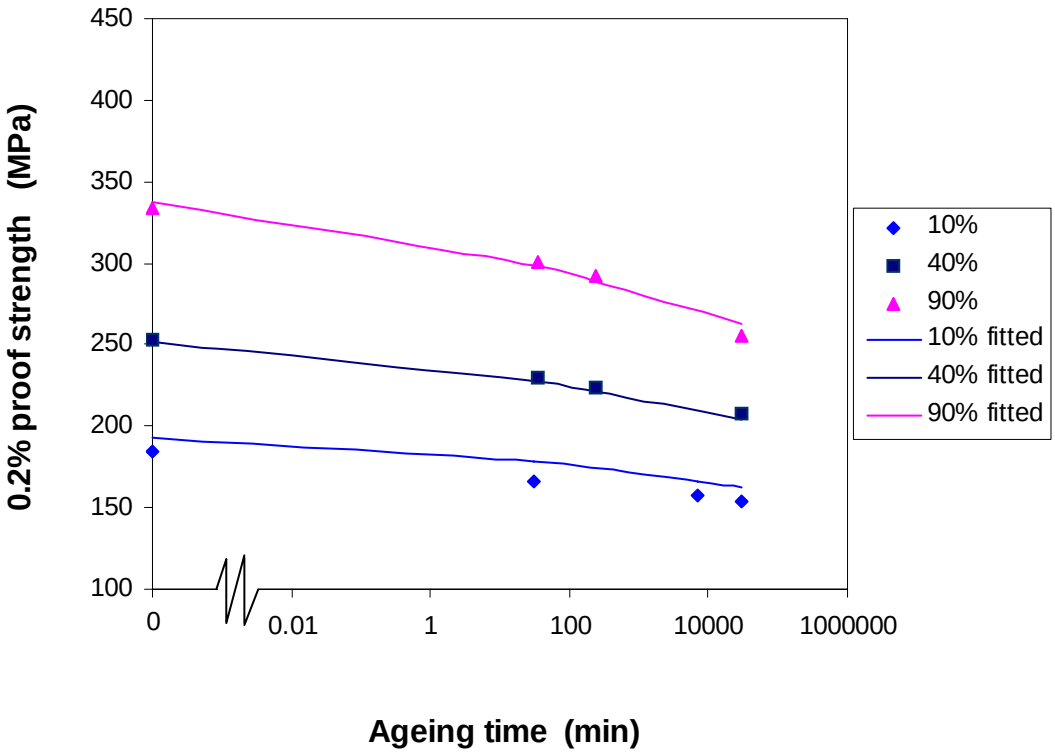

Figure 6.13 Measured and predicted PS for alloy A3 by the recovery model only

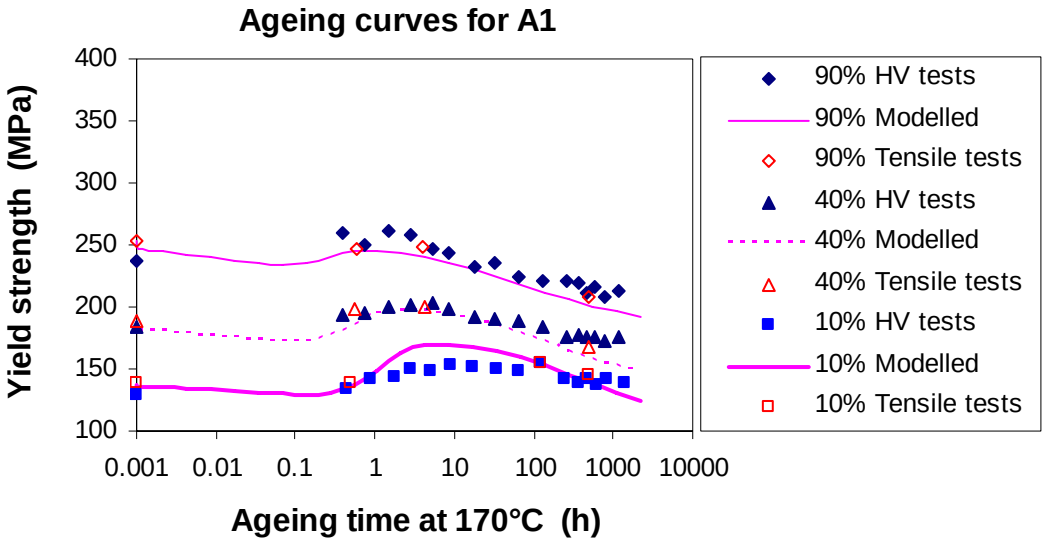
Ageing curves for A1
Yield strength (MPa)
400
350
300
250
200
150
100
0.001
0.01
0.1
1
10
100
1000
10000
Ageing time at 170°C (h)
90% HV tests
90% Modelled
90% Tensile tests
40% HV tests
40% Modelled
40% Tensile tests
10% HV tests
10% Modelled
10% Tensile tests

a.

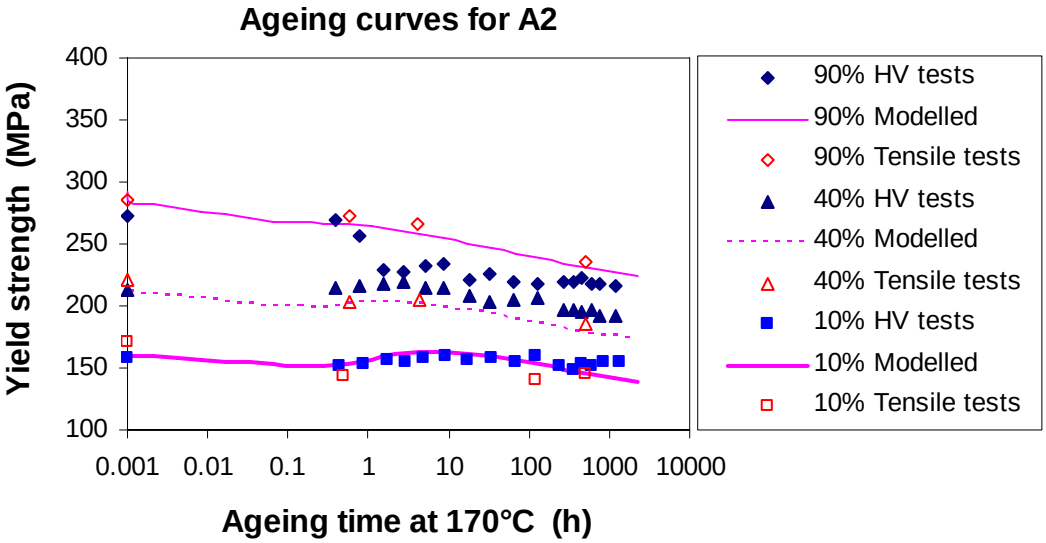
Ageing curves for A2
Yield strength (MPa)
400
350
300
250
200
150
100
0.001
0.01
0.1
1
10
100
1000
10000
Ageing time at 170°C (h)
90% HV tests
90% Modelled
90% Tensile tests
40% HV tests
40% Modelled
40% Tensile tests
10% HV tests
10% Modelled
10% Tensile tests

b.

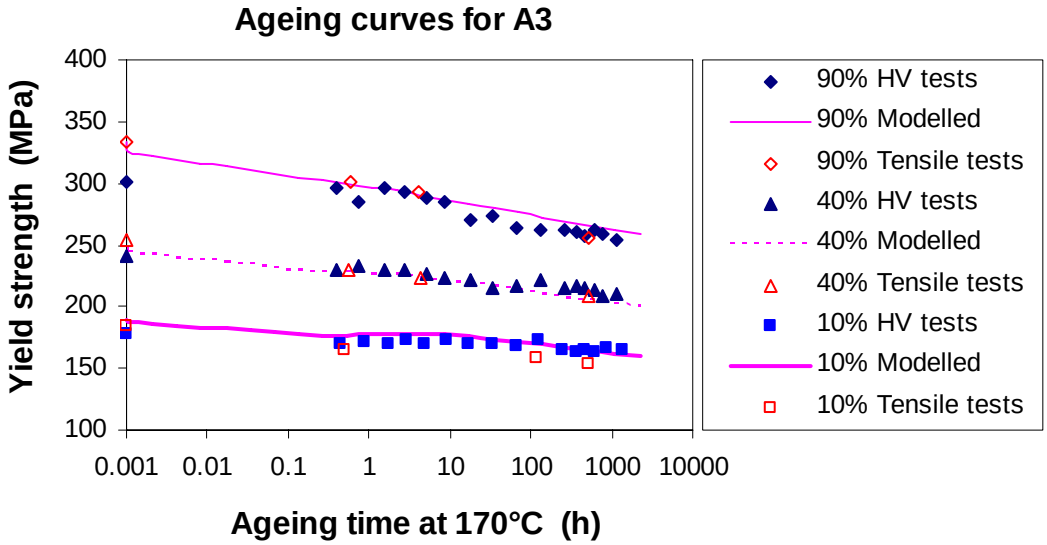
Ageing curves for A3
Yield strength (MPa)
400
350
300
250
200
150
100
0.001
0.01
0.1
1
10
100
1000
10000
Ageing time at 170°C (h)
90% HV tests
90% Modelled
90% Tensile tests
40% HV tests
40% Modelled
40% Tensile tests
10% HV tests
10% Modelled
10% Tensile tests

c.

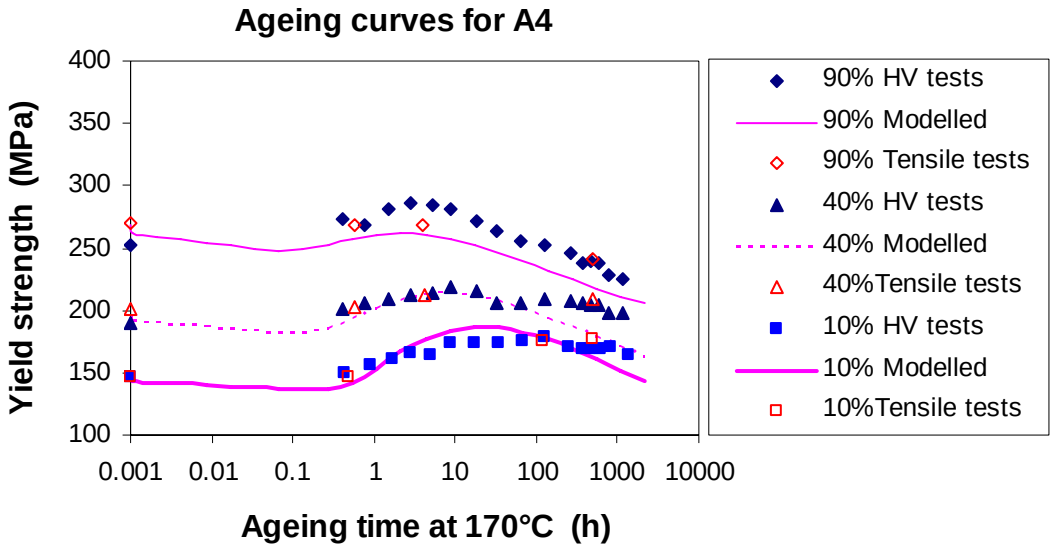
Ageing curves for A4
Yield strength (MPa)
400
350
300
250
200
150
100
0.001
0.01
0.1
1
10
100
1000
10000
Ageing time at 170°C (h)
90% HV tests
90% Modelled
90% Tensile tests
40% HV tests
40% Modelled
40%Tensile tests
10% HV tests
10% Modelled
10%Tensile tests

d.

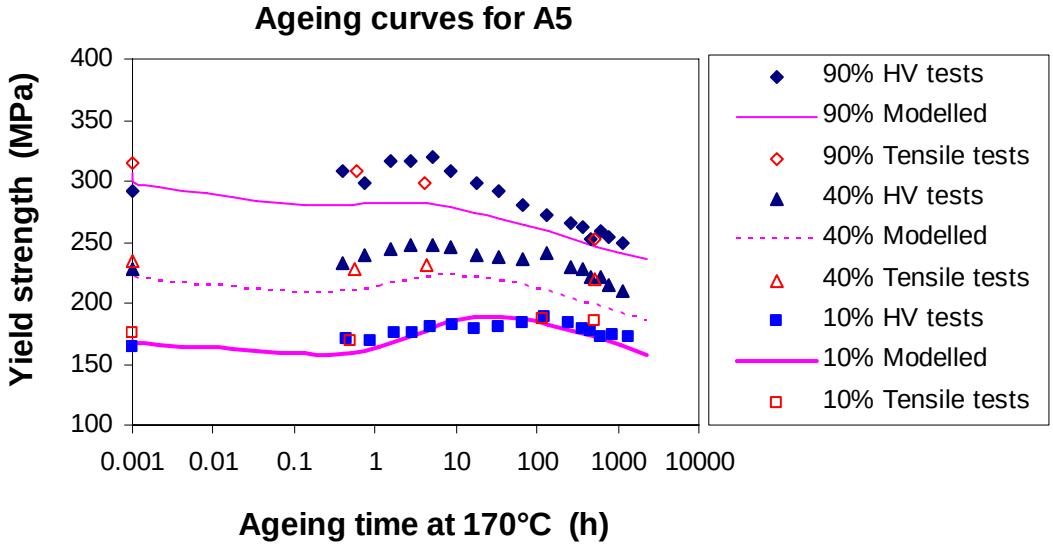
Ageing curves for A5
Yield strength (MPa)
400
350
300
250
200
150
100
0.001
0.01
0.1
1
10
100
1000
10000
Ageing time at 170°C (h)
90% HV tests
90% Modelled
90% Tensile tests
40% HV tests
40% Modelled
40% Tensile tests
10% HV tests
10% Modelled
10% Tensile tests

e.

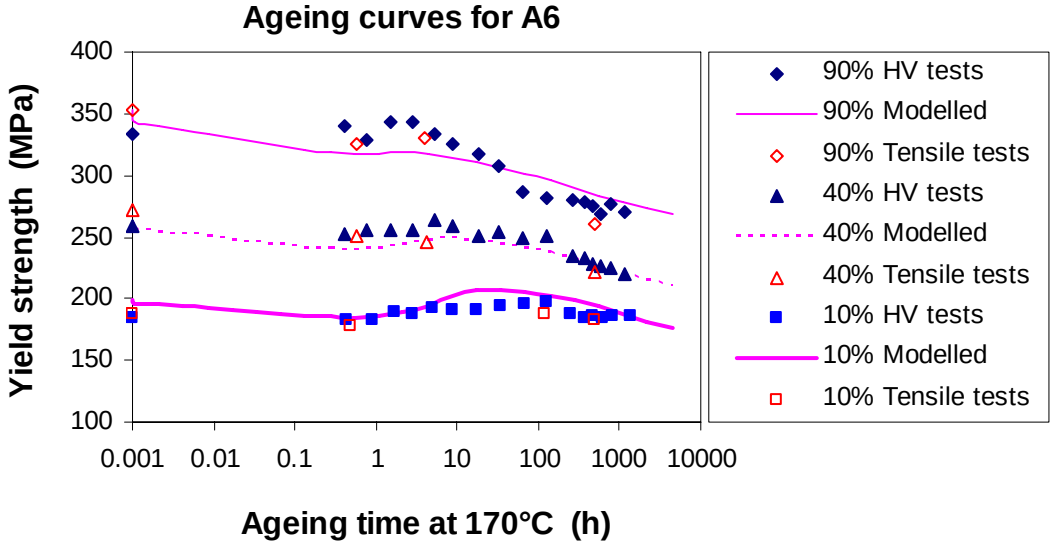
Ageing curves for A6
Yield strength (MPa)
400
350
300
250
200
150
100
0.001
0.01
0.1
1
10
100
1000
10000
Ageing time at 170°C (h)
90% HV tests
90% Modelled
90% Tensile tests
40% HV tests
40% Modelled
40% Tensile tests
10% HV tests
10% Modelled
10% Tensile tests

f.

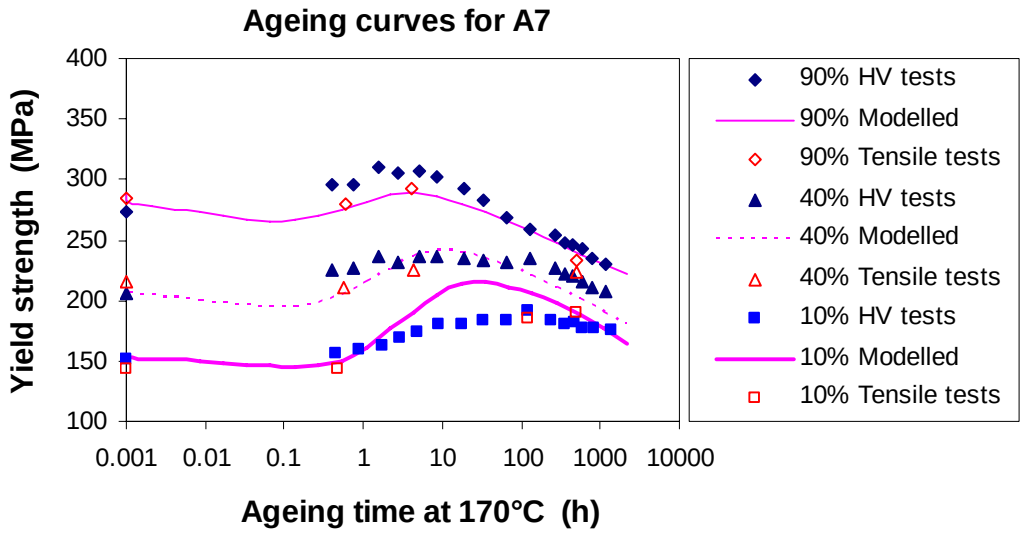

g.

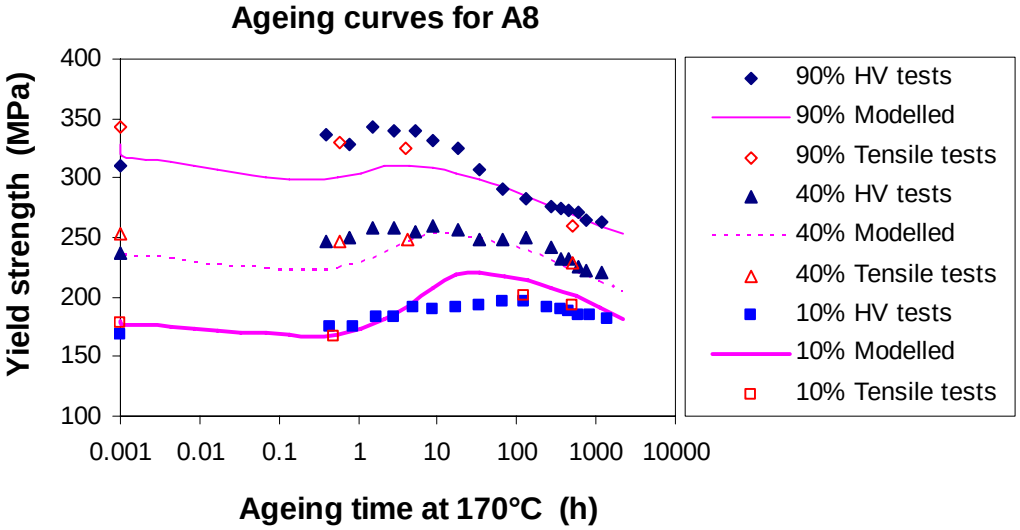

h.

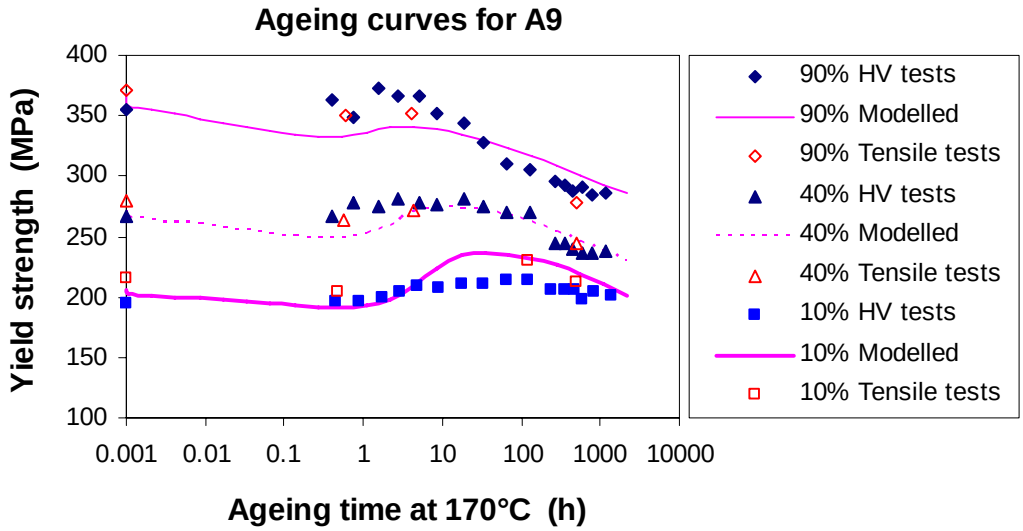

i.

Figure 6.14 Measured yield strengths and modelling results using method I for alloys: a. Al, b. A2, c. A3, d. A4, e. A5, f. A6, g. A7, h. A8, i. A9

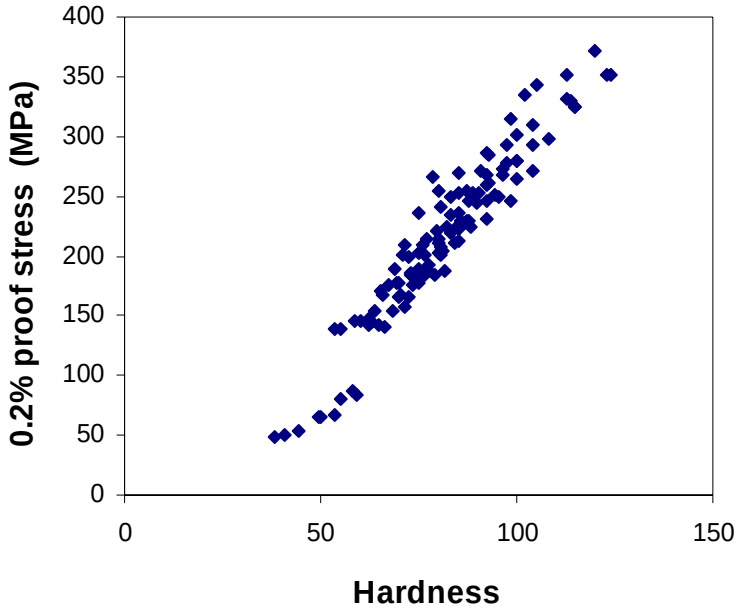

Figure 6.15 Measured hardness and 0.2% PS

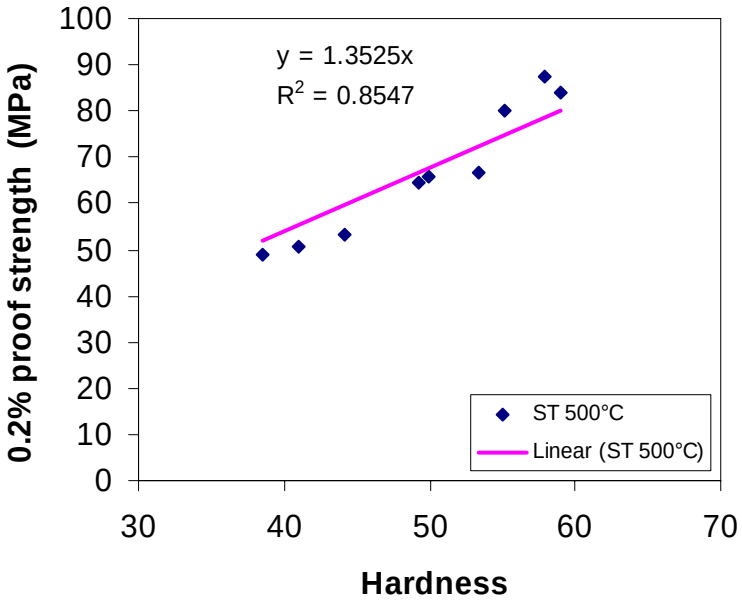

Figure 6.16 Measured hardness and 0.2% PS for solution-treated alloys

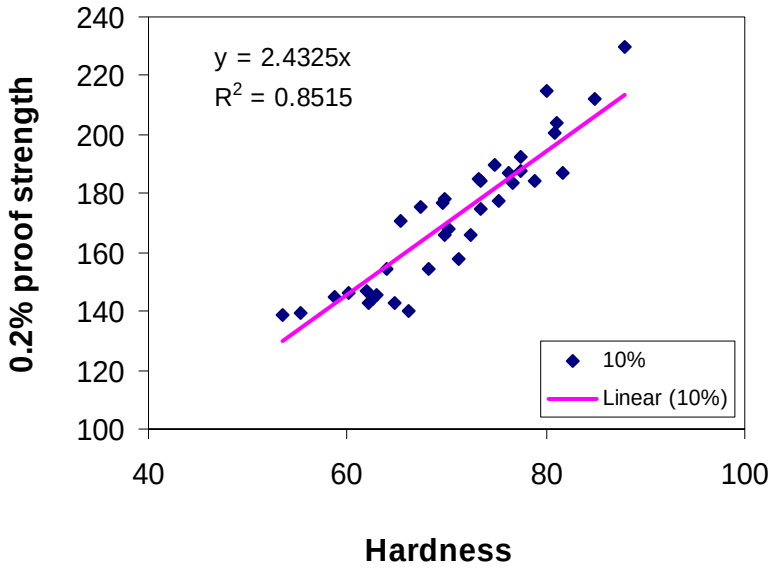

Figure 6.17 Measured hardness and 0.2% PS for alloys with 10% reduction

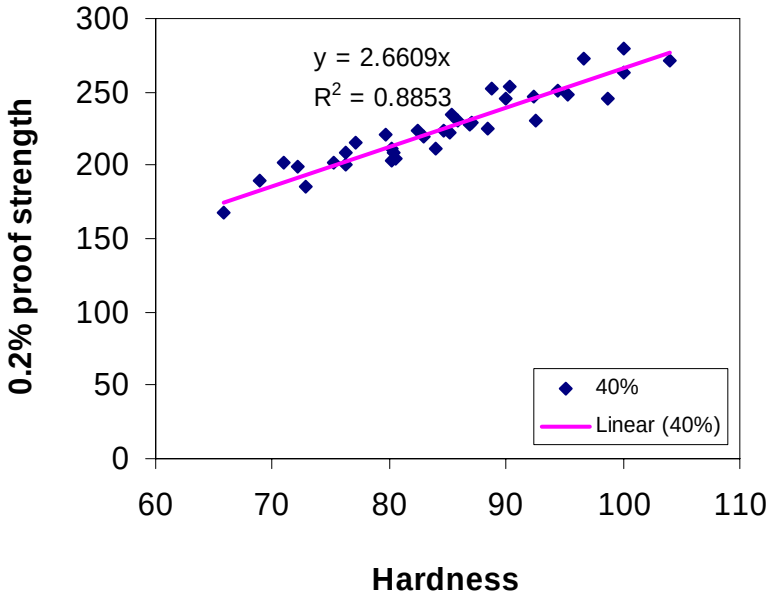

Figure 6.18 Measured hardness and 0.2% PS for alloys with 40% reduction

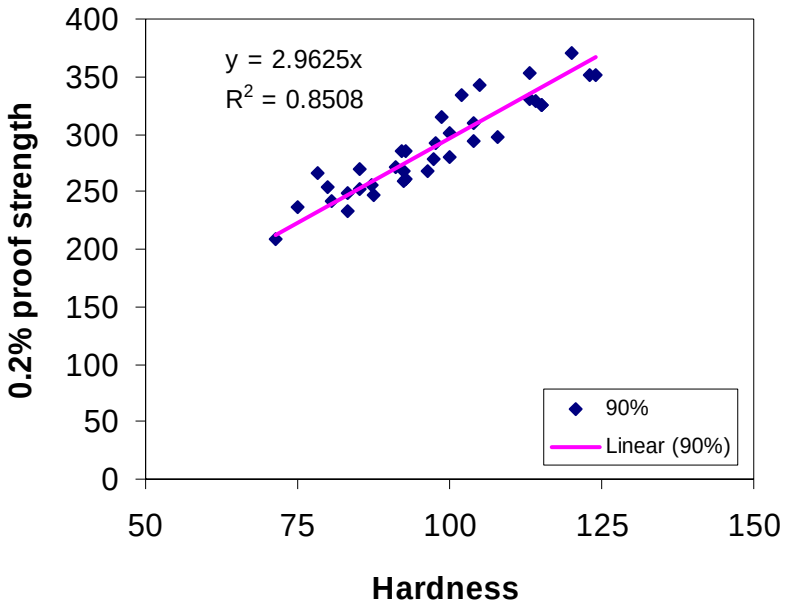

Figure 6.19 Measured hardness and 0.2% PS for alloys with 90% reduction

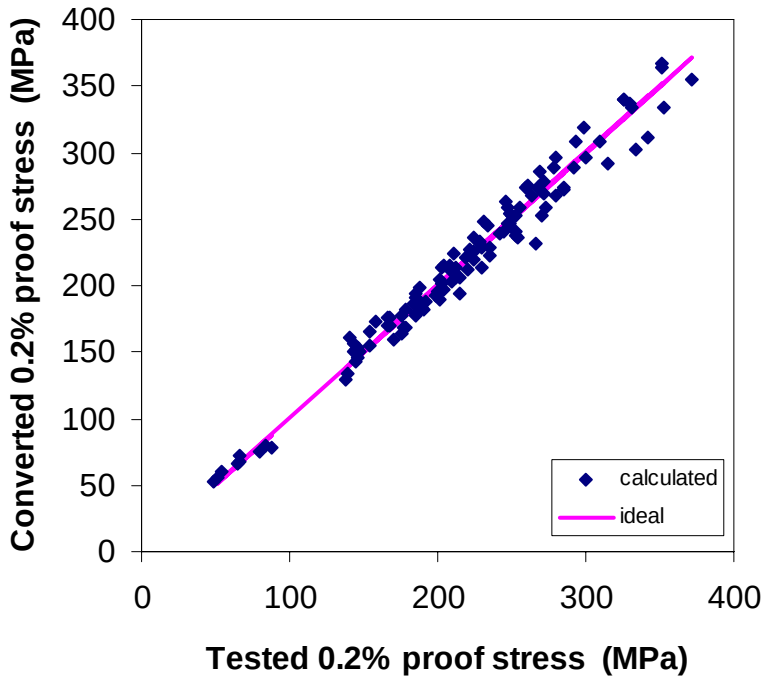

Figure 6.20 Converted PS from hardness vs. measured PS

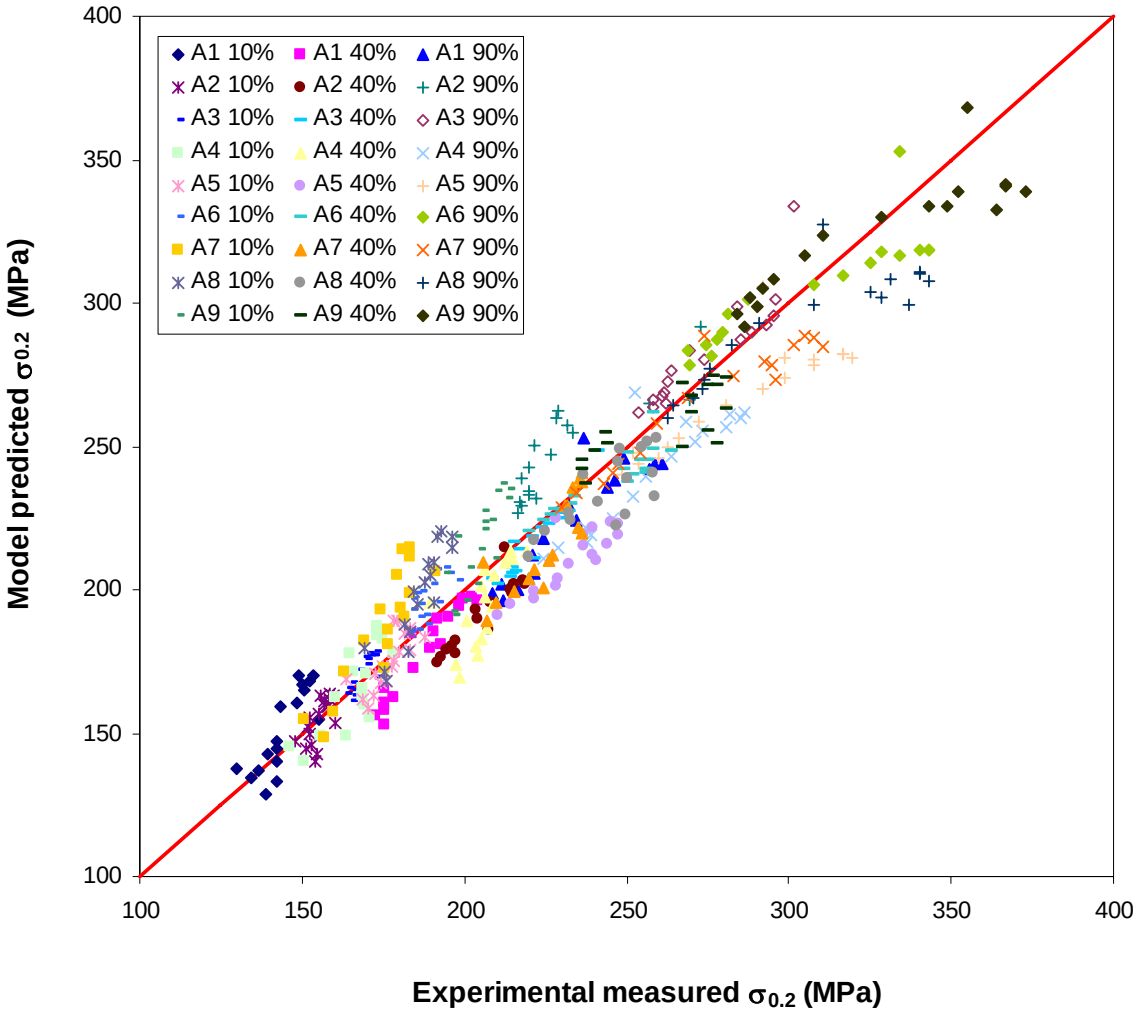

Figure 6.21 Measured $\sigma_{0.2}$ data (converted from hardness data) vs. model predicted $\sigma_{0.2}$ using method I

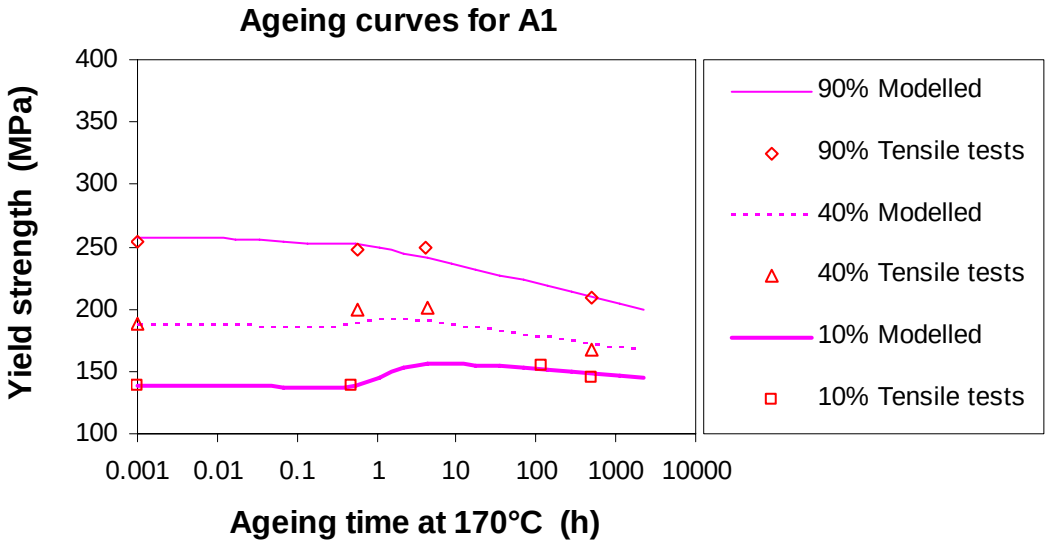

a.

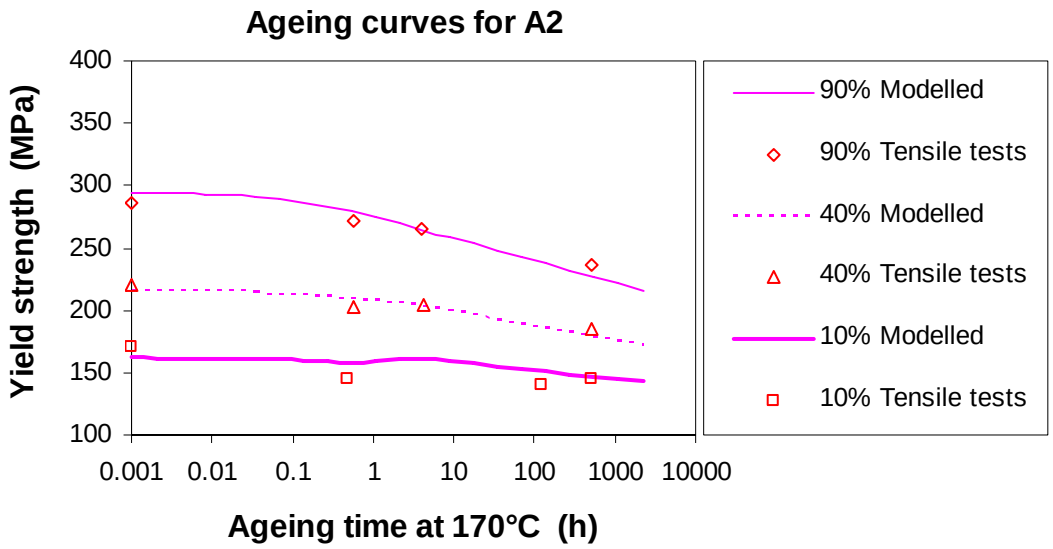
Ageing curves for A2
Yield strength (MPa)
400
350
300
250
200
150
100
0.001
0.01
0.1
1
10
100
1000
10000
Ageing time at 170°C (h)
90% Modelled
90% Tensile tests
40% Modelled
40% Tensile tests
10% Modelled
10% Tensile tests

b.

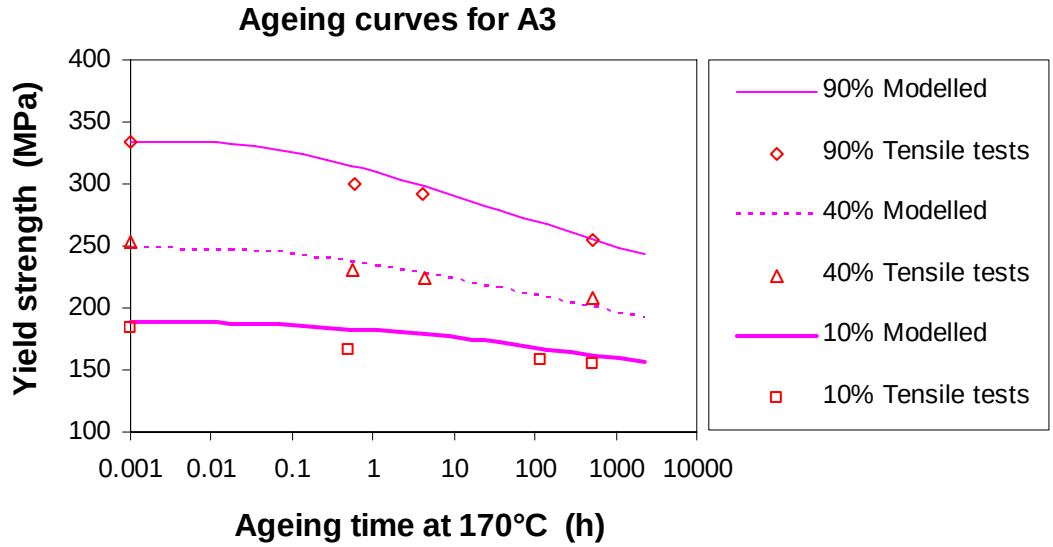
Ageing curves for A3
Yield strength (MPa)
400
350
300
250
200
150
100
0.001
0.01
0.1
1
10
100
1000
10000
Ageing time at 170°C (h)
90% Modelled
90% Tensile tests
40% Modelled
40% Tensile tests
10% Modelled
10% Tensile tests

c.

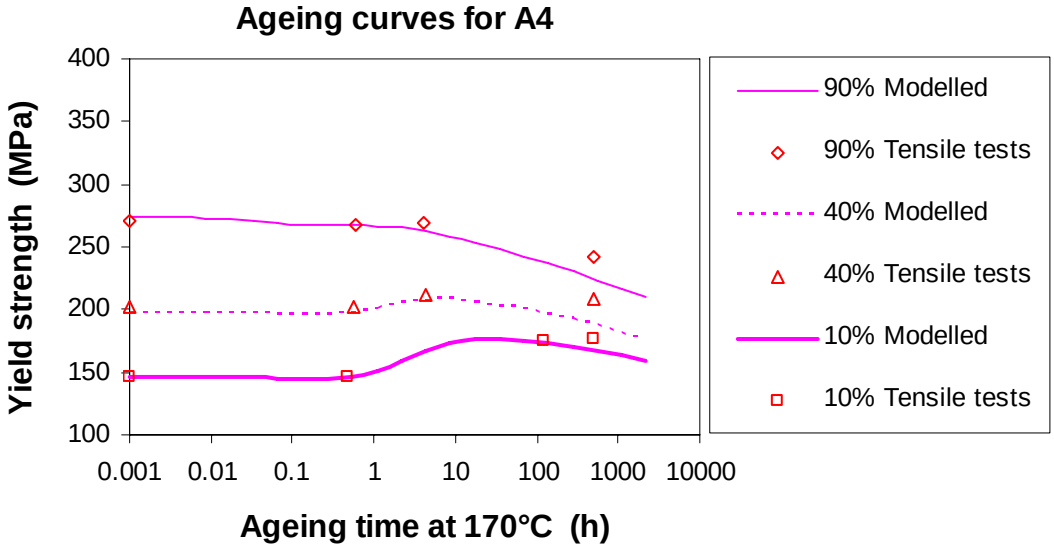
Ageing curves for A4
Yield strength (MPa)
400
350
300
250
200
150
100
0.001
0.01
0.1
1
10
100
1000
10000
Ageing time at 170°C (h)
90% Modelled
90% Tensile tests
40% Modelled
40% Tensile tests
10% Modelled
10% Tensile tests

d.

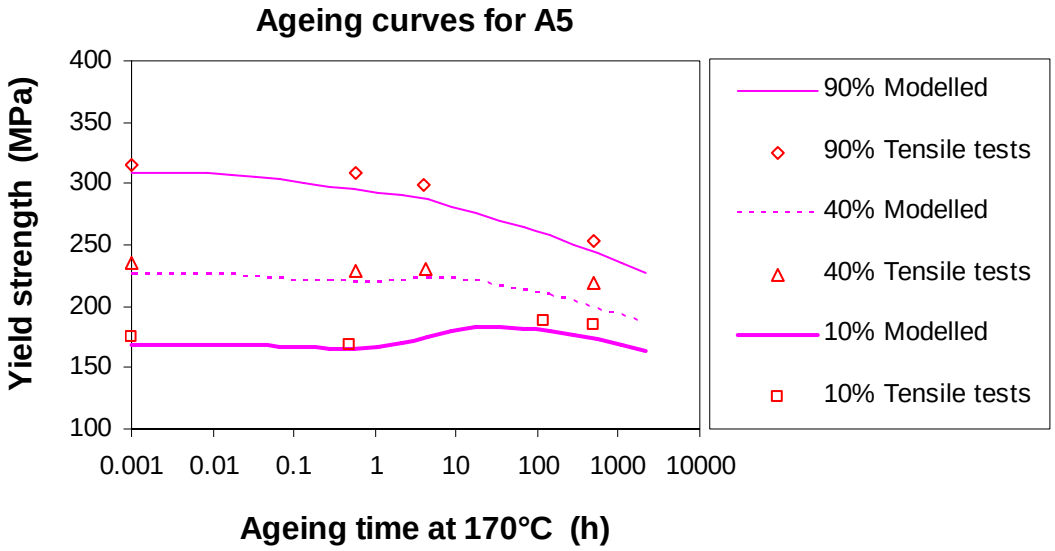
Ageing curves for A5
Yield strength (MPa)
400
350
300
250
200
150
100
0.001
0.01
0.1
1
10
100
1000
10000
Ageing time at 170°C (h)
90% Modelled
90% Tensile tests
40% Modelled
40% Tensile tests
10% Modelled
10% Tensile tests

e.

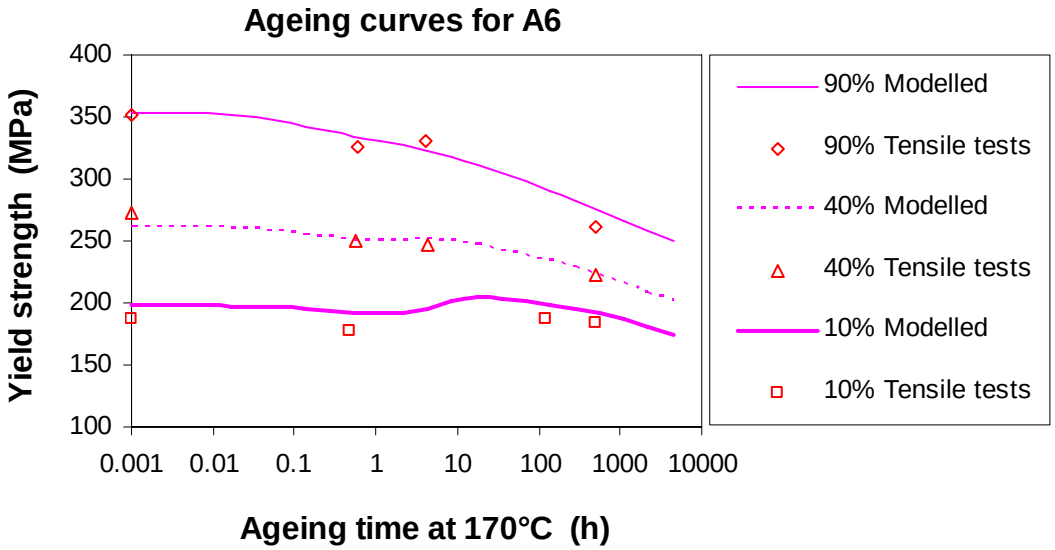
Ageing curves for A6
Yield strength (MPa)
400
350
300
250
200
150
100
0.001
0.01
0.1
1
10
100
1000
10000
Ageing time at 170°C (h)
90% Modelled
90% Tensile tests
40% Modelled
40% Tensile tests
10% Modelled
10% Tensile tests

f.

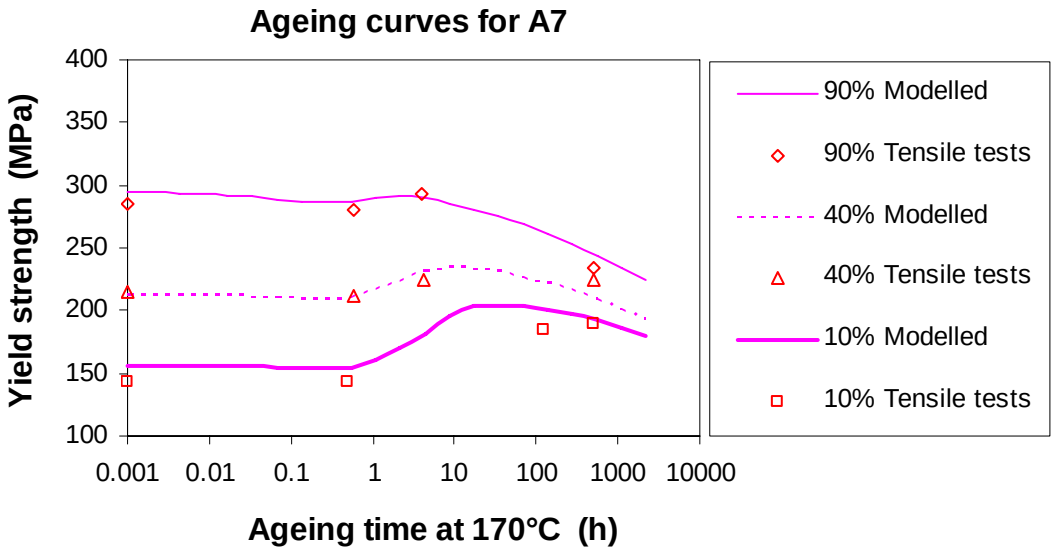
Ageing curves for A7
Yield strength (MPa)
400
350
300
250
200
150
100
0.001
0.01
0.1
1
10
100
1000
10000
Ageing time at 170°C (h)
90% Modelled
90% Tensile tests
40% Modelled
40% Tensile tests
10% Modelled
10% Tensile tests

g.

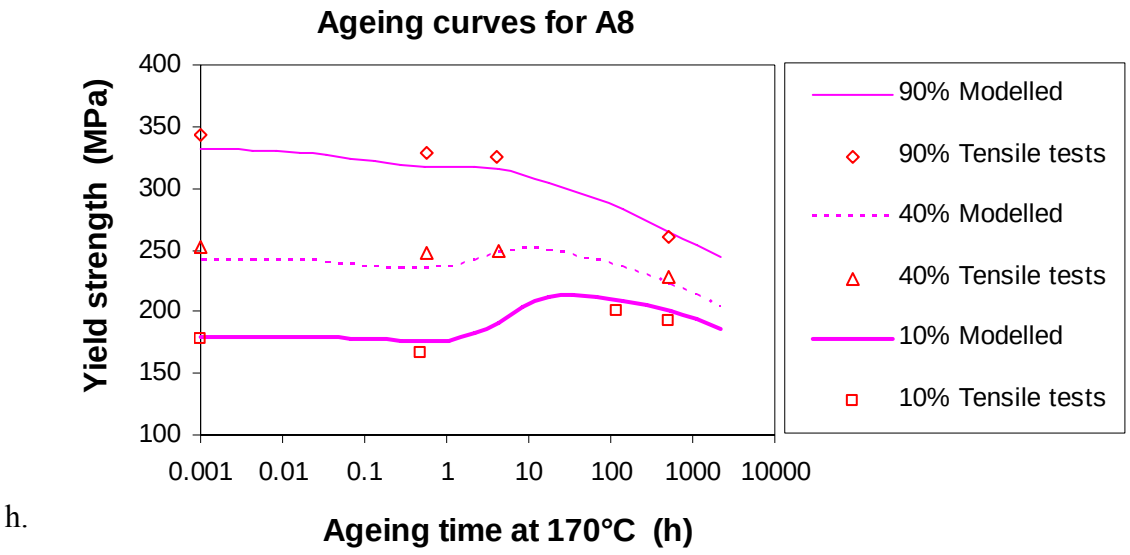

h.

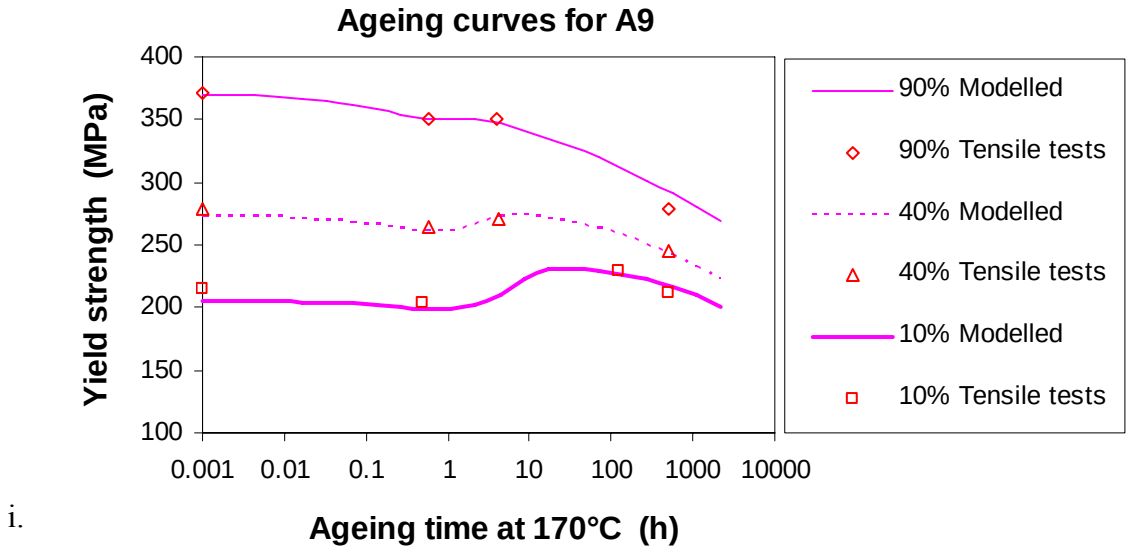

i.

Figure 6.22 Measured yield strengths and modelling results using method II for alloys: a. A1, b. A2, c. A3, d.A4, e. A5, f. A6, g. A7, h, A8, i. A9

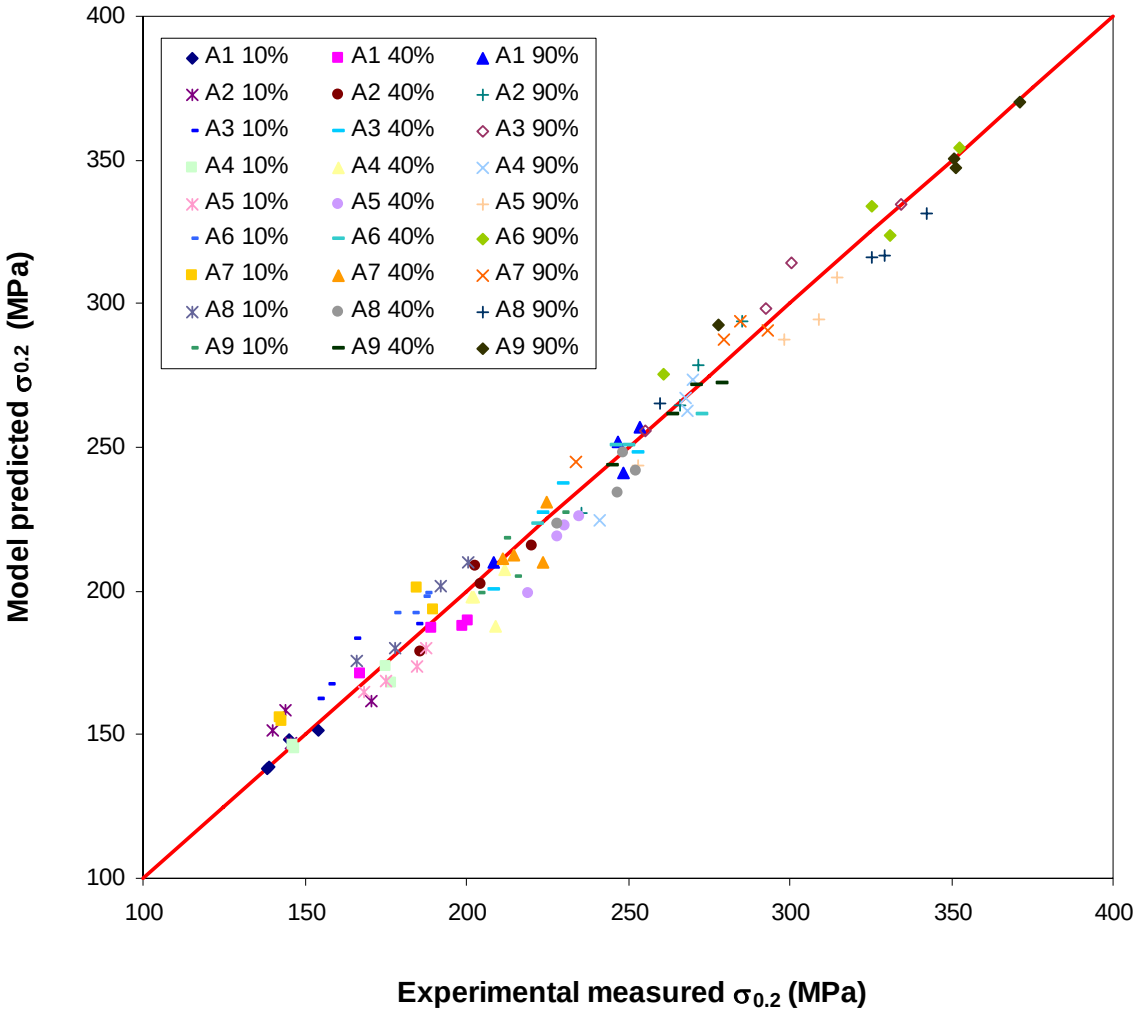

Figure 6.23 Predicted $\sigma_{0.2}$ using method II vs. measured $\sigma_{0.2}$

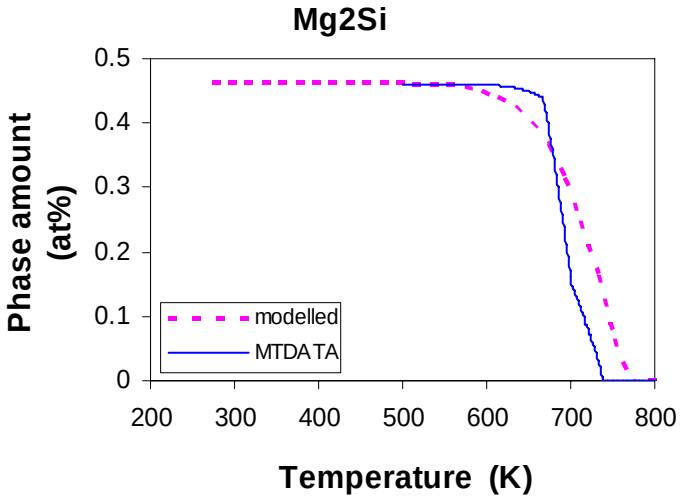

Figure 6.24 Calculated amounts of Mg_2Si formed vs. temperature for alloy A1

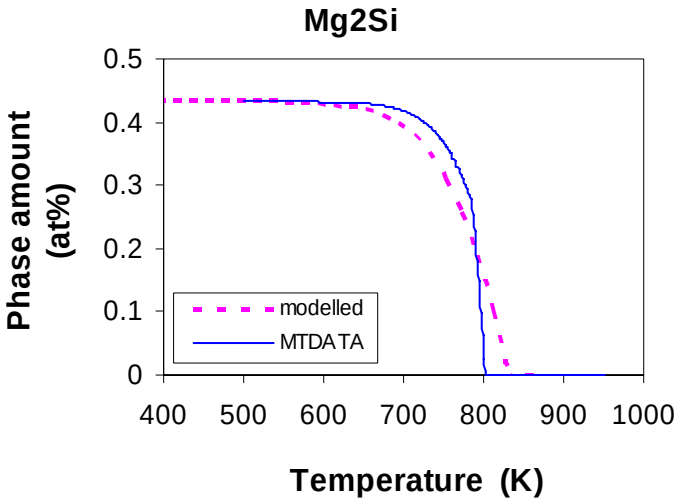

Figure 6.25 Calculated amounts of Mg_2Si formed vs. temperature for alloy A2

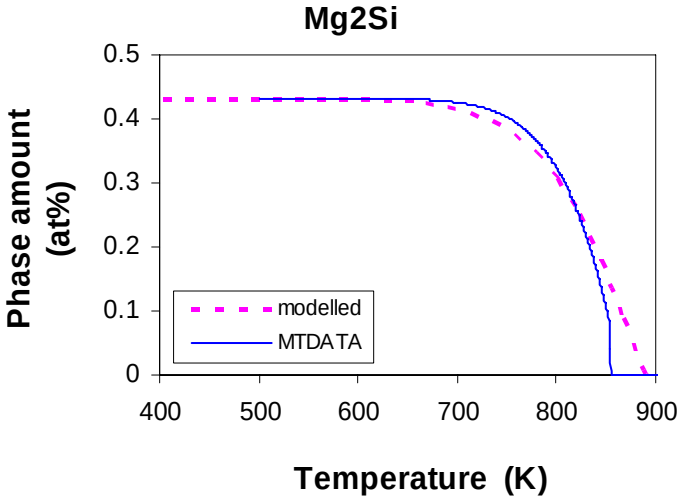

Figure 6.26 Calculated amounts of Mg_2Si formed vs. temperature for alloy A3

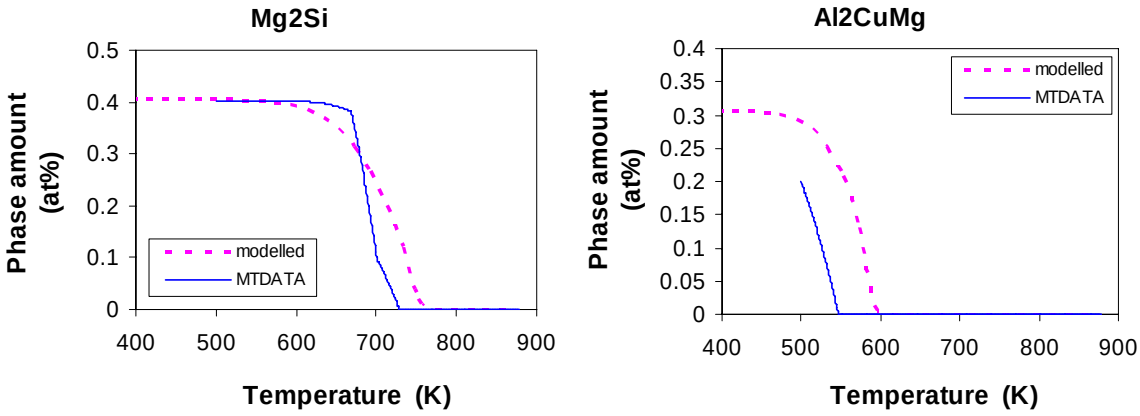

Figure 6.27 Calculated amounts of Mg_2Si and S formed vs. temperature for alloy A4

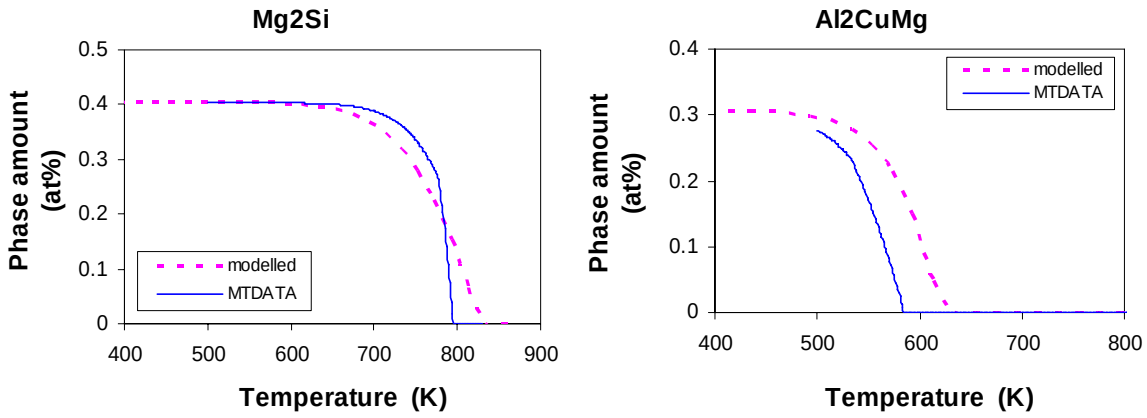

Figure 6.28 Calculated amounts of Mg_2Si and S formed vs. temperature for alloy A5

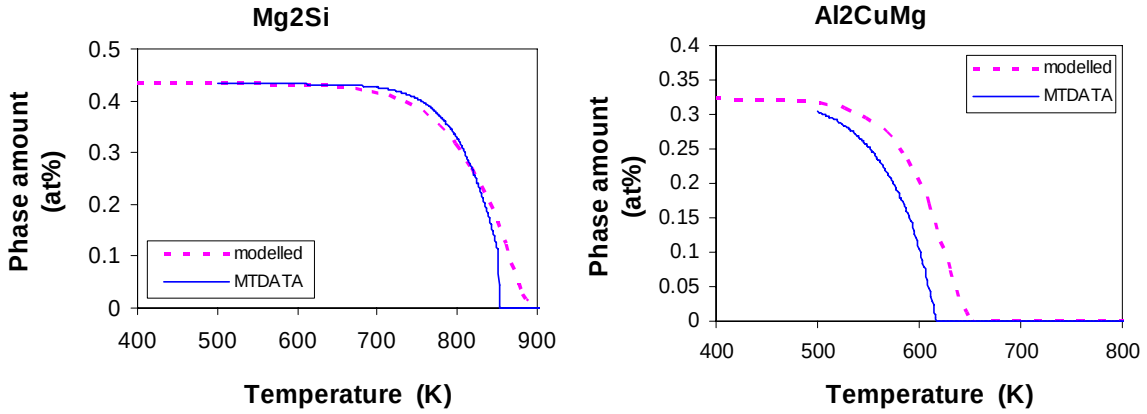

Figure 6.29 Calculated amounts of Mg_2Si and S formed vs. temperature for alloy A6

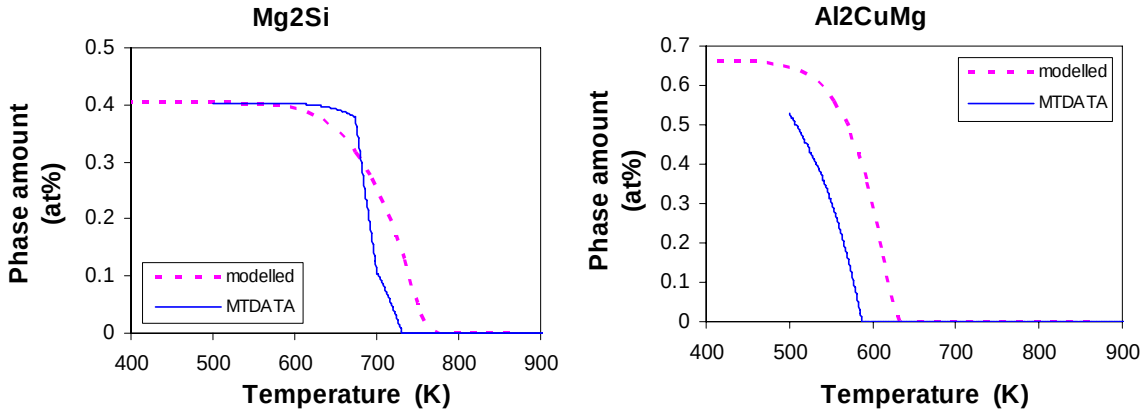

Figure 6.30 Calculated amounts of Mg_2Si and S formed vs. temperature for alloy A7

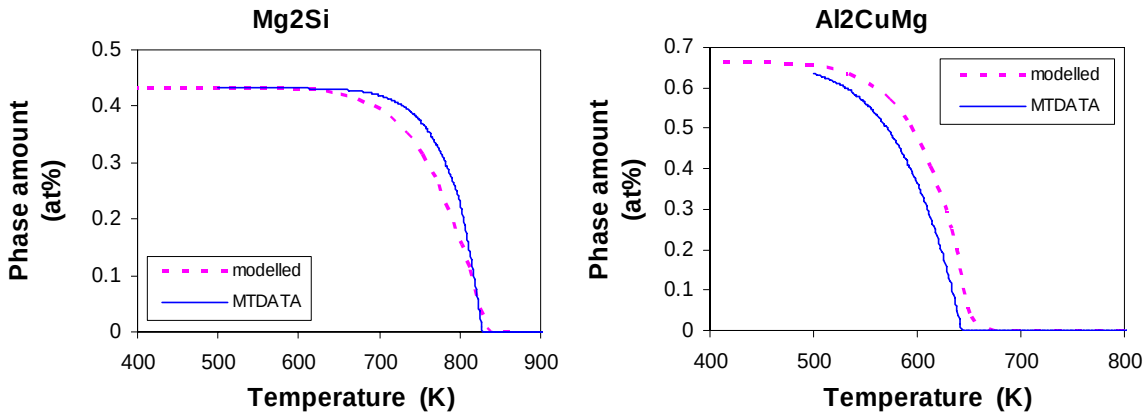

Figure 6.31 Calculated amounts of Mg_2Si and S formed vs. temperature for alloy A8

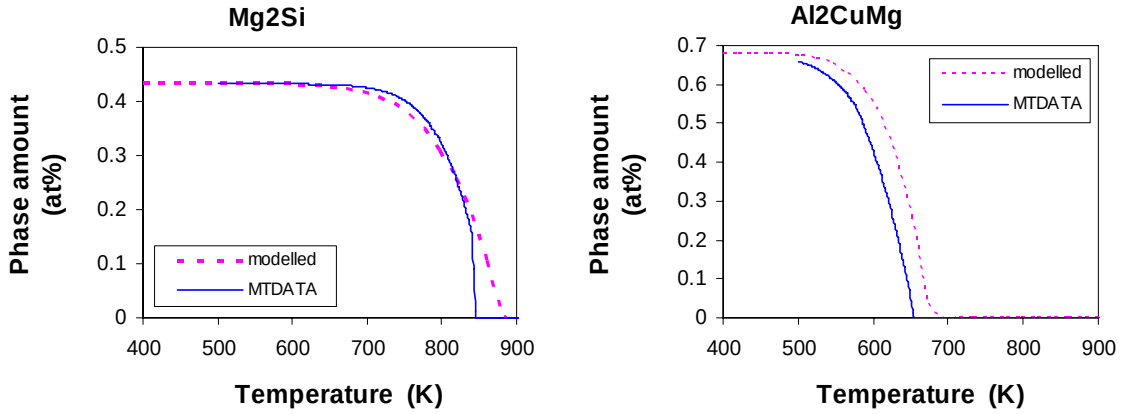

Figure 6.32 Calculated amounts of Mg_2Si and S formed vs. temperature for alloy A9

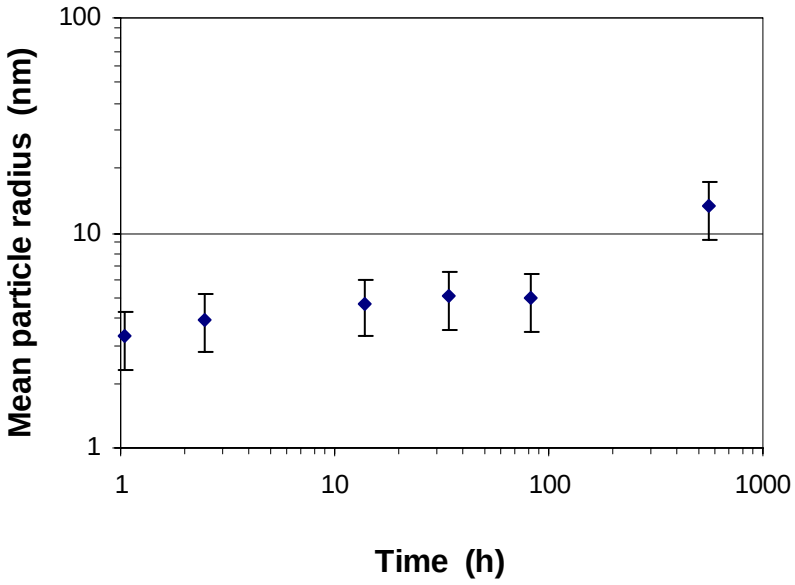

Figure 6.33 Observed radius of precipitates with time in an Al-Mg-Si alloy from [4]

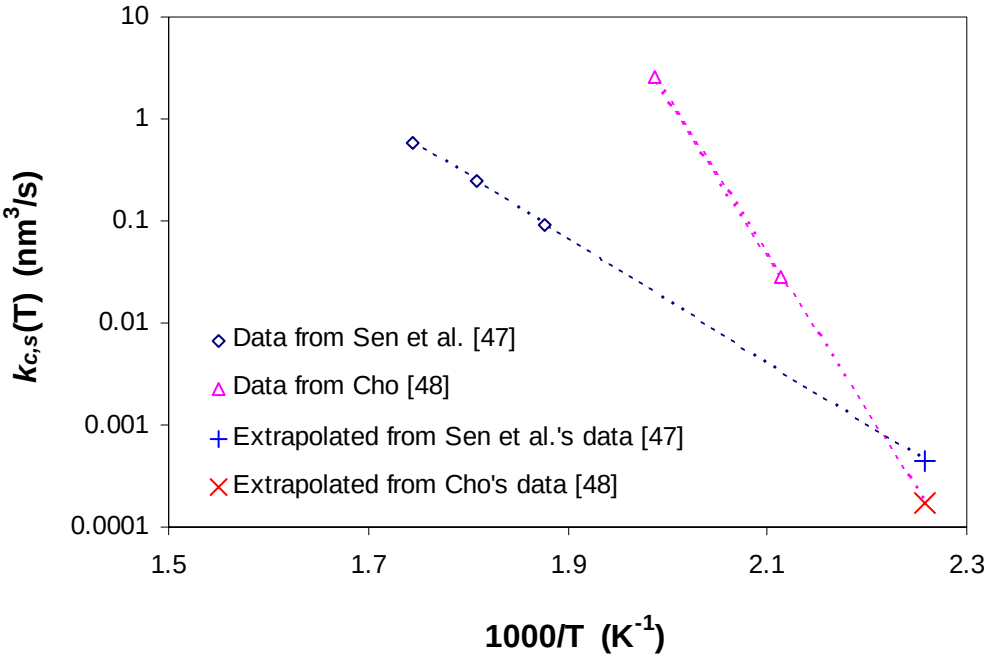

Figure 6.34 Coarsening parameter $k_{c,S}(T, \varepsilon = 0)$ for S phase from literature and extrapolated values at 170°C

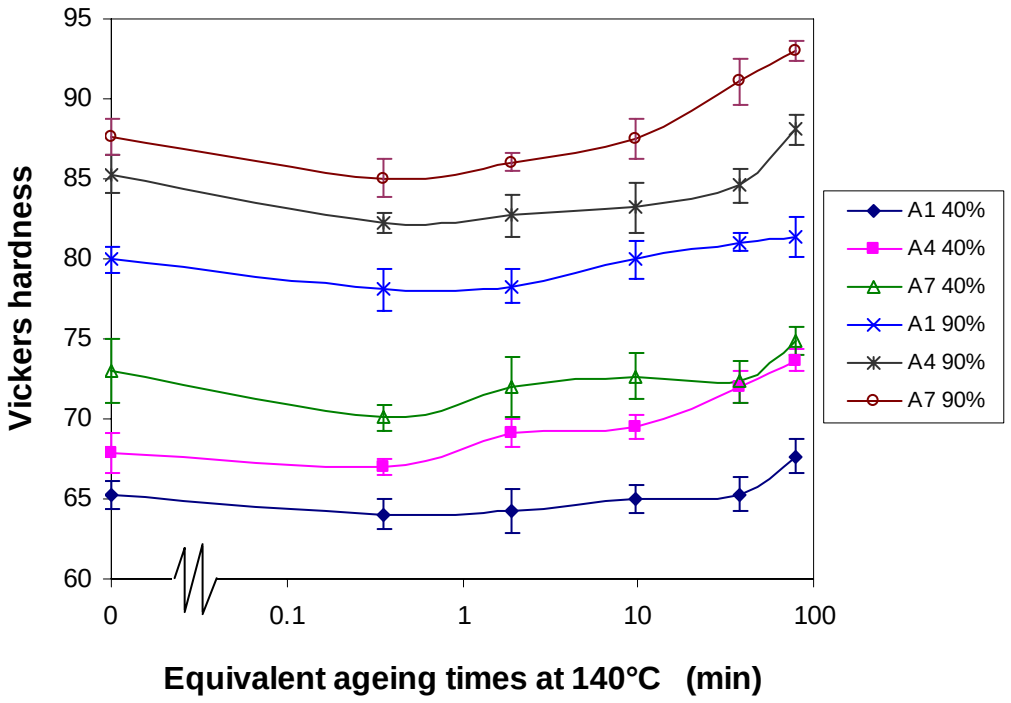

Figure 6.35 Hardness of alloys A1, A4 and A7 during isothermal ageing at 140°C

References

1. Bratland, D.H., Grong, ∅., Shercliff, H., Myhr, O.R. and Tjotta, S., Acta Mater., **45**, 1997, p. 1.
2. Starink, M.J. and Wang, S.C., Acta Mater., **51**, 2003, p. 5131.
3. Yan, J., ***Strength modelling of Al-Cu-Mg type alloys***, PhD thesis, School of Engineering Sciences, University of Southampton, 2006.
4. Myhr, O.R., Grong, ∅. and Andersen, S.J., Acta Mater., **49**, 2001, p. 65.
5. Starink, M.J. and Zahra, A.M., Thermochim. Acta, **292**, 1997, p. 159.
6. Starink, M.J. and Zahra, A.M., Philos. Mag. A, **77**, 1998, p. 187.
7. Smithells, C.J., ***Smithells Metals Reference Book*** (7th edition), Brandes, E.A. and Brook, G.B. (Editors), Oxford, Butterworths-Heinemann, 1992.
8. Zurob, H.S., Brechet, Y. and Purdy, G., Acta Mater., **49**, 2001, p. 4183.
9. Zurob, H.S., Hutchinson, C.R., Brechet, Y. and Purdy, G., Acta Mater., **50**, 2002, p. 3075.
10. Kocks, U.F. and Mecking, H., Prog. Mater. Sci., **48**, 2003, p. 171.
11. Cheng, L.M., Poole, W.J., Embury, J.D. and Lloyd, D.J., Metall. Mater. Trans. A, **34A**, 2003, p. 2473.
12. Wang, S.C., Zhu, Z. and Starink, M.J., J. Microsc.-Oxf., **217**, 2005, p. 174.
13. Starink, M.J., Int. Mater. Rev., **49**, 2004, p. 191.
14. Zhen, L. and Kang, S.B., Mat. Sci. Technol., **14**, 1998, p. 317.
15. Zhen, L., Fei, W.D., Kang, S.B. and Kim, H.W., J Mater. Sci., **32**, 1997, p. 1895.
16. Dutkiewicz, J. and Litynska, L., Mater. Sci. Eng. A, **324**, 2002, p. 239.
17. Miao, W.F. and Laughlin, D.E., Scripta Mater., **40**, 1999, p. 873.
18. Gupta, A.K., Lloyd, D.J. and Court, S.A., Mater. Sci. Eng. A, **316**, 2001, p. 11.
19. Gupta, A.K., Lloyd, D.J. and Court, S.A., Mater. Sci. Eng. A, **301**, 2001, p. 140.
20. Borrego, A. and Gonzalez-Doncel, G., Mater. Sci. Eng. A, **245**, 1998, p. 10.
21. Hatta, H., Matsuda, S., Tanaka, H. and Yoshida, H., ***Effects of natural aging conditions on the bake hardenability of Al-Mg-Si alloys***, in *the 9th International Conference on Aluminium Alloys (ICAA9)*, Nie, J.F., Morton, A.J. and Muddle, B.C. (Editors), Brisbane, Australia, 2004, p. 564.
22. Buha, J., Munroe, P.R., Lumley, R.N., Crosky, A.G. and Hill, A.J., ***Positron studies of precipitation in 6061 aluminium alloy***, in *the 9th International Conference on*

Aluminium Alloys (ICAA9), Nie, J.F., Morton, A.J. and Muddle, B.C. (Editors), Brisbane, Australia, 2004, p. 1028.

23. Quainoo, G.K. and Yannacopoulos, S., J. Mater. Sci., **39**, 2004, p. 6495.
24. Ravi, C. and Wolverton, C., Acta Mater., **52**, 2004, p. 4213.
25. Starink, M.J. and Yan, J.-L., ***A model for strengthening of Al-Cu-Mg alloys by S phase***, in *1st International Symposium on Metallurgical Modelling for Aluminum Alloys, ASM Materials Solution 2003*, Tiryakioglu, M. and Lalli, L.A. (Editors), Pittsburgh, Pennsylvania, ASM International, 2003, p. 119.
26. Starink, M.J., Wang, P., Sinclair, I. and Gregson, P.J., Acta Mater., **47**, 1999, p. 3841.
27. Sivaprasad, P.V., Venugopal, S. and Venkadesan, S., Mat. Sci. Technol., **20**, 2004, p. 350.
28. Lloyd, D.J. and Kenny, D., Metall. Trans. A, **13A**, 1982, p. 1445.
29. Nes, E., Acta Metall. Mater., **43**, 1995, p. 2189.
30. Kuhlmann-Wilsdorf, D., Philos. Mag. A, **79**, 1999, p. 955.
31. Friedel, J., ***Dislocations***, London, Pergamon Press Ltd., 1964.
32. Nabarro, F., ***Theory of crystal dislocations***, Oxford, University Press, 1967.
33. Gypen, L.A. and Deruyttere, A., J. Mater. Sci., **12**, 1977, p. 1028.
34. Gomiero, P., Brechet, Y., Louchet, F., Tourabi, A. and Wack, B., Acta Metall. Mater., **40**, 1992, p. 857.
35. Estrin, Y., ***Dislocation-Density-Related Constitutive Modeling***, in *Unified Constitutive Laws of Plastic Deformation*, Krausz, A.S. and Krausz, K. (Editors), Toronto, Academic Press, 1996, p. 69.
36. Clausen, B., Lorentzen, T. and Leffers, T., Acta Mater., **46**, 1998, p. 3087.
37. Starink, M.J., Wang, P., Sinclair, I. and Gregson, P.J., Acta Mater., **47**, 1999, p. 3855.
38. Donnadieu, P., Dirras, G.F. and Douin, J., Mater. Sci. Forum, **396-4**, 2002, p. 1019.
39. Dirras, G.F., Donnadieu, P. and Douin, J., Probl. Mater. Sci., **1**, 2003, p. 33.
40. Starink, M.J., Li, X.M. and Wang, S.C., ***Models for the yield strength of Al-Zn-Mg-Cu alloys***, in *1st International Symposium on Metallurgical Modelling for Aluminum Alloys, ASM Materials Solution 2003*, Tiryakioglu, M. and Lalli, L.A. (Editors), Pittsburgh, Pennsylvania, ASM International, 2003, p. 119.
41. Brown, L.M. and Ham, R.K., ***Dislocation-particle interactions***, in *Strengthening methods in crystals*, Kelly, A. and Nicholson, R.B. (Editors), London, Elsevier publishing company limited, 1971, p. 9.
42. Schlesier, C. and Nembach, E., Acta Metall. Mater., **43**, 1995, p. 3983.

43. Davis, J.R., ***ASM Specialty Handbook®: Aluminium and Aluminium Alloys***, ASM International®, 1993.
44. Lloyd, D.J. and Court, S.A., Mat. Sci. Technol., **19**, 2003, p. 1349.
45. Jiang, D.M., Kang, S.B. and Kim, H.W., Mat. Sci. Technol., **15**, 1999, p. 1401.
46. Rainforth, W.M. and Jones, H., J. Mater. Sci. Lett., **16**, 1997, p. 420.
47. Sen, N. and West, D.R.F., J. Inst. Met., **97**, 1969, p. 87.
48. Cho, H.K., J. Korean Inst. Met., **16**, 1978, p. 160.
49. Zurob, H.S., ***Effects of precipitation, recovery and recrystallization on the microstructural evolution of microalloyed austenite***, PhD thesis, Materials engineering, McMaster University, 2003.
50. Zhu, Z. and Starink, M.J., ***Recovery and precipitation in cold-rolled Al-(1-3)Mg-(0-0.4)Cu-Mn alloys***, in *Proceedings of the 9th PG conference in engineering materials*, Southampton, UK, 2003, p. 27.

7 Characterisation and Preliminary Modelling of Work Hardening of Al-Mg(-Cu)-Si-Mn Alloys during Tension

7.1 Introduction

In the previous chapter, a yield strength model has been developed and applied to model the age hardening/softening behaviour of nine cold-worked Al-Mg(-Cu)-Si-Mn alloys. In this chapter, the work hardening behaviour of these alloys will be extensively analysed and a basic model will be proposed to explain the main trends observed experimentally for the work hardening behaviour of as solution-treated, cold-rolled and cold-rolled-and-aged alloys. In the work hardening model, some input parameters, e.g., effective dislocation density, precipitate size and volume fraction of precipitates, will be taken from the output of the yield strength model, which was presented in the previous chapter.

This chapter is structured as follows. Plastic stress and plastic strain calculated from tensile testing data will first be presented. Subsequently, two methods to evaluate work hardening rate will be applied and discussed. Finally, preliminary models based on KM and KME models (see section 3.2) will be applied with an aim to explain the main trends observed in the work hardening behaviour of the solution-treated, cold-rolled and cold-rolled-and-aged alloys. To the author's knowledge, this is the first attempt, accessible in open literature, that addresses a work hardening model for range of alloys and processing conditions as wide as the present one.

7.2 Plastic stress and plastic strain curves

The true stress-true strain curves of the tensile tests of aluminium alloys have two main stages: elastic deformation associated with linear stress-strain relation and plastic deformation. Plastic strain (ε_p) is defined as the unrecoverable strain after unloading, see Figure 7.1. The total strain is the sum of the plastic strain and the elastic strain:

$$\varepsilon = \varepsilon_p + \varepsilon_e \qquad \textbf{(7.1)}$$

where ε is the total tensile true strain, ε_p is the plastic strain and ε_e is the elastic strain, which can be determined by

$$\varepsilon_e = \frac{\sigma}{E} \quad \textbf{(7.2)}$$

where σ is the total true stress at strain ε, E is the elastic modulus of the material.

The plastic strain thus can be determined by

$$\varepsilon_p = \varepsilon - \frac{\sigma}{E} \quad \textbf{(7.3)}$$

The plastic stress (σ_p) is defined as

$$\sigma_p = \sigma - \sigma_y \quad \textbf{(7.4)}$$

So the plastic stress-plastic strain can be determined from the true stress-true strain curves of tensile tests. Analyses were performed on solution-treated samples, cold-worked samples and cold-work-and-aged samples to study the influence of solution treatment, the level of cold work and ageing conditions on the work hardening behaviour.

The results for solution-treated alloys are shown in Figure 7.2. In this figure, noise reduction was achieved through sampling with a period equal to 100 data points. As shown in the figure, although there is still noise remaining on the curves, clear trends can be observed. The plastic stress, σ_p, increases with increasing Mg and Cu contents, especially at larger plastic strains (see curves for alloys A1, A2 and A3 for the influence of Mg content and curves for alloys A1, A4 and A7 for the influence of Cu content). This evidences again that the work hardening rate (WHR) increases with increasing Mg and Cu contents.

For the cold-worked samples, the influence of level of cold work is illustrated in Figure 7.3 to Figure 7.5, using alloys A4, A6 and A7 as examples. The figures reveal that the level of cold work significantly influences work hardening: the WHR decreases with increasing level of cold work. Solution-treated samples have the highest work hardening rates, and the WHR dramatically reduces when the samples is cold-worked with 10%

reduction. The WHR decreases more gradually on increasing the level of cold work from 10% to 90%.

The influence of isothermal ageing is much more complicated. It depends on the alloying content, level of cold work and ageing time, which determines the interactions of recovery and precipitation during ageing prior to tensile tests. Some selected results are shown in Figure 7.6 to Figure 7.14 (Complete results are available on CD). As shown in the figures, generally the WHR is lowest for the cold-worked samples. On ageing for 30 minutes at 170°C, σ_p increases substantially compared to the cold-worked sample at the same level of plastic strain for all alloys. Further evolution of σ_p with ageing depends on alloy. For alloys that do not show substantial age hardening, e.g., alloys A2 and A3, no change in σ_p on continued ageing is observed (see Figure 7.7 and Figure 7.8). For the alloys which show substantial age hardening, pronounced changes in σ_p with ageing can be observed (see Figure 7.6 and Figure 7.9 to Figure 7.14). This indicates that precipitation occurs, within the aged samples or changes in solute content of the Al phase influencing the work hardening behaviour during tensile tests. This will be further studied in the following section by means of work hardening rate analyses.

7.3 Work hardening rate analyses

The work hardening rate, WHR (Θ), is defined as:

$$\Theta = \frac{d\sigma}{d\varepsilon} \qquad \textbf{(7.5)}$$

The instantaneous WHR generally cannot be directly obtained from the original true stress-true strain data recorded during tensile testing due to noise in the original data. This is a common problem noted in several papers [1-5]. Thus the average stress-strain values of 100-300 points (depending on the sampling rates of the original data) obtained from the original data were used to derive the WHR. Analyses were performed on solution-treated samples, cold-worked samples and cold-work-and-aged samples. The evolution of work hardening will be illustrated in the plots of Θ vs. (σ-σ_y), which are usually referred to as work hardening rate plots or Kocks-Mecking plots [2, 6-11].

For solution-treated alloys, the values of average stress and average strain of about 200 points are used to derive the WHR (Θ) and the results represented by the Kocks-Mecking plots are shown in Figure 7.15. The figure reveals the following main trends:

- The WHR decreases with increasing (σ-σ_y).
- The WHR increases with increasing Mg and Cu contents.

Theses observations are consistent with the observations obtained through the analyses of the plots of (σ-σ_y) vs. ε_p (i.e., the plots of plastic stress-strain) in the previous section.

To determine the influence of level of cold work on the work hardening rates, some selected results are shown in Figure 7.16 to Figure 7.19. As illustrated in the figures, the level of cold work significantly influences the work hardening rate evolution during the tensile test. The solution-treated samples have the highest WHR, and the WHR is dramatically reduced when the samples are subject to 10% cold work. Although there is noise on the curves, usually the WHR decreases with increasing level of cold work from 10% to 90% (see Figure 7.16 to Figure 7.18). However, sometimes the samples with 40% cold work have slightly higher WHR than those with 10% cold work, e.g., Figure 7.19. This unexpected observation might be due to the influence of noise, the measurement errors from the determination of σ_y and/or the inaccurate measurements of stress and strain during tensile tests. Imperfect sample shape (e.g., samples could be slightly bent due to residual stresses) can have caused the latter two sources of inaccuracies.

For the influence of ageing condition, some selected results are shown in Figure 7.20 to Figure 7.28 (Complete results for each alloy with 3 levels of cold work are available on CD).

The following main observations were made from these results:

(1) There is a very high initial WHR and it decreases dramatically due to the transition from elastic deformation to plastic deformation.

(2) After the transition, the WHR either decreases gradually or is approximately constant, depending on alloy composition, pre-reduction and ageing condition. For example, for alloy A4 with 90% reduction (see Figure 7.23), it almost remains

constant. For alloy A2 with 10% reduction and alloy A6 with 40% reduction, the WHR decreases gradually with stress (see Figure 7.21 and Figure 7.25 respectively).

(3) For most alloys, the cold-rolled samples have the lowest WHR. On ageing for 30 minutes at 170°C the WHR usually increases.

Due to the influence of noise, it tends to be difficult to distinguish small changes in the WHR in these aged conditions (see Figure 7.20 to Figure 7.28). Another method to analyze work hardening rate is therefore proposed. The average work hardening rate is calculated in a certain range of true strain (0.01-0.03 in this study), which is defined by:

$$\Theta = \frac{\sigma_2 - \sigma_1}{\varepsilon_2 - \varepsilon_1} \qquad \textbf{(7.6)}$$

where σ_1 and σ_2 are the true stresses at the true strains ε_1 and ε_2, respectively.

In order to reduce the influence of noise, within one test five pairs of strain-stress data (ε_1, σ_1) and (ε_2, σ_2) shown in Figure 7.29 were used to calculate the average WHR as follows.

First, the work hardening rate related with each pair of strain-stress data within one test was calculated as expressed in the following equation:

$$\Theta_i = \frac{\sigma_2^i - \sigma_1^i}{\varepsilon_2^i - \varepsilon_1^i} \qquad (i = 1, 2, \ldots, 5) \qquad \textbf{(7.7)}$$

Then the average WHR within one test was taken as the mean of the five values of the WHR calculated using equation. (7.7):

$$\Theta = \frac{\sum_{i=1}^{5} \Theta_i}{5} \qquad \textbf{(7.8)}$$

When two or more valid tests were performed, the mean of the average WHR (Θ) of all valid tests is taken as the final average WHR.

Before showing some detailed results of the analyses of the average WHR, the analysis of the errors of the average WHR will be discussed. There are two methods to express the errors.

First, the error of the average WHR can be expressed as the standard deviation of the five values of WHR (Θ_i) within one test, which is called the error within one test. Second, the error can be expressed as the standard deviation of the values of the average WHR (Θ) of two or more tests, which is called the error of all tests. If only one test is valid, the standard deviation calculated by the first method is used. The error calculated using the second method is used when two or more tests are valid. The standard deviations of all tested conditions are listed in Table 7.1. As illustrated in the table, the errors at specific testing conditions are very large (around hundreds of MPa, and the largest error is 405 MPa). This reflects the difficulties in the accurate measurement of the WHR. These larger errors can also be expected and explained. Supposing that the error of the measured stress difference between two tests is about 5 MPa, the error of the WHR will be about 250 MPa (i.e., 5 MPa/($\varepsilon_2 - \varepsilon_1$)). The error of 5 MPa for stress measurement is very reasonable for aluminium alloys (for the alloys studied, the stress goes up to about 400 MPa). Hence an error within 250 MPa for the WHR is considered to be reasonable and acceptable. Checking through the errors listed in the table, all except two are within 250 MPa. It is noticed that the overall average error of the measured average WHR is 59.1 MPa. The average error over the ones without a star (simplified as the non-star ones) is 76.6 MPa, whilst that over the star ones is 28.2 MPa. The average error over the non-star ones is the more realistic average error for the experimental measurement. The typical standard deviation over the non-star measurements is 74.3 MPa, which is very close to the average error for the non-star ones (i.e. 76.6 MPa). Both are realistic representations of the WHR measurement error. The frequency distribution of the measured WHR errors for the overall tests and non-star ones are shown in Figure 7.30 and Figure 7.31, respectively. The distributions for the two cases are very similar. The frequency for the measured WHR errors greater than 150 MPa is very small compared with that for the measured WHR

errors lower than 150 MPa, especially that for the measured WHR errors within 0-50 MPa.

Table 7.1 Standard deviations of the average WHR

Condition	Standard deviations of WHR (MPa)								
	A1	A2	A3	A4	A5	A6	A7	A8	A9
ST	80.6 *	24.3	12.2	19.3	26.5	74.9	4.7	67.7	63.6
10% cw	12.2 *	19.0 *	40.6 *	6.1 *	9.3 *	16.4 *	5.3 *	19.4 *	10.2 *
10% 30min	29.0 *	21.3 *	79.5 *	10.6 *	10.8 *	79.5 *	10.4 *	11.2 *	28.5 *
10% 5d	13.3 *	17.1 *	69.4 *	6.9 *	10.1 *	14.1 *	9.5 *	27.9 *	27.9 *
10% 3w	15.8 *	10.2 *	9.6 *	23.4 *	6.3 *	14.2 *	18.8 *	15.6 *	18.7 *
40% cw	31.6 *	39.9	83.2	79.2	1.4	111.3	56.4	161.3	142.4
40% 30min	35.0	9.1	0.5	16.5 *	47.6	106.1	58.9	97.6	51.4
40% 4h	244.4	78.0	103.7	9.5	49.3	26.1	8.5	59.9	67.9
40% 3w	21.9 *	11.3	118.5	31.4	208.1	106.8	14.0	220.3	110.6
90% cw	16.5	7.1	142.7 *	2.3	39.4	99.3	120.6	98.4	137.2 *
90% 30min	76.9	35.5 *	233.8	37.2	262.9	47.5	72.8	128.7	131.5
90% 4h	2.4	30.2	109.3	90.2	195.6	35.9	27.7	87.1	67.9
90% 3w	19.4	44.6	202.1	30.1	6.9	96.1	32.1	405.2	1.5

* only one reliable test conducted, error is based on variations and noise within the one test

Using the method discussed above, the average work hardening rate of all alloys at different testing conditions can be determined, and therefore, the relation between WHR and level of cold work, Mg or Cu alloying contents and ageing time can be further analysed. These results are plotted in Figure 7.32 to Figure 7.35.

As shown in Figure 7.32, level of cold work significantly influences the average WHR. The average WHR decreases substantially when level of cold work increases from 0% (i.e., solution-treated samples) to 10%. The WHR decreases more gradually with cold work level increasing from 10% to 90%, although noise and measurement error appears to obscure some of the weaker trends.

The influences of Mg and Cu contents are shown in Figure 7.33 and Figure 7.34. As shown in Figure 7.33, there is a clear increase of WHR with increasing Mg content. This trend is most distinct for solution-treated samples (see Figure 7.33a). The average WHR also tends to increase with Cu content (see Figure 7.34a). However, the trend is weak for cold-worked samples and cold-work-and-aged samples (see Figure 7.34b, c and d). This

suggests that the influence of Cu content on the WHR may be reduced after the samples are subjected to cold work or ageing.

The influence of ageing time on the average WHR is very complicated as illustrated in Figure 7.35. It depends on alloy composition and level of cold work. Although there is influence of noise and measurement error, the following main observations can be made:

(1) The as cold-rolled samples usually have the lowest work hardening rate regardless of level of cold work.

(2) On isothermal ageing for 30 minutes at 170°C, the WHR significantly increases for all alloys, regardless of level of cold work. This suggests substantial recovery occurring during the first 30-minute ageing.

(3) The further evolution of the WHR depends on alloy composition. For the alloys that do not show substantial hardening, e.g, alloys A2 and A3, the WHR usually increases with ageing time (see curves for A2, A3 in Figure 7.35 and consider the error listed in Table 7.1). For alloys that show age hardening, e.g., alloys A1, A4, A5, A6, A7, A8 and A9, the WHR may decrease after the first 30-minute ageing, reaching a minimum value broadly around the stage of peak ageing. This minimum in the WHR is usually higher than that of as cold-worked samples, but it may be lower than that of cold-worked status if the cold work level is very low and the alloy has substantial age hardening. The local minimum can be seen most clearly in the samples with 10% pre-reduction (see Figure 7.35a). After peak ageing, due to the coarsening of the precipitates, the WHR may increase which can also be clearly observed in the samples with 10% pre-reduction. For the alloys with 90% and 40% reductions, as illustrated in Figure 7.35a and b, the WHRs at peak ageing and at overageing are very close to each other and sometimes a local minimum around peak ageing cannot be evidenced. This is probably due to the measurement error, weak precipitation in all the alloys and some limited coarsening of precipitates at higher cold-rolling reductions. It is noticed that the lowest WHR occurring in the peak aged condition compared with the underaged and overaged conditions is consistent with the observation of the evolution of WHR in an AA7050 alloy by Dumont et al. [12].

7.4 Preliminary modelling of work hardening

In the previous sections, work hardening during tension of the nine Al-Mg(-Cu)-Si-Mn alloys was characterized using three different methods, i.e., the plastic strain-stress curves, Kocks-Mecking plots and the average WHR. In this section, a model based on the KM and KME models will be applied to explain the main trends observed.

7.4.1 Modelling the influence of the level of cold work

The experimental results revealed that for cold-worked samples the WHR decreases with increasing level of cold work. Since no precipitates are formed in cold-worked samples, the KM model described in the section 3.2.1 may be applicable. It will be applied to quantitatively describe the experimental data for the average WHR of the cold-worked samples.

7.4.1.1 The model

According to the KM model [6, 7, 11, 13-17] presented in Chapter 3, the dislocation density evolution with strain for polycrystalline materials is given by:

$$\frac{d\rho}{d\varepsilon} = M(k_1\rho^{1/2} - k_2\rho) \qquad \textbf{(7.9)}$$

So the dislocation density can be written by:

$$\rho = \rho_s[1-(1-(\frac{\rho_0}{\rho_s})^{1/2})\exp(-\frac{Mk_2}{2}\varepsilon)]^2 \qquad \textbf{(7.10)}$$

where $\rho_s = (k_1/k_2)^2$ and ρ_0 is the initial dislocation density of the sample before tensile test, which can be determined by the work hardening model, so it is an output parameter from the yield strength model.

Thus the following equation can be used to calculate the instantaneous WHR:

$$\Theta = \frac{d\sigma}{d\varepsilon} = M^2\frac{d\Delta\tau_d}{d\gamma} = \Theta_0(1-\frac{\Delta\tau_d}{\tau_s}) \qquad \textbf{(7.11)}$$

where $\Theta_0 = \frac{1}{2}M^2\alpha_\rho Gbk_1$, $\tau_s = \alpha_\rho Gb(k_1/k_2)$ and $\Delta\tau_d = \alpha_\rho Gb\rho^{1/2}$.

The average WHR between $\varepsilon_1 = 0.01$ and $\varepsilon_2 = 0.03$ can be determined from the flow stresses at these two strains. In this study, a similar treatment to the summation of the overall yield strength described in Chapter 6 is used to sum the different contributions to the flow stress:

$$\sigma_j = \sigma_b + M[\Delta\tau_{ss} + (\Delta\tau_d)_j] = \sigma_b + M(\Delta\tau_{ss} + \alpha_\rho Gb\rho_j^{1/2}) \quad (j = 1, 2) \qquad \textbf{(7.12)}$$

In the above equation, ρ_j is expressed by equation (7.10).

Therefore the average WHR between strains at 0.01 and 0.03 can be obtained from:

$$\overline{\Theta} = \frac{\sigma_2 - \sigma_1}{\varepsilon_2 - \varepsilon_1} = M\alpha_\rho Gb\frac{\rho_2^{1/2} - \rho_1^{1/2}}{\varepsilon_2 - \varepsilon_1} \qquad \textbf{(7.13)}$$

In order to use the KM model, the relation of alloying content with the two parameters k_1 and k_2 has to be determined first. k_1 is related with the work hardening rate at stage II (θ_{II}) and it is expressed by equation (3.5). Since θ_{II} changes with alloys, k_1 varies with alloy composition. The experimental results showed that the WHR increases with increasing Mg and Cu contents (see section 7.3), and thus k_1 will need to be dependent on Mg and Cu contents. Moreover, according to the KM model (see equations (3.8) and (3.9)), the yield strength of cold-worked samples (σ_{wh}) is proportional to k_1:

$$\sigma_{wh} \propto k_1$$

According to tensile test results shown in Figure 5.41 and 5.42, there is a linear relationship between σ_{wh} and Mg/Cu contents, and hence a linear relation exists between k_1 and Mg/Cu contents. So the following expression is here proposed:

$$k_1 = k_1^{Mg} c_{Mg} + k_1^{Cu} c_{cu} + k_1^0 \qquad \textbf{(7.14)}$$

where k_1^{Mg}, k_1^{Cu} and k_1^0 are constants.

According to literature, k_2 is associated with dynamic recovery and it is a function of temperature and strain rate [9]. In order to limit model complexity and in the absence of evidence to the contrary, it is assumed that k_2 does not vary with Mg or Cu content. In

this study, all tensile tests were conducted at room temperature and at a constant strain rate of 0.001 s^{-1}, and hence, k_2 is a single constant throughout all tests.

7.4.1.2 Calibrating and testing of the model

In order to use the model described above, the values of the four parameters: k_1^{Mg}, k_1^{Cu} k_1^0 and k_2 have to be determined. In this study, the train and test method used in the previous chapter for yield strength modelling will be applied to determine the values of the parameters and test the model in a single step.

Table 7.2 Calibrated parameters for modelling the influence of cold work on the average WHR

Parameter	Value	Unit
k_1^{Mg}	$3.74*10^7$	m^{-1}
k_1^{Cu}	$2.42*10^8$	m^{-1}
k_1^0	$1.67*10^8$	m^{-1}
k_2	4.07	-

The average WHR data of alloys A1, A3, A5 and A9 were used to calibrate the model and the WHR data of the other alloys were used to test the model. The calibrated parameters are listed in Table 7.2. The training error is 154.4 MPa and the training results are shown in Figure 7.36. Some examples with measurement error bar are shown in Figure 7.37. The testing error of the model is 212.3 MPa and the testing results are shown in Figure 7.38. Some examples with measurement error bars are shown in Figure 7.39 for comparison of the measurements and predictions. The testing error of 212.3 MPa for the WHR (which is about 12.5% relative error) corresponds to about 4.2 MPa for the stress measurement error.

The model can predict unseen WHR data within an accuracy that is about three times of the average measurement accuracy of the WHR in the present measurement. This is considered a reasonable accuracy. It is still clear that the model cannot quite capture the very rapid change in the WHR between solution-treated samples and 10% cold-worked samples. On the one hand, this may suggest that there is some systematic error involved in the measurement of the difference in the WHR between as-quenched and quenched-and-cold-worked samples. Another possible explanation could be that the KM model, which considers work hardening to be caused by a single parameter (the average

dislocation density), cannot accurately model the changes occurring in going from solution-treated condition to 10% cold work condition.

7.4.2 Modelling the influence of ageing

To explain the influence of ageing on the WHR, the KME model (instead of the KM model) will be applied to account for the influence of precipitates on the WHR of these aged samples.

7.4.2.1 The model

According to the KME hybrid model [9, 18-21] (see section 3.2.2.2), the dislocation density evolution equation is given by:

$$\frac{d\rho}{d\varepsilon} = M(k_d + k_1\rho^{1/2} - k_2\rho) \qquad \textbf{(7.15)}$$

where $k_d = (bl_d)^{-1}$ determined by the spacing between precipitates l_d, which can be derived from the following equation [22]:

$$l_d = 1.15\bar{r}\sqrt{\frac{2\pi}{3\bar{f}}} \qquad \textbf{(7.16)}$$

where $\bar{r}$ and $\bar{f}$ are the average precipitate sizes and volume fraction of precipitates, respectively.

Since there are two types of precipitates (i.e., β″ and S) considered in the yield strength model, a weighted average is used to calculate $\bar{r}$:

$$\bar{r} = \frac{f_\beta r_\beta + f_s r_s}{f_\beta + f_s} \qquad \textbf{(7.17)}$$

$\bar{f}$ is the sum of the volume fractions of β″ and S phases:

$$\bar{f} = f_\beta + f_s \qquad \textbf{(7.18)}$$

where subscripts β and S stand for the precipitates of β″ and S phase, and *r* and *f* are the equivalent radius and volume fraction of precipitates, respectively. These parameters can be obtained from the yield strength model.

Since the differential equation (7.15) does not have an analytical solution, the numerical method (e.g., point slope method) will be applied to calculate the dislocation density and from that the stress contribution due to dislocation strengthening ($\Delta\tau_d$) can be obtained. The total flow stress is then derived from the following superposition law:

$$\sigma_j = \sigma_b + M(\Delta\tau_{ss} + \sqrt{[(\Delta\tau_d)_j]^2 + (\Delta\tau_{ppt})^2}) \quad (j = 1,2) \qquad \textbf{(7.19)}$$

where $\Delta\tau_{ppt}$ is the stress contribution due to precipitates. To limit model complexity, it is assumed that the size and volume fraction of the precipitates will not change during room temperature storage (i.e., natural ageing) after isothermal ageing at 170°C or during tensile testing at room temperature.

According to the above assumption, $\Delta\tau_{ppt}$ is a constant during tensile tests and can be obtained directly from the yield strength model. Hence the average WHR is given by:

$$\overline{\Theta} = M\frac{\sqrt{[(\Delta\tau_d)_2]^2 + (\Delta\tau_{ppt})^2} - \sqrt{[(\Delta\tau_d)_1]^2 + (\Delta\tau_{ppt})^2}}{\varepsilon_2 - \varepsilon_1} \qquad \textbf{(7.20)}$$

7.4.2.2 Testing of the model and discussion

The model described in section 7.4.2.1, with the parameters calibrated in section 7.4.1.2 and the volume fraction and size of the precipitates obtained from the yield strength model, failed to catch the main trends observed in the experimental data. There are a number of reasons that may explain the failure of this model for the WHR of the cold-worked-and-aged samples.

First, in the model, only the overall or effective dislocation density was considered. Actually, there are two types of dislocations: mobile dislocations and immobile dislocations and they may form a cell structure which can evolve on ageing [10]. Hence such one-parameter model may become inaccurate when the work hardening behaviour of the cold-worked and subsequently aged alloys is considered. A more accurate and complex microstructure-based two-parameter model [18, 19, 23, 24] (see section 3.2.3.1), three-parameter model [25-27] (see section 3.2.3.2) or Nes model [10, 28-37] (see section 3.2.3.3) may be able to achieve better results.

Second, even if spatial distributions of dislocations are modelled more realistically, there are still some issues concerning the interactions of dislocations and precipitates and/or solutes, which are not incorporated in any of these models. These include the influences of precipitates and/or solutes on dislocation generation and annihilation, which is generally poorly understood. It is noticed that no studies on such issue have been reported so far in the literature. In the KME model applied in this study it is assumed [9] that the mean free path prescribed by the particle spacing (l_d) for the particle strengthened materials is constant. Hence the athermal storage rate of dislocations would be constant (i.e., k_d is constant). Actually, the particles or precipitates may be affected or even broken up during deformation. Thus the mean free path or particle spacing for precipitate strengthened materials may change with strain. In that case, the assumption in the KME model that the mean free path is constant is not valid.

Effect of precipitates on dislocation annihilation and recovery is also poorly understood. For instance, the influence of precipitates on cell formation has not been studied in any detail. The Nes model [10] (see section 3.2.3.3 for more details), which is the only work hardening model considering cell size influence in the cell structure, the principle of microstructural scaling (or similitude) was utilized simply to assume that the cell size scales with the dislocation density inside a cell (ρ_i) (see equation 3.33). No consideration of the influence of precipitates on the cell formation is included in the model (probably enforced by a lack of quantitative experimental observations). In the KME model which was used in this study, the formation of cells is not considered, let alone the influence of the precipitates on the cell formation.

One or all of the factors discussed above may be the cause of the inability to capture changes in the WHR for the cold-worked alloys on ageing by the present model. This discussion illustrates the limitations of the KME model and as well as other models proposed in the literature when the WHR behaviour of cold-worked samples on ageing is considered. It is suggested that future work should consider applying the two- or three-parameter models or Nes model, which are more realistic in presenting the microstructure evolution of cold-worked alloys on ageing. However, it is likely that more detailed models other than those proposed in the literature will need to be built. For example, models for quantitative descriptions of the influence of precipitates on dislocation generation or annihilation, for the influence of precipitates on the cell formation and evolution, and for

the influence of shearing/by-passing or a possible transition from shearing to by-passing will need to be developed and will need be verified by quantitative experimental studies.

7.5 Summary

The work hardening behaviour during uniaxial tension of nine Al-Mg(-Cu)-Si-Mn alloys was analysed, which includes that of solution-treated samples, cold-worked samples and cold-worked-and-aged samples. The influences of cold work level, alloying contents (e.g., Mg and Cu) and ageing conditions on the work hardening behaviour have been analysed. A model based on the KM model has been proposed to predict the influence of cold work level and alloying contents on the average WHR. The model works reasonably well. However a model based on the KME model attempting to predict the influence of ageing on the average WHR was not successful. Possible reasons causing such failure have been discussed and suggestions for future modelling the work hardening behaviour of the cold-worked-and-aged alloys have been proposed.

Figures

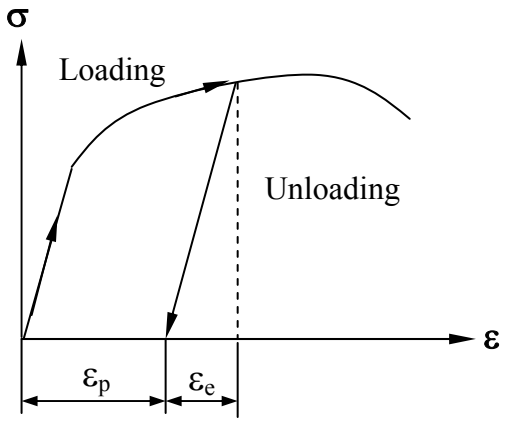

Figure 7.1 Sketch of the definition of elastic strain and plastic strain

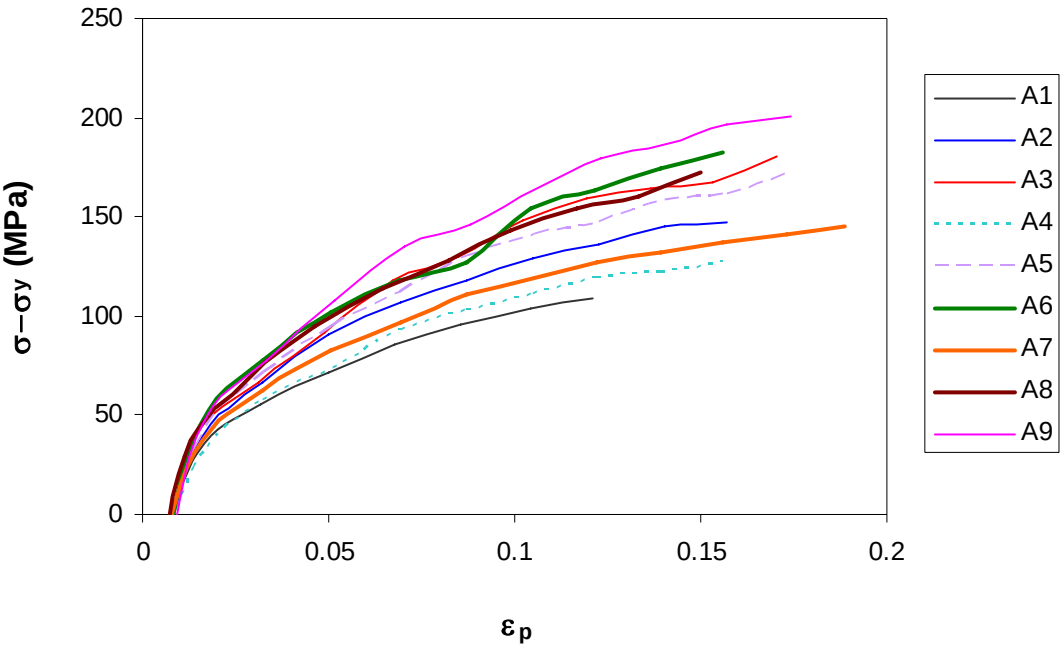

Figure 7.2 Plastic stress and strain for solution-treated alloys

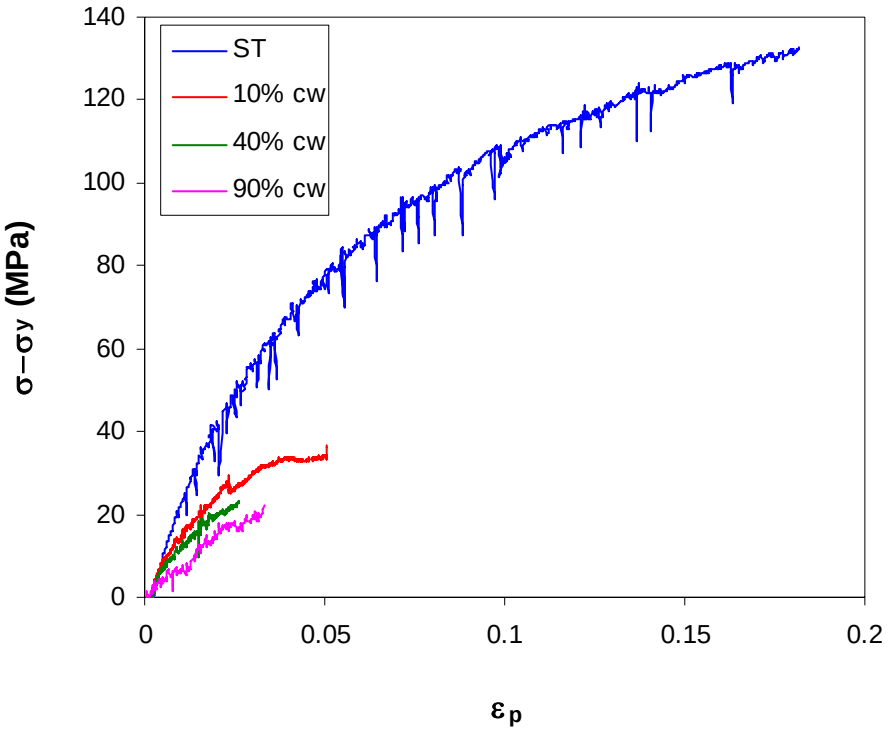

Figure 7.3 Influence of level of cold work on the plot of (σ-σ_y) vs. ε_p for alloy A4

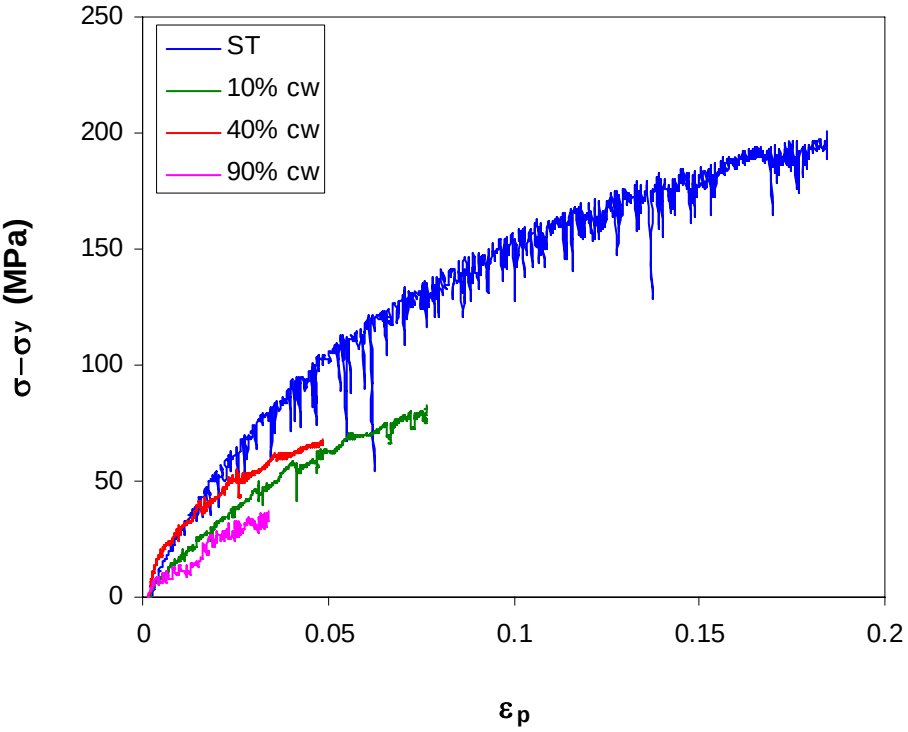

Figure 7.4 Influence of level of cold work on the plot of (σ-σ_y) vs. ε_p for alloy A6

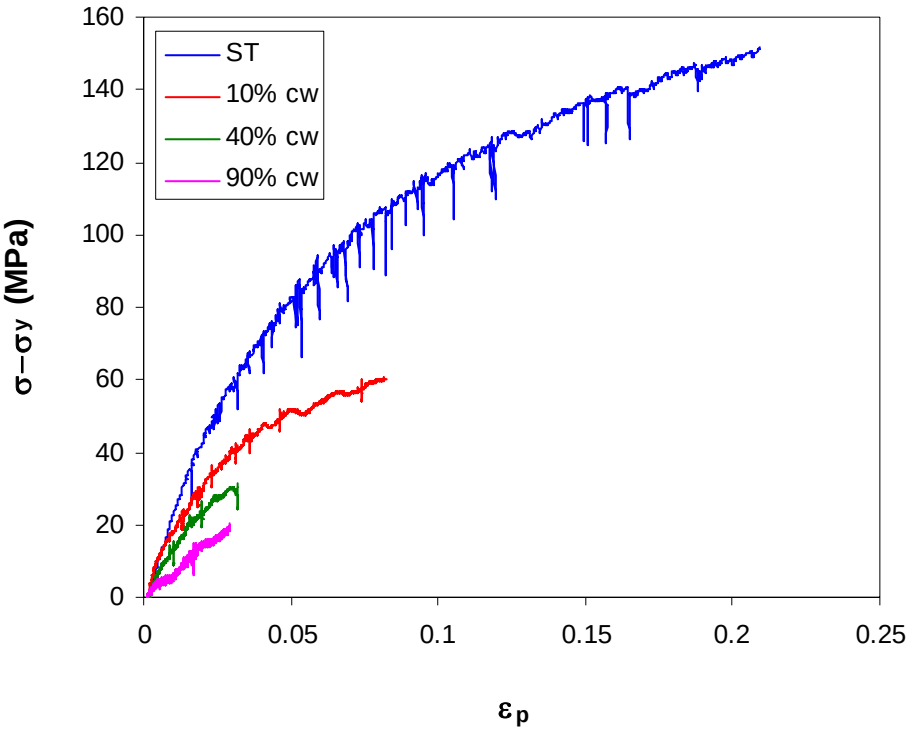

Figure 7.5 Influence of level of cold work on the plot of (σ-σ_y) vs. ε_p for alloy A7

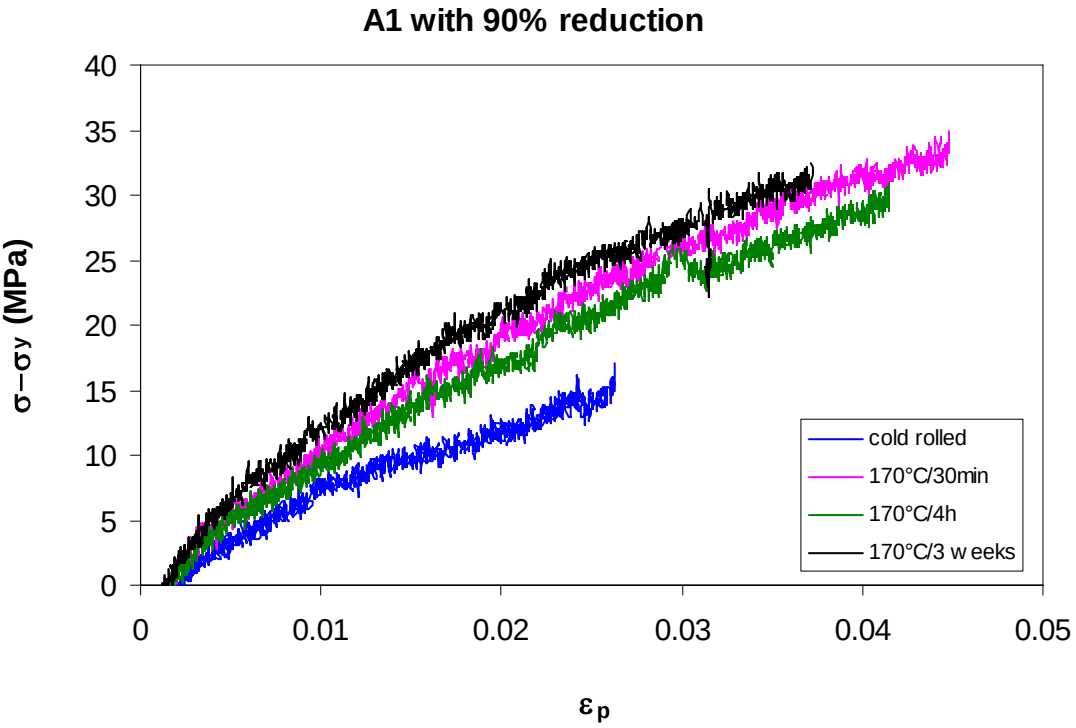

Figure 7.6 The plastic stress-plastic strain for alloy A1 with 90% cold work

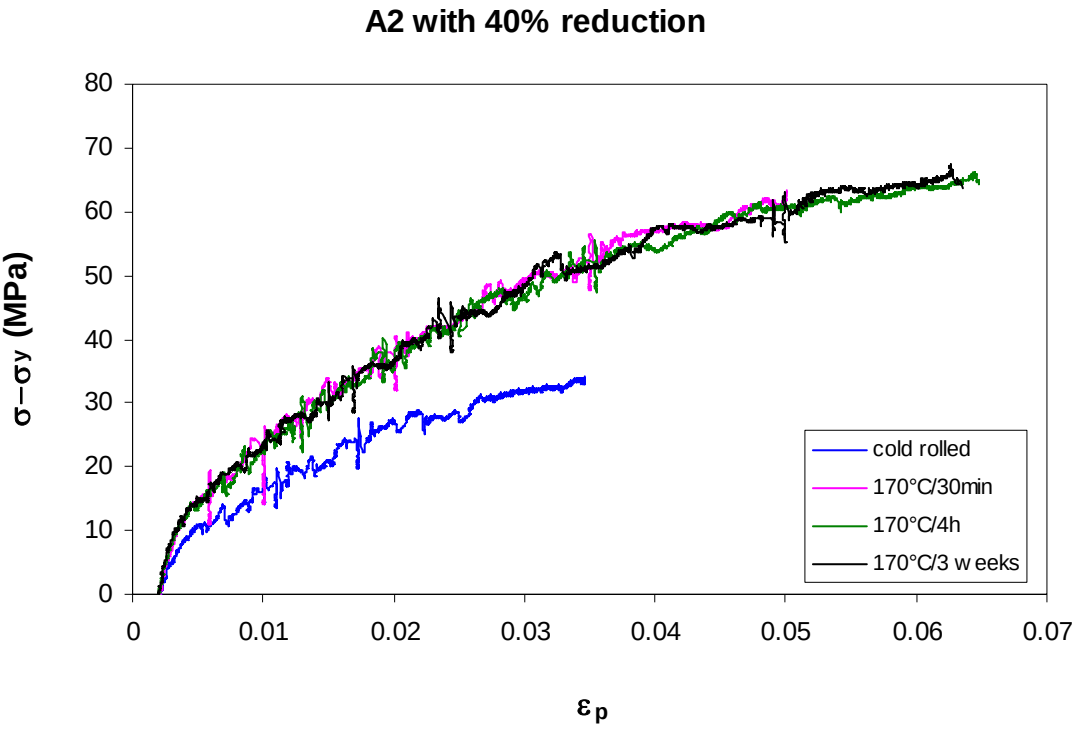

Figure 7.7 The plastic stress-plastic strain for alloy A2 with 40% cold work

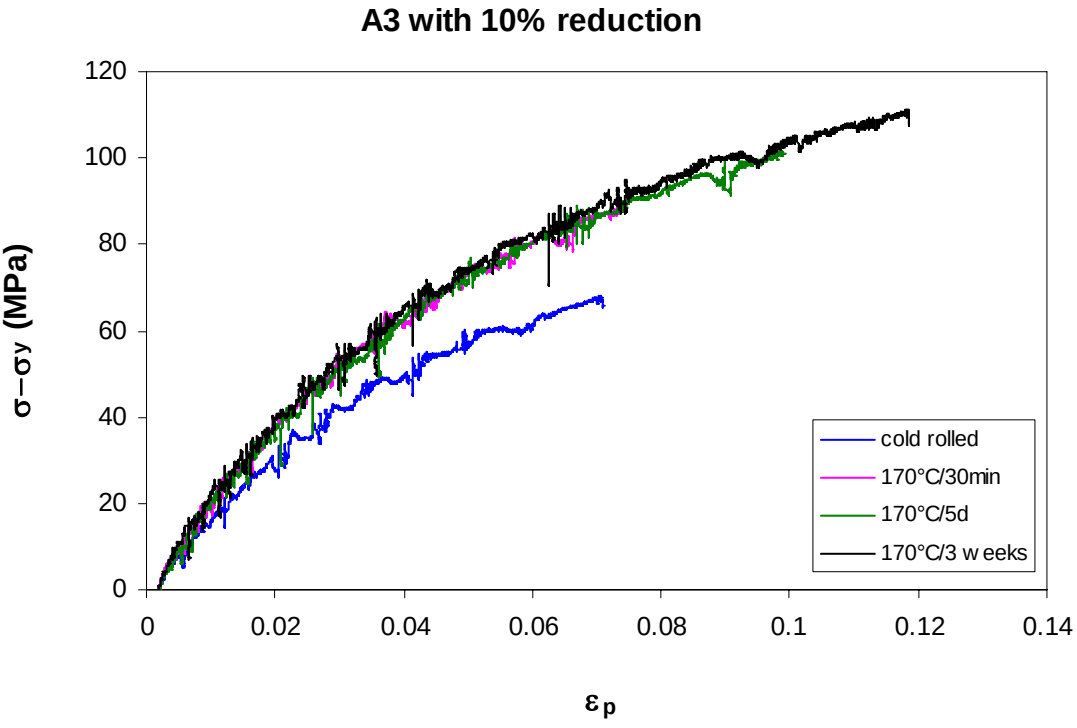

Figure 7.8 The plastic stress-plastic strain for alloy A3 with 10% cold work

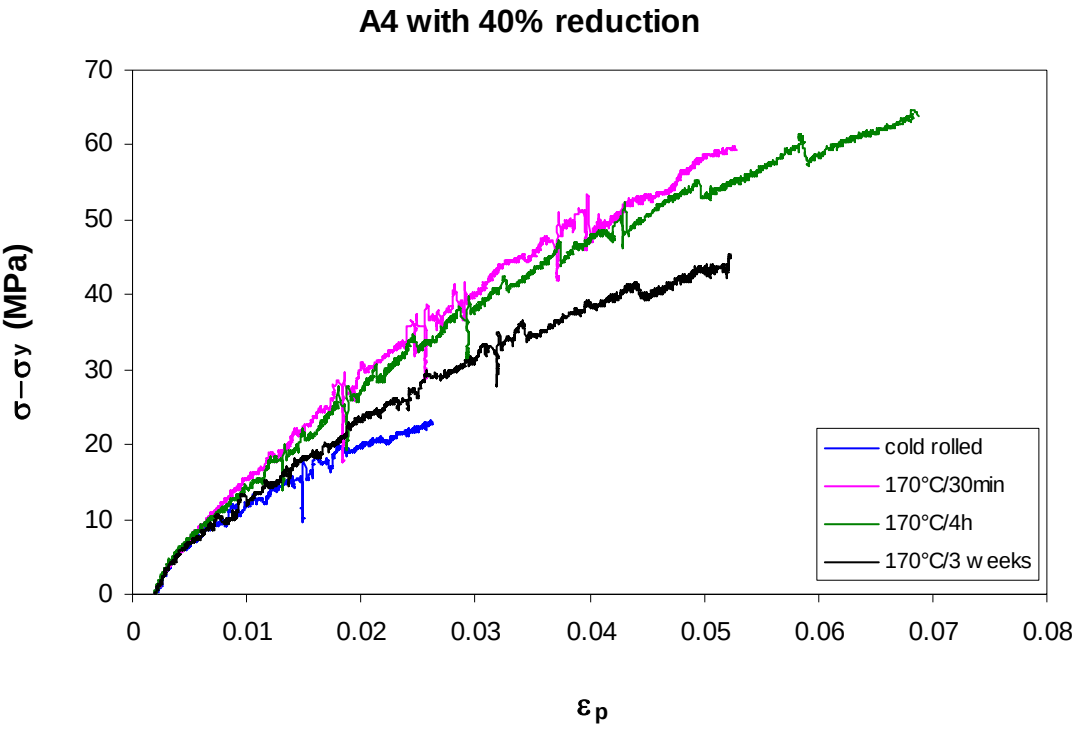

Figure 7.9 The plastic stress-plastic strain for alloy A4 with 40% cold work

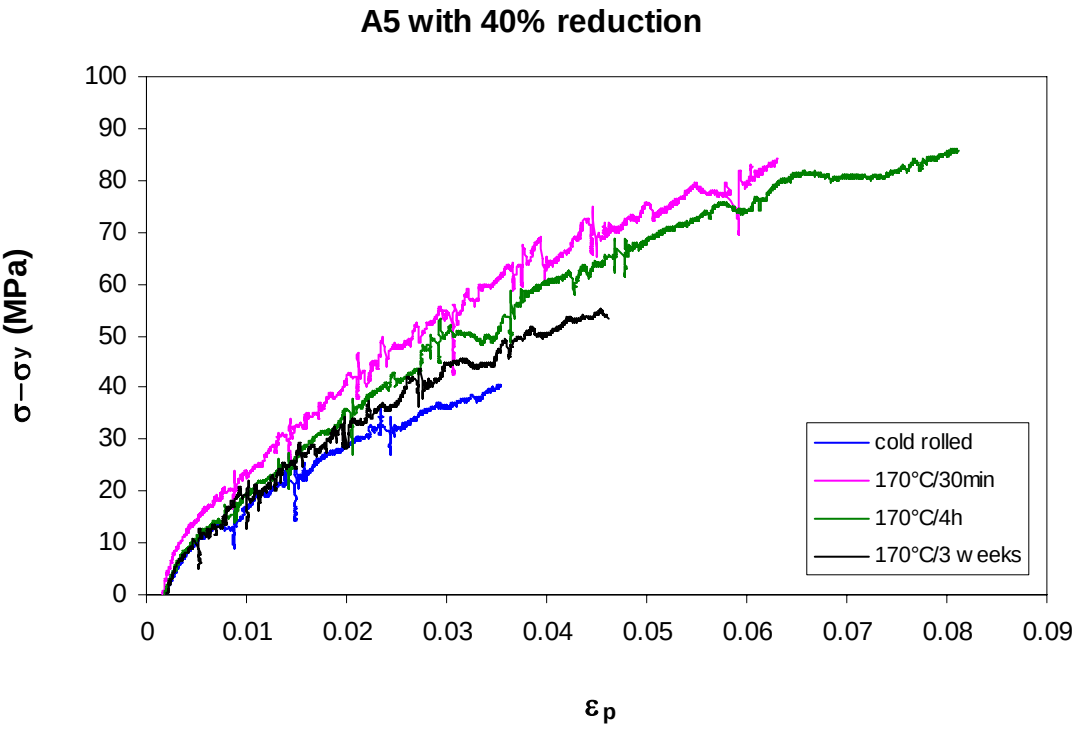

Figure 7.10 The plastic stress-plastic strain for alloy A5 with 40% cold work

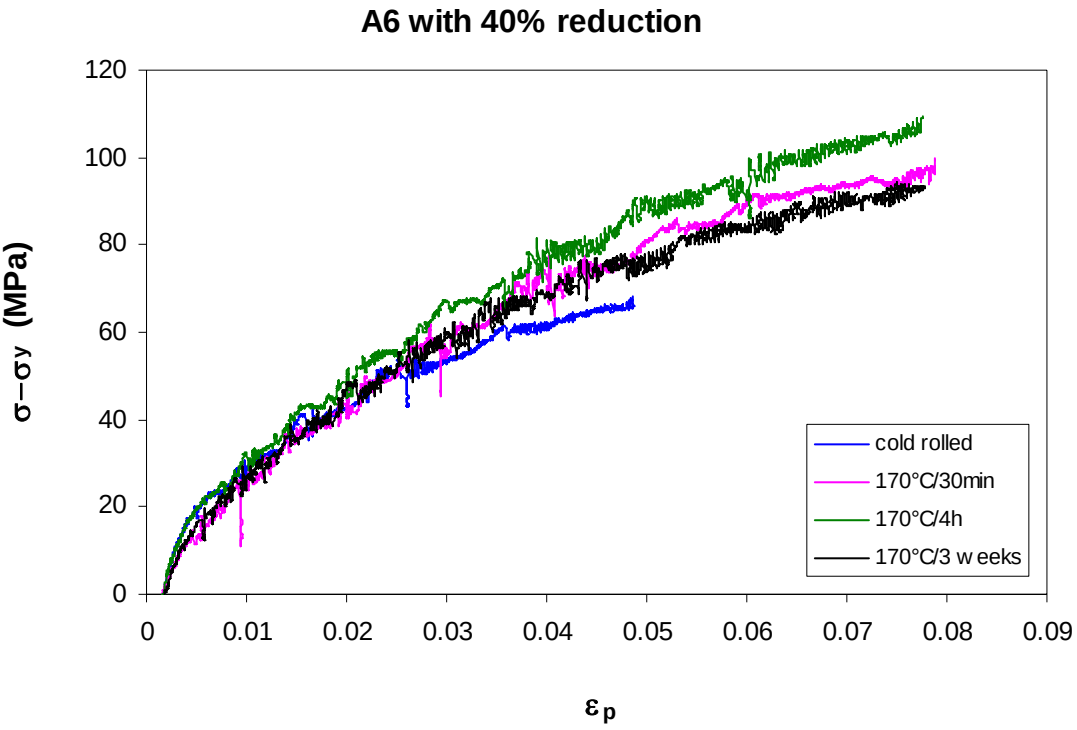

Figure 7.11 The plastic stress-plastic strain for alloy A6 with 40% cold work

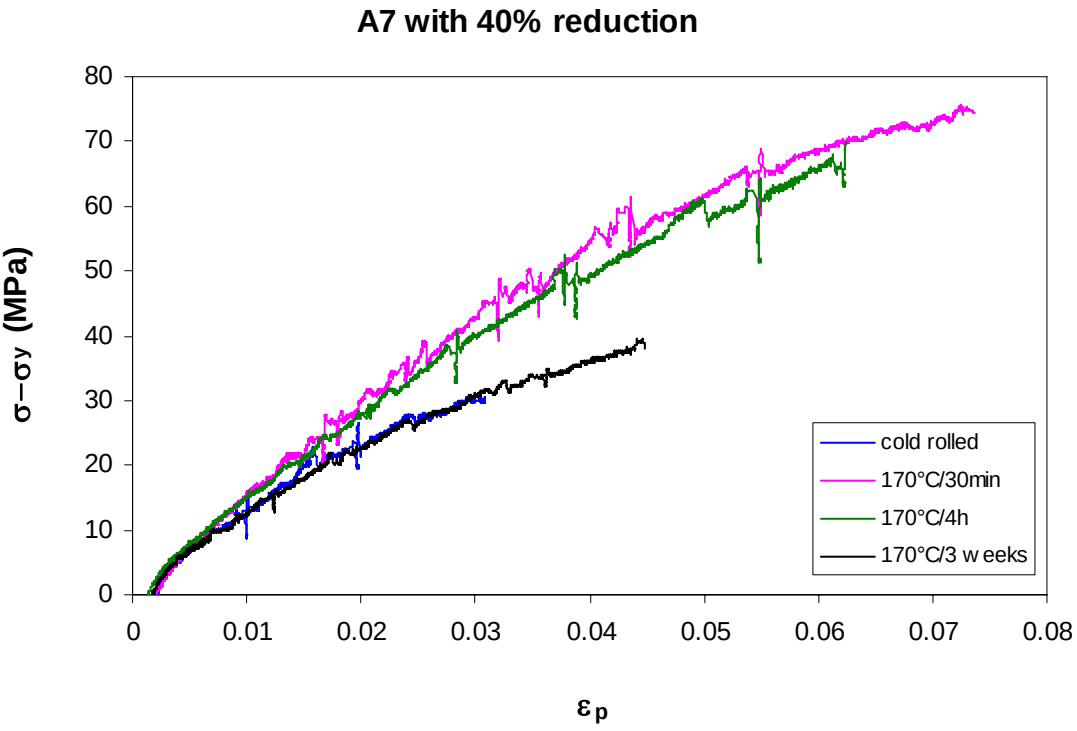

Figure 7.12 The plastic stress-plastic strain for alloy A7 with 40% cold work

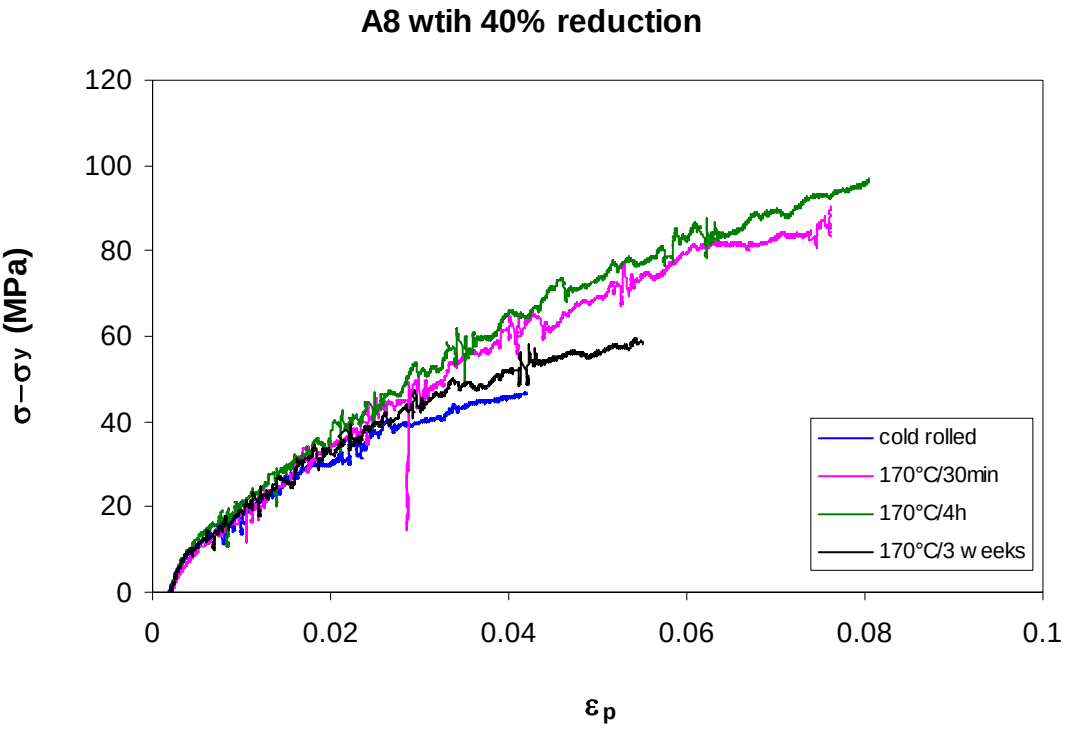

Figure 7.13 The plastic stress-plastic strain for alloy A8 with 40% cold work

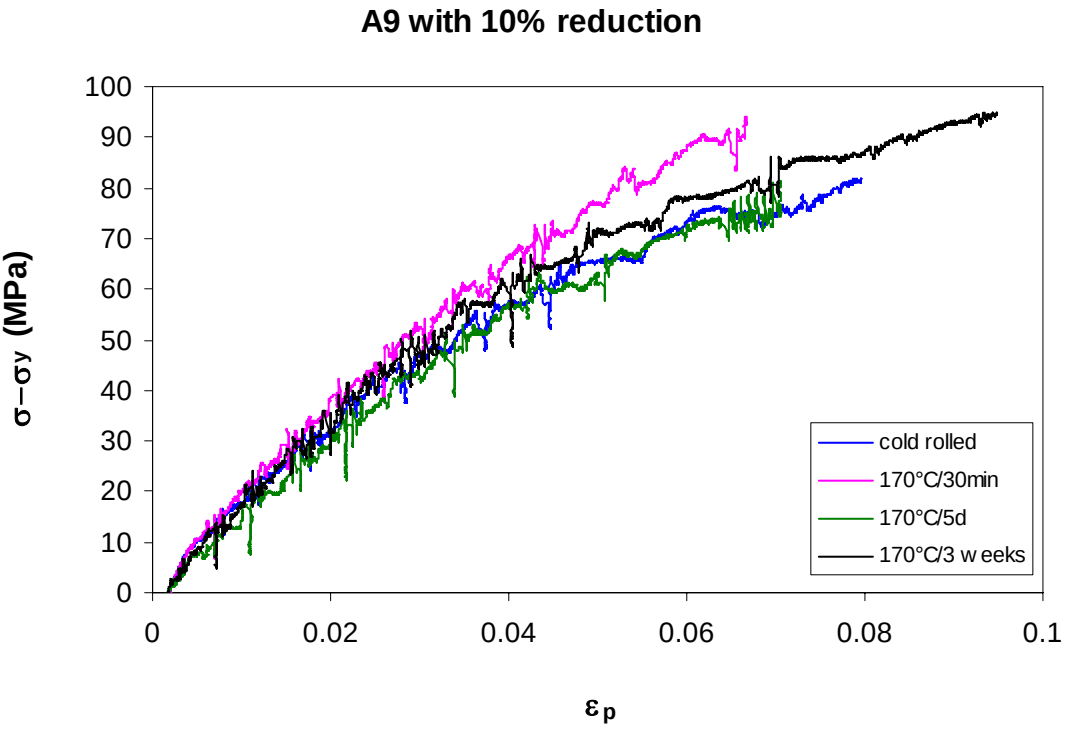

Figure 7.14 The plastic stress-plastic strain for alloy A9 with 10% cold work

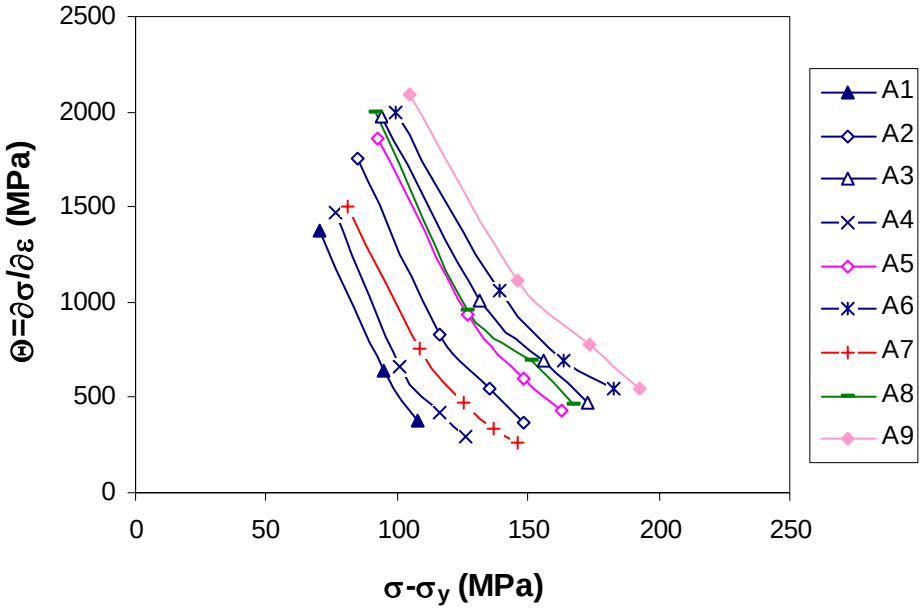

Figure 7.15 Work hardening rate plots for solution-treated alloys

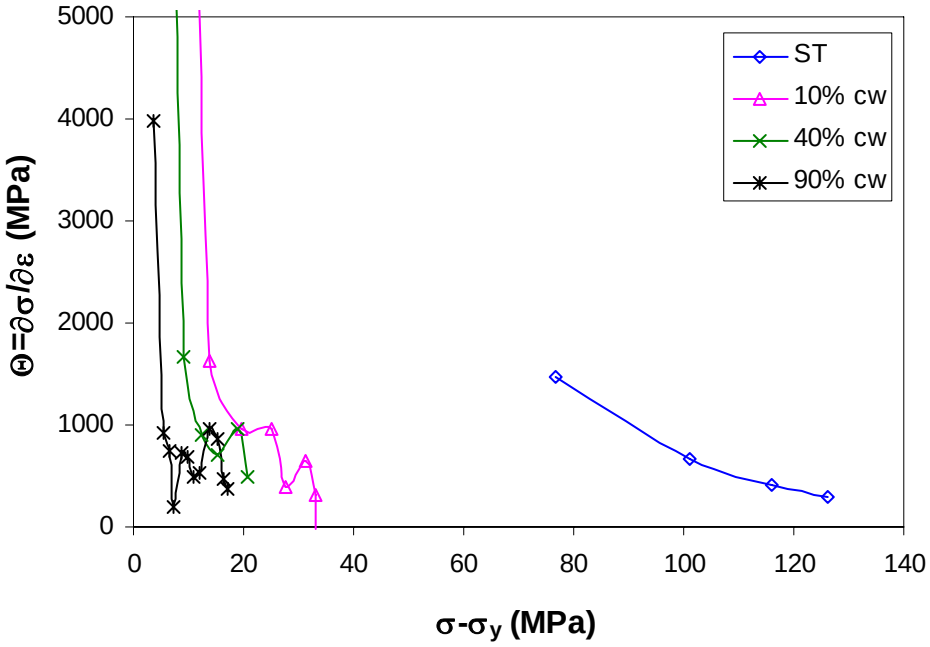

Figure 7.16 Influence of cold work level on work hardening rate plots for alloy A4

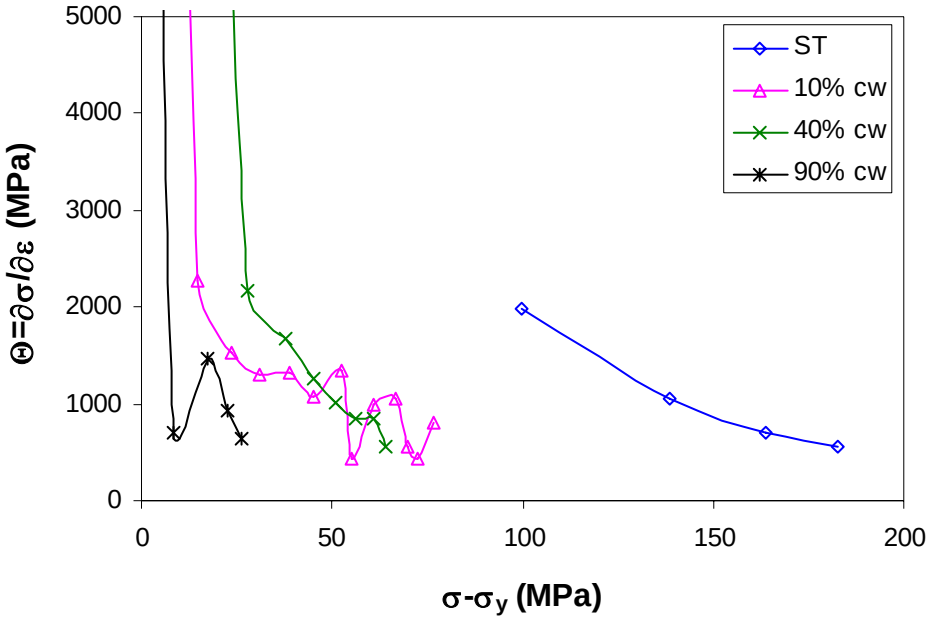

Figure 7.17 Influence of cold work level on work hardening rate plots for alloy A6

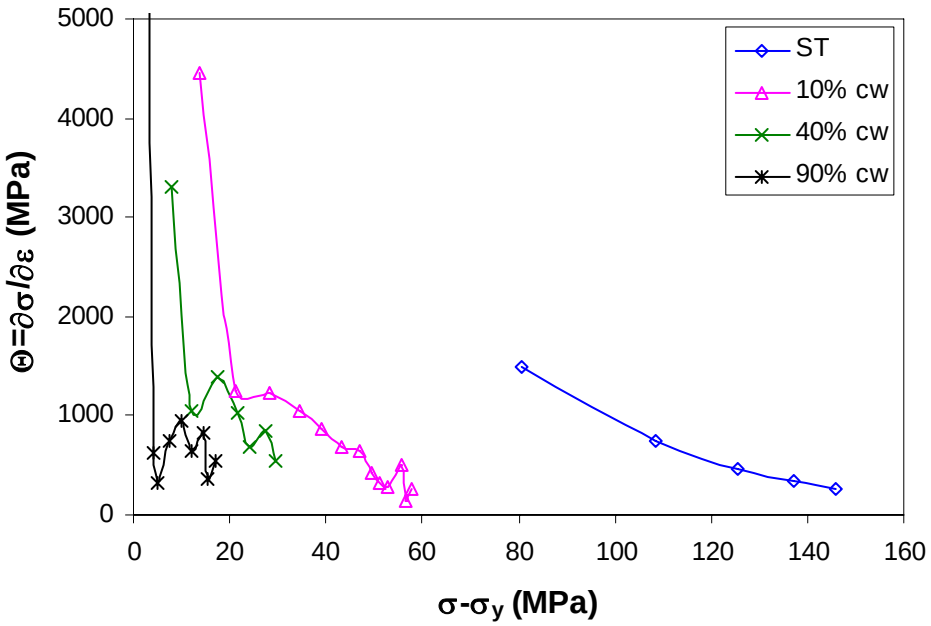

Figure 7.18 Influence of cold work level on work hardening rate plots for alloy A7

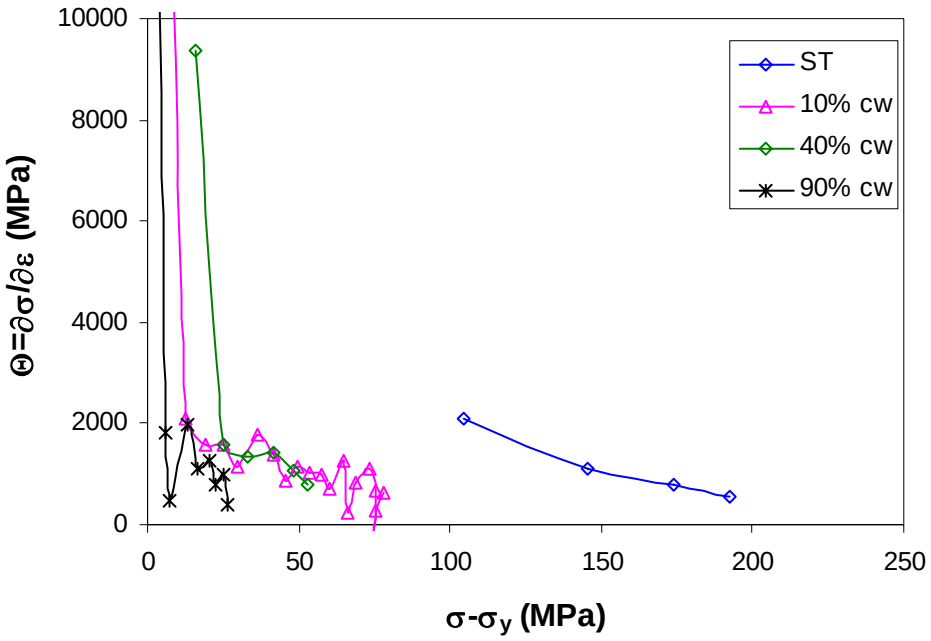

Figure 7.19 Influence of cold work level on work hardening rate plots for alloy A9

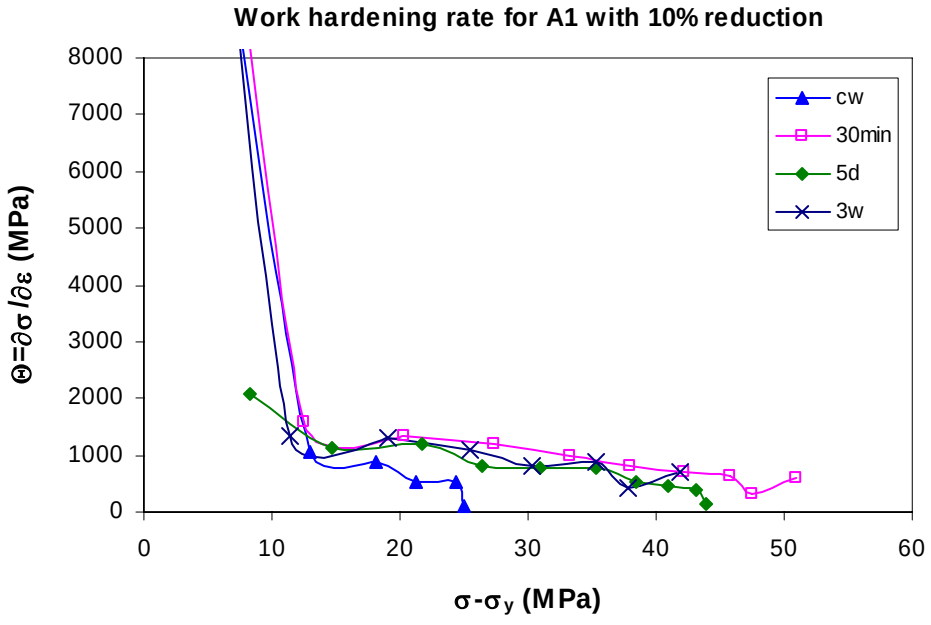

Figure 7.20 Work hardening rate plots for alloy A1 with 10% reduction

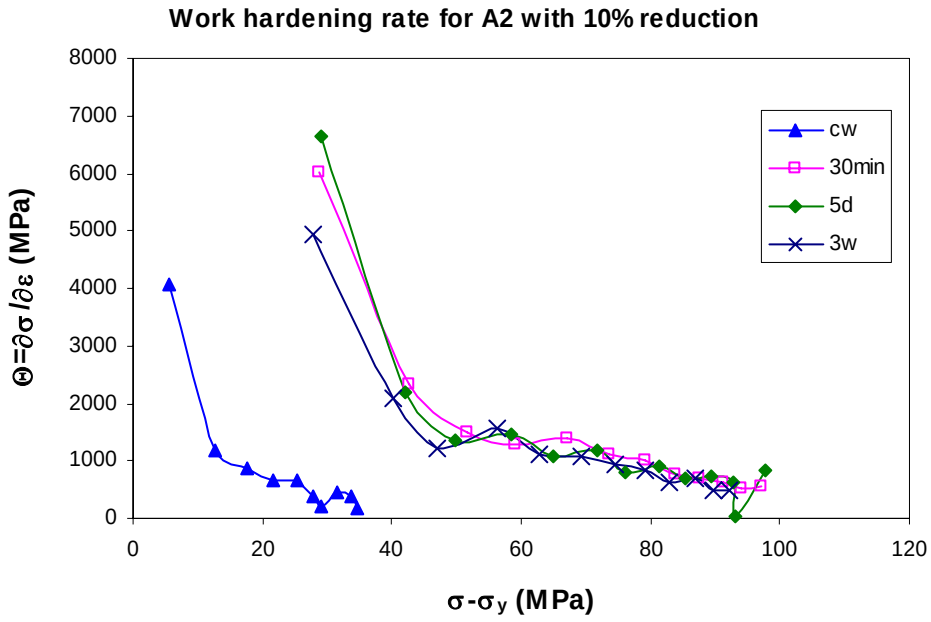

Figure 7.21 Work hardening rate plots for alloy A2 with 10% reduction

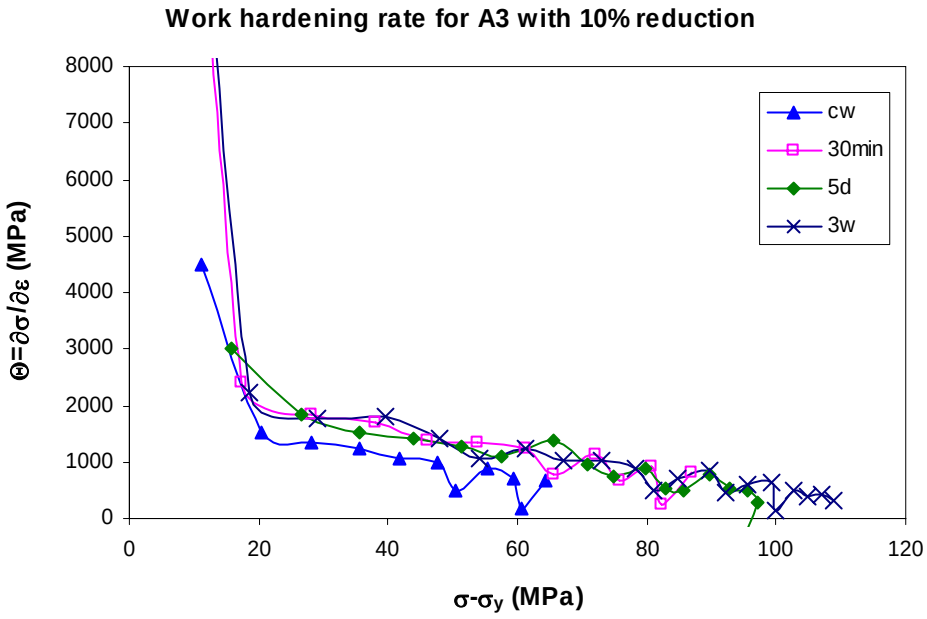

Figure 7.22 Work hardening rate plots for alloy A3 with 10% reduction

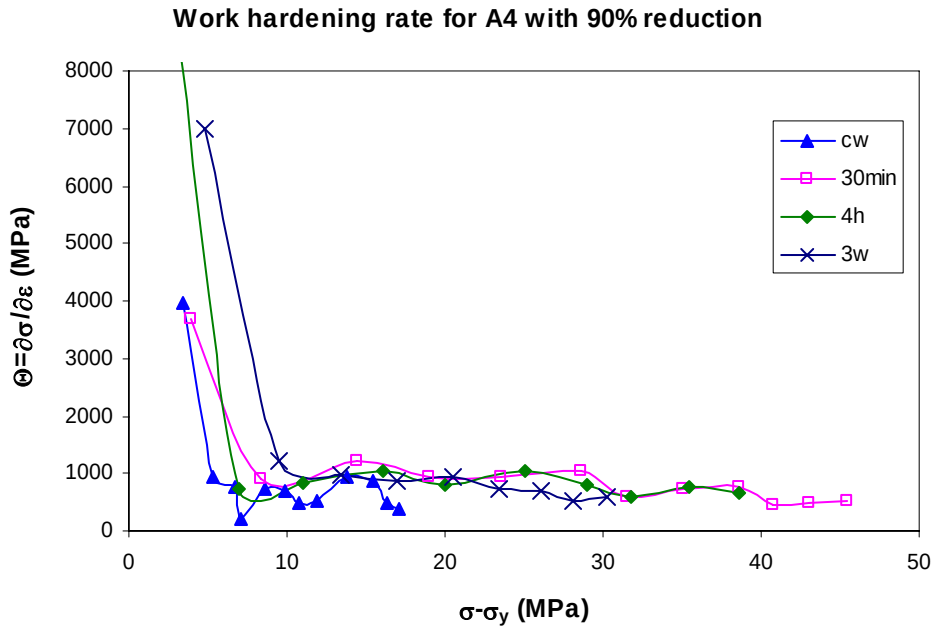

Figure 7.23 Work hardening rate plots for alloy A4 with 90% reduction

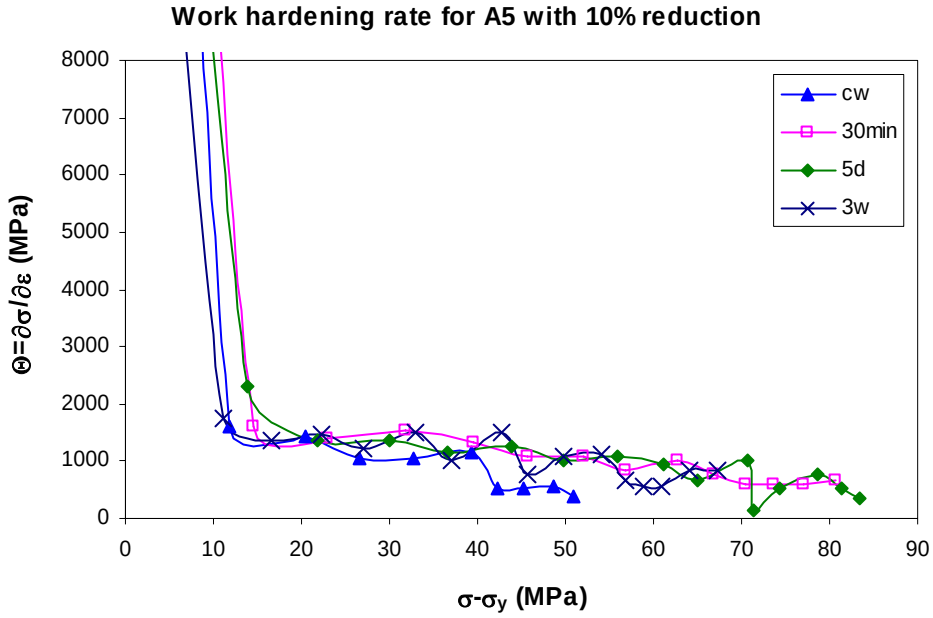

Figure 7.24 Work hardening rate plots for alloy A5 with 10% reduction

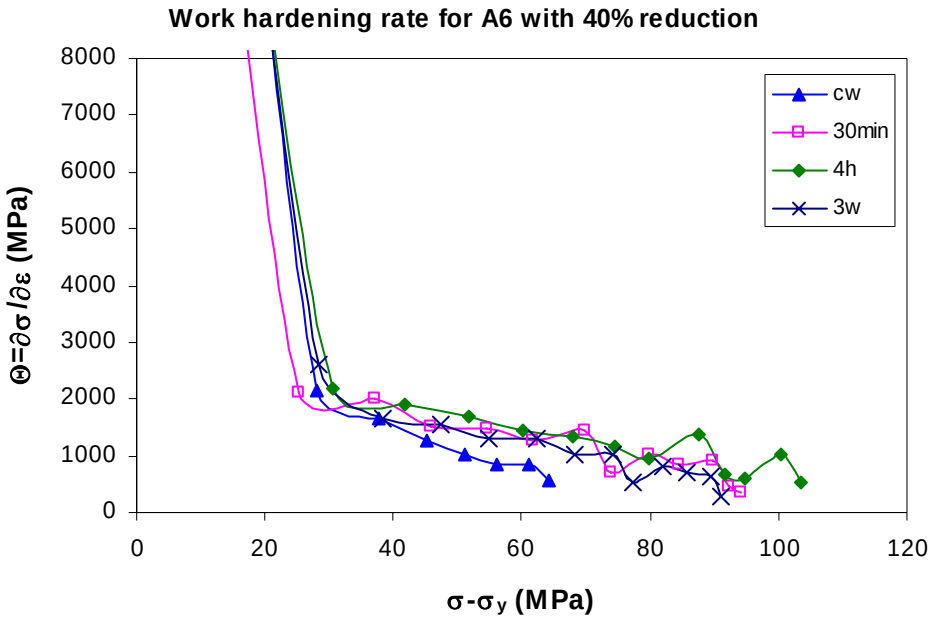

Figure 7.25 Work hardening rate plots for alloy A6 with 40% reduction

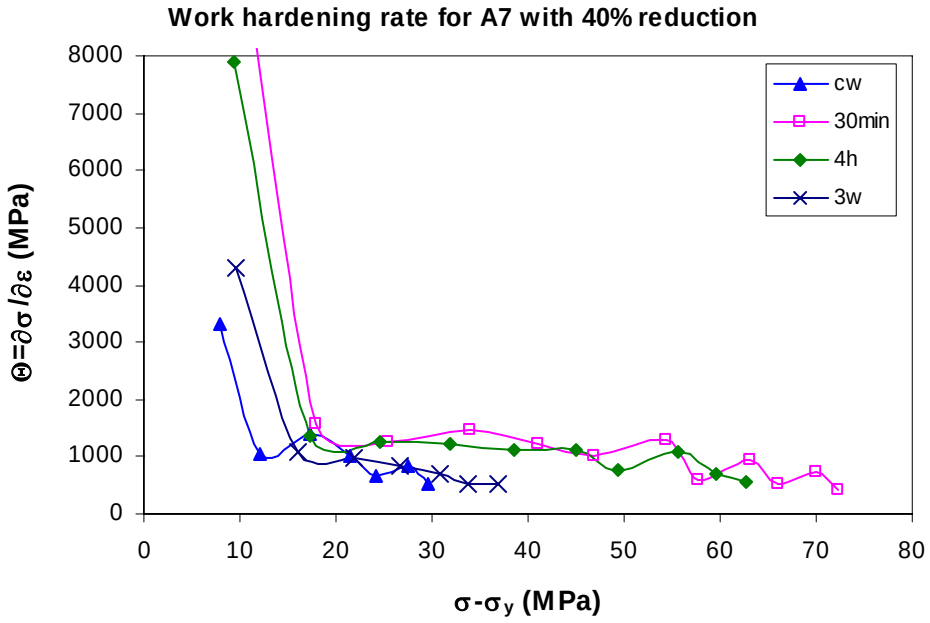

Figure 7.26 Work hardening rate plots for alloy A7 with 40% reduction

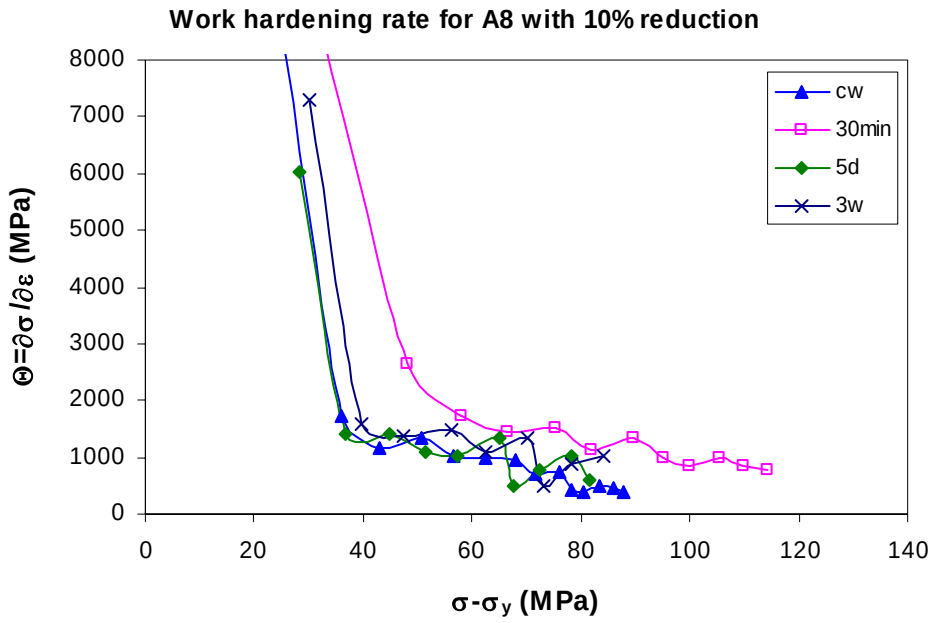

Figure 7.27 Work hardening rate plots for alloy A8 with 10% reduction

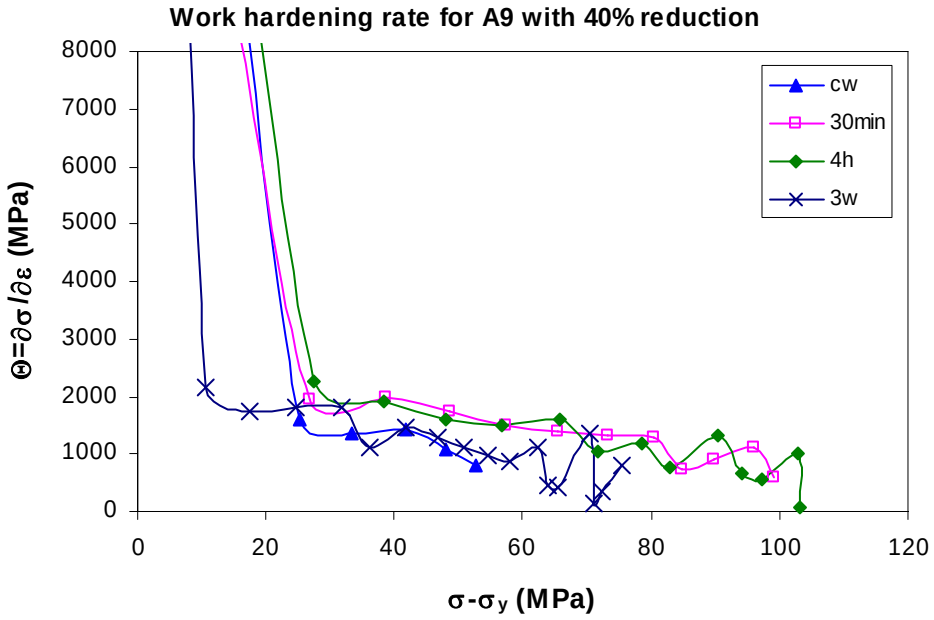

Figure 7.28 Work hardening rate plots for alloy A9 with 40% reduction

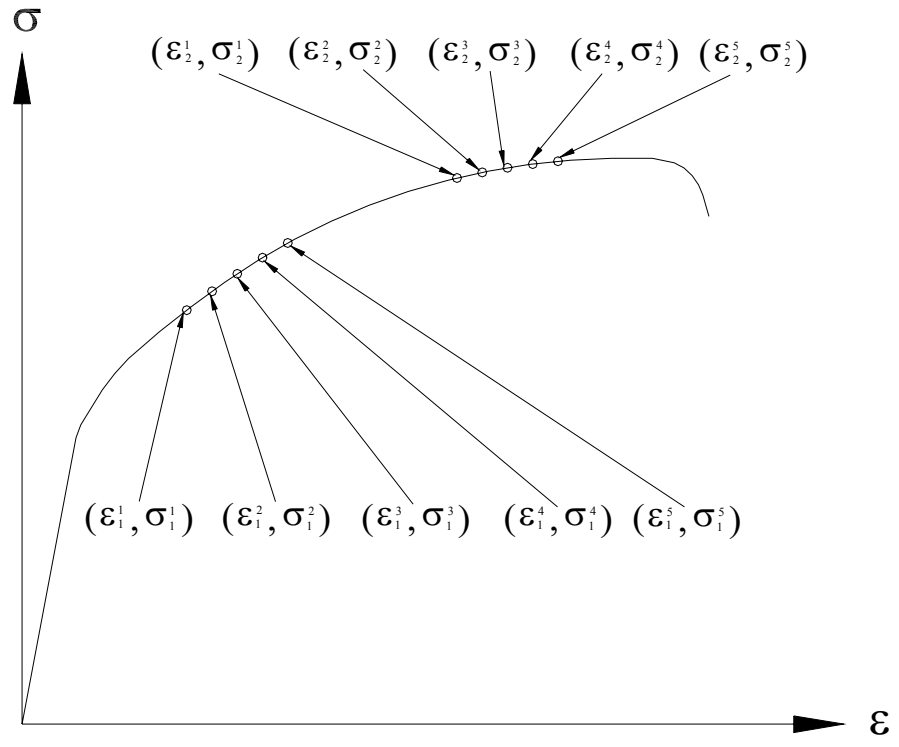

Figure 7.29 A schematic drawing showing data selection for calculation of the average WHR between ε =0.01 and 0.03

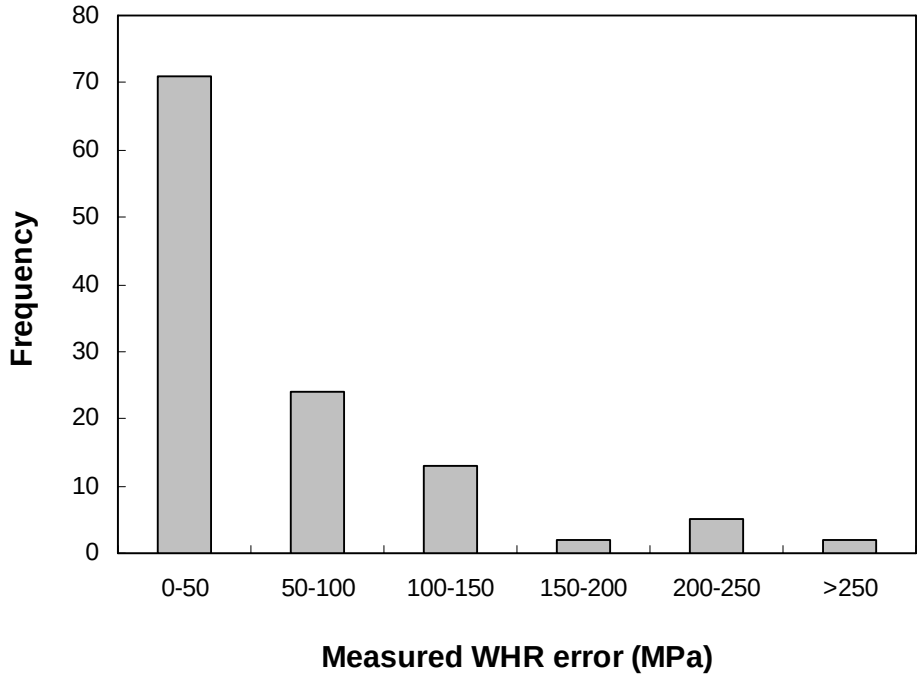

Figure 7.30 Frequency distribution of the measured WHR errors for overall tests

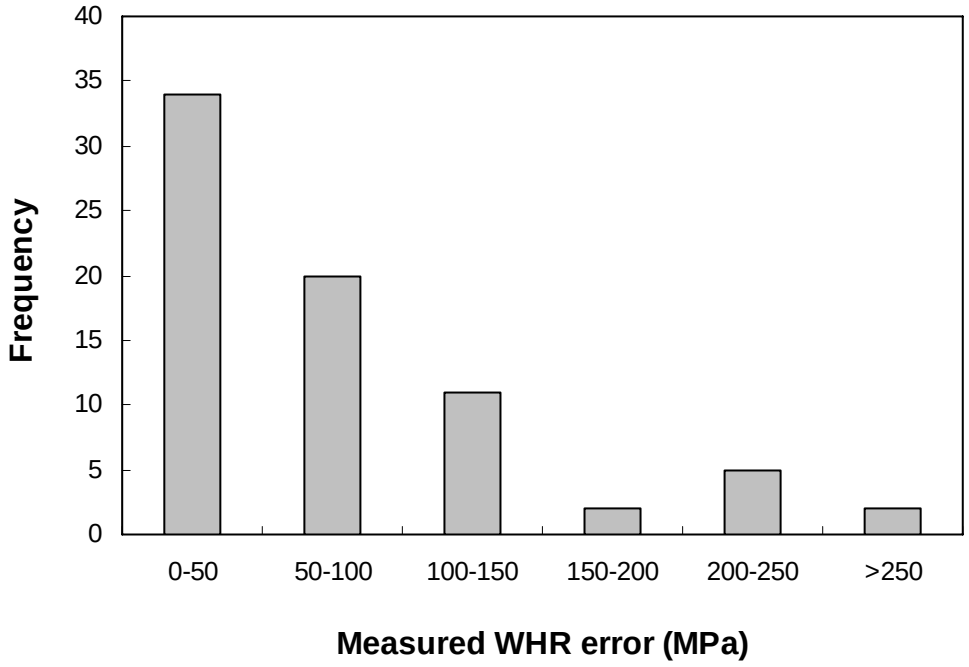

Figure 7.31 Frequency distribution of the measured WHR errors for non-star tests listed in Table 7.1

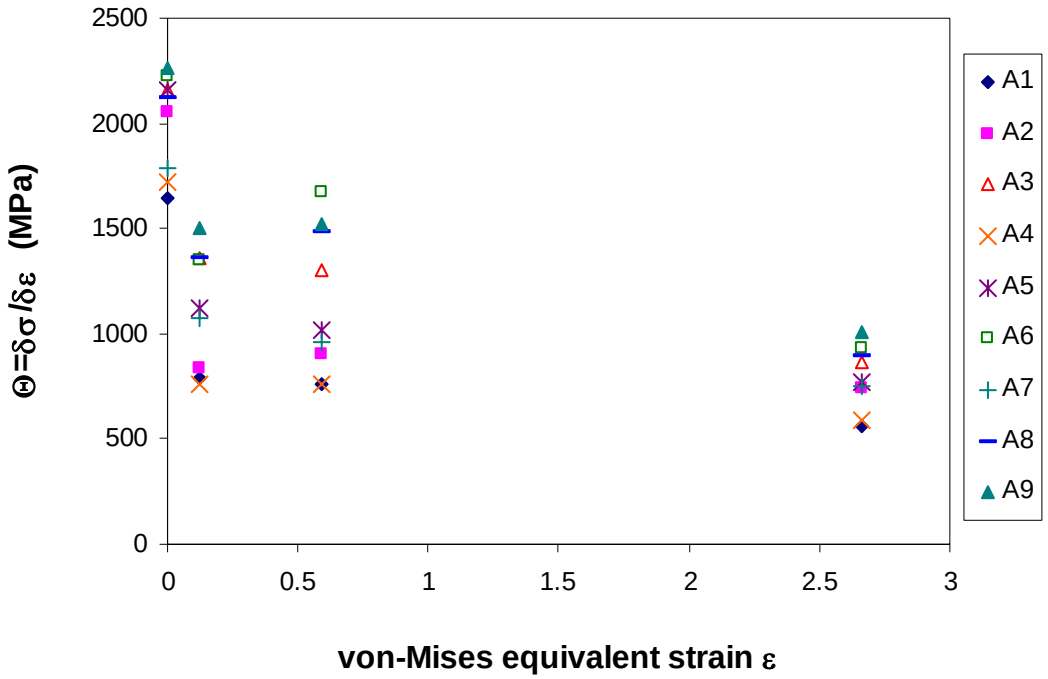

Figure 7.32 The influence of level of cold work on the average WHR between ε =0.01 and 0.03

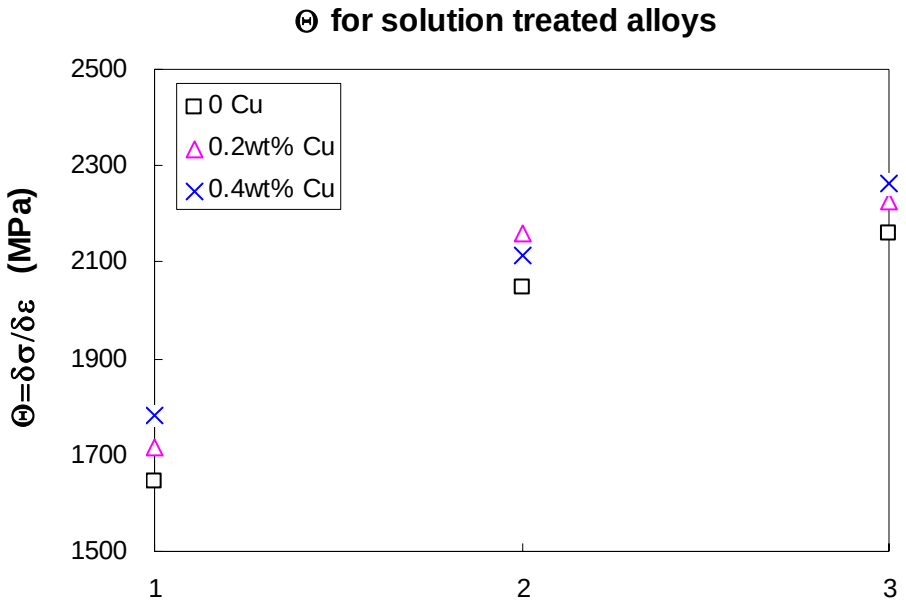
Θ for solution treated alloys
Θ=δσ/δε (MPa)
2500
2300
2100
1900
1700
1500
0 Cu
0.2wt% Cu
0.4wt% Cu
1
2
3
Mg content in wt%

a.

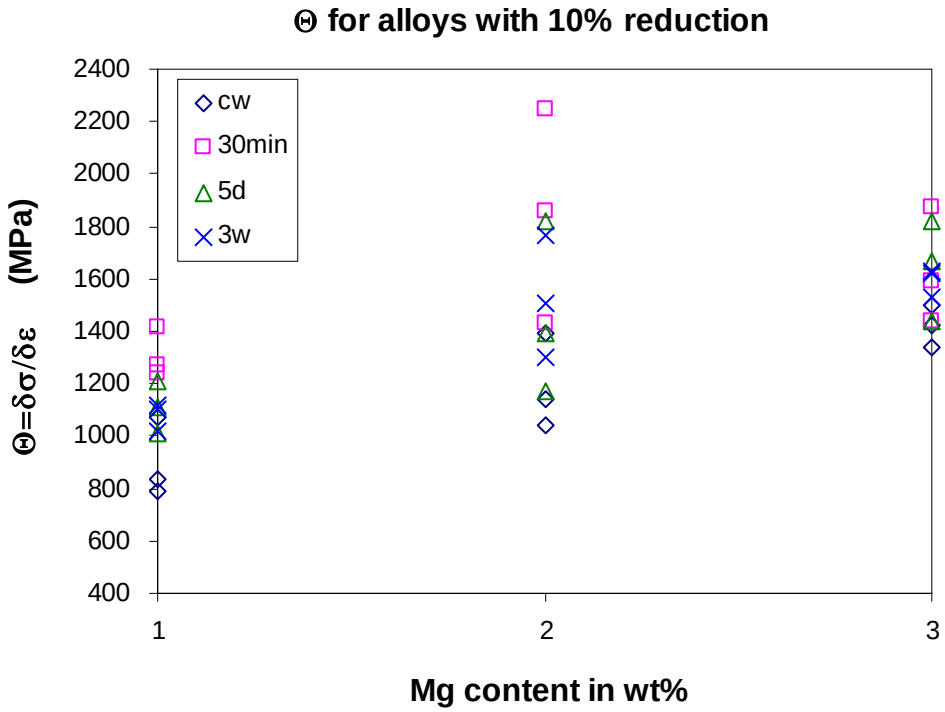
Θ for alloys with 10% reduction
Θ=δσ/δε (MPa)
2400
2200
2000
1800
1600
1400
1200
1000
800
600
400
cw
30min
5d
3w
1
2
3
Mg content in wt%

b.

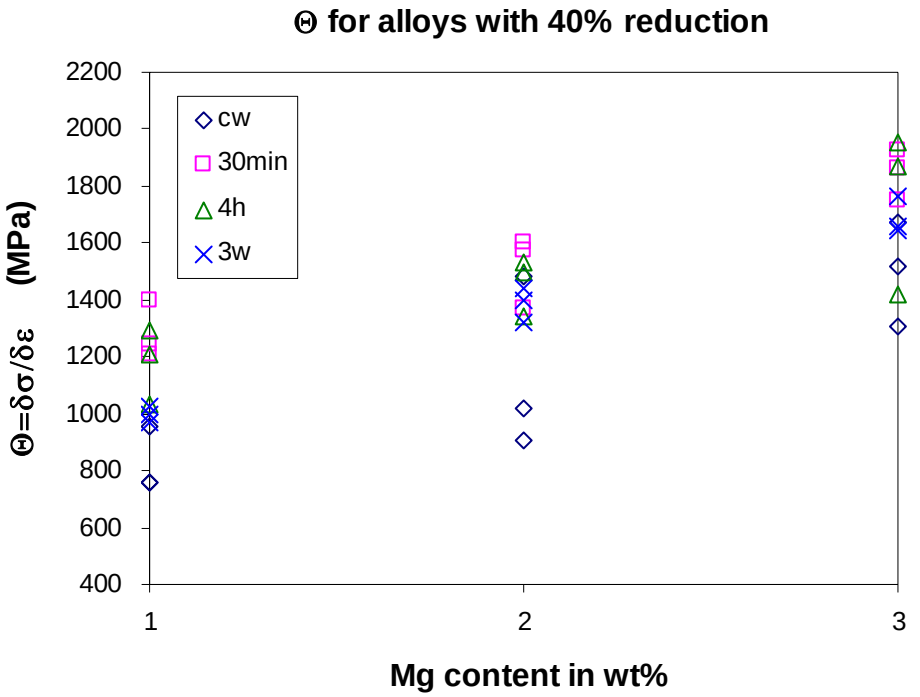

c.

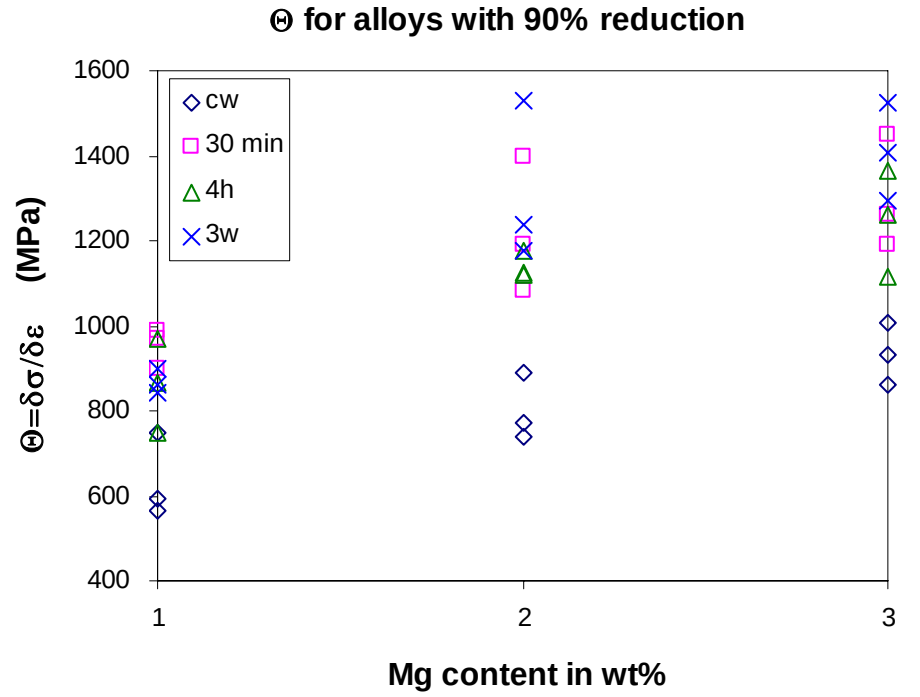

d.

Figure 7.33 The influence of Mg content on the average WHR between ε =0.01 and 0.03 at different cold-rolling reductions: a.0%, b. 10%, c. 40%, d. 90%

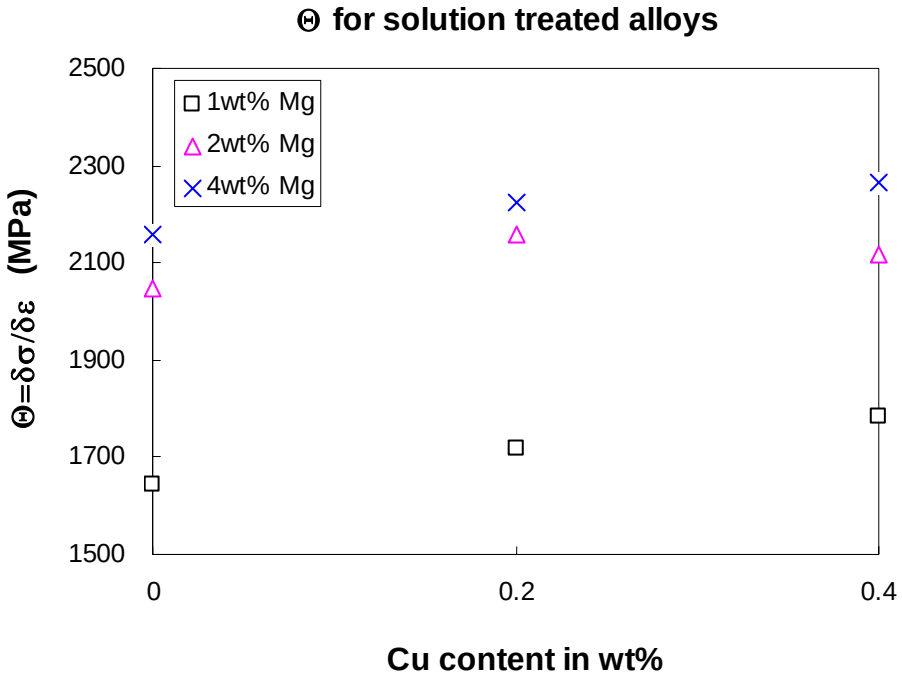
Θ for solution treated alloys
1wt% Mg
2wt% Mg
4wt% Mg
Θ=δσ/δε (MPa)
2500
2300
2100
1900
1700
1500
0
0.2
0.4
Cu content in wt%

a.

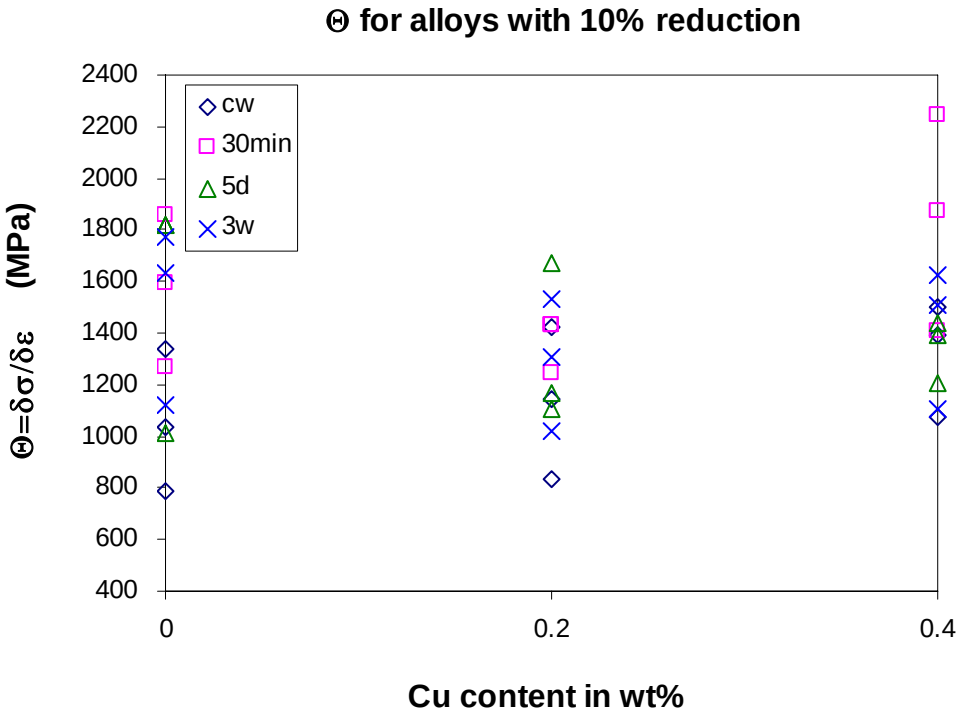
Θ for alloys with 10% reduction
cw
30min
5d
3w
Θ=δσ/δε (MPa)
2400
2200
2000
1800
1600
1400
1200
1000
800
600
400
0
0.2
0.4
Cu content in wt%

b.

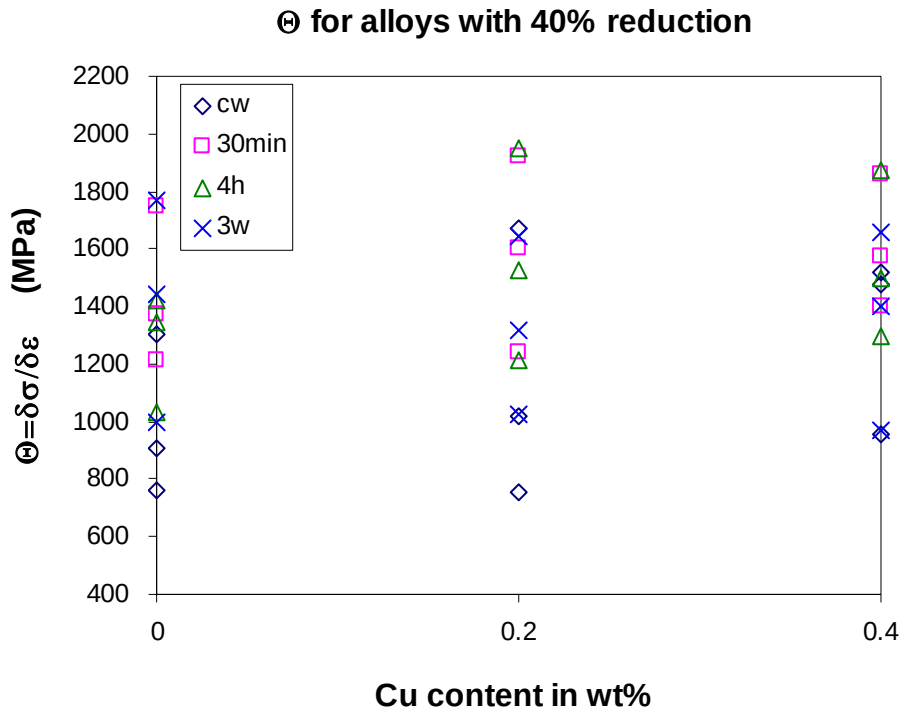

c.

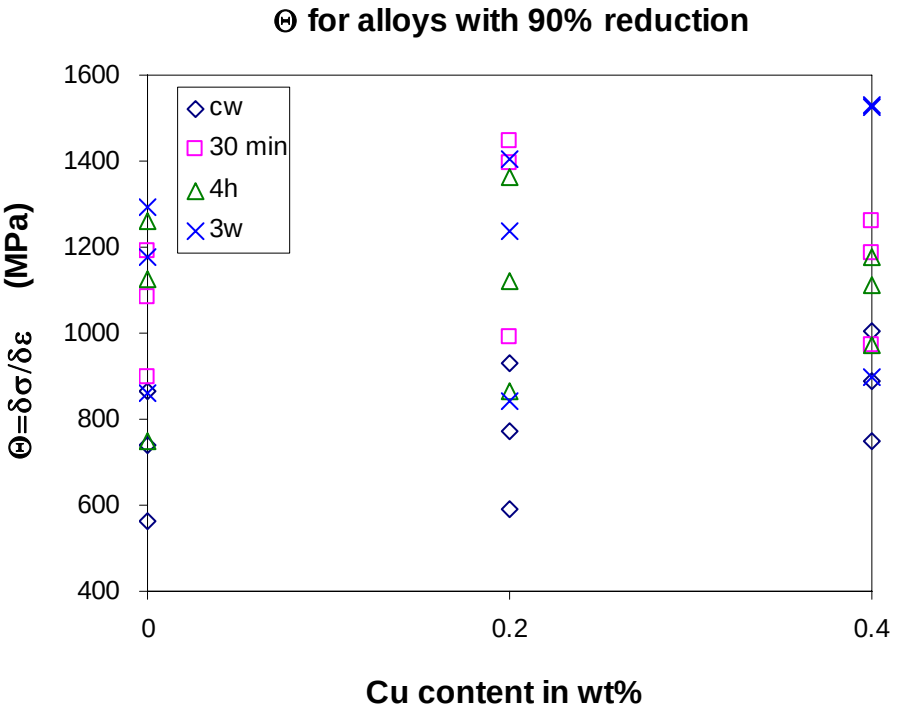

d.

Figure 7.34 The influence of Cu content on the average WHR between ε =0.01 and 0.03 at different cold-rolling reductions: a. 0%, b. 10%, c. 40%, d. 90%

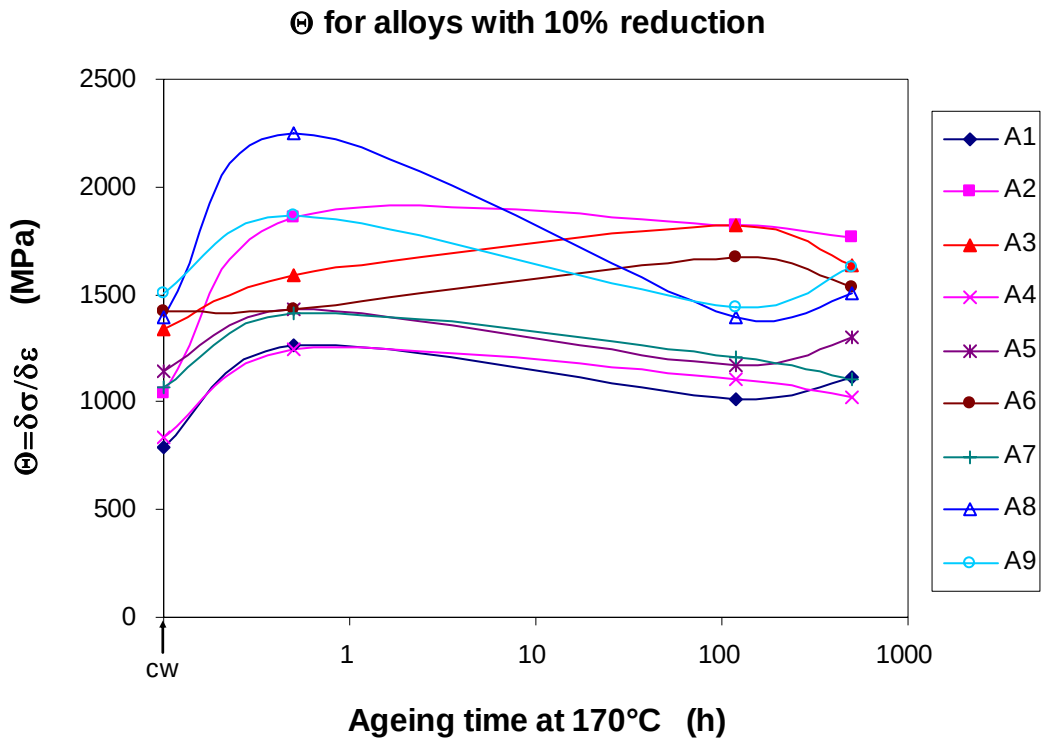
Θ for alloys with 10% reduction
Θ=δσ/δε (MPa)
2500
2000
1500
1000
500
0
cw
1
10
100
1000
Ageing time at 170°C (h)
A1
A2
A3
A4
A5
A6
A7
A8
A9

a.

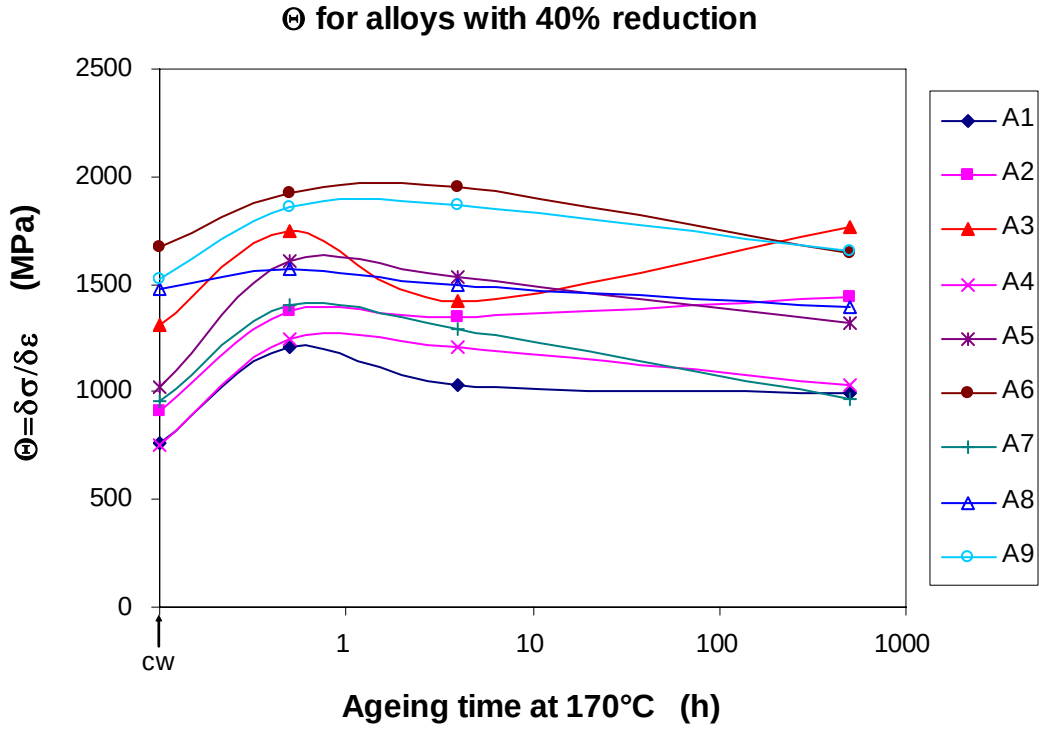
Θ for alloys with 40% reduction
Θ=δσ/δε (MPa)
2500
2000
1500
1000
500
0
cw
1
10
100
1000
Ageing time at 170°C (h)
A1
A2
A3
A4
A5
A6
A7
A8
A9

b.

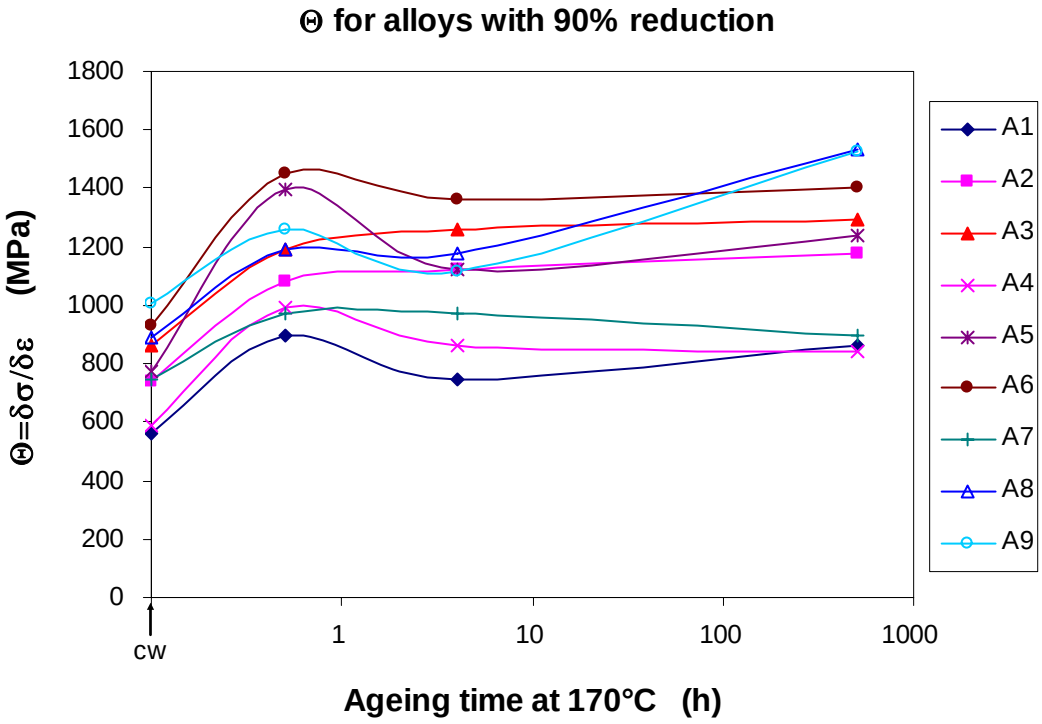

c.

Figure 7.35 The influence of ageing time on the average WHR between ε =0.01 and 0.03 at different cold-rolling reductions: a. 10%, b. 40%, c. 90%

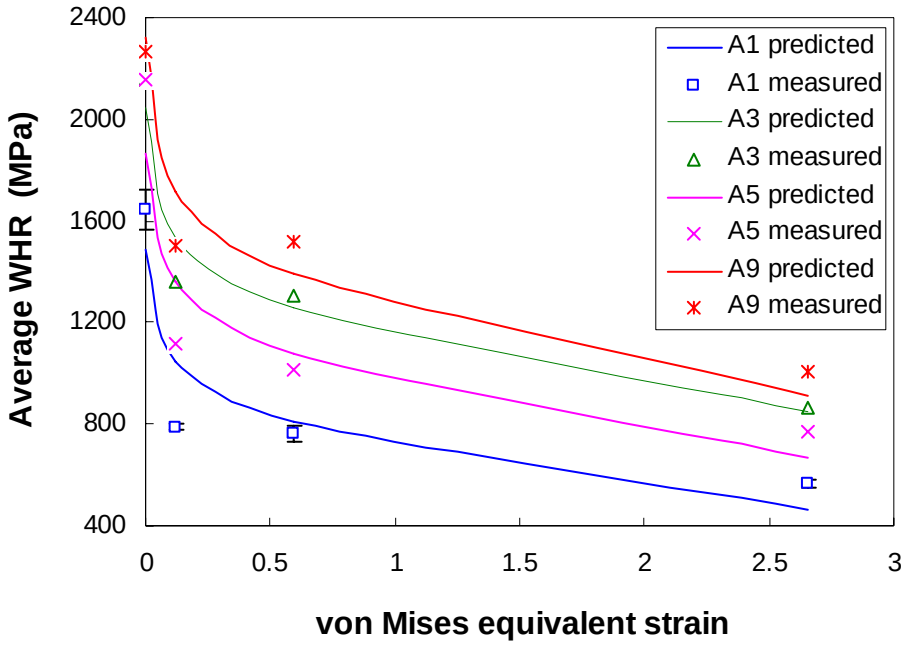

Figure 7.36 The training results for modelling the influence of cold work on the average WHR between ε =0.01 and 0.03

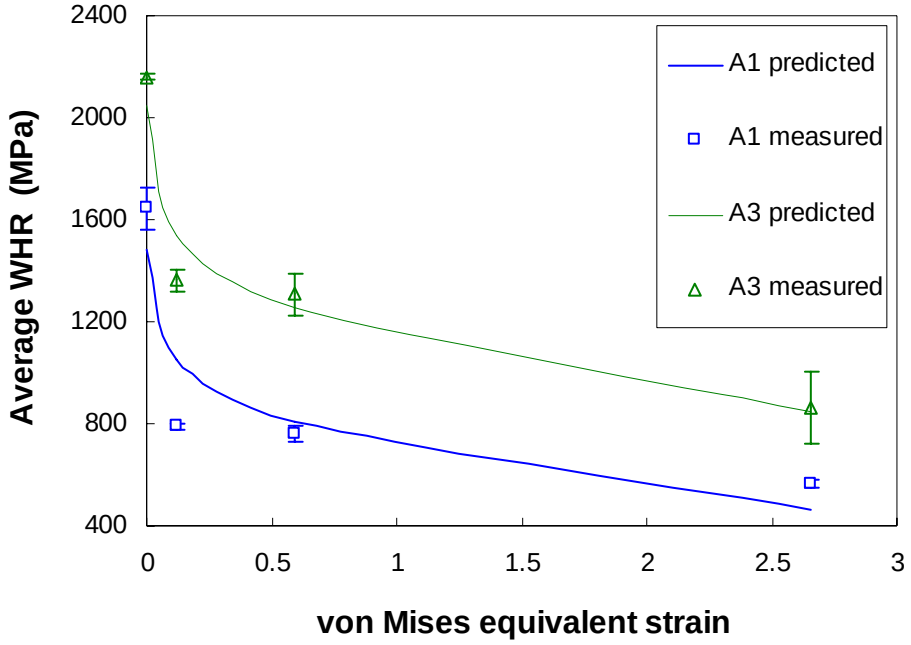

Figure 7.37 Examples of the training results for modelling the influence of cold work on the average WHR between ε =0.01 and 0.03 with error bars for the measurement results

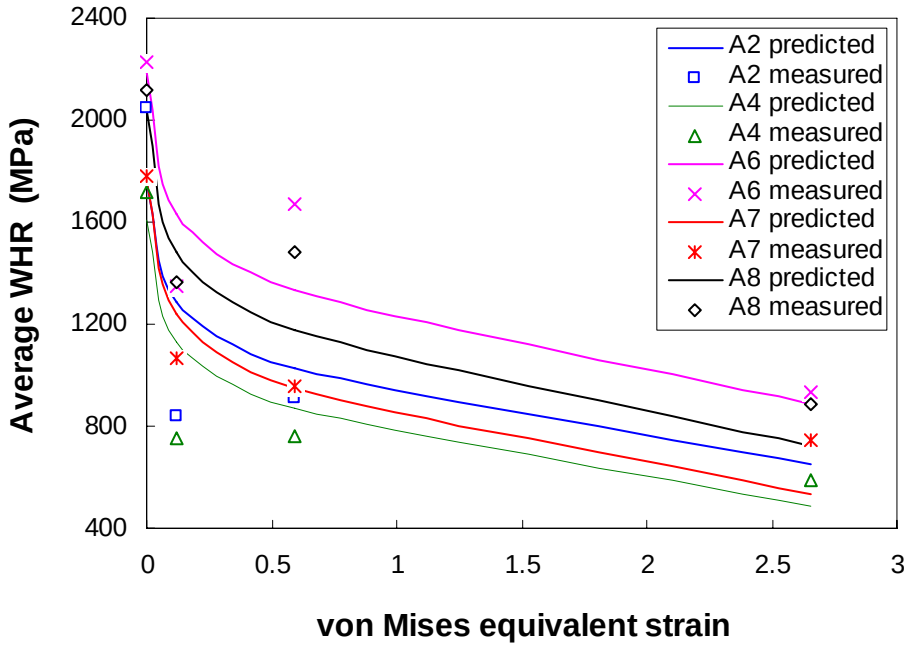

Figure 7.38 The testing results of modelling the influence of cold work on the average WHR between ε =0.01 and 0.03

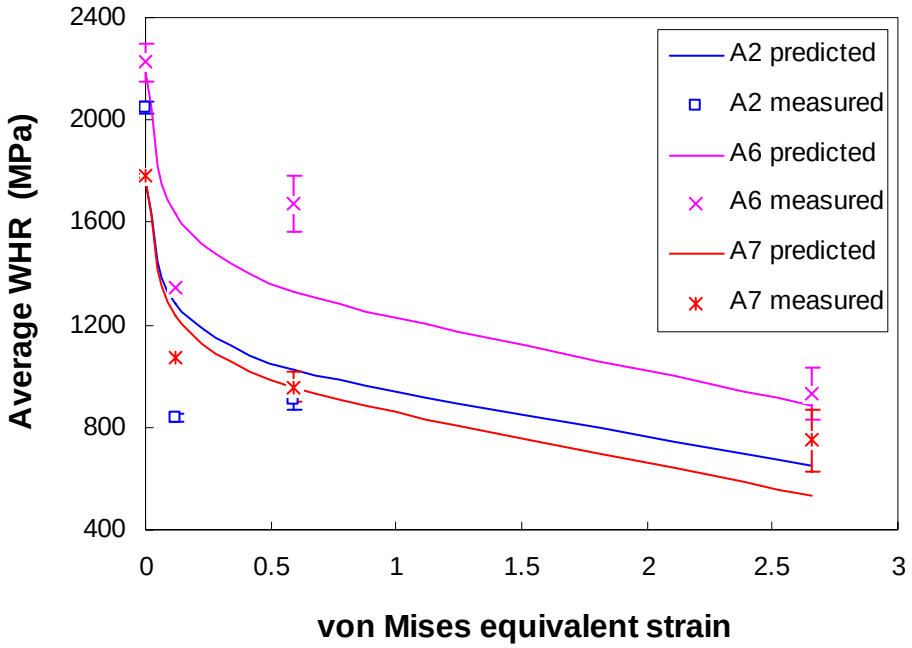

Figure 7.39 Examples of the testing results of modelling the influence of cold work on the average WHR between ε =0.01 and 0.03 with error bars for the measurement results

References

1. Deschamps, A., Niewczas, M., Bley, F., Brechet, Y., Embury, J.D., Le Sinq, L., Livet, F. and Simon, J.P., Philos. Mag. A, **79**, 1999, p. 2485.
2. Deschamps, A., Esmaeili, S., Poole, W.J. and Militzer, M., J. PHys. IV France, **10**, 2000, p. 151.
3. Esmaeili, S., Cheng, L.M., Deschamps, A., Lloyd, D.J. and Poole, W.J., Mater. Sci. Eng. A, **319**, 2001, p. 461.
4. Cheng, L.M., Poole, W.J., Embury, J.D. and Lloyd, D.J., Metall. Mater. Trans. A, **34A**, 2003, p. 2473.
5. Poole, W.J., Wang, X., Lloyd, D.J. and Embury, J.D., Philos. Mag., **85**, 2005, p. 3113.
6. Kocks, U.F., J. Eng. Mater.-T. ASME, **98**, 1976, p. 77.
7. Mecking, H. and Kocks, U.F., Acta Metall. Mater., **29**, 1981, p. 1865.
8. Mecking, H., ***Strain hardening and dynamic recovery***, in *Dislocation modelling of physical systems*, Ashby, M.F. (Editor), Oxford, Pergamon press, 1981, p. 197.
9. Estrin, Y. and Mecking, H., Acta Metall. Mater., **32**, 1984, p. 57.
10. Nes, E., Prog. Mater. Sci., **41**, 1997, p. 129.
11. Kocks, U.F. and Mecking, H., Prog. Mater. Sci., **48**, 2003, p. 171.
12. Dumont, D., Deschamps, A. and Brechet, Y., Mater. Sci. Eng. A, **A356**, 2003, p. 326.
13. Kocks, U.F., Philos. Mag., **13**, 1966, p. 541.
14. Kocks, U.F., Argon, A.S. and Ashby, M.F., Prog. Mater. Sci., **19**, 1975, p. 1.
15. Mecking, H., Nicklas, B., Zarubova, N. and Kocks, U.F., Acta Metall. Mater., **34**, 1986, p. 527.
16. Kocks, U.F., ***Constitutive Behavior Based on Crystal Plasticity***, in *Unified Constitutive Equations for Creep and Plasticity*, Miller, A.K. (Editor), London, Elsevier Applied Science, 1987, p. 1.
17. Kocks, U.F., Mater. Sci. Eng. A, **317**, 2001, p. 181.
18. Estrin, Y. and Kubin, L.P., Acta Metall. Mater., **34**, 1986, p. 2455.
19. Estrin, Y., ***Dislocation-Density-Related Constitutive Modeling***, in *Unified Constitutive Laws of Plastic Deformation*, Krausz, A.S. and Krausz, K. (Editors), Toronto, Academic Press, 1996, p. 69.
20. Estrin, Y., J. Mater. Process. Tech., **80-81**, 1998, p. 33.
21. Estrin, Y., Arndt, S., Heilmaier, M. and Brechet, Y., Acta Mater., **47**, 1999, p. 595.
22. Deschamps, A. and Brechet, Y., Acta Mater., **47**, 1999, p. 293.
23. Estrin, Y., Toth, L.S., Molinari, A. and Brechet, Y., Acta Mater., **46**, 1998, p. 5509.
24. Toth, L.S., Molinari, A. and Estrin, Y., J. Eng. Mater. Technol.-Trans. ASME, **124**, 2002, p. 71.

25. Roters, F., Raabe, D. and Gottstein, G., Acta Mater., **48**, 2000, p. 4181.
26. Goerdeler, M. and Gottstein, G., Mater. Sci. Eng. A, **309**, 2001, p. 377.
27. Karhausen, K.F. and Roters, F., J. Mater. Process. Technol., **123**, 2002, p. 155.
28. Furu, T., Orsund, R. and Nes, E., Acta Metall. Mater., **43**, 1995, p. 2209.
29. Furu, T., Orsund, R. and Nes, E., Mater. Sci. Eng. A, **214**, 1996, p. 122.
30. Marthinsen, K. and Nes, E., Mater. Sci. Eng. A, **234**, 1997, p. 1095.
31. Forbord, B., Marthinsen, K. and Nes, E., Mater. Sci. Forum, **331-3**, 2000, p. 557.
32. Marthinsen, K. and Nes, E., Mater. Sci. Forum, **331-3**, 2000, p. 1231.
33. Nes, E., Pettersen, T. and Marthinsen, K., Scripta Mater., **43**, 2000, p. 55.
34. Marthinsen, K. and Nes, E., Mat. Sci. Technol., **17**, 2001, p. 376.
35. Nes, E., Marthinsen, K. and Ronning, B., J. Mater. Process. Technol., **117**, 2001, p. 333.
36. Holmedal, B., Abtahi, S., Marthinsen, K. and Nes, E., Mater. Sci. Forum, **396-4**, 2002, p. 315.
37. Nes, E. and Marthinsen, K., Mater. Sci. Eng. A, **322**, 2002, p. 176.

8 Conclusions and Recommended Future Work

8.1 Experimental findings

In this thesis, nine Al-(1-3)Mg-(0-0.4)Cu-0.15Si (wt%) alloys have been studied. These alloys were cast, homogenised, hot rolled, solution treated and cold-rolled with three different reductions: 10%, 40% and 90%. During subsequent ageing of the cold-rolled samples, recovery and precipitation may occur depending on the alloy's composition. Several experimental techniques were used to study: 1) the microstructure, nano- and micro-structure evolution of cold-worked samples during isothermal ageing; 2) mechanical properties of cold-worked and cold-worked-and-aged samples; 3) recovery/recrystallisation, precipitation, work hardening and their interactions. The experimental findings of this study can be summarized as follows.

8.1.1 Microstructure

FEG-SEM and EBSD were conducted to study intermetallic particles, grain structure and texture. Predictions of phase diagrams using MTDATA software in conjunction with proprietary thermodynamic database were performed by Innoval Technology. The following conclusions can be drawn based on the experiments and predictions:

(1) Intermetallic particles align along the rolling direction. The size of the grains and particles decreases with increasing cold rolling reduction.

(2) Mainly three types of particles were observed and predicted in the cold-worked alloys: Mg_2Si, $Al_6(Fe,Mn)$ and $Al_{12}(Fe,Mn)_3Si$. For Cu containing alloys, some Cu may be present in the two types of Fe and Mn containing phases.

(3) No Mg_2Si particles were detected in the cold-worked samples of alloys with 1 wt% Mg, whilst they are present in the cold-worked samples of alloys with higher Mg (Mg>1wt%). This is consistent with MTDATA predictions.

(4) Based on the predictions, the maximum amount of Si removed by $Al_{12}(Fe, Mn)_3Si$ particles is about 55% of that taken out by Mg_2Si particles, when they are present.

(5) The texture becomes stronger with increasing level of cold work. Weak texture was detected in 10% cold-rolled samples, and in 40% cold-rolled samples the main component of the texture was identified to be {110} <211> (Brass) texture.

8.1.2 Recovery and recrystallisation

Hardness tests and tensile tests were performed on cold-worked samples isothermally aged at 170°C. DSC analysis of cold-worked specimens and cold-work-and-aged (two weeks at 170°C) specimens was conducted. The following primary observations for recovery and recrystallisation were made from these tests:

(1) No heat effect due to recovery was detected by the DSC runs. A clear heat effect around 320°C due to recrystallisation was detected in all the 90% cold-worked samples and a recrystallisation effect around 340°C was detected in some 40% cold-worked alloys by DSC. However, no recrystallisation effect was detected in any 10% cold-worked samples by DSC.

(2) Hardness tests revealed that on continued ageing after peak hardness, 90% cold-worked samples showed rapid recovery. The rate of recovery of hardness/strength decreases with decreasing cold rolling reduction.

(3) Work hardening rate (WHR) analysis based on tensile data showed a substantial increase in the WHR from the cold-worked state to the 30-minute aged condition. This indicates that during the first 30-minute ageing at 170°C, substantial recovery occurs in all the cold-worked alloys.

8.1.3 Precipitation

Age hardening during ageing at 170°C was assessed for cold-worked samples and solution treated samples solutionised at 550°C and 500°C (i.e. STH and STL samples). Precipitation hardening was measured by hardness tests and tensile tests. DSC was employed to assess the kinetics of reactions responsible for precipitation hardening. From these experimental results, the main conclusions are:

(1) Hardness tests on STH samples show substantial hardening during isothermal ageing for all alloys. DSC analyses suggest that for Cu-free alloys, the precipitation hardening is due to β″ (Mg_2Si) precipitation, whilst for Cu-bearing alloys, the precipitation hardening is due to Q ($Al_5Cu_2Mg_8Si_6$) sequence.

(2) For cold-worked samples, all the alloys except the Cu-free alloy A3 showed precipitation hardening during ageing. The Cu-free alloy A2 showed very little precipitation hardening.

(3) The precipitation hardening in the cold-worked Cu-free alloys is due to the β precipitation sequence.

(4) Both the β and S (Al_2CuMg) precipitation sequences may occur in the cold-worked samples of Cu-containing alloys. The DSC data suggest that high Mg/Cu content and high level of cold work facilitate the S precipitation sequence with the β precipitation sequence suppressed, whilst low Mg/Cu content and low level of cold work enhance the β precipitation sequence.

(5) For cold-worked samples, the time to peak hardness increases with decreasing cold rolling reduction. The enhanced precipitation reaction rate at higher cold-rolling reduction is due to a larger amount of dislocations which act as nucleation sites.

(6) DSC data indicate that the precipitation reactions in the STL sample of each alloy are similar to those in the cold-worked sample, which was confirmed by hardness tests.

8.1.4 Work hardening

Work hardening was studied by tensile tests at a constant strain rate of 0.001 s^{-1}. Analyses were performed on cold-worked samples, cold-worked-and-aged samples and solution treated samples. The following main observations are obtained:

(1) Generally the cold-worked conditions have the lowest work WHR, and ageing for 30 minutes at 170°C increases the WHR substantially regardless of alloy composition and prestrain. This is thought to be due to substantial recovery occurring in the first 30-minute ageing.

(2) On further ageing, the evolution of the WHR depends on the age hardening response of the alloys. For the non-heat-treatable alloys, the WHR increases with increasing ageing time. However, for alloys showing precipitation hardening, the WHR decreases with ageing time and it reaches a local minimum roughly at peak hardness. Subsequently it starts to increase with ageing time after peak hardness. The minimum WHR at peak hardness is usually higher than that of the cold-

worked state. But it can be lower than that of the cold-worked state if the level of cold work is low and the alloy has substantial age hardening.

(3) The WHR of cold-worked samples decreases with increasing cold rolling reduction. It increases with increasing Mg and Cu contents, especially for solution treated samples.

8.2 Modelling

A yield strength model has been developed and applied to describe the yield strength evolution of cold-worked samples of the nine alloys studied. Work hardening models based on the Kocks-Mecking (KM) model and Kocks-Mecking-Estrin (KME) model have been utilized to study the work hardening behaviour of the cold-worked samples and the cold-worked-and-aged samples, respectively. The following conclusions were made from the modelling work.

8.2.1 Yield strength modelling

For the ageing behaviour of cold-worked samples, a multi-mechanistic yield strength model for hardening and softening has been derived, which includes the following main components:

- Dissolution of intermetallic phases during solution treatment. Mg_2Si is the main phase responsible for differences in age hardening response between the alloys.
- Precipitation of two strengthening phases: β″ phase and S phase
- Strengthening contributions from solution strengthening, dislocation strengthening (i.e. work hardening and recovery) and precipitation hardening due to the two types of precipitates

The model has been trained and tested. An accuracy of about 8.6 MPa is achieved for unseen data (about 4.1% of the total range of strengths). Model predictions are generally consistent with microstructural data obtained from SEM/EDS, thermodynamic calculations, TEM/EDS and DSC, which includes the following main points:

- Undissolved intermetallic Mg_2Si particles are present in alloys with Mg≥2wt%
- For Cu-free alloys, age hardening is suppressed with increasing Mg content

- For alloys with 1wt% Mg and Cu≥0.2wt%, age hardening is due to both β″ and S precipitation
- For alloys with Mg≥2wt% and Cu≥0.2wt%, age hardening is mainly due to S phase precipitation

8.2.2 Work hardening modelling

Modelling of work hardening has been preliminarily conducted. For cold-worked samples, the KM model was applied to describe dislocation generation due to work hardening and dislocation annihilation due to dynamic recovery. The model works reasonably well with an accuracy of ~212 MPa for unseen data (about 12.5% relative accuracy). For the cold-worked-and-aged samples, the KME model which considers the additional contribution of precipitates on dislocation generation has been used. However, the model is insufficient to capture some of the trends observed in experiments. The failure of the KME model suggests that a new model will need to be devised in order to predict the WHR evolution of cold-worked samples during ageing.

8.3 Recommended future work

Based on the work conducted in this thesis, the recommended future work lies in experimental and modelling aspects.

8.3.1 Experimental

The following experiments may be rewarding:

- Ageing behaviour study of the cold-worked samples at different ageing temperatures. Some selected ageing conditions may be determined for tensile testing, the results of which can be used for the yield strength modelling. The influence of the activation energy of precipitation for the strengthening phases on the accuracy of the model can be critically assessed by the yield strength modelling at different ageing temperatures;
- TEM observations on 40% and 90% cold-worked and subsequently aged samples may be useful. But due to the high dislocation density, it may be very difficult to obtain some valuable results;

- TEM observations on selected solution treated and subsequently aged samples may be helpful for understanding age hardening of the STH and STL samples and provide some evidence for the corresponding DSC analysis;

8.3.2 Modelling

8.3.2.1 Yield strength modelling

The following work is recommended for the yield strength modelling:

(1) Further improvement of the current yield strength model for ageing behaviour of cold-worked samples. These include:

- Consider the dependency of the Taylor factor M on level of cold work
- Improve the models for work hardening, recovery and precipitation used in this study, for instance by applying the KME model (see 3.2.2) for dislocation evolution (work hardening), by applying a fractional approach or a sequential approach for recovery of flow stress (see section 3.3.2) and by applying the Kampman-Wagner approach [1-4] for precipitate evolution
- Incorporate the interactions between precipitation and recovery in the model

(2) Development of a yield strength model for ageing behaviour of solution treated samples

- Different precipitation sequence may occur in the STH and STL samples, which may be different from that of cold-worked samples.

8.3.2.2 Work hardening rate modelling

Work hardening rate measurement and modelling are always challenging. The following future work is suggested:

- To improve the accuracy of the KM model, the relation of k_2 (the dynamic recovery factor in the dislocation density evolution equation (7.9)) with alloy composition may need to be considered
- For cold-worked samples, other model rather than the KM model may be considered in order to improve the model accuracy
- For the cold-worked-and-aged samples, a new model other than the KME model may need to be developed to capture the main trends observed

References

1. Kampmann, R. and Wagner, R., in *Decomposition of Alloys: The Early Stages*, Haasen, P., Gerold, V., Wagner, R. and Ashby, M.F. (Editors), Oxford, Pergamon Press, 1986, p. 91.
2. Wagner, R. and Kampmann, R., in *Materials Science and Technology: A Comprehensive Treatment*, Cahn, R.W., Haasen, P. and Kramer, E.J. (Editors), VCH, Weinheim, Germany, 1991, p. 213.
3. Myhr, O.R. and Grong, ∅., Acta Mater., **48**, 2000, p. 1605.
4. Robson, J.D. and Prangnell, P.B., Acta Mater., **49**, 2001, p. 599.